UNIVERSITY OF LEEDS

Application of Geodesy to Improve Spatial Observations of Volant Insects using Weather Surveillance Radar

Freya Ione Addison

Submitted in accordance with the requirements for the degree of PhD. Climate and Atmospheric Science

The University of Leeds

Faculty of Environment

School of Earth and Environment

June 2025

Intellectual Property

The candidate confirms that the work submitted is her own and that appropriate credit has been given where reference has been made to the work of others.

This copy has been supplied on the understanding that it is copyright material and that no quotation from the thesis may be published without proper acknowledgement.

Acknowledgements

This thesis has been a labour of love and grit. Being a spoonie threw many more rocks and opened up pitfalls in this journey, but through the brain-fog I have persevered. The subject has evolved through wonderful collaborations with my colleagues exploring different avenues and questions in animated discussions and desperate meetings. I am proud of the individual work I have achieved in this thesis, but as with all science, I could not have done it without support.

George, my husband, this time has tested us in a multitude of ways, and despite everything we are still here. You have supported me through thick and thin. You have been my rubber duck and tech support. Thank you for helping back up my work, fixing my computer, providing servers when JASMIN failed, listening to me excitedly or exasperatedly explain my work and introducing me to coffee in the final months. I was only able to finish this, by you having my back.

My dearest daughter Ophelia, I hope you see this as a sign of resilience, not to give up on your dreams, and that you find your own passion. I love you and I am sorry for the late nights and missed bedtimes.

Thank you to my colleagues and advisors in the NCAS Radar Group, the Biodar Group and our collaborators at Chilbolton Observatory.

Another thank you goes out to Tim Darlington and Robert Scovell at the Met Office for their advice and collaboration.

Thank you to my family. It has been 20 odd years since I expressed an interest in science and doing a PhD, thank you for supporting my dreams and helping them turn into reality.

This thesis would not exist without Liz, Tom and Will, who have been enthusiastically in my corner since we took an abrupt turn into aeroecology and I am forever in their debt for their bug expertise and writing sessions. Liz, thank you for your mentorship, the swifty sparkle and the unwavering support.

Outside the academic hub, I would like to thank my Potter-heads group chat, and my Dungeons and Dragons group, in particularly Neil, who have been my cheerleading team, given me adventuring respites, writing sessions and have been a great sounding board.
Lastly, my PhD supervisor Neely, thank you. Neely has been my biggest supporter before I even started this PhD. Even when I thought I would give up, just a casual discussion about science completely unrelated, would give me the spark I needed to ignite that stubborn curiosity to complete what I had started. We have had numerous back and forths both supportive and full of debate about various ideas and analysis but really it is his kindness that makes him an exceptional supervisor and so understanding of all the bumps along the way.

Abstract

This work introduces an innovative approach for the precise positioning of weather surveillance radar (WSR) beam by applying geodesic methods in combination with corrections including atmospheric refraction to situate the observations within a global reference frame. In this unified framework, the collocation of disparate observational datasets may be accomplished. One of the products of this thesis is the collocation code, which pairs observations in the same space or identifies the closest matches, resulting in combining data from collocated radar voxels from WSRs Chenies and Thurnham from the UK Met Office (UKMO). This is essential for utilising WSR observations to examine ecological problems. The UK's "Flying Ant Day" is a unique phenomenon, characterised by the mass emergence of winged ants (*Lasius niger*) making it an ideal case study. To enable this, using high-fidelity anatomical scans, the radar cross-sections (RCS) of male and queen ants were simulated via electromagnetic modelling software. Combining these RCS values with UKMO WSR observations the biomass and number of ants was estimated: The average number of ants per km^3, where there was ant activity was between $10^4 - 10^5$. These observations were collocated against a Citizen Science (CS) Survey of $\sim$ 4700 responses over the period 2021 to 2022 of sightings of winged ants. The results show insect activity at altitude above 200 m, peaks a few hours before the peak of the CS responses of activity on the ground. The impact of the geodesic code written, underscores a significant enhancement in accuracy within WSR applications. The altitude of ant emergences typically could reach heights of $8\,km$. The improvement in altitude will facilitate research which requires high fidelity in the vertical. The aeroecology study has demonstrated an approach for quantifying the emergence patterns of these ant species with the UK Met Office, thereby laying the groundwork for broader aeroecological monitoring that can be synergized with diverse datasets.

Contents

List of Figures

List of Tables

Chapter 1

Introduction and Background

In an era of monumental environmental change and general ecosystem decay, robust monitoring, prediction and modelling is vital. The increasing frequency of extreme climate events, such as heatwaves and storms (H. Lee et al., 2023; AghaKouchak et al., 2020; Fischer et al., 2021), underscores the urgent need for continuous environmental observation. Weather Surveillance Radar (WSR) plays a crucial role in providing meteorological data that supports both weather forecasting and climate modelling (Saltikoff et al., 2019). Whilst insects serve as valuable bioindicators (Chowdhury et al., 2023) with significant ecological roles (D. L. Wagner et al., 2021), their monitoring remains largely confined to local scales including radar aeroecology (Didham et al., 2020). This interdisciplinary thesis seeks to advance WSR data processing techniques to enable more extensive aeroecological insect monitoring, bridging the gap between meteorological tools and ecological observation.

1.1 Aeroecology

Aeroecology is the study of *ecology*, life forms and how they interact with their surroundings in *aero*, the aerosphere (atmosphere). The very nature of aeroecology is inherently interdisciplinary, ecologists monitor and interpret the movement and behavioural trends of birds and insects, atmospheric scientists provide insight into the atmospheric dynamics and drivers of conditions for flight, engineers develop and maintain the instruments, data analysts store, analyse, and disseminate information, and conservationists follow the shifts in patterns and help to shape policy to implement protection (Chilson et al., 2017). Although aeroecology was first

defined in 2008 (Kunz et al., 2008), its origins date back to the 1940s and 1950s when weather radar was first used to study the movement and migration of birds (Lack and Varley, 1945; Lack, 1959; J. Gauthreaux, 1970), demonstrating its history of interdisciplinary collaboration between radar and ecology which continues to this day (Chilson et al., 2017; Shamoun-Baranes et al., 2019; van Gasteren et al., 2019).

The aerosphere is an integral part of the ecosystem, host to an abundance of fauna that rely on the aerosphere for at least part, of their lifecycle (Wilcove & Wikelski, 2008). Migration is one of such life stage (J. W. Chapman et al., 2015), with the iconic Monarch butterfly's journey from Mexico to Canada serving as a well-known example (Reppert & de Roode, 2018). Insectivorous aerial-hawking birds and bats (Norberg, 1986), depend on the aerosphere for feeding. One particularly fascinating phenomenon, Flying Ant Day (Hart et al., 2018), serves as the focal point of this thesis. During this event, ants exclusively use the aerosphere for mating and courtship, marking a critical phase in their lifecycle (Noordijk et al., 2008; Helms IV, 2018). This thesis will explore how advancements in radar technology can highlight different dynamics of this behaviour.

1.2 Insect Monitoring Methods

Monitoring insects presents unique challenges due to their small size and overwhelming numbers. The sheer diversity of insect species, combined with limited understanding of their status, has led the International Union for Conservation of Nature (IUCN) Red List to categorize many insects as "data deficient" (IUCN, 2022). However monitoring is critical to understand the scale and drivers of declines (Didham et al., 2020).

The study of fauna in the aerosphere presents distinct challenges to scientists, primarily due to the physical inaccessibility and dynamic nature of the atmospheric environment. Historically, human observation provided the earliest insights into aerial fauna, and this method remains fundamental in contemporary monitoring practices. Today, biodiversity monitoring serves purposes such as assessing population dynamics and tracking ecological health. The IUCN categorizes biodiversity monitoring techniques into six main types: acoustic devices and sensors, optical devices, remote sensing, telemetry and tracking tools, olfactory devices and

genetic methods (D. Dalton et al., 2024). Each approach has their own advantages and disadvantages, with suitability varying according to environmental conditions, target species, and monitoring objectives. Long-term monitoring schemes are typically preferred, as they provide insights into persistent trends and ecological changes beyond isolated case studies. However, many of the listed techniques are labour-intensive, temporally and spatially constrained.

Monitoring of insects is typically spatially and temporally restricted due to the standard methods employed. Each methodology has their biases and generally focusses on diurnal insects.

Malaise Trapping involves a big, typically white, tent, and a killing bottle, the insects flight path is intercepted by the tent and funnelled up into the killing bottle which is typically filled with ethanol (Uhler et al., 2022). Whilst the malaise trap can be deployed continuously, it still lacks the temporal resolution, as its only when the trap is emptied the cumulative biomass is collected.

Pan trapping involves a stake in the ground, and three brightly coloured bowls of different colours representing a variety of flowers to attract different insects. The pans are just above the ground and are typically filled with water and a little dish-soap to break the surface tension to drown the insects, over the course of the day (O'Connor et al., 2019). Pan trapping is good for pollinator insects but is not representative for beetles in the vicinity (Campbell & Hanula, 2007).

Transect walks are where the entomologist walks along a set track periodically throughout the day. They will use a net to catch and identify any airborne insects in the $1\ m^3$ volume space in front of them; This is a non-lethal way of identifying insects but does require a certain level of expertise not only to identify but also to catch insects efficiently. Transect walks are most suitable for grassland and vegetative areas, but not suitable sweeping nets for tree insects because they are not in air. These transect walks are used by the UK Butterfly Monitoring Scheme (UK Butterfly Monitoring Scheme, 2024) and Pollinator monitoring scheme (UK Pollinator Monitoring Scheme, 2024), providing consistent and annual data crucial for detecting population trends.

Habitat surveys are localised site reports which assess the availability of critical resources;

for example number and diversity of native and non-native plants, the amount of flowering plants for pollinators generally or for specific species such as bees (O'Connor et al., 2019). These can be combined with direct observations of insect activity Flower-Insect Timed (FIT) counts, where over a designated time period usually in the temporal order of minutes, one flower is monitored to count the number of visits from insects (UK Pollinator Monitoring Scheme, 2024). Habitat surveys, can be part of a long-term monitoring scheme or to assess the impact or potential impact of a new development of the land use (O'Connor et al., 2019).

Suction traps Rothamsted research operates a network of 16 suction-traps across the UK. The traps use a fan to suck in a volume of air up to $40\,m$ above the traps which stand at $12.2\,m$ tall. The traps are monitored and emptied daily from spring through autumn, but weekly over winter. Despite catching all small $=< 5\,mg$ insects, general biomass is not recorded in these traps, rather just an aphid count. The aphids are filtered and then sorted from the rest of the by-catch manually, which is an intensive process. This is an example of long-term monitoring of a specific species (Petsopoulos et al., 2021) and is used to provide farmers with a "risk forecast" of pests.

Light-traps Rothamsted also operate a network of 84 light-traps. The traps are monitored largely by volunteers and contractors so collection varies, typically they are emptied daily for the moths to be identified and recorded, no samples are taken (Bell et al., 2020; Bell et al., 2013; Montgomery et al., 2021).

Acoustic Sensors are passive sensors which record the soundscape of their environment, to understand ecological communication, wingbeats, abundance etc (Hill et al., 2018). Frequency of the sensor and base-line noise of the environment can be limiting factors to this methodology along with the intensive processing of data to isolate signals of relevance (Montgomery et al., 2021).

Citizen science initiatives now play a significant role in insect monitoring. Annual surveys such as the Big Butterfly Count (UK Butterfly Monitoring Scheme, 2024) and POMS' pollinating monitoring (UK Pollinator Monitoring Scheme, 2024), to rapid responses to pests with Asian Hornet Watch (Biological Records Centre, 2024). Involving the public enables a geographic reach that could not be achieved otherwise. And can provide in-

sight on temporal or environmental trends which may not have been recognised otherwise (Garratt et al., 2019; Sumner et al., 2019; Cunningham-Eurich et al., 2023). The Zooniverse organisation (Zooniverse, 2024), provides another example of citizen science, which empowers people to contribute to various forms of identification and provides a margin of error (Fortson et al., 2011), not seen in any other format. Engaging the public can improve science literacy, expand knowledge and interest in a subject, and has the potential to mobilise local change (Walker et al., 2021; Jallad et al., 2022; Roy et al., 2024).

The diversity of methods show there is not one, universal solution to monitoring insects. This multifaceted approach to monitoring will continue to be relevant. Radar is not part of this standard tool kit of monitoring, despite the research of Vertical Looking Radars (VLRs) in the early 2000s, and I think the summary of this thesis will help take us the next step forward to considering WSRs for part of the mix.

1.3 Insects

Insects play a vital role in the Earth's ecosystem, serving numerous beneficial functions. They are a nutrient-rich food source for a wide range of wildlife, significantly contribute to decomposition processes and soil health, and provide essential biological control, such as ladybirds preying on aphids. Crucially, insects are indispensable pollinators, with approximately three-quarters of global crop species depending directly on insect pollination (Bartomeus et al., 2014). Terrestrial arthropods, including insects, outnumber humans by over threefold, with an estimated biomass of 0.2 gigatons on Earth compared to humans' 0.06 gigatons (Bar-On et al., 2018). Insects also contribute significantly to biodiversity with an estimated 2-3 million species (Grimaldi & Engel, 2005). The majority of insects are capable of flight or are wind dispersed at least one stage in their lifecycle (Wilson, 1969).

Insects are among the most successful and adaptable organisms on the planet, having colonised nearly every type of habitat on Earth; from the hottest deserts of the Sahara to the coldest deserts of Antarctica; insects adapt to each extreme environment that would be inhospitable to most other forms of life. Temperate and tropical rainforests are places where insects flourish within the rich and intricate ecosystem at all levels, from below ground, to the forest floor, right up into the canopies. Freshwater ecosystems host an abundance of insects and even the

air forms the primary habitat for many insect species.

There are several factors that enable insects to exploit a wide range of ecological niches. Their small size gives insects advantages such as allowing them to live in microhabitats such as within the soil, inside plant tissues or on larger animals; their size can also help them conserve energy, an important factor in environments where resources are scarce. On a similar vein, the diversity of diets insects can survive on, contribute to their success in colonising all over the globe. Insects can also have rapid reproductive cycles, from the order of days to several months. Fruit flies, *Drosophila melanogaster*, are an example of this with their entire reproductive cycle completing in around 10 days under ideal conditions (Kumar, 2014). Comparing this to birds which is typically 4-12 weeks and mammals from a few months to a few years (Starrlight et al., 2019), this rapid cycle can lead to large influxes of insects responding to the environment before this is reflected further up the food web (Thompson, 1998).

Insects play a fundamental role in various ecological processes and ecosystem services. Around 90% of plants (Tong et al., 2023) rely on the animal kingdom, largely insects, for pollination. Pollination is critical for the fertilisation of flowering plants which can then go on to produce nuts, seeds and fruits. Insects have different rates of effectiveness for pollination, with honeybees typically the highest 39.8% (Garratt et al., 2019). However this is not the only factor, quantity, type of insect and insect diversity can all have an impact on the quality of the fruit produced; Garratt et al. (2014) study found that mineral levels differed and found yield in apple trees tripled when 25 different species of honey bee and hoverflies were present.

One of the benefits of pollinators, as they move from plant to plant, cross-pollination can occur, if the plant is of the same species. This accidental cross-pollination, has wide-reaching benefits, increasing diversity, which in turn helps the species adapt to a changing environment, disease and pests. As well as pollen, tiny seeds can also be transported by insects and ants, playing an active role in seed dispersal (Li Vigni & Melati, 1999).

Without insects decomposition would look very different, carpenter ants are an example of breaking down rotting woods which assists in decay and nutrient cycling with enriching the soil. Staying with nutrients, insects are nutrient rich and a high protein source for birds and small

mammals (Mwansat et al., 2015). Insects themselves are a complex web, with some, such as ladybirds acting as "pest control" eating aphids which would otherwise demolish an entire plant.

Taxonomic classification is broken down into 7 broad categories, shown in Figure 1.1, with the example being *L. niger*. Kingdom is the overarching category, encompassing all animals. The next level is Phylum, there are roughly 35 animal phyla with humans belonging to Phylum Chordata and insects to Arthropoda. Phylum Arthropoda are defined by segmented animals with hard exo-skeletons. Order follows class, hymenoptera covers ants, wasps and bees, with the defining features of four membranous wings. The two hindwings connect to the forewings with multiple hooks. Another distinguishing factor is the females having a particular ovipositor composed of three parts that can also pierce. Ants belonging to the family of formicidae. Genus follows family, with lasius being one type. Species is the final classification, there are 115 known species of lasius. *Lasius niger* is the species that is assumed it most dominant when examining emergences in Chapter 5, (Boomsma and Leusink, 1981; Hart et al., 2018).

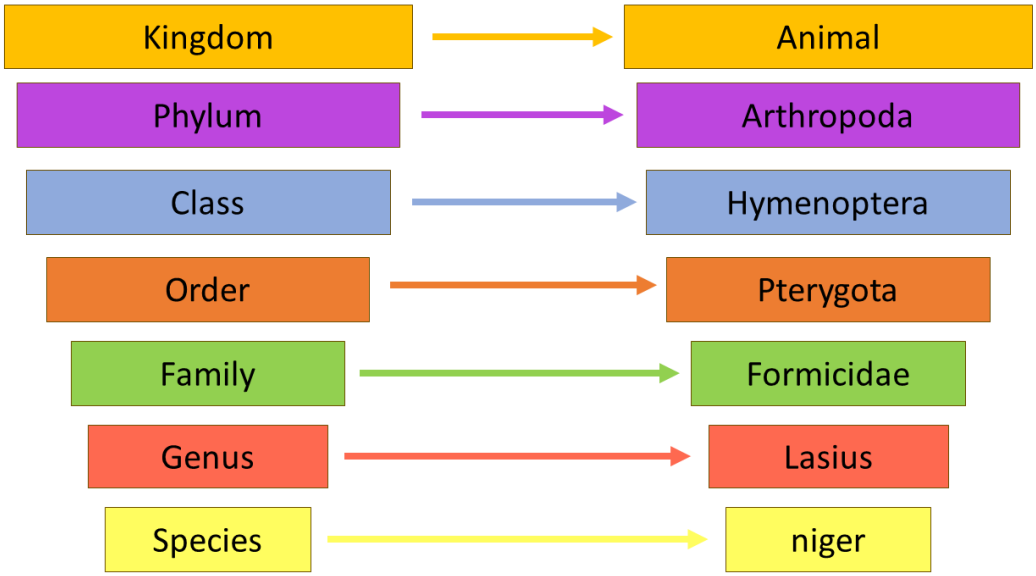

Figure 1.1: Taxonomic Classification for *Lasius niger*, from Kingdom to Species.

There are approximately 60 species of ant in the UK, with *L. niger*, also referred to as the common black garden ant, as one of the most prevalent species (Boomsma & Leusink, 1981), (Hart et al., 2018). Each year the new Queens leave the nest (Hart et al., 2018) on their nuptial flight, to mate with the smaller, winged males, to then go and establish their own new colony where the Queens can live for the next 20 or so years; having fertilised all their eggs in that

single day the Queens have no reason to leave the nest again. The males, having fulfilled their purpose, do not last more than a single day after their flight. The emergence of these winged ants is colloquially known as "Flying Ant Day", however, this is a bit of a misnomer as there are actually multiple days of mass flights during the summer season (June-September) (Van der Have et al., 2011), with Hart et al. (2018) narrowing this period down to July-August, with 97% of observations from the study occurring during this reduced time frame.

1.4 Global Declines in Insect Species

Insects are the largest and most diverse group of fauna on Earth. Their sheer abundance, makes totalitarian statements of trends harder to make, and thus alarming when made. The trend of global declines in insects is significant, with many high-profile studies (D. L. Wagner et al., 2021; Hallmann et al., 2017; R. M. Dalton et al., 2023) highlighting the devastating effect of the catastrophic loss of biodiversity and implications for ecosystems and ecosystem services. The general trend of global insect declines has been documented over all insect taxa indiscriminate of environment. Estimates predict around 40% of all insect species are at risk of extinction (Sanchez-Bayo & Wyckhuys, 2019). In some areas such as the Puerto Rican rainforests, the loss is even further pronounced with 98% of observed insect biomass decreased over 35 years (Lister & Garcia, 2018). In Europe and the UK this trend is reflected in insect population numbers, with Germany specifically showing a 75% decrease in flying insect biomass over 27 years in protected areas in Germany (Hallmann et al., 2017), and in the UK a 55% decline in upland pollinators (Powney et al., 2019). The loss of one insect species, may not signal the collapse of an entire ecosystem, for example the black bog ant (Goulson, 2019) has disappeared from wet heaths in Dorset and Hampshire in the UK with no apparent impact. However, we are not just talking about the loss of one species, but "death by a thousand cuts", with multiplicity of factors contributing to this decline, within the wider picture of climate change (D. L. Wagner et al., 2021).

1.5 Radar

Radar is an acronym that stands for RAdio Detection And Ranging (Doviak & Zrnic, 1993). The concept of using radio waves for detecting targets has been around since the late 1800s (Spartan Colloege of Aeronautics and Technology, 2021). In 1936, the pulsed radar was intro-

duced (Probert-Jones, 2014) but it is not until 1941, when it is said to be, the start of using radar for meteorology when a thunderstorm was tracked over the English Channel (Probert-Jones, 2014). Although radars were initially used to track aircraft, meteorological signals could always be seen (Probert-Jones, 2014) and towards the end of the 1940s, radar was developed specifically for weather surveillance (Bent, 1943).

Weather Surveillance Radar (WSR) are specialised radar systems primarily used to monitor atmospheric conditions and detect precipitation, storms, and other meteorological phenomena from the micro- and local scales ($< 1\,km$) to continental scale where multiple radars are used in a network. WSRs emit pulses of electromagnetic (EM) radiation, typically in the microwave spectrum, which reflect off precipitation droplets, ice crystals, insects, birds and other atmospheric constituents. By analysing the strength, timing, and frequency shift (doppler effect) of the returned signals, WSR systems can provide detailed real-time information on:

- Precipitation intensity and distribution
- Storm motion and structure
- Wind speed and direction
- Direction of severe weather phenomena (e.g., thunderstorms, tornadoes, hail)
- Monitoring of biological targets (e.g., insect and bird movements)

Now, dedicated radars for meteorology operate at much higher frequencies ($\sim 1.4 - 18.7$ GHz) (English, 2019; Meteoworld, 2015) than those used for detecting aircraft, because hydrometeors are an order or two smaller in magnitude, thus using shorter wavelengths allows the hydrometeors to be better detected (English, 2019). WSRs incidentally observe biomatter, e.g birds and insects (Vaughn, 1985; J. W. Chapman et al., 2011; Cui et al., 2019), in clear air, which in meteorology circles is classified as clutter. The European Network for the Radar Surveillance of Animal Movement (ENRAM) (Nilsson et al., 2019) and BirdCast (Eschliman & Horton, 2023) use WSR to track birds. There are target cases of using WSR for insect monitoring e.g Vaughn (1985), Cui et al. (2019), Stepanian et al. (2020), Anjita and J (2023), but this is yet to become an integrated practice.

Many countries have an established network of WSRs; for the United Kingdom (UK), the Met Office (UKMO) operate 15 WSRs, providing near, complete national coverage as shown by Figure 1.2.

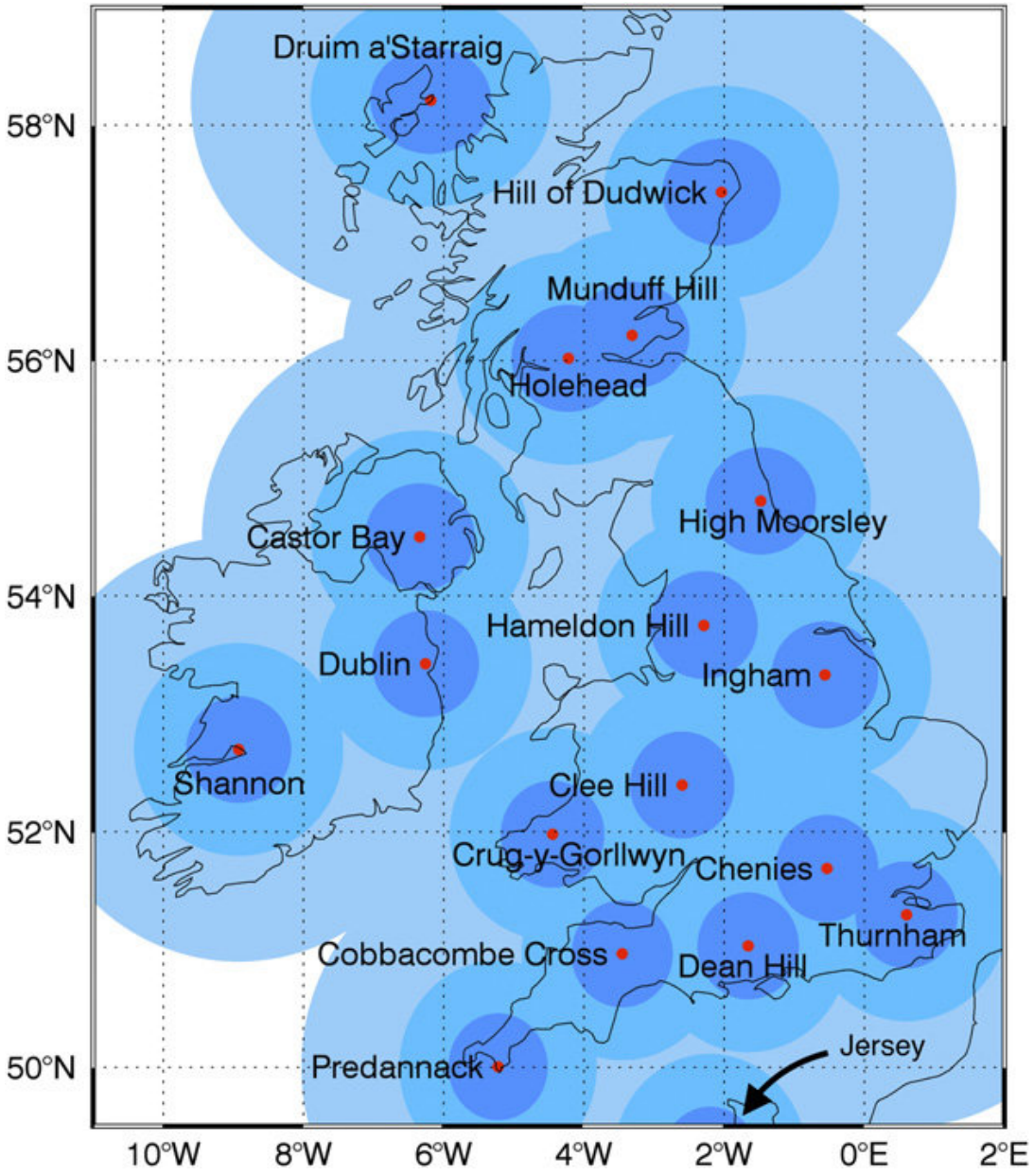

Figure 1.2: "Locations of Met Office and Met Eirrean radar sites (labelled red dots) comprising the Met Office 1-km radar-derived precipitation composite. The filled circles indicate distances of 50, 100, and 200 km from the individual radars." (Fairman et al., 2017)

Radars emit pulses of electromagnetic (EM) radiation. The emitted waves travel through the atmosphere until they hit a target, where they are either absorbed or scattered (reflected or refracted). After emission, the radar array will then switch to listen for the return echo; the backscattering of the pulse it last emitted. In this listening period, the radar estimates the

direct distance to each pulse using Equation 1.1, and bins the signals into their appropriate range gates. A range gate is the binned distance, with the total distance defined as the time delay between emission and receiving, equating to an approximate distance of "range". The direct distance between the target and the radar is calculated by using the speed of the EM wave and the time taken between emission and the received echo shown by Equation 1.1 where c is the speed of light, t is the pulse interval and r is the range.

$$r = \frac{ct}{2} \tag{1.1}$$

Equation 1.1 is representative of a wave travelling through free space, in the Earth's atmosphere, refraction alters the path of the wave and thus this equation is not representative of the actual condition and is used merely as an estimate.

1.5.1 Scanning Geometry

A radar has a geophysical location (ϕ, λ, h_r) on a global reference frame. The altitude as a standard format should refer to the altitude of the antenna above MSL and not the physical footing of the radar on the ground. The horizontal pointing angle of the radar is referred to as azimuth, as this azimuth is elevated, its reference frame is from the radar antenna. The elevation angle θ, is also relative to the radar antenna, at $\theta = 0^o$ the angle from the ground to the antenna is approximately 90^o at the local horizon, also demonstrated in Figure 1.3, at $\theta = 90^o$, the antenna is zenith pointing (straight up).

There are nominally three different scanning strategies that a WSR employs; a Plan Position Indicator (PPI), which changes in azimuth but has a fixed elevation; a Range Height Indicator (RHI), which is the opposite of a PPI with a fixed azimuth and changes in elevation; and the stare, typically done in the vertical for geophysical calibration of Z_{DR} (Fabry, 2015). WSR, for meteorological offices around the world (Rennie, 2012; Darlington et al., 2016; Min et al., 2019) typically use PPIs at a number of elevations, as this is the most efficient strategy that covers the largest spatial area in the shortest time. A PPI can show the area that a storm is covering and track it. RHIs are able to give greater detail in the vertical than a PPI, and are able to show with greater specificity in vertical detail.

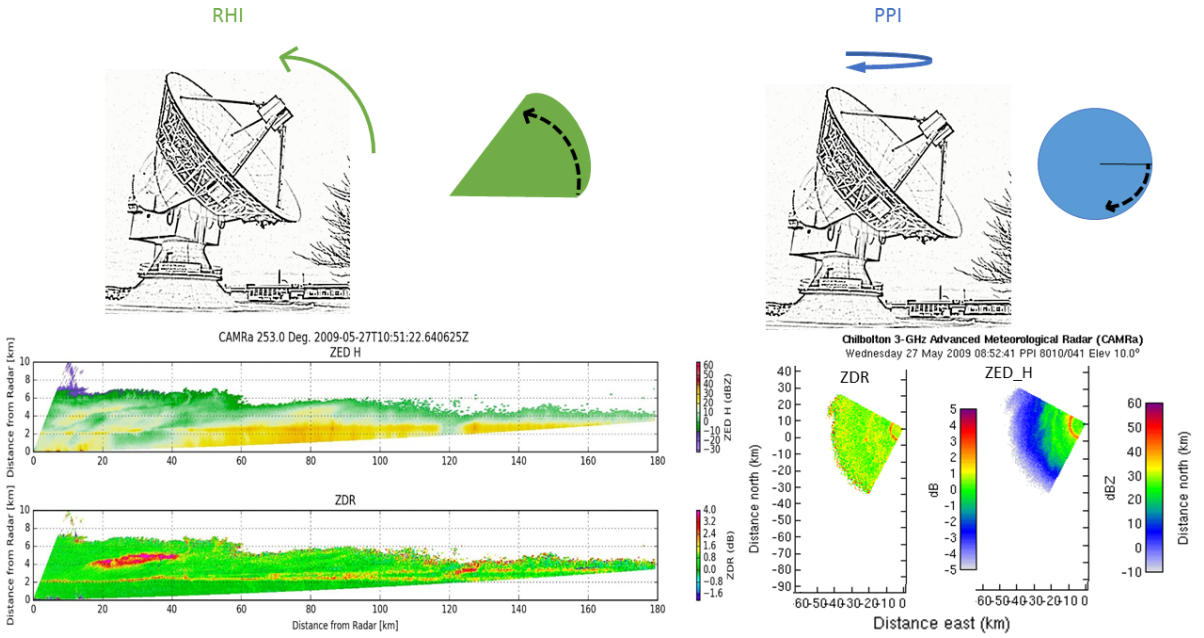

Figure 1.3: Demonstration of Radar scans and their outputs. In green is the Range Height Indicator (RHI) where the antenna has a fixed azimuth and rotates along the x-z plane, for a change in elevation, the output shows a long range and detail in height at that angle (a vertical cross-section). In blue is the Planned Position Indicator, which has a fixed elevation and rotates along the x-y plane, so changes its position in the azimuth doing a full sweep to get a horizontal cross section of the sky. The outputs are produced from Chilbolton Advanced Meteorological Radar (CAMRa), created for Freya I. Addison's MRes Dissertation 2017.

1.5.2 Volume

The radar beam is a volume; To visualise the beam, the radiation pattern of a radar is shown graphically in Figures 1.4 and 1.5. The further out in range from the radar, the wider the beam becomes. Equation 1.2 shows the relationship between range and volume, r_{rg} is the length of a range gate, or the distance between the midpoint of two consecutive range gates. The main lobe, refers to the area of peak intensity. The main lobe would be what is considered the theoretical radar beam in Figure 1.4, with the width the same as the beamwidth, as shown in Equation 1.2. The main lobe is shown clearly labelled as the peak power curve in the top centre of the diagram of the horizontal radiation pattern (Figure 1.4), and the sidelobes cover all the other curves. Typically the main lobe is where the information for the return is received and used, however in the case of a WSR, sometimes when there is an extended signal, which fills a larger volume of space than the main lobe, the signal is truncated to the region of highest sensitivity. Each radar will have its own unique radiation pattern, it is important to ascertain where the sidelobes are and to reduce noise from the sidelobes. High sidelobe attenuation (the

distance between the main lobe and sidelobe) is good and sidelobes can be further suppressed with additional antennae typically used in the military where precision is important (Wolff, n.d.).

$$V_{Beam} = \frac{\pi}{4} r^2 (\Delta r_{rg}^2) \theta_{BW}^2 \tag{1.2}$$

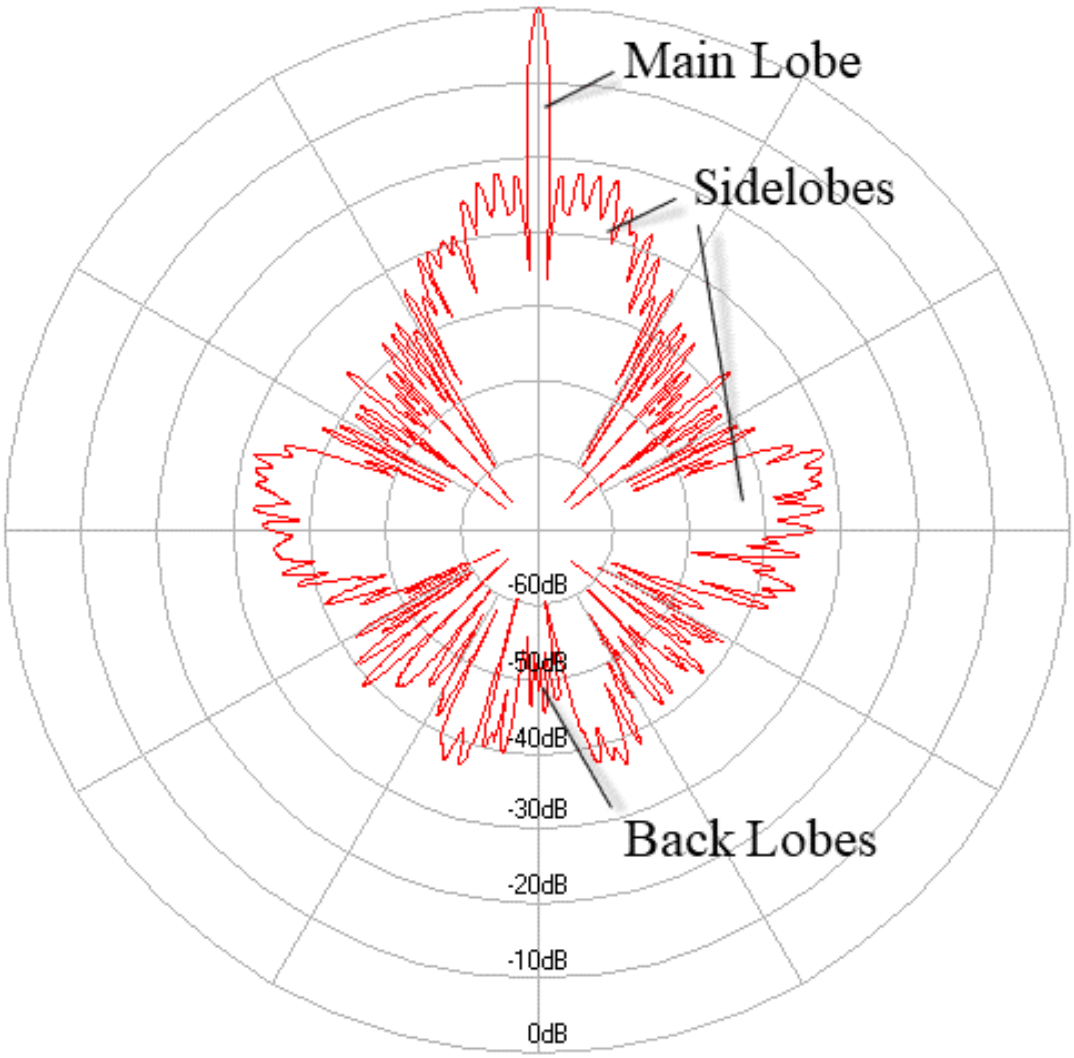

Figure 1.4: Horizontal cross-section of a radiation pattern with the main lobe (main beam), due north, and the antenna at the center (0,0), the sidelobes and back lobes representing the maximas of diffraction. (Wolff, n.d.)

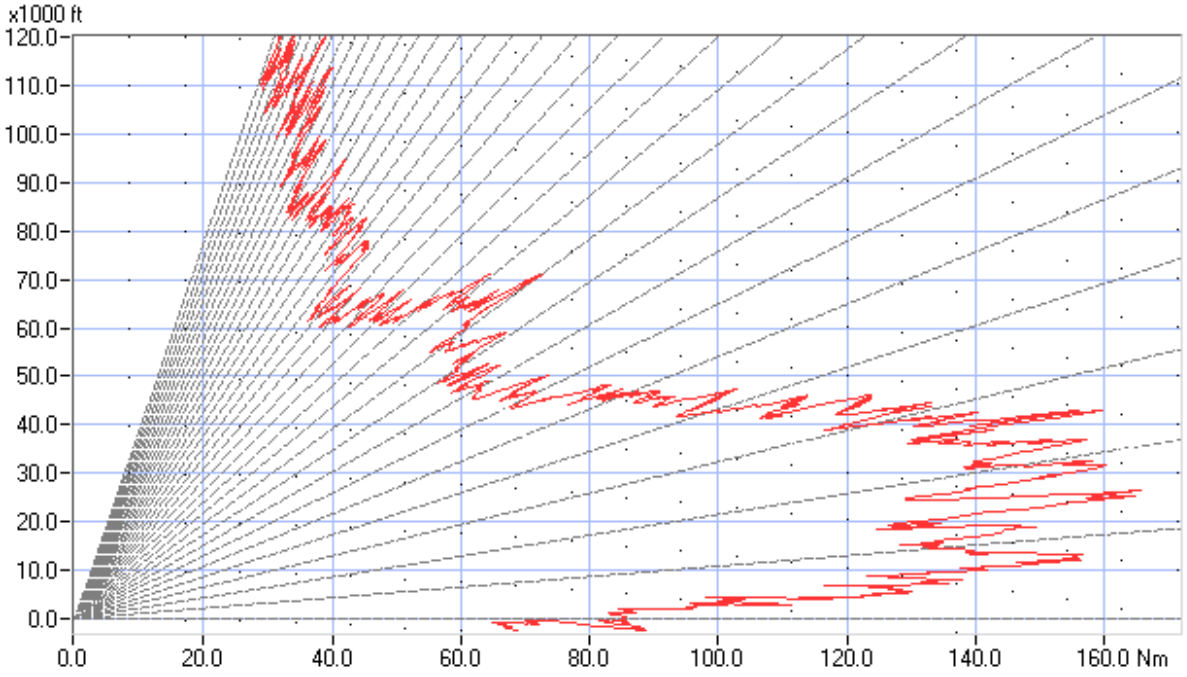

Figure 1.5: Vertical cross-section of a radiation pattern, x-axis in Nautical miles and y-axis in feet. The lines are 0.5^o steps (Wolff, n.d.)

A radar voxel, (the area of observation), is a volume section of the radar beam along a given azimuth and elevation, at a specified range. The radar beam is broken up along the range into range gates, of set length shown by Figure 2.2. In Figure 1.3, the pixels represent a radar voxel. Due to the radar's beam divergence, voxels closer to the radar have smaller spatial volumes and thus higher resolution, accommodating fewer maximum targets. In comparison, voxels at greater distances encompass larger volumes, reducing resolution by including more potential targets.

$$V_{voxel} = \frac{\pi}{3} r_g \tan\frac{\theta_{bw}}{2}(r_i^2 + r_{i-1}^2 + r_i r_{i-1}) \tag{1.3}$$

Range resolution is dependent on the pulsewidth, the target, and the efficiency of the radar receiver. To distinguish between targets the minimum distance between is half the pulse width time as shown in Equation 1.4, with c, the speed of light, PW the pulsewidth and BW the beamwidth.

$$r_{res} = c \cdot \frac{PW}{2} = \frac{c}{2BW} \tag{1.4}$$

The angular resolution is related to the beamwidth and beamheight of the radar, it is defined by Equation 1.5, with r the direct distance between the voxel and the radar, and half the

beamwidth angle θ_{bw}. The beam width is a Gaussian curve, where the power is greater than the given set of lower limits of power. At a given range the resolution is approximately $3dB$ the BW of the radar (American Meteorological Society, 2024a). The voxel resolution is proportional to distance with the volume calculated in Equation 1.3. Equations 1.5 and 1.3 both make the assumption that the beamwidth and beamheight are the same for simplicity's sake, but note this is not always the case. The beam width and height can be configured independently, for example creating a wider beam height to cover a larger range of altitudes, useful for tracking.

$$AngularResolution = 2r \sin \frac{\theta_{bw}}{2} \tag{1.5}$$

1.5.3 Radar Cross Section

The radar cross section (RCS) is the signature of the reflected energy of an object. RCS is determined by the size, shape and reflectivity (its material and dielectric constant) of the object as well as the radar's emission frequency (Addison et al., 2022). A spherical object composed of a single, uniform material possesses an inherent symmetry in terms of its radar cross-section (RCS), which remains constant regardless of its orientation relative to the radar system because its scattering equally distributes the radar energy in all directions (Li & Kiang, 2005). Conversely, real-world objects such as aircraft or birds exhibit anisotropic scattering characteristics due to their non-spherical shapes and complex structures. As a result, their RCS varies significantly depending on the direction from which the radar wave approaches or interacts with them. This variation in RCS with orientation is a critical factor in radar target detection, classification, and identification. The RCS of an ant is modelled in Chapter 4.

1.5.4 Radar Outputs

Single-polarization radars emit waves with a single orientation of the electric field, typically either horizontally or vertically. On the other hand, dual-polarization radars emit signals with both horizontal and vertical orientations simultaneously, as illustrated in Figure 1.6. This dual-polarization capability allows for the collection of more information from the radar's target area. This additional information enhances the radar's ability to distinguish between different types of targets, as depicted on the right-hand side of 1.6. It is important to note that the direction of the radar wave is perpendicular (orthogonal) to both the orientation of the electric

field (determined by polarization) and the direction of wave propagation. This characteristic of radar waves plays a significant role in how they interact with targets and surfaces.

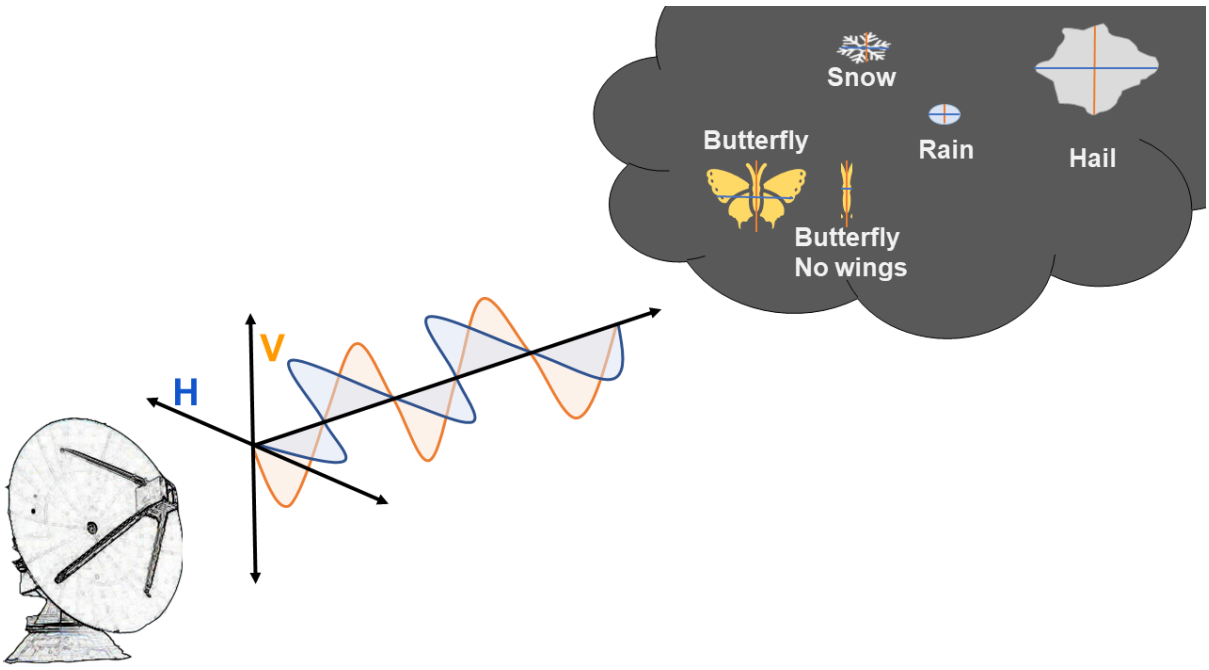

Figure 1.6: Dual Polarisation for Radar impact on targets

The radar equation refers to the proportion of power received and is related to the radar parameters, the path the signal takes and the properties of the target. Equations 1.6 (Fabry, 2015) is an example of a radar equation; P_r is the returned power, and P_t is the transmitted power. A, is a group of constants. The first fraction of Equation 1.6 relates to the radar parameters, with τ the length of the pulse, D, the diameter of the antenna, and λ the wavelength. The second fraction is the path that the wave takes, T refers to the transmittance of the atmosphere between the radar, point 0, and the range (r). σ, the final part of the equation relates to the target properties (Fabry, 2015). The radar equation has different variations, in the case of a weather radar, certain assumptions have to be made about the target, for example the target properties if rain, would include the dielectric constant $||K||^2 = 0.93$ (Fabry, 2015).

$$P_r = A\frac{P_t \tau D_a^2}{\lambda 4}\frac{T(0,r)^2}{r^2}\sigma i \tag{1.6}$$

In this thesis, the focus is on using WSR to survey insects, thus only select radar variables are used; The reflectivity factor, Z, differential reflectivity Z_{DR}, the cross correlation ratio ρ_{HV} and the depolarization ratio DR.

The reflectivity factor, Z, henceforth known as reflectivity, refers to the ratio of power received by the radar antenna due to backscattered signals from a target. It quantifies the proportion of incident radar energy that is returned and detected by the radar system. Equation 1.7 shows that reflectivity, Z, is equal to the sum of the number of targets per unit volume $N(D)$ and D is the diameter of the target. Reflectivity can also be related to the Radar Equation 1.6, when defined in logarithmic units dBZ. Equation 1.8, is specific for rain as the dielectric constant is 0.93 for water, and η refers to the radar reflectivity of precipitation (American Meteorological Society, 2024b). A high reflectivity means a high proportion of backscatter, which indicates there is a large surface area to be scattered back from, this could be from lots of tiny objects or something very large.

$$Z = \int_0^\infty N(D)D^6 dD \tag{1.7}$$

$$Z = \frac{\eta\lambda^4}{0.93\pi} \tag{1.8}$$

Differential Reflectivity, Z_{DR}, is the difference between the vertical and horizontal signals. Z_{DR} can indicate the shape of the targets' profile that is facing the direction of the radar. If Z_{DR} is approximately zero then the face is close to a circle/spherical, if it is positive it is larger in the horizontal orientation than the vertical and if negative, larger in the vertical orientation than horizontal, the bigger the difference the greater the elongation.

$$Z_{DR} = 10log(\frac{Z_H}{Z_V}) \tag{1.9}$$

Cross Correlation coefficient (ρ_{HV}) is the similarity between different targets within a scan. It compares the power and phase for the returns in the horizontal and the vertical; very high ρ_{HV} would mean the targets are similar, expected for a rain cloud.

In meteorological targets, it is common to have high ρ_{HV} **and** $Z_{DR} \simeq 1$ in linear units compared to all other targets (Kilambi et al., 2018). Equation 1.10 is the depolarization ratio DR which represents this uniform relationship. It can be used to help identify the presence of non-spherical particles, or other scattering mechanisms that can alter the polarization state of

the emitted wave.

$$DR = \frac{Z_{DR} + 1 - 2Z_{DR}^{\frac{1}{2}}\rho_{hV}}{Z_{DR} + 1 + 2Z_{DR}^{\frac{1}{2}}\rho_{hV}} \tag{1.10}$$

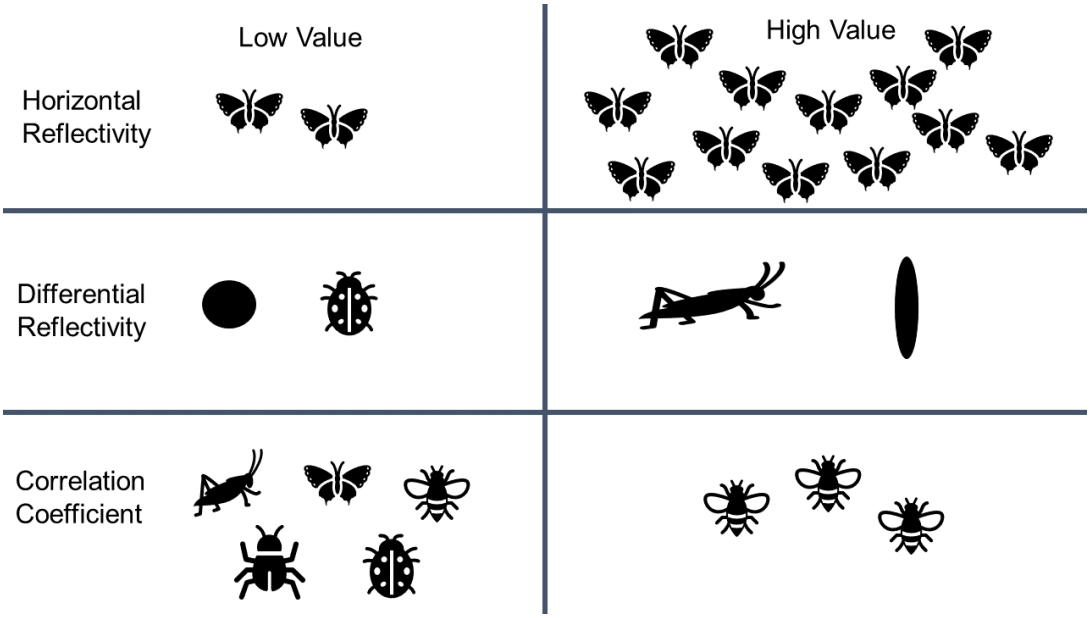

Figure 1.7: Radar variables with idealised correlation to insect descriptors

Figure 1.7 shows an idealised version of what each radar variable could indicate in terms of bioscatterers. Reflectivity is correlated with the number of targets, so a higher value of Z, could indicate the presence of greater activity e.g of insects. Differential reflectivity is the ratio between horizontal and vertical, with a low value of Z_{DR} possibly indicating more spherical targets, such as a rounded bee fly, and high values indicate elongated insects, so on a microscale this could be thrips and on a larger scale, locusts. Directionality also plays a role in Z_{DR} and this is explored further in Chapter 4; for example, a bee, where the wings are not picked up on the radar, head on could have very low Z_{DR} when facing head on towards the radar. Low ρ_{HV} could suggest greater diversity in the bioscatterers as shown in Figure 1.7. Migrating insects falling at $\rho_{HV} = 0.7$ (Bachmann & Zrnic, 2007) or for insect swarms $0.8 \leq \rho_{HV} \leq 0.9$ and precipitation above 0.9 (S. Gauthreaux & Diehl, 2020). DR can be used to filter out the meteorological targets, leaving the rest of the data to be potential bioscatterers.

1.6 Unifying Reference Frame

The methods of this thesis focus is on collocation; using multiple observations of a target, together. To compare observations of a target, the frame of reference must be shared. For WSR, the location of the instrument is given on a global reference frame, but the beam which contains the observable measurements, is only relative to the radar, therefore either this position must be transformed to also be on the global reference frame or, all other measurements made by another instrument transformed onto the same reference frame as the radar beam.

The choice of a reference frame significantly impacts the utility and accuracy of cartographic representations. Cartography originated from the practical need to navigate and retrace routes, necessitating clear and functional maps. Traditionally, maps have been presented as flat, two-dimensional images; however their usefulness does not depend strictly on realism but rather on adequately capturing features necessary for their intended purpose. On local scales, the projection of Earth onto two dimensions typically presents minimal distortion as exemplified by the detailed Ordnance Survey maps of Great Britain, where altitude is effectively represented by contour lines on a uniformly gridded surface. Nevertheless, when individual maps are combined or scaled up, projection overlaps and distortions becomes evident. Different projections prioritise different attributes; for instance, the Mercator projection preserves shape fidelity at the expense of greatly distorting landmass areas. Ultimately, discrepancies between the Earth's true shape and the chosen projection directly influence coordinate accuracy, emphasising the critical importance of selecting an appropriate reference frame for specific mapping objectives.

A geographic coordinate system establishes a three-dimensional grid over the surface of the Earth. In contrast, a projected coordinate system represents a two-dimensional rendition of the geographic coordinate system, achieved through a process of flattening that accentuates specific regions while introducing distortions. Coordinate systems are therefore designed with different intentions and that should be acknowledged. Latitude and longitude are not unique to a single point in geophysical space as shown in Figure 1.8 (Ordnance Survey, 2020), where the same coordinates are used over three different systems, Ordnance Survey (OS), World Geodetic System 1984 (WGS-84) and European Datum 1950 (ED50) showing a distance of $\sim 100\,m$ apart. So, although coordinates can be transformed between systems, this transformation is

only perfect in geometric theory, and thus there is error involved, where there is error in one coordinate transformation, anything using that or multiple, there is the propagation of errors. Hence a local coordinate system may initially give greater accuracy, reducing the amount of transformations and working on a global scale, allowing continuity and greater definition of errors (S.-J. Lee and Yun, 2025; Zhang, 2005; Yi, 2007).

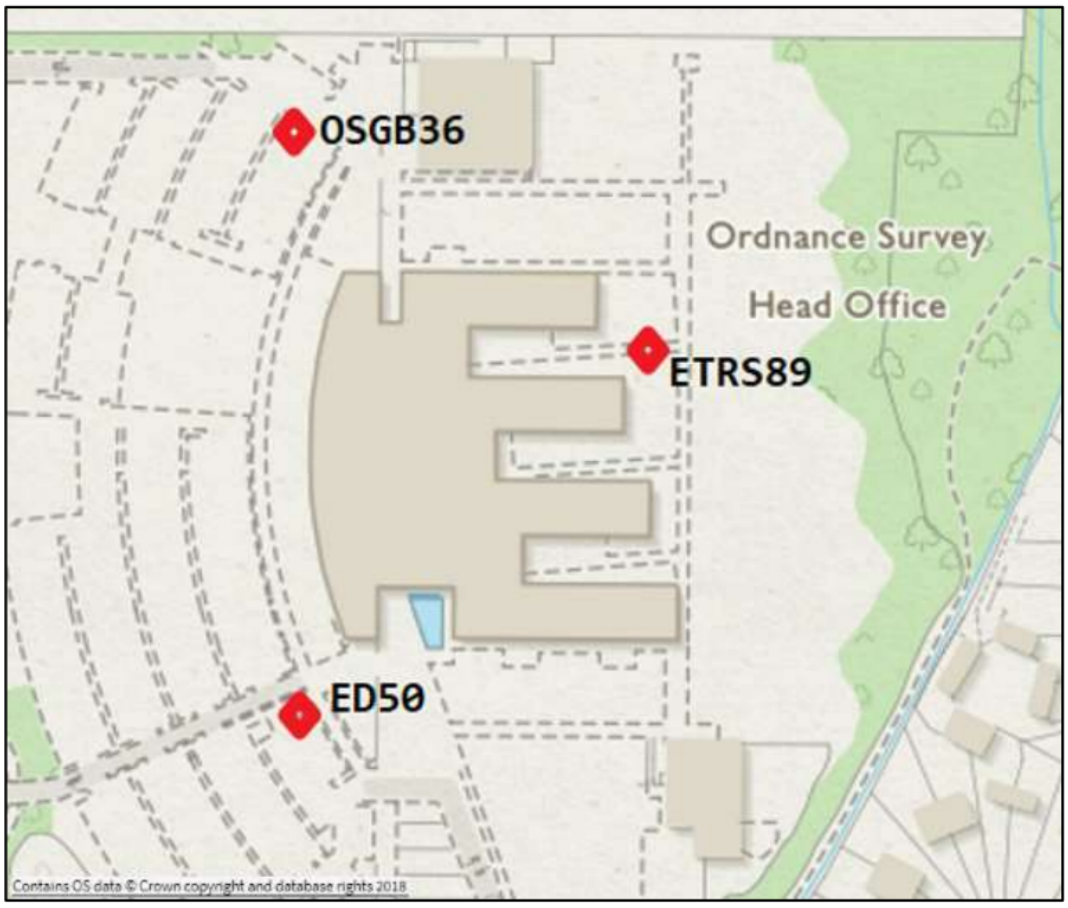

Figure 1. Three points with the same latitude and longitude in three different coordinate systems. The map extract is approximately 300m wide.

Figure 1.8: Ordnance Survey comparison of a single location in latitude and longitude across three different coordinate systems: OSGB36, WGS-84 and ED50, showing the 100 meters difference (Ordnance Survey, 2020).

The EPSG (European Petroleum Survey Group), holds a registry of all geodetic datums. In this thesis, two coordinate systems are used, WGS-84 which uses the geodetic datum WGS-84 (EPSG:4326) (International Association of Oil and Gas Producers, 2023), and the UK's postcode system based on the British National Grid (BNG) which uses the geodetic datum OSGB36 (Ordnance Survey of Great Britain 1936) (EPSG:27700) (Ordnance Survey, 2022), these are discussed in further detail below.

The World Geodetic System 1984 (WGS-84), first established in 1984, is a dynamic datum continuously updated to reflect changes in the Earth's physical characteristics. It employs an Earth-centered geodetic model, incorporating gravity and magnetic field variations to accurately represent Earth's shape and orientation in three dimensions. Unlike two-dimensional projections, WGS-84 provides a comprehensive geographic coordinate system directly accounting for Earth's ongoing transformations, such as tectonic plate movements and subtle gravitational fluctuations. Regular updates ensure that the datum remains precise, underpinning its widespread adoption as the standard reference for global positioning systems (GPS), satellite navigation, and aviation. The accuracy provided by WGS-84 ultimately enhances the fidelity of coordinate projection and mapping applications worldwide.

The citizen science survey records postcodes, which operate on a local system. This system has lots of idiosyncrasies, which are dealt with in Chapters 2 and 5, but to understand where they come from, here, the background of the countries is explained. Great Britain is formed from three countries; Scotland, England and Wales. The United Kingdom of Great Britain and Northern Ireland, often shortened to the "UK", is made up of four countries, Scotland, England, Wales and Northern Ireland. The Republic of Ireland (RoI) is a separate country and is a member of the European Union. There are three crown dependencies: the Bailiwicks of Jersey and Guernsey which form the Channel Islands, and the Isle of Man. Whilst they have their own governance, laws and fiscal system, the monarch remains the reigning British Monarch, (at the time of writing, King Charles III), thus the UK government on behalf of the Crown is responsible for the islands' defence and international relations. With this in mind, although international stamps are not required to send post between the UK countries or its crown dependencies, and the crown dependencies have their own post office, the postcode system is the same across the UK and the crown dependencies. Postcodes operate on a local system, and although these boundaries are not uniform, using grid references there is a transformation to a global reference frame.

For a universal reference frame, one coordinate system is used, and for this thesis WGS-84 was chosen. WGS-84 is a standard coordinate system in many areas, is international and is used for the UK's atmospheric research aircraft, which this thesis originally incorporated. In

addition, using WGS-84 coordinate system allows for consistency between the various datums and models that could be used.

1.7 General Shape

The shape of the Earth can be posed as a philosophical question, in practice it comes down to perspective, who is asking the question and for what purpose? In terms of gravity, the Earth is a blotchy ball, with indents and peaks. A person in the Netherlands might look out across the land and visually interpret the Earth to be flat, but a sailor making a voyage out into the everlasting horizon might disagree. An astronaut staring out of the ISS will see the Earth as this magnificent sphere, "the blue marble". Geometrically different shapes at different scales can be applied for the shape of the Earth but the closest geometric fit for the Earth's shape is an oblate spheroid, a rotational ellipsoid.

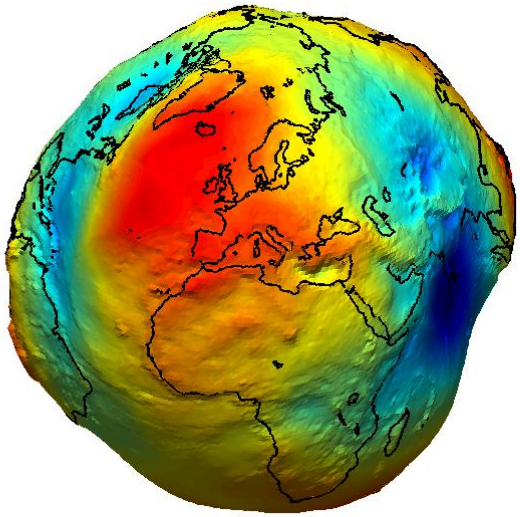

Figure 1.9: Geoid courtesy of European Space Agency

Although the shape of the Earth can be geometrically defined as an ellipsoid, it is important

to consider the topography. The Earth has no set discernible shape with undulating terrain, mountains and great swathes of water. The mean sea level (MSL) is the estimated altitude of the water if it covered the entirety of Earth. The Geoid is used to model the approximate MSL between the ellipsoid and the Earth's topography whilst also taking into account gravity, the resultant shown by Figure 1.9. In terms of the radar, topography can result in beam blocking, and altitude of the radar impacts refraction.

A coordinate system is mathematically tied to the model of the Earth. The datum provides the reference point of origin and orientation, mapping the coordinate system to a relative position on the Earth. The geoid, sits between the real and modelled Earth. All of these parts have to be considered in order to estimate the projected radar voxel relative to the Earth as opposed to the projected voxel relative to the radar.

1.7.1 Models

Let us take a step back to frame the problem; from the radar's perspective, how could the location of the radar beam be estimated? This question involves selecting an appropriate Earth model, each offering varying degrees of complexity and accuracy. It is here we can consider the different possible models of the Earth; Flat Earth (FE), Spherical Earth (SE), Ellipsoidal Earth (EE), plus the Earth's Geoid (GE). s_{12} is the shortest path along the reference single surface between two points. The initial location of the radar is known on our chosen coordinate system (ϕ_1, λ_1, h_a). The radars scanning information of azimuth (α_{12}), elevation (θ_1) and direct range (r) gives the relative position to the radar, but using all six of these variables, s_{12} can be estimated through the calculations covered in Chapter 2. The subsequent sections below provide detailed descriptions and comparisons of these Earth models for the accurate calculations of s_{12} and ultimately the position of the radar voxels on the chosen coordinate system.

1.7.2 Flat Earth

The first model is Flat Earth (FE). Figure 1.10 shows the FE model with a radar at an altitude of h_0 above the ground. To determine its distance (s_{FE}) along the surface of the FE ground, the trigonometric Equation 1.11 is used, with the known hypotenuse our radar range between the radar and the radar voxel, the elevation (θ) as the angle. This model is simple and quick to compute. However, this is the least accurate model particularly with range from the

radar as it does not take into account the shape of the Earth demonstrated by the increasing gap between the bottom ray and the axes of the RHI in Figure 1.3.

$$s_{FE} = r \cdot \cos\theta \tag{1.11}$$

$$h_{rg} = h_0 + r \cdot \sin\theta \tag{1.12}$$

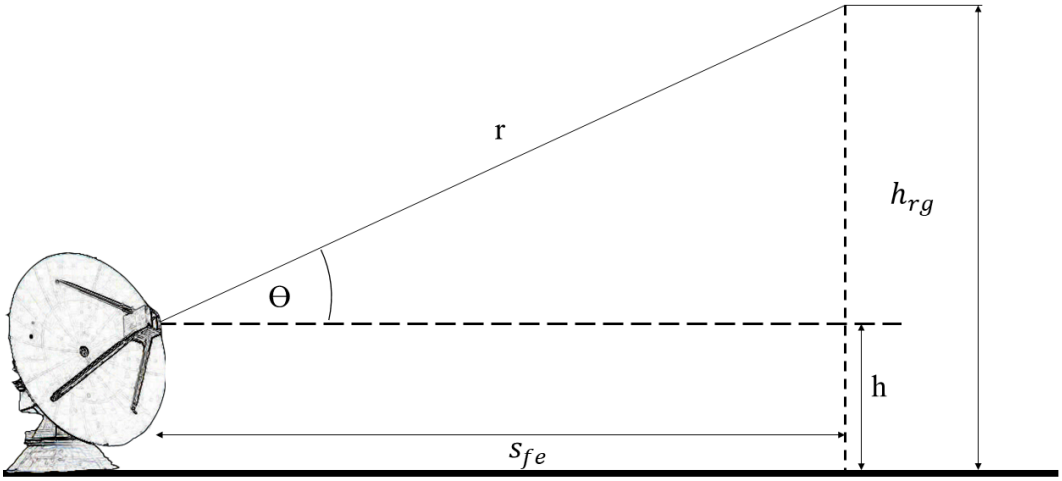

Figure 1.10: Geometric calculations of radar beam relative to a Flat Earth Model. Radar range (r); Altitude (h); Elevation (θ); Distance along the Earth (s)

1.7.3 Spherical Earth

The second model is Spherical Earth (SE). For the distance along the surface of the sphere, a larger triangle is drawn out bisecting the sphere, as shown by Figure 1.11. Equation 1.13 defines the arc distance with ϕ from Equation 1.14 using the Cosine Rule. This model also is efficient taking, and is most commonly used for radar (Prather & Hsua, 2019).

$$s_{SE} = (R + h_0)\phi \tag{1.13}$$

$$\phi = (r^2 + (R + h_0)^2 - 2r(R + h_0)\cos\frac{\pi}{2} + \theta \tag{1.14}$$

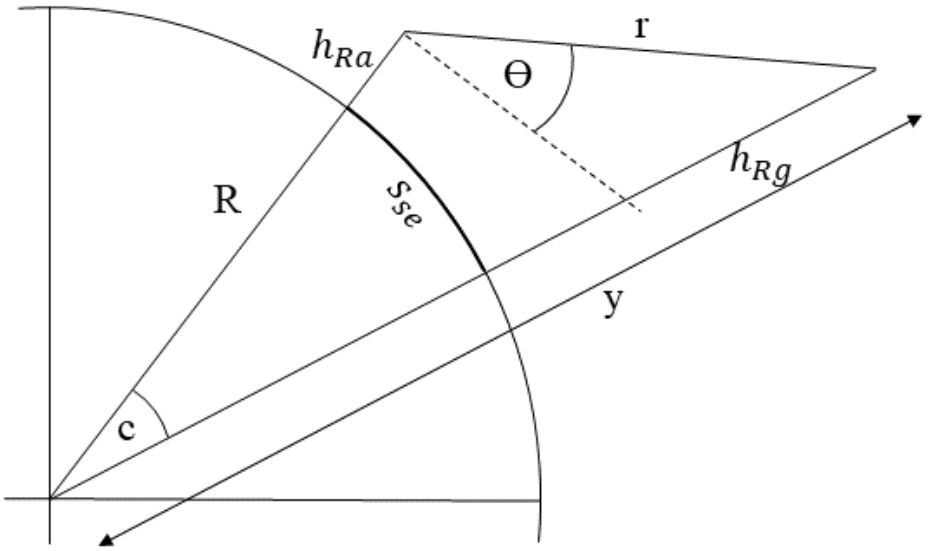

Figure 1.11: Geometric calculations of radar beam relative to a Spherical Earth Model. Radar range (r); Altitude (h); Elevation (θ); Distance along the Earth (s); Radius of the Earth (R); Angle of geometric centre of Earth, between radar and normal of radar beam (c); Normal of radar beam (y).

1.7.4 Elliptical Earth

The third model is Elliptical Earth (EE). An ellipse in the first instance may appear simple, an altered circle. However, although the equations of an ellipse are well known (Weisstein, n.d.), they can not be expressed by the elementary functions which cover addition, logarithmic and trigonometry (Weisstein, n.d.). Elementary functions are finite. For an ellipse, elliptical integrals are used which, in principle are infinite. This means most calculations using Elliptical Integrals will be truncated to produce a result thus having a limiting factor on accuracy (Bessel, 1825).

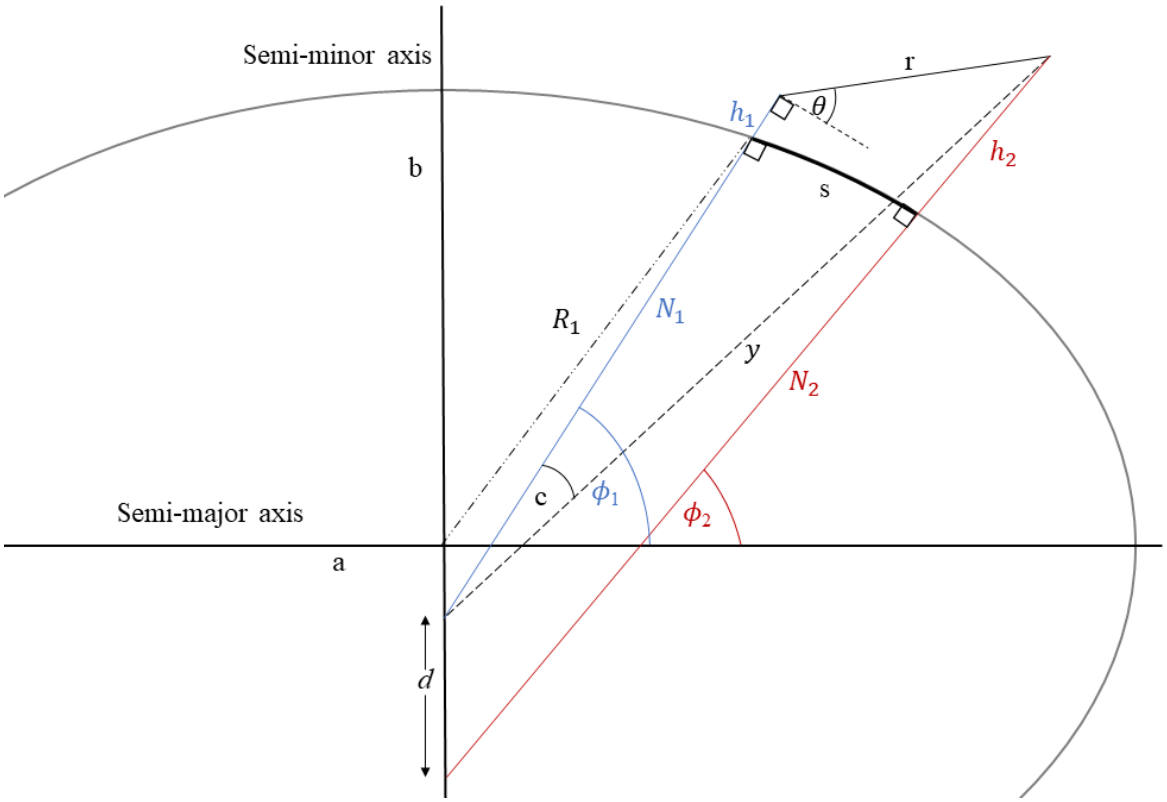

Figure 1.12: Geometric calculations of radar beam relative to a Ellipse Earth Model. Radar range (r); Altitude (h); Elevation (θ); Distance along the Earth (s); Radius of the Earth (R); Semi-major axis radius of the Earth (a); Semi-minor axis radius of the Earth (b); Angle of geometric centre of Earth, between radar and normal of radar beam (c); Normal of radar beam (y); Latitude (ϕ); Distance between Normals centre of the Earth (d).

Equation 1.15 is the equation of an ellipse, in Cartesian coordinates, with a semi-major axis, a and semi-minor axis, b, consistent with Figure 1.12. The relationship between a and b is defined by eccentricity (e), the amount it deviates from a circle. Eccentricity lies between 0 (a circle) and 1, it is defined by Equation 1.16. The Earth's axis of rotation is about its semi-minor axis, resulting in the Earth's shape as an oblate spheroid, bulging at the equator, and squashed at the poles. A rotational ellipsoid is made up of multiple of the same ellipse, or in this example, one ellipse spun along the North-South Pole axis. Thus the equations of the ellipsoid can be broken down to first examine the arc length of a single ellipse, and if the angle is along the meridian lines latitude and longitude only one ellipse would ever need to be used.

$$\frac{x^2}{a} + \frac{y^2}{b} = 1 \tag{1.15}$$

The arc length is defined by Equation 1.17 (Karney, 2013) and is then written as an Elliptical

Integral in order to be solved, with k the modulus of the ellipse and ϕ the amplitude. There are multiple different Elliptical Integrals for different situations. Commonly used in cartography (Fukushima, 2011) the Incomplete Elliptical Integral of the second kind is the length of the meridional arc of a rotating ellipse, with the ϕ being the geodetic latitude and amplitude the eccentricity. The Incomplete Elliptical Integral of the second kind is also used in (Rosch, 2011), and has an existing "Ellipeinc" Equation 1.18 from *scipy.special.ellipeinc* thus, combined with its intentional use in geodesy and cartography, this is the equation that is subsequently used.

$$e = (a^2 - b^2)^{\frac{1}{2}} \cdot a^{-1} \tag{1.16}$$

$$ds = \sqrt{(-a\sin\phi)^2 + (b\cos\phi)^2}d\phi \tag{1.17}$$

$$E(\phi, k) = \int_0^{\phi} [1 - k\sin^2(\phi)]^{\frac{1}{2}} d\phi \tag{1.18}$$

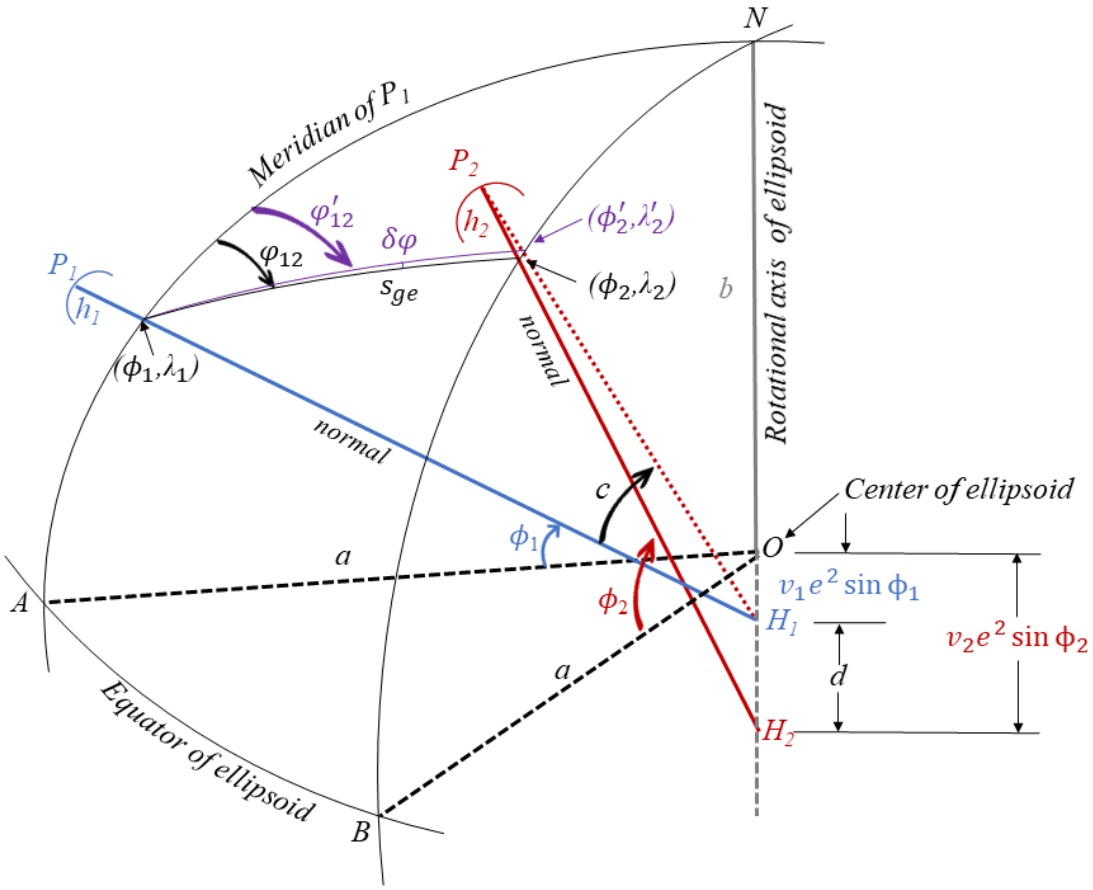

Figure 1.13: Normal section curve on an ellipsoid adapted from (Deakin, 2009). Geometric calculations of radar beam relative to a Ellipse Earth Model. Radar range (r); Altitude (h); Elevation (θ); Distance along the Earth (s); Radius of the Earth (R); Semi-major axis radius of the Earth (a); Semi-minor axis radius of the Earth (b); Angle of geometric centre of Earth, between radar and normal of radar beam (c); Normal of radar beam (y); Latitude (ϕ); Longitude (λ); Azimuth (ψ); Distance between Normals centre of the Earth (d); Radius of curvature (υ); Eccentricity (e).

Figure 1.12 shows a single ellipse, two dimensional, but the Earth is three dimensional, a three dimensional version of an ellipse is an ellipsoid; Figure 1.13 shows a section A-B of an ellipsoid, with the axis of rotation as b. The radar would be at point P_1 and the radar voxel at P_2. In both Figures 1.12 and 1.13 the symbols represent the same values. For a sphere, the normal of a point above the surface goes directly through the centre of the sphere $y = N_2$, but for the ellipse, with the exception of the poles and equator, the normal bisects the axis of rotation (b), as shown by Figure 1.13, $y \neq N_2$. Equation 1.19 shows the trigonometric calculation for y, and Equation 1.20 for the normal, N.

$$y = [(N_1 + h_1)^2 + r^2 + 2(N_1 + h_1)r\cos(\theta + \frac{\pi}{2})]^{\frac{1}{2}} \tag{1.19}$$

$$N = a[1 - e^2 \sin^2 \phi]^{-\frac{1}{2}} \tag{1.20}$$

1.7.5 Geoid

The final way to define s_{12} is by using the geoid. The geoid is shown in Figure 1.9, it establishes the Mean Sea Level (MSL) as if the whole of the Earth was covered in water. The geoid model is an approximation of the true shape of the Earth, combining the ellipsoid, topography and gravitational elements (Burkholder, 2008). To establish a position on the geoid, corrections are added from the ellipsoid equations to adjust between the models (Karney, 2011). Here, the elliptical equations are put into context. For the case of the ellipsoidal Earth there are two different approaches to elliptical integrals, either using latitudes, or using reduced latitudes. Skew corrections are also included for the geodesic (Karney, 2013) and are detailed in Chapter 2, Sections 2.2.3 and 2.3.

1.7.6 Geodesy

With WGS-84 as the coordinate system; the geodesic distance is the shortest path (s_{12}) between two points (ϕ_1, λ_1, ϕ_2, λ_2) along a single surface. There are two general problems to be solved using Geodesy; One is the "Direct Problem", where (ϕ_1, λ_1, s_{12}, α_{12}) are known and (ϕ_2, λ_2) are to be calculated, and the "Indirect Problem", where (ϕ_1, λ_1, ϕ_2, λ_2) are known and (s_{12}, α_{12}) are to be calculated. Charles F. Karney published the python Geographiclib module which solves the direct and indirect problem (Karney, 2013). The Geographiclib truncates the Bessel Equation (Bessel, 1825) so it can be computed with a finite solution, the truncation error is smaller than the rounding when using Institute of Electrical and Electronics Engineers (IEEE) double precision (Karney, 2013), thus is a reasonable place to curtail the equation. Bessel's Equation gives solutions to Laplace and Helmholtz equations in spherical coordinates.

A global reference frame is required to compare observations of the same target from two or more different instruments. WGS-84 is the chosen global reference frame for this thesis. In terms of the radar, the position of the radar and where the beam is pointing (ϕ_1, λ_1, α_{12}) is known, but the position (ϕ_2, $\lambda 2$) of the voxel is unknown; however the direct range between the voxel and the radar is known and this is the foundation to estimate (s_{12}). Depending on the model of the Earth that is being used, this can have a variety of different lengths.

1.7.7 Summary

The reference frame for all observations must be the same for comparison. To know where the radar beam is relative to the Earth, it is proposed that using Geodesy, remaining within a single reference frame, the position of the radar beam could be known with greater accuracy to the surface of the Earth.

1.8 Aim of the Thesis: Integrating Geodesy into WSR Observations for Aeroecology

WSRs remain an underutilised resource in aereoecological observations, despite their widespread deployment and potential for high-resolution atmospheric observations (Bauer et al., 2019). This thesis specifically addresses the central research question:

"How can the application of geodesy improve the integration of weather radar with other observations in aeroecology?"

To effectively tackle this overarching question, the thesis is guided by several specific research questions:

1. How can the implementation of geodesic calculations improve the spatial accuracy of radar voxel positioning
2. What impact does enhanced spatial precision have on collocating radar data with supplementary ecological and environmental observations?
3. How do these improvements affect ecological interpretations derived from radar data, specifically regarding insect monitoring during significant insect emergent events?

Each question is systematically addressed through a structured series of investigations outlined below:

Chapter 2: Methodology

- Presents the detailed development and implementation of the Geodesic Coding Radar Toolkit. This pythonic toolkit integrates radar specific positioning with complex

geophysical calculations from foundational work set out by Deakin (2010), advanced geodetic computations using the GeographicLib Module (Karney, 2013), refractive corrections laid out by Doerry (2013). It is designed specifically to enhance the accuracy of radar voxel positioning and streamline interdisciplinary use; Users simply input their standard radar data, and the module does the back-end calculations and produces a positioning file, so the users can focus on the results rather than understanding all of the complex mathematics.

Chapter 3: Verification and Initial Results

- Demonstrates the improved accuracy in radar voxel positioning achieved through the implemented geodesic methodologies. This foundational step verifies that the geodesic approach provides measurable improvements and establishes the precision required for effective collocation.

Chapter 4: Determining the RCS of Alate Ants

- Before exploring a practical application of the enhanced collocation method, Chapter 4 assesses the RCS of flying ants, which will be used in conjunction with the collocation method to quantify the abundance of ants in Chapter 5, using anatomical modelling of ants versus ellipsoids, partitioning body parts with representative materials and analyses of presence of wings.

Chapter 5: Flying Ant Day

- Chapter 5 investigates the ecological significance of accurate voxel positioning and data collocation by analysing insect activity during Flying Ant Day. It addresses questions regarding the altitude distribution peaks of these emergences, general dispersal and biomass quantification, highlighting the ecological behaviours made possibly by improved radar precision.

1.8.1 Novelty and Hypothesis

The novel contributions of this thesis include:

- Development of a robust geodesic-based radar location toolkit to enhance spatial accuracy in radar data analysis, accessible to interdisciplinary researchers without specialized

geophysical training.

- Empirical testing and demonstration of the impact of geodesic precision on radar voxel accuracy and collocation reliability.
- Detailed radar cross-section analyses of alate ants, with implications for improving species-level identification capabilities.
- Comprehensive ecological assessments enabled by accurate collocation, facilitating deeper ecological insights during major aeroecological events.

1. Spatial Precision Hypotheses:
    - Null: Increased spatial precision via geodesy does not significantly alter radar observation outcomes.
    - Alternative i): Enhanced spatial precision consistently results in measurable improvements in radar data accuracy and interpretation.
    - Alternative ii): The impact of improved spatial precision is context-dependent, varying significantly with different observational scenarios.
2. Radar Cross Section Hypotheses:
    - Null: No significant difference exists between male and female ants' RCS.
    - Alternative: A measurable and significant difference exists between the RCS of male and female ants.
    - Null: Ant wing presence does not significantly alter RCS values.
    - Alternative: Wing presence significantly impacts the RCS of ants.

Through addressing these clearly articulated questions and hypotheses, this thesis aims to substantially advance the integration of geodesy with weather radar technologies, thereby enhancing the precision, reliability and ecological applicability of WSR data in aeroecological research.

Chapter 2

Methods

The following chapter describes the tools used for observations and the methods for processing. The chapter begins with the tools used; radar and a citizen science survey. The majority of the chapter is on applying geodesy to the primary instrument for observations, the ground-based weather surveillance radar. The methods will use the geodesic mathematics laid out in Chapter 1, Section 1.6, and step by step show how it is implemented for calculating the geodesic position information for every radar voxel, the Radar Voxel Location Code. The second part is the Collocation Code, collocating between a ground-based radar and a secondary source. All code produced has been written in Python by the author, Freya I. Addison, making up the major body of the thesis. All code is appended, demonstrating the extensive work carried out. The final description of this code demonstrates how methods one and two are applied to a case study, Flying Ant Day and the validity of using these methods as shown in Results Chapters 4 and 5. This chapter concludes with the simulation of the radar cross section (RCS), using the software Wipl-D (B. Kolundzija et al., 1996) and the further evolution of techniques which the author Freya I. Addison originally developed for (Addison et al., 2022). The RCS provides a tangible reference point of flying ants for the radar observations. The term biometeors is used to indicate radar targets that are likely biological of nature; the conditions of the methodologies focusing on isolating insects over plants/birds and more specifically flying ants.

2.1 Instruments and Techniques

This section details the tools used within the research. The instruments were ground-based weather surveillance radars (WSR) (X and C-band) and a citizen science survey, conducted over a period of two consecutive summers. The radar is the primary instrument for observations and the main subject of geodesic applications. Whilst the citizen science survey provides a method of validation and wider context for the results from the Flying Ant Day case studies.

2.1.1 Weather Surveillance Radars

One research radar was used alongside the UK Met Office radars. Using multiple radars demonstrates the versatility of the code with the aim of facilitating future integration into standard radar processing practices.

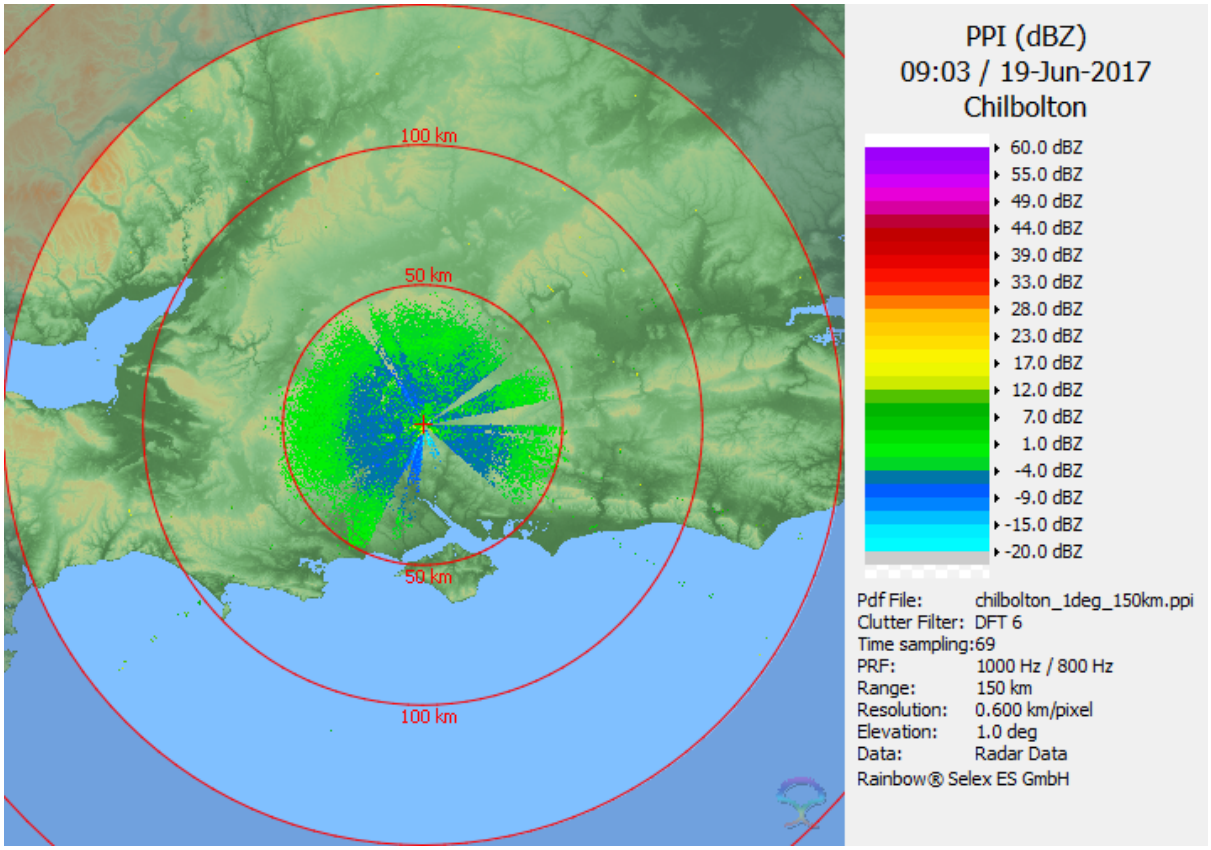

Figure 2.1: NXPol 1deg PPI, dated 19/06/2017, location Chilbolton Observatory. The activity is from biological scatters, most likely insects, appearing largely in the close range, first 50 km radius from the radar.

NXPol is the National Centre for Atmospheric Science (NCAS) mobile X-band dual polarisation Doppler weather radar. This mobile weather radar was designed to detect different forms

Radar	Frequency (GHz)	Wavelength (cm)	Beamwidth (^{o})	Distance between Range Gates (m)
NXPol	9.375	3.2	0.98	150
MO	5.625	5.3	1.10	600

Table 2.1: Radar Specifications

of precipitation with a focus on cloud microphysics and dynamics, however during clear days insect activity is easily observed as shown by Figure 2.1, with the activity limited to the close range of the radar, fairly homogenous and dominant in the lower dBZ range (under 15 dBZ). Biometeors can be better detected by scanning at slower speeds at close range, and optimising the radar (Neely III et al., 2018). Table 2.1, shows the relevant specifications of the NXPol radar for the datasets used, with the full range of the radar being 150 km. The NXPol radar has a wavelength of 3.2 cm so radar will be most sensitive to targets in this size factor.

The Met Office operates a network of 15 dual-polarisation C-band radars, covering the entirety of the United Kingdom and Northern Ireland, complemented by an additional research radar situated at Wardon Hill. This radar network employs a standardized scanning strategy and operates continuously with regular calibration performed approximately every few months to maintain accuracy. Detailed radar specification are provided in Table 2.1. Although minor variations exist across the network, such as differences in beamwidth, the provided specifications accurately represent the radars utilized in this study. Whilst the maximum operation range of the Met Office radar network is approximately 255 km (Met Office, n.d.), however for the purpose of biometeor observations, limiting to below 75 km, in line with the "good quantatitive" data limits (Met Office, 2023) of the radar, and that due to the small size of insects, typically biometeors are observed under 50 km from the radar (Stepanian and Wainwright, 2018; Dokter et al., 2019).

Jersey has its own radar, and funded its own upgrade to dual-polarisation, in line with the Met Office in 2016, whom they work closely with and share data. The RoI radars, are owned and operated by the Republic of Ireland's own meteorology office, Met Èireann, and are not to the same standard as the UK and Jersey, being single-polarisation, however the Shannon radar is being upgraded to a dual-polarisation radar in 2023 (Met Eireann, 2023).

The MO radar, Wardon Hill, is used in Chapter 3 for the verification of geodesic positioning of the radar beam. The requirement is a calibrated radar of known location, to observe a highly reflective target of known location, for example a transmission mast. The Wardon Hill radar was used by Darlington (2015) in his thesis, which included the calibration of the radar with the Stockland Hill Mast, thus this was chosen due to the history.

The MO radar, Chenies is located at (51.68916^o, -0.53055^o) (Met Office, 2023), is used in Chapter 5 for the case studies for Flying Ant Day. This radar was chosen, as was the closest radar for the majority of the case studies on that day, with an average distance (s) of 51 km between the radar and the survey respondents.

Post-processing backdated radar observations for biometeors is possible; however this would only be advisable for as far back as the dual-polarisation upgrade. This is to give greater confidence in classifying insects. However, the geodesic radar voxel location algorithms, could be applied to any radar data, but most usefully applied to those wishing for detailed analysis and corrections and collocated comparisons with other instruments or models.

2.1.2 Citizen Science Data

In response to the COVID-19 global pandemic and the UK Lockdown in 2020, where fieldwork could not be carried out, alternate methods of research were employed by the Biodar group; The author, Freya I. Addison, initiated a study on Flying Ant Day (FAD) engaging fellow colleagues Dr Elizabeth Duncan and Dr Thomas Dally to support the expanded scope, and together conducted a citizen science (CS) survey to detect the emergence of ants on their nuptial flight. As the survey involves human participants, an ethics statement was written and approved. This included the privacy of participants, protected by General Data Protection Regulation (GDPR), which resulted in the locations of winged ants sightings reported to the first half of the postcode only. The Ethics Number: LTSBIO-034, approved by the Faculty of Biological Sciences Research Ethics Committee, University of Leeds, first in 2020 and then updated for 2021 and the subsequent years.

The CS survey targeted the entirety of the UK and the Republic of Ireland to record sightings of winged ants. There are approximately 60 species of ant in the UK with *Lasius niger*, also

known as the common black ant, the most common species of ant that resides in the UK (Gamble, Gavin, 2020). Each year, the new Queens leave the nest on their nuptial flight, to mate with smaller, winged males, and establish new colonies. The males, do not last more than a few days after their flight, but the Queens can live around 20 years, having fertilised all their eggs in a single day (Kramer et al., 2016) . The emergence of ant is colloquially known as "Flying Ant Day", however this is a bit of a misnomer as there are actually multiple days with mass flights during the summer season (June-September) (Hart et al., 2018).

The survey collected the following details: Date and time of the sighting, duration of the sighting, whether the winged ants were on the ground or in the air, an approximate quantity of ants, and the location given by the first part of the postcode. The citizen science data points, are used as a reference as evidence of ants, to compare the radar voxel locations.

General Processing

The CS survey responses have to be processed before use due to the volume of data, as there was over 2500 responses each year; the processing is to remove any erroneous data and format it to make it more user-friendly. The survey was collected on a Google form, processed in a jupyter-notebook, written by Freya I. Addison (the author), see Appendix and the outputs provided in both a .nc and a .csv format with an additional .pkl file for the specific shape geometry of postcode boundaries.

Time Processing

A quirk of the Google form was, that dependent on the device used, the date was either inputted as $dd/mm/yy$ or $mm/dd/yy$. Initially, the date question asked for users to input $dd/mm/yy$ until the issue was discovered and the question was amended. To counter this problem, the inputted date of observation was checked to see if it matched the date of entry or a previous date.

Another issue encountered, was using the right time. This issue was predicted and thus asked in addition to the time of first sighting, whether it was in the morning or afternoon. Part of the processing of the data, the time of the first sighting was converted to the 24-hour clock and checked against the submission timestamp.

In total the datetime processing removed around 6 responses from the total dataset.

Postcode Processing

Firstly this checks to see if the postcode valid; does it exist in the postcode list (UK Government, 2021), is there a common typographical error, for example a numeral zero where there should be the letter "O", or if is there an extra digit. If the postcode is invalid it is not appended to the output file, but is printed out in the terminal for prosperity, these mainly appear to be the postcode incodes.

If the postcode was within Great Britain, the area and boundary, in the form of a multi-polygon, of that postcode is fetched from the ONS dataset. Using the Python module geographiclib (Karney, 2022), the central coordinates of each postcode are cross-referenced against the positional coordinates of the MO radars, the Jersey radar, and those in the Republic of Ireland. If the radar is within 200 km of the centroid of the postcode, then the radar number and distance is appended to be used for collocation. When an area was provided from the ONS dataset, it is appended, otherwise, 999.99 or nan is used without an area/polygon dataset.

The postcode area polygons are outputted to a separate file using pickle due to their complexities of having some single multi-polygons for a postcode district, and multiple for a postcode area, creating a large file. For the survey responses 2021-2022 the polygon file was 287.3 MB compared to the other file which was 7.6 MB.

2.2 Geodesic Coding Radar Toolkit

The author, Freya I. Addison has produced two working and integrable products for the radar community. The development of this toolkit involved extensive scientific study, the analysis of multiple models and the integration of complex mathematical techniques. The multiple layers of mathematics were rigorously tested to work with each other and adapted where necessary. The iterations were tested dynamically across different conditions to achieve a product that was adaptable, streamlined and accurate. The toolkit is appended for prosperity and is registered with a doi: 10.5281/zenodo.15747473 (Addison, 2025).

There are two main modules. The first, Voxel Location, uses only the radar data and calculates the position (ϕ, λ, h) of every voxel in the radar beam. The second piece of code, Collocation, is the collocation between the radar dataset and another instrumentation. The Collocation code is the most important aspect for users, but is dependent on the first piece, which is where the improvement lies between traditional and geodesic radar voxel location.

The radar data processing framework developed in this thesis consists of two primary components: Voxel Location and Collocation. The first component, Voxel Location, operates exclusively on the WSR data to compute the geodetic position, latitude (ϕ), longitude (λ), and altitude (h), of every voxel within the radar beam. This geolocation is essential for spatially resolving radar returns and underpins all subsequent spatial analysis. The second component, Collocation, establishes spatial correspondence between the radar-derived voxel data and external observational dataset (e.g., instruments or survey points). While the Collocation module is the most immediately valuable for applied users, it relies fundamentally on the accuracy of the voxel positioning computed by the Voxel Location module. The advancement presented in this thesis lies in replacing traditional radar voxel positioning methods with a geodesic framework, offering improved spatial accuracy over large distances or non-planar surfaces.

The full list of external Python modules used is documented in the code repository included in the appendix. A key dependency is the GeographicLib library (GeographicLib), which enables both direct and inverse geodesic calculations following the algorithms described by Karney (Karney, 2013).

- Direct geodesic method, inputs the starting location (ϕ_1, λ_1), initial azimuth (α_{12}) and the geodesic distance (s_{12}) to output the secondary coordinates (ϕ_2, λ_2)
- Indirect geodesic method, given the location of points one (ϕ_1, λ_1) and two (ϕ_2, λ_3), the azimuth (α_{12}) and geodesic distance (s_{12}) can therefore be solved.

These algorithms are essential for accurately computing the spatial footprint of the radar voxels on a geoid Earth reference frame an enables precise spatial integration with external geospatial datasets.

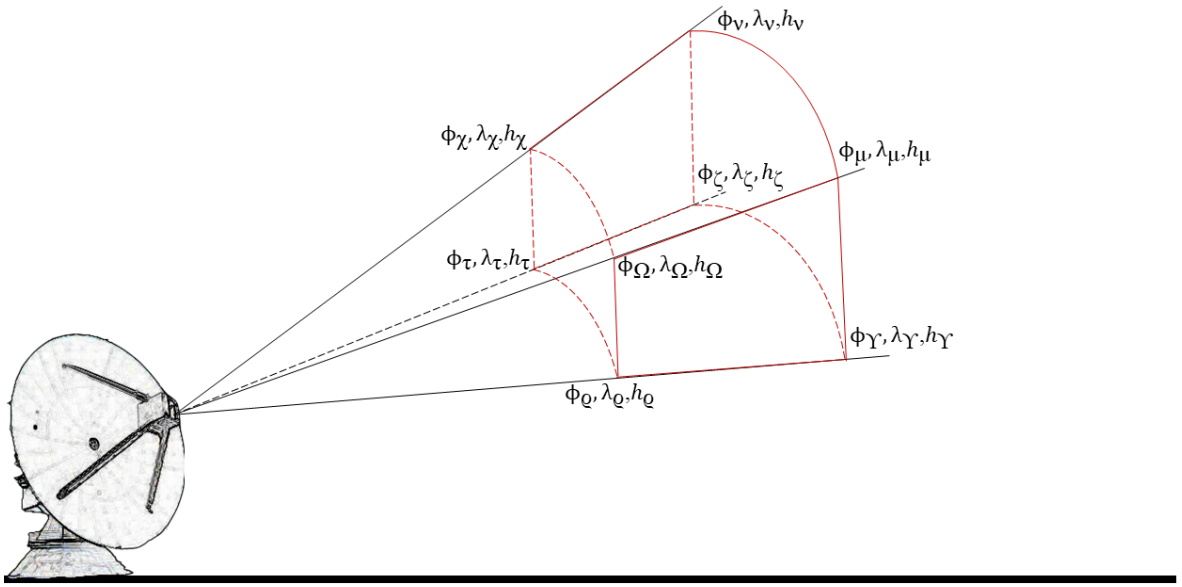

Figure 2.2: Diagram of radar beam and estimated voxel corner coordinates, latitude (ϕ), longitude (λ), altitude above mean sea level (h).

The code is optimised to use matrices for the majority of the mathematics, however the GeographicLib module (Karney, 2022) only accepts one-dimensional arrays which creates a bottleneck. Further efficiencies could be achieved through parallelisation and by reducing the number of corners outputted from the Voxel Location code, dependent on the purpose of using the locations. The option to not include refraction will also slightly improve the time but reduces the accuracy.

Ranges (km)		10	15	20	25	30	40	50	75	100	150	200
Theoretical Voxel Volume (km^3)	$BW = 0.98^o$ RG=0.15km	0.00345	0.00775	0.0138	0.0215	0.0310	0.0551	0.0862	0.194	0.345	0.775	1.38
	$BW = 1.10^o$ RG=0.6km	0.0174	0.0391	0.0695	0.109	0.156	0.278	0.434	0.977	1.74	3.91	6.95
Cornered Voxel Volume (km^3)	$BW = 0.98^o$ RG=0.15km	0.00324	0.00733	0.0131	0.0204	0.0295	0.0525	0.0820	0.185	0.329	0.740	1.32
	$BW = 1.10^o$ RG=0.6km	0.0156	0.0358	0.0644	0.101	0.146	0.261	0.410	0.926	1.65	3.72	6.61

Table 2.2: Voxel Volume Differences with Range for Theoretical Idealised Volume and Cornered Volume

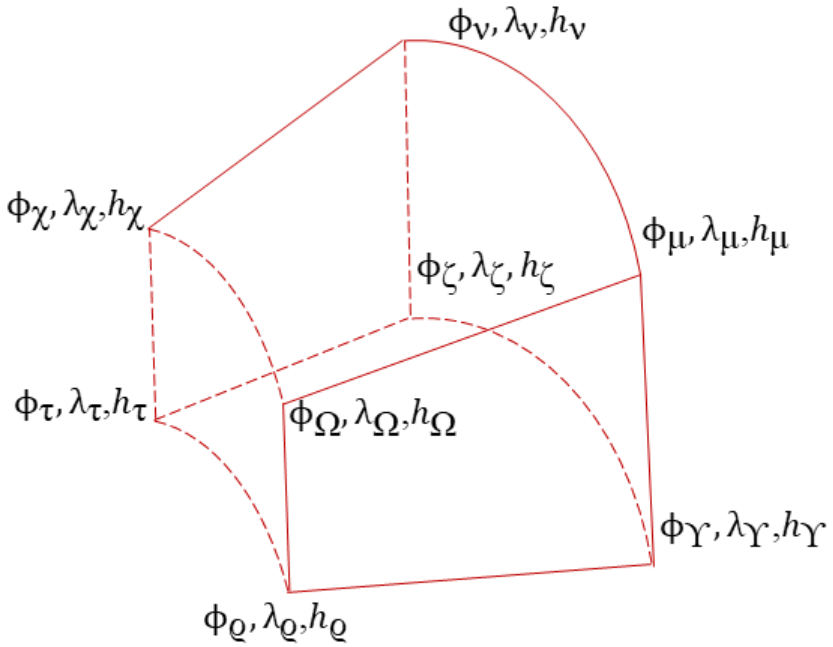

Figure 2.3: Diagram of radar voxel shape and coordinates, latitude (ϕ), longitude (λ), altitude (h).

	Elevation	Azimuth	Range Gate
Mid	θ	α	r
Ω	Max	Min	Min
χ	Max	Max	Min
Υ	Min	Max	Max
ζ	Min	Min	Max
ϱ	Min	Max	Min
τ	Min	Min	Min
μ	Max	Min	Max
ν	Max	Max	Max

Table 2.3: Estimated Radar Voxel Points

2.2.1 Radar Voxel Location

The first piece of code computes the geodetic positions of the eight corners, referred to in the code by the phonetic alphabet whisky, xray, yankee, zulu, sierra, tango, uniform and victor (Ω, χ, Υ, ζ, ϱ, τ, μ and ν) and the midpoint of the voxel for every voxel in the main lobe of the radar beam, as illustrated by Figure 2.3. While a true radar voxel has no sharply defined edges, these corner positions, based on the half-power beam width, in Table 2.3, serve as a practical approximation of the WSR observation and limit the bounds of the uncertainty in its representivity. A conceptual representation of the voxel's partial beam-filling geometry is shown in Figure 1.4.

Voxel corners are estimated using the minimum and maximum values of the radar's elevation, azimuth and range gates, as outline in Table 2.3. These boundary values define a frustrum shown in Figure 2.3 that approximates the spatial extent of each voxel.

Table 2.2 presents a comparison between theoretical voxel volumes (calculated using idealised beam propagation equations) and those computed from the approximated corner-based method, for two radar configurations differing in beamwidth and range gate length. The analysis shows that the discrepancy in voxel volume is most pronounced near the WSR, where geometric distortion is greatest. However the difference decreases with range, and remains within approximately 10%, a level of precision acceptable for most applications.

Importantly, the volume computed using the corner-based method is always smaller than the theoretical value, ensuring that the approximated voxel lies entirely within the true beam footprint. This conservative estimation enhances spatial accuracy when interpreting volumetric data and is particularly valuable for defining strict collocation boundaries with external datasets. The rationale for defining voxel corners is twofold:

1. To enable clearer spatial interpretation and visualisation of voxel geometry.

2. To support precise spatial filtering and matching criteria during collocation with other observational instruments.

Initially the radar information gives use the geodesic position of the radar, the range, elevation

and azimuth of the beam. To calculate the geodesic position of the beam, the geodesic distance, s must be calculated, which requires N, y and c as depicted from Figure 1.12.

The appendix has the full version of the code or at doi (Addison, 2025) and Figure 2.4 shows a summarised version of the code and is broken down into descriptive bullet points here.

Step 1. Read Radar Metadata The radar file is read in extract essential positional and scanning parameters, including:

- Radar latitude, longitude, and altitude above mean sea level (MSL)
- Beam azimuth, elevation and range
- Beamwidth, beamheight, and range gate resolution

Optionally, the surface refractivity index N_s can be specified based on model output or observations. If not provided, a default value of $N_s = 313$ is used, following (Doerry, 2013). These parameters are passed into a custom function named maths.

Step 2: Define Geodetic Constants Fundamental Earth constants from the WGS-84 ellipsoid model, semi-major axis (a) and semi-minor axis (b), are defined for subsequent calculations.

Step 3: Unit Conversion All angular measurements are converted into radians for use in trigonometric operations. Units are reverted to degrees as needed later in the process.

Step 4: Dimensional Tiling Any 1D arrays (e.g., azimuth or range) are tiled into 2D arrays to allow calculations across the full beam volume.

Step 5: Initial Geometric Calculations Basic ellipsoidal geometry, depicted in Figure 1.12, is computed, including:

- The ellipsoid normal (N) at the radar location
- Geometric parameters; angle c and length y angle c and length y. y is estimated first using the Cosine rule and then c is estimated using Equation 2.1.

Step 6: Midpoint Estimation via Geoid Function The initial geodesic mid point of each voxel is estimated using the Geoid function, described in Section 2.2.2.

Step 7: Refraction Correction Refraction adjustments are applied based on the model presented in Section 2.3. This yields corrected elevation angles for the voxel center,

Step 8: Update Angle Calculations With the corrected elevations, the angle c is recalculated for all points within each voxel.

Step 9: Full Voxel Geolocation The Geoid function is rerun to compute the final geodetic coordinates of all eight voxel corners and the midpoint.

Step 10: Altitude Band Verification A final height consistency check ensures that the new altitudes remain within their designated atmospheric bands for refractive correction.

Step 11: Export Output File The final output is saved as a NetCDF file, containing the full geolocation (eight corners and midpoint) of each voxel, along with the associated azimuth, elevation and range values.

$$\begin{aligned} \theta = 0; \qquad & c = \tan^{-1}\left(\frac{r}{R_{Ra}}\right) \\ \theta \neq 0; \qquad & c = \cos^{-1}\left(\frac{y^2 + R_{Ra}^2 - r^2}{2yR_{Ra}}\right) \\ c = Nan; \qquad & c = \tan^{-1}\left(\frac{r\sin(\theta + \frac{\pi}{2})}{y}\right) \end{aligned} \tag{2.1}$$

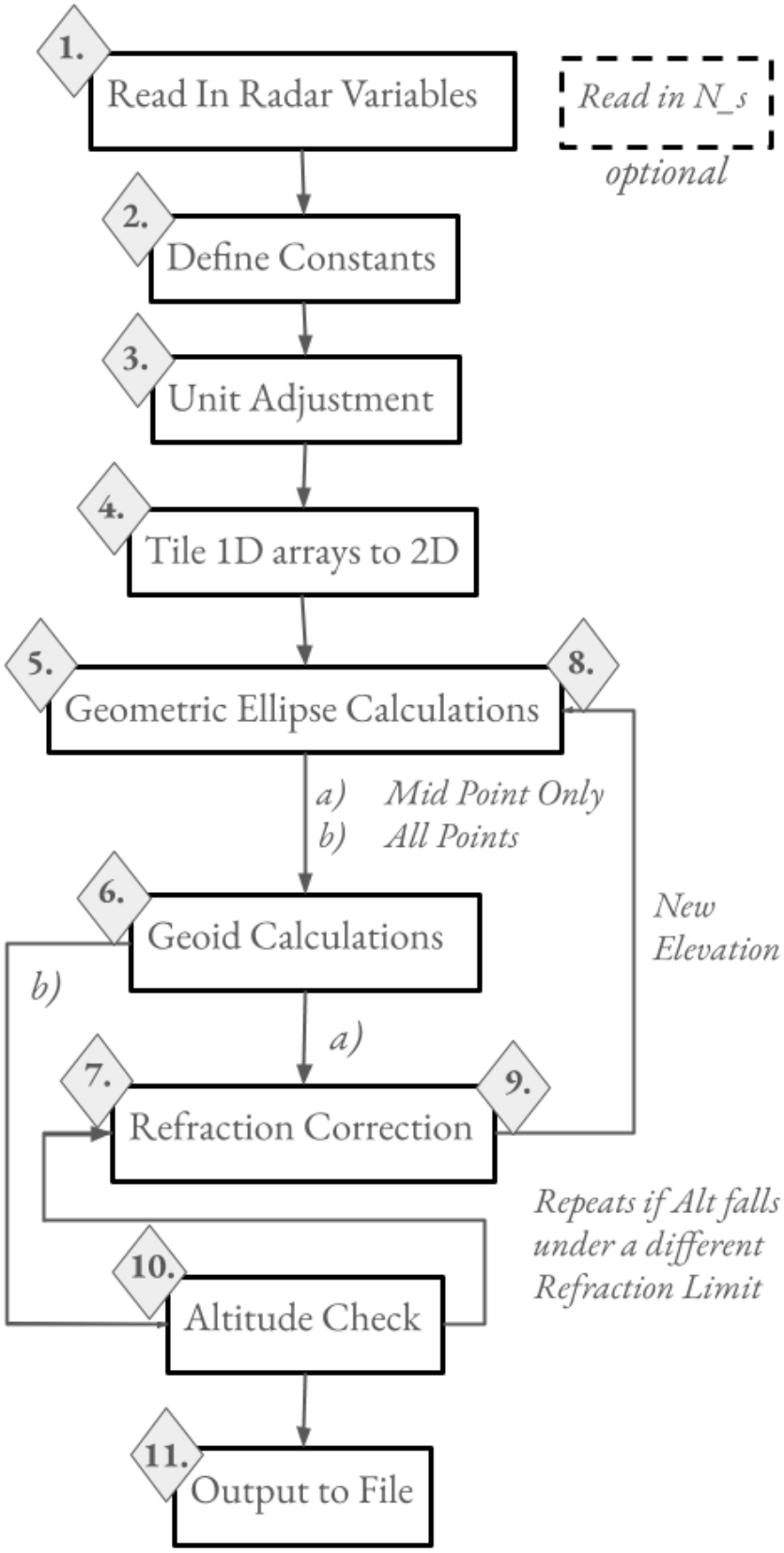

Figure 2.4: Flowchart of the Voxel Location Code, which inputs radar variables, and then outputs the voxel location points.

2.2.2 Geoid Function

Figure 2.5 shows the flowchart of the iterative process of the Geoid Module. This module takes the initial positional information of the radar and the ellipsoid calculations to estimate the geodesic distance s, between the radar and the voxel point. ϕ_2 is first estimated using Equation 2.2, the great circle, then s is estimated using the elliptical equations, this is then used to calculate the first geodesic estimates of ϕ_2 and λ_2 (position of the radar voxel point) using the GeographicLib module (Karney, 2022). The correction for the offset, from great circle and ellipsoid to geoid, as shown by Figure 2.2 needs to be added, to make it a proper geodesic estimation; The skew normal correction (Equation 2.4) is applied first, which alters the azimuth (α) value, and then the reduced latitude correction (Equation 2.5), (which takes it from the great circle spheroid, to an oblate spheroid, an ellipsoid) (Vincenty, 1975) . These iterative incremental changes improve upon each set of assumptions to go from the positional information given for the radar voxels, range, to the geodesic distance across the Earth, to achieve an estimate for the geodesic position of each radar voxel as the most accurate positional information that can be achieved.

$$\begin{aligned} \pi < \alpha < 1.5\pi; \qquad & \phi_2 = \phi_1 + c \\ otherwise; \qquad & \phi_2 = \phi_1 - c \end{aligned} \tag{2.2}$$

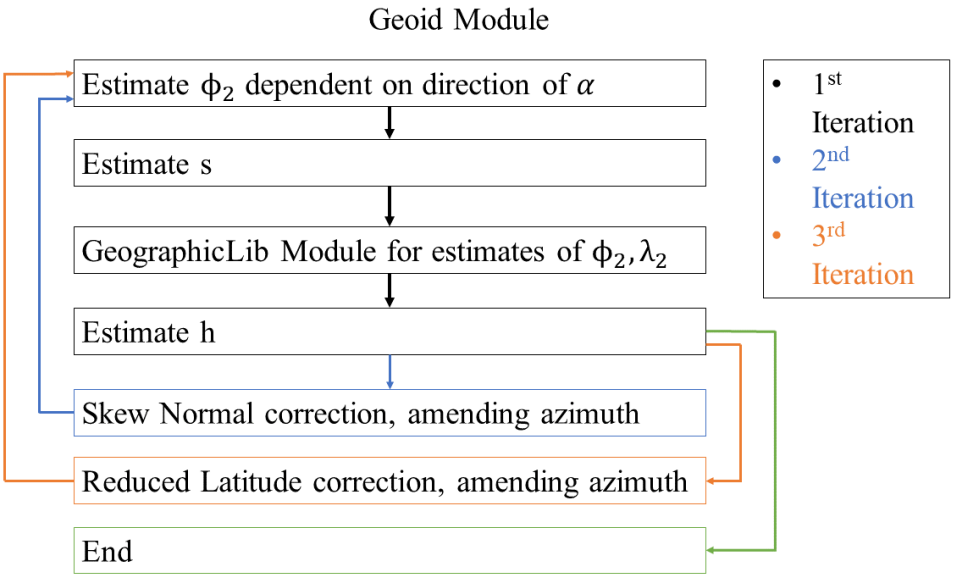

Figure 2.5: Flowchart of the Geoid module, demonstrating the iterative steps to produce the second position points.

2.2.3 Corrections

For a sphere, the normal of a point above the surface goes directly through the centre of the sphere, but for the ellipse, with the exception of the poles and equator, the normal bisects the axis of rotation as shown by Figure 1.13. The normal length, y, is not the sum of the radius and the altitude on an ellipsoid. The distance (d) between the centre of the ellipsoid and the bisection of the normal is given by Equation 2.3 and shown in Figure 1.12.

There are two corrections, the normal (skew) correction, which is applied first followed by the target height correction. The two corrections should approximately be equal and opposite in sign (Krakiwsky & Thomson, 1974). The skew correction has less variation than the target height correction, with the former not in excess of 0.03 across 100 km and the latter normally below 0.5 arc seconds (Burkholder, 2008). The skew correction, Equation 2.4 is from Burkholder (2008)'s Equation 7.73, using ρ_{cc} to convert to coordinate geometry. The target height correction uses M, which is the meridian radius of curvature and N which is the radius of curvature in the prime vertical. The target height correction is taken from Krakiwsky and Thomson (1974)'s Equation 58. These incremental changes correct the position of the target latitude and longitude point adjusting from elliptical to full geodesic coordinates.

$$d = \upsilon e^2 \sin\phi \upsilon = a(1 - e^2 \sin^2\phi) \tag{2.3}$$

$$\delta\alpha_{sn} \cong \frac{\rho_{cc} e^2 s^2}{12 N_1^2} \cos^2 \frac{\phi_1 + \phi_2}{2} \sin 2\alpha \tag{2.4}$$

$$\delta\alpha_{th} \cong \frac{M_m}{\rho_m} \frac{e^2 s^2 \sin\alpha \cos\alpha \cos\phi_2}{12 N_m} \tag{2.5}$$

2.2.4 Gravity Corrections

FE, SE and EE are models based on geometry, when working with real-world data, there are further physical facets that impact the shape of the Earth. If the ellipsoid is used as the base shape, what adjustments or corrections are required to get to the geoid?

The Earth bulging at the equator is broadly down to three things, centrifugal force, gravity and density distribution. If the Earth was a single density that did not distort but was covered in a layer of water (the sea), the gravitational pull would cause a bulge by only a single km.

The actual measured axes are the semi-major axis of the Earth at $a = 6378137.0000\,m$ and the semi-minor, $b = 6356752.3142\,m$ which is a difference of 21384.685 m or $\sim 0.3\%$ (Newtspeare, 2011).

Merry and Vanicek (1974) uses an astronomical reference frame, and gives a gravitational correction in the order of $10^{-2}\,m$. The Helmert method transforms between coordinate systems, there are some variations that take into account local gravity but these adjustments are also in the order of $10^{-2}\,m$. So far these corrections cover the surface of the Earth. The atmosphere is not a vacuum and thus has a mass and gravity (Lin et al., 2020). However Lin et al. (2020) shows that using a general gravitational affect is sufficient given the magnitude of altitude and range of the radar. Therefore adding the atmospheric mass to the Earth's centre of mass, adds 0.87 mGal to observations made at mean sea level which is the equivalent of a $\sim 5\,m$ height offset, which is accounted for when using the geoid (Vanicek & Krakiwsky, 1982).

2.3 Refraction Correction

Refraction is the change in direction of an electromagnetic wave as it passes from one medium to another. The bending occurs in the direction of the denser medium. Snell's Law, Equation 2.7 is the relationship between the incident and refractive angle for an electromagnetic wave travelling through the boundary of medium one and two. Figure 2.6 demonstrates the refractive phenomenon very clearly in the real-world example of a ship appearing to float in the air above the ocean. The example in Figure 2.6 (Morris, David, 2021) is a result of the difference in air density, cold air is denser than warm air; at sea level, there is a layer of cold air and then warmer air above, this bends the light from observer's perspective on the shore. This effect causes an apparent mismatch in locations according to the frame of the reference of the observer, as shown by Figure 2.7. Refraction has an impact on the local elevation angle, height and range of the target.

Figure 2.6: Floating Boat courtesy David Morris via BBC (Morris, David, 2021)

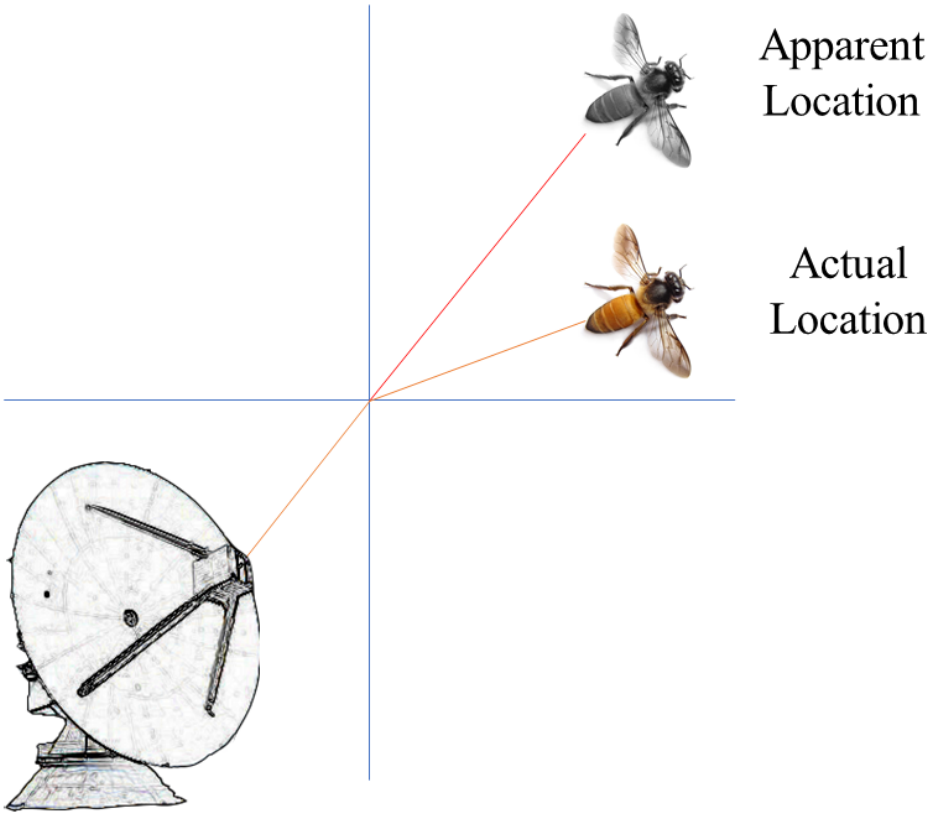

Figure 2.7: Refraction Phenomenon

Calculating atmospheric refraction requires knowledge of the current atmospheric conditions,

for individual ray tracing. Measuring the density gradient for a single ray, is difficult, thus an average gradient could be used, this could be measured or modelled given various assumptions. One model, could assume there is no change in the medium, the atmosphere is of uniform density and thus no influence from refraction. Another model could examine how the mass of Earth's atmosphere is distributed; broadly speaking as altitude is increased the less dense the atmosphere becomes. Another method could incorporate meteorology.

The Effective Earth's Radius Model ($\frac{4}{3}$R model) is widely used in meteorology circles (American Meteorological Society, n.d.), and approximates a constant impact due to refraction. The $\frac{4}{3}$R model assumes that refractivity is directly inversely proportional with height and assumes the model of the Earth is spherical. The corrected range from the $\frac{4}{3}$R model is shown in Equation 2.6, where $k = \frac{4}{3}$. This theory is $k = 0.143$ (Sjoberg & Shirazian, 2012) for Geodesy. However, the $\frac{4}{3}$R model has been widely criticised, as far back as Bean and Thayer 1959 who compared the $\frac{4}{3}$R model to two proposed new methods. The work was brought about due to the newer "long-range applications" (Bean & Thayer, 1959). From this study and in more recent studies Haering and Whitmore (1995), Zeng et al. (2014) and Doerry (2013) it is clear that the $\frac{4}{3}$R model is not an effective correction for refraction for altitudes above 1 km.

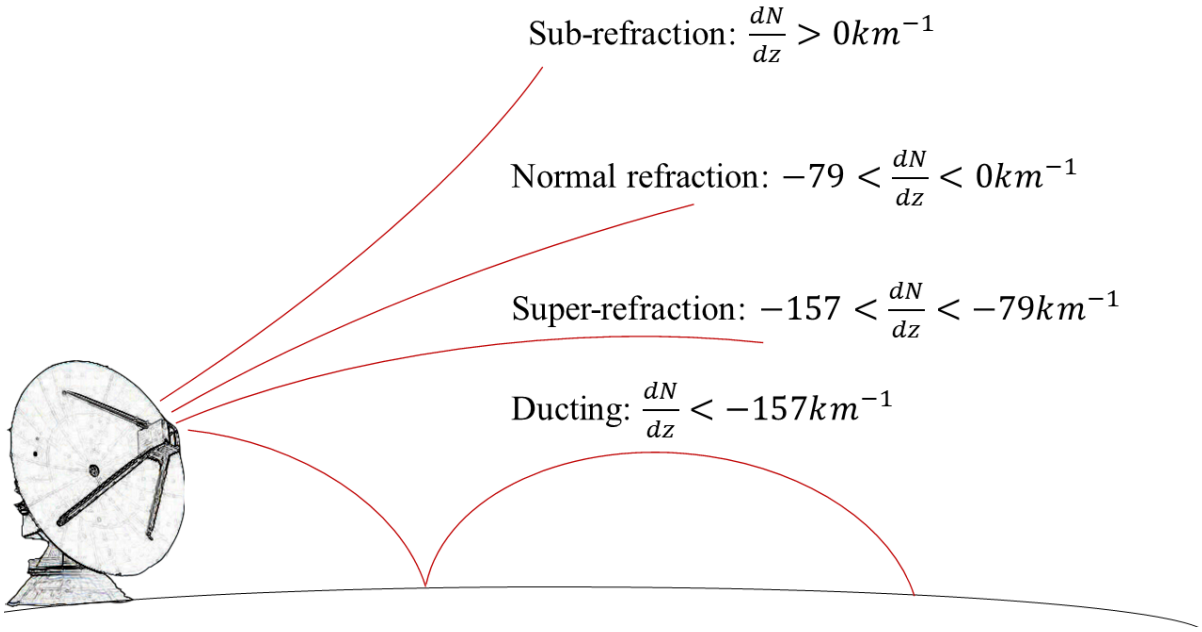

Figure 2.8: Refraction Diagram

Four main papers were assessed to determine an improved method to the $\frac{4}{3}$R model, Haering

and Whitmore (1995), Doerry (2013), Zeng et al. (2014) and Lin et al. (2020). The Sandia Report (Doerry, 2013), first offers a relationship between refraction and altitude from (Bean & Thayer, 1959) where the altitude is split into three ranges; 0-1 km, 1-9 km and above 9 km, whilst it shows an improvement on the initial $\frac{4}{3}$R model there were other models that performed better. Sandia (Doerry, 2013) compares 2 main models to the $\frac{4}{3}$R model, the first an iterative numerical integration technique (INIT) and the average radius of curvature technique (ARCT). The conclusions of the Sandia Report, suggest that making an estimation of N even if it is wrong produces a better model than the $\frac{4}{3}$R model. The INIT is better than ARCT however the ARCT has the advantage of a single formula, both can take surface refraction but a best guess can be used if unavailable.

$$r = ka(\sqrt{\sin^2\phi + \frac{2h}{ka}} - \sin\phi) \tag{2.6}$$

Haering and Whitmore (1995) and Zeng et al. (2014) both use temperature data in a gradient refraction method. The gradient refraction method segments the beam to calculate the local elevation angle. Each segment uses the previous local elevation angle to make incremental adjustments due to refraction. Haering and Whitmore (1995) chose segment lengths of 1000 ft along the ray, and also truncated the number of segments to improve on computation time. Some of the errors that can arise from this method are the fact that the refraction constant and the meteorological data are all assumed to be constant along the same altitude layers, both in space and time. And the relationship between refraction and altitude is unrealistic.

The general conclusion to draw is that using weather balloon observations/modelled temperature for specific observations gives the most precise refraction; This is evident among the studies (Haering and Whitmore, 1995; Doerry, 2013; Zeng et al., 2014). All of these methods were examined using spherical and ellipsoidal Earth models, and treat the atmosphere in generalised layers, the addition of meteorological data improves this, but in cases of mountainous regions or deep valleys, this would need reexamining. If temperature data i.e from a radiosonde is available NASA/Zengs gradient refraction method would give the most accurate refraction detail for the radar beam. However if no temperature data is available, Sandia's INIT with

approximation method is the best.

$$n_{i1}\theta_{i1} = n_{t1}\theta_{t1} \tag{2.7}$$

$$t = \int_i^t \frac{n}{c} dr = min \tag{2.8}$$

$$\rho_{avg} = \frac{1}{h_a - h_s} \int_{h_s}^{h_a} \rho dh \approx (\frac{H_b}{10^{-6} N_s \cos\psi_g})(\frac{e^{\frac{h_a - h_s}{H_b}} - 1}{\frac{h_a - h_s}{H_b}}) \tag{2.9}$$

$$k_{avg} = \frac{1}{1 - \frac{R_e}{\rho_{avg}}} \approx [1 - (\frac{10^{-6} N_s \cos\phi_g R_e}{H_b})(\frac{\frac{h_a - h_s}{H_b}}{e^{\frac{h_a - h_s}{H_b}} - 1})]^{-1} \tag{2.10}$$

2.3.1 Refraction

The resultant refraction correction is broken down by altitude with the conditions specified as followed: If the initial altitude of the voxel location, h_a is under 6 km, the Bean and Thayer (1959) conditions for N_b and H_b are used. If $6 < h_a \leq 9.5\,km$ then Doerry (2013)'s Equation 26 are used for the conditions which are based on the relationship between refraction and altitude, and an improvement from Bean and Thayer (1959). If the $9.5 < h_a < 100\,km$ then the iterative numerical integration method from Doerry (2013) is used. μ is the convergence parameter, which was determined to be $1 \cdot 10^{-5}$ and η, m are the iteration parameters Doerry (2013)'s Equation 51. The new elevation angle is estimated from either Lin et al. (2020) at $H_b = 0$ otherwise Doerry (2013).

2.3.2 Collocation

In the context of this thesis, the definition of collocation is when two observations occur at the same point in physical space and time of the same target. In empirical applications, collocation may not be achievable between instruments, thus determining the difference between sets of observations will guide users between the ability to use observations together or independently. The collocation code has two main variants, a column and the closest approach.

The column collocation code is a variation of a CVP (Column Vertical Product) found in the radar community (Lukach et al., 2022 and Murphy et al., 2020). The new column product is designed to compare radar voxels with a single point location, for example a citizen science report which gives a singular coordinate value. The user first defines the radius of the column. Then, using the previously specified corners of the radar voxel (Ω, χ, Υ, ζ), the geodesic

distance, s is computed between each corner and the single point using the Inverse from the GeographicLib Module (Karney, 2022). The conditions are set as shown in Equation 2.11, that all four corners to single point, geodesic distance s_{12} must be equal or within the radius limit of the column. If these are met then the corresponding voxels and indexes values are saved for output. Figure 2.9 demonstrates what this column would look like, of a 5 km radius around a single point, an insect light trap, this was made using the NXPol radar, when it was based at Chilbolton Observatory on the 14th of February 2018.

$$\begin{aligned} s_{\Omega} &\leq radius_{column} \\ s_{\chi} &\leq radius_{column} \\ s_{\Upsilon} &\leq radius_{column} \\ s_{\zeta} &\leq radius_{column} \end{aligned} \tag{2.11}$$

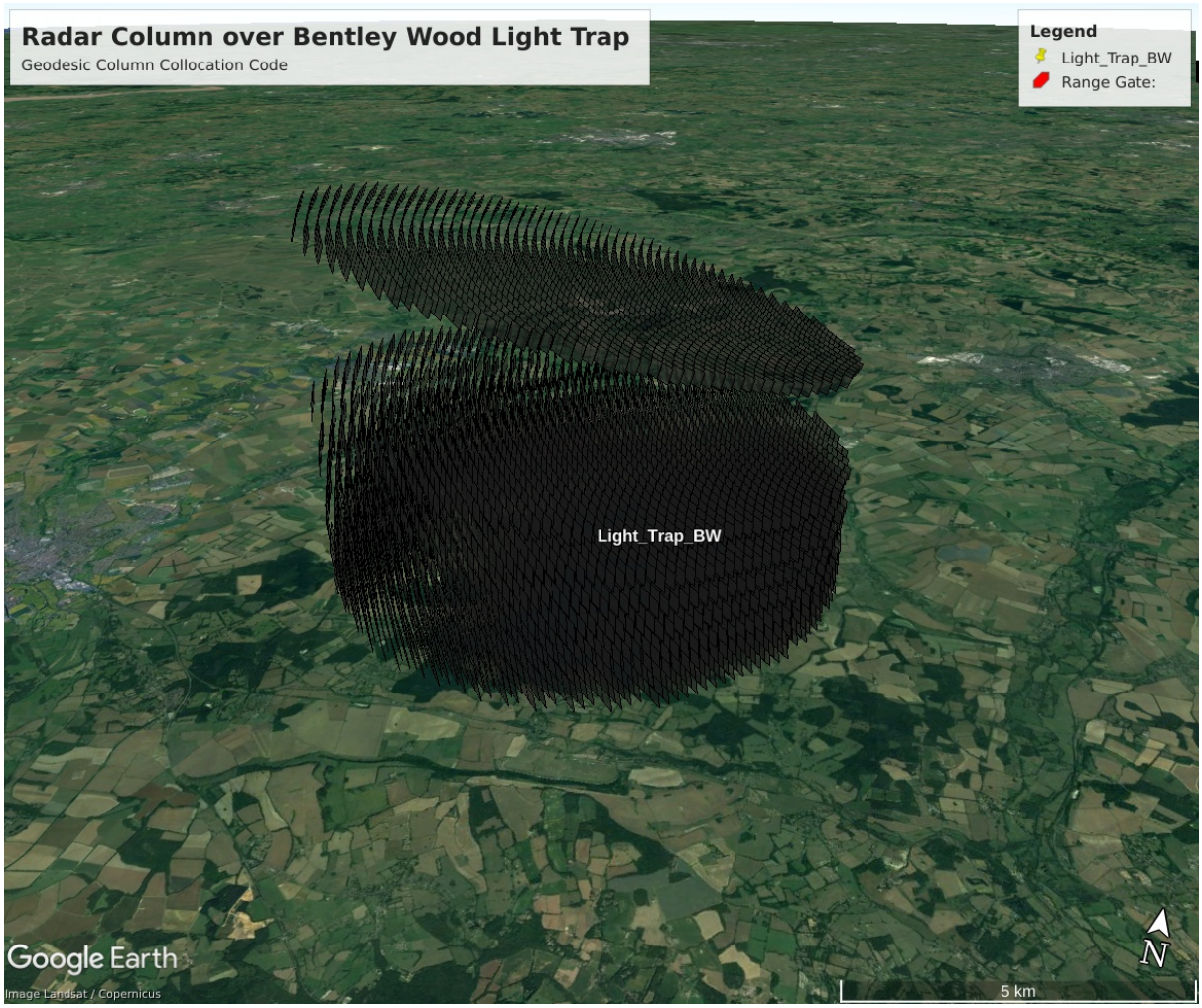

Figure 2.9: 5 km radius of column of radar voxels over Bentley Wood Light Trap from the NXPol Radar, located at Chilbolton Observatory on 14/02/2018.

The closest approach was created for multiple point comparisons, i.e when the secondary instrument is changing its position in time. Collocation occurs, in this scenario, when the secondary instrument is within the radar voxel at the same time. Time is limited in the first instance, before the rest of the code. In Cartesian coordinates limits of an area would be imposed by using $y = mx + c$ however in a geodesic plane the limits imposed use the lines of azimuth from each coordinate corner. Figure 2.10 shows, independent of altitude, the 4 corners of the radar voxel, representing the minimum and maximum positions. If the azimuth line between Ω corner and the secondary instrument is between the azimuths from Ω to χ and Ω to Υ and the same from ζ then there is collocation. For the closest approach Equation 2.12 shows how these limits are implemented. The limits are set by the user and should be informed by the specifications of the radar. Then using numpy module arg partition (Numpy, n.d.) the closest voxel to the secondary instrument is determined by s, altitude and approximate direct distance,

so the user can determine the most appropriate voxel to use for their needs.

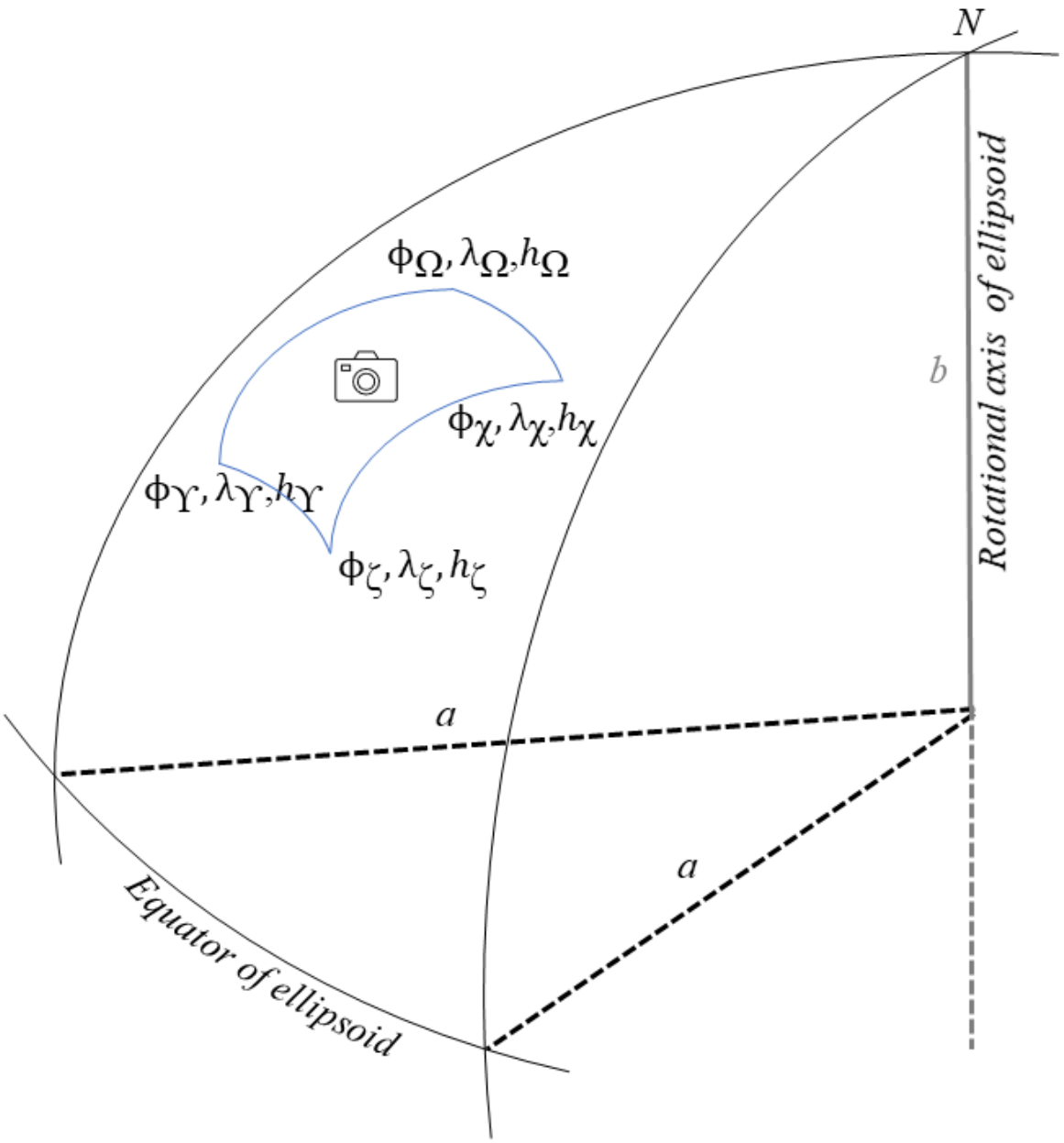

Figure 2.10: Four corners of the radar voxel on defined by the s, the geodesic distance along the surface of the earth, as a birds eye view of the area covered on the surface of the Earth.

$$
\begin{aligned}
s_{mid} - gat < s_{12} < s_{mid} + gat \\
h_\Upsilon \leq h_2 \leq h_\Omega \\
\alpha_{rg_{min} - \frac{1}{2}\theta_{BW}} \leq \alpha_{12} \leq \alpha_{rg_{max} + \frac{1}{2}\theta_{BW}}
\end{aligned}
\tag{2.12}
$$

2.4 Simulating Radar Cross Section

The radar cross section (RCS) represents the electromagnetic "fingerprint" of a target as detected by a radar system. Under idealised conditions, this fingerprint can be simulated using the WiPL-D Pro 3-D Electromagnetic Solver (B. M. Kolundzija, 1999; B. M. Kolundzija and Djordjevic, 2002), a full-wave method-of-moments solver widely used for complex target modelling. Prior to 2022, most electromagnetic (EM) modelling of biological targets, particularly insects, assumed that wing structures had negligible influence on RCS. Standard modelling approaches typically approximated insect bodies using simple geometric shapes, most commonly ellipsoids e.g., Drake et al. (2017), Mirkovic et al. (2019) and Wang et al. (2022).

The NERC funded BioDAR project (NE/S001298/1) challenged this assumption by asking whether anatomically detailed insect models, including wings, significantly alter the simulated RCS compared to ellipsoidal approximations. The findings demonstrated that wing structures have a substantial effect on the resulting RCS.

In response, a novel RCS simulation methodology was developed by the author, Freya I. Addison, and published as part of the BioDAR project (Addison et al., 2022). This methodology incorporates anatomically accurate insect geometries into EM simulations. For the purposes of this thesis, the approach has been further refined and extended to simulate the RCS of both a male and female *Lasius niger* (common black garden ant) during flight.

The first step in generating a detailed model for RCS simulations involves acquiring a high-resolution 3D scan of the insect specimen. This scan captures the overall morphology, including key features such as the body, wings, and legs. However, raw scans often contain imperfections, such as surface noise, holes, or missing anatomical structures, which must be corrected prior to simulation.

To address these issues, the scan is either digitally cleaned or used as a reference for manually reconstructing the insect in 3D modelling software. The goal is to produce a watertight, single-surface mesh that accurately represents the exterior geometry of the insect. In many cases, incomplete or absent structures (e.g., wings or legs) are reconstructed manually to en-

sure anatomical fidelity. Once the complete surface mesh is generated, it is reformatted and exported into a format compatible with the electromagnetic simulation software, specifically, WiPL-D Pro. The final model is then ready for input into the RCS simulation pipeline.

As described in Addison et al. (2022), insect specimens were scanned using the Micro-CT scanner at the Natural History Museum (NHM), which generated 3D volumetric reconstructions by capturing a sequence of 360^o 2D X-ray projections around the specimen. These projections are computationally stacked and processed to produce a high-resolution 3D volume of the target.

To ensure anatomical accuracy, particularly for winged insects, the specimens were prepared with wings spread in a mid-flight position, similar to standard entomological display practices (see Figure 2.11). This orientation maximises visibility of the full wing structure during scanning.

For larger specimens (typically those exceeding 5 mm in length), such as Queen ants, the insects were sputter-coated with gold-palladium. This metallic coating enhanced the contrast of the insect's exterior in the X-ray images by increasing surface reflectivity and helped to reduce penetration depth, thereby limiting visualisation to the outer morphology. Prior to scanning the central mounting pin (commonly inserted through the thorax for transport or display, as shown in Figure 2.11), was carefully removed. Each specimen was than positioned on a foam support to stabilise it during the scan, ensuring minimal movement and optimal orientation.

Figure 2.11: *Lasius niger* taken by Dr Elizabeth Duncan in her laboratory. Pinned with wings spread out in the mid-flight position; the right-hand side hindwing is missing, but the rest of the specimen is intact, with all segments of antenna and legs present.

The native resolution of the Micro-CT scans obtained from the NHM was 0.0226 mm per voxel. Due to the large files sizes generated, particularly for larger specimens such as the Queen ant, data optimisation was necessary to facilitate downstream processing. As advised by the NHM staff, the scan data were downsampled using the software Drishti (Y. Hu et al., 2020), reducing the file size of the Queen ant model from 1.69 GB to approximately 26.9 MB without significantly loss of anatomical detail.

The downsized volume was then imported into 3D Slicer (Fedorov et al., 2012), an open-source platform for medical image analysis and 3D visualisation. Within 3D Slicer, a series of preprocessing steps were applied:

- The scissor cropping tool was used to remove the extraneous material, such as the foam support beneath the specimen.

- A thresholding filter was applied to isolate pixel intensities within a defined range, thereby enhancing contrast, reducing background noise, and highlighting the physical structure of the insect.

- The model was then segmented to exclude areas outside the thresholded intensity range, enabling focused analysis of the insect anatomy.

During this segmentation process, it is possible to enhance specific internal structures (e.g., organs), although certain fine features, particularly delicate appendages like wings, may be lost if their intensity values fall outside the defined threshold range.

To repair surface discontinuities or minor gaps in the mesh, a smoothing algorithm was applied. The final model was then exported in STL (.stl) format for the use in 3D modelling and electromagnetic simulation. Figure 2.12 displays the processed Queen ant specimen within 3D Slicer. It should be noted, that this particular specimen was scanned without wings.

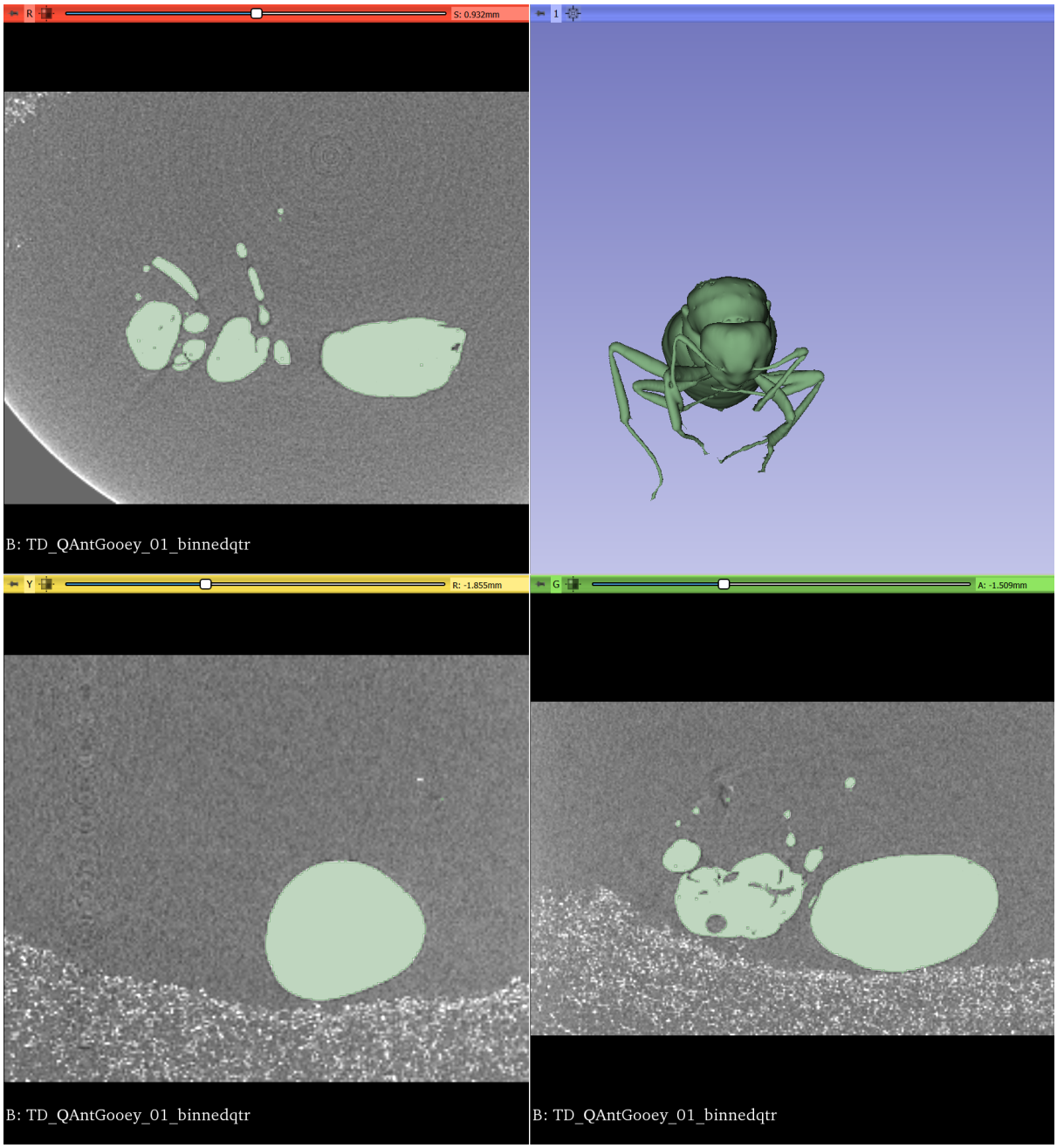

Figure 2.12: Slicer Software, the top right box shows the model created from the slices, 2D stack of CT images, the other 3 boxes show the 2D images from different angles. This specimen is of a Queen Ant at 0.25 resolution of the original scan.

Following segmentation and export, the 3D insect models were imported into Blender, an open-source 3D graphics and animation software (Blender Online Community, n.d.), for final clean-up and alignment prior to simulation.

Within Blender, each specimen was reorientated to standardise the spatial configuration across all models, ensuring consistency for simulation and comparison. The following alignment

protocol was applied:

- The origin of the coordinate system was set to the geometric centre of the insect model.
- The head of the insect was orientated to face the positive x-axis.
- The ventral side of the abdomen (i.e., the underside, typically where the legs are positioned) was aligned with the negative z-axis.

This consistent orientation ensures that anatomical comparisons across different insect models are performed relative to a uniform reference frame, which is essential for reproducible RCS simulations and analyses.

Once the insect model is correctly orientated in Blender, a clean up process is performed to isolate the external structure for simulation. The model is first split using Blender's "Separate by Loose Parts" function. All disconnected components, typically artefacts or scanning noise, are removed, ideally leaving only the main insect geometry.

The internal structure is then examined. If internal features are minimal and easily distinguishable, they are manually separated and deleted. In cases where internal geometry is too complex or poorly defined, remeshing tools are used to create a simplified surface mesh by tracing over the original geometry. Any defects in the model, such as holes or missing limbs, are corrected by duplicating similar features or manually reconstructing them.

In the case of the Queen ant model, internal structure was minimal and easily removed, allowing the external geometry to be edited directly. Wings were absent in the scan and were reconstructed using two reference images, Figures 2.13(a) from Pfeiffer (2017) and 2.13(b) from Reddit (2017). These images were imported into Blender, then scaled and rotated to align with the model. Using Blender's polygon tool, wing outlines were traced and then extruded to form a 3D structure consistent with the anatomical appearance.

The cleaned and completed model was exported as an STL (.stl) file and imported into WiPL-CAD, the companion software to the WiPL-D Pro 3-D Electromagnetic Solver (B. M. Kolundzija & Djordjevic, 2002). Within WiPL-CAD, the mesh was automatically rerendered

(a) *Lasius niger* Queen ant, dorsal view from (Pfeiffer, 2017)

(b) Alate Queen ant, side on profile (Reddit, 2017)

Figure 2.13: Reference images of alate Queen ants, used as a guide for shape and size to in simulation model.

to reduce the number of plates whilst preserving the original geometry. This mesh optimisation step is critical for ensuring simulation efficiency and accuracy. Plate size was configured based on the radar wavelength, with the maximum plate dimension $2\lambda^2$ and any holes to $< \frac{1}{2}\lambda$. An optimised mesh was generated for each radar band used in simulation, specifically, X-band, C-band, and S-band, ensuring compatibility with the different wavelengths. The right mesh can reduce the amount of unknowns and improve the run time of the WiPL-D Pro simulation. Thus one is created for each radar band, (e.g X-band, C-band, and S-band).

The WiPL-D simulations were run using the following standard configuration:

- Di3 Files: Off
- Integral Advanced: Enhanced 1
- Precision: Double
- Observation Mode (OM): Monostatic
- Units: mm, GHz, V

Following the approach in (Addison et al., 2022), the insect model was segmented into anatomical parts; body, wings and limbs shown in Figure 2.14, to allow dominant material-specific electromagnetic properties to be assigned, yellow for chitin, red for homogenised lesser borer beetle. Using Blender's manipulations tool, mesh plates corresponding to each anatomical region were grouped and tagged accordingly. Material properties were assigned based on previous studies:

- The body was given the dielectric constant of a "homogenized blend of lesser grain borer beetles" as used in (Nelson et al., 1998), (Stepanian et al., 2018a) and (Addison et al., 2022) with a complex dielectric constant of $\varepsilon = 34.3 - j8.6$
- The wings and limbs, primarily composed of chitin, were assigned a dielectric constant of $\varepsilon = 4.1 - j0.16$, following values reported in (Chen et al., 2020).

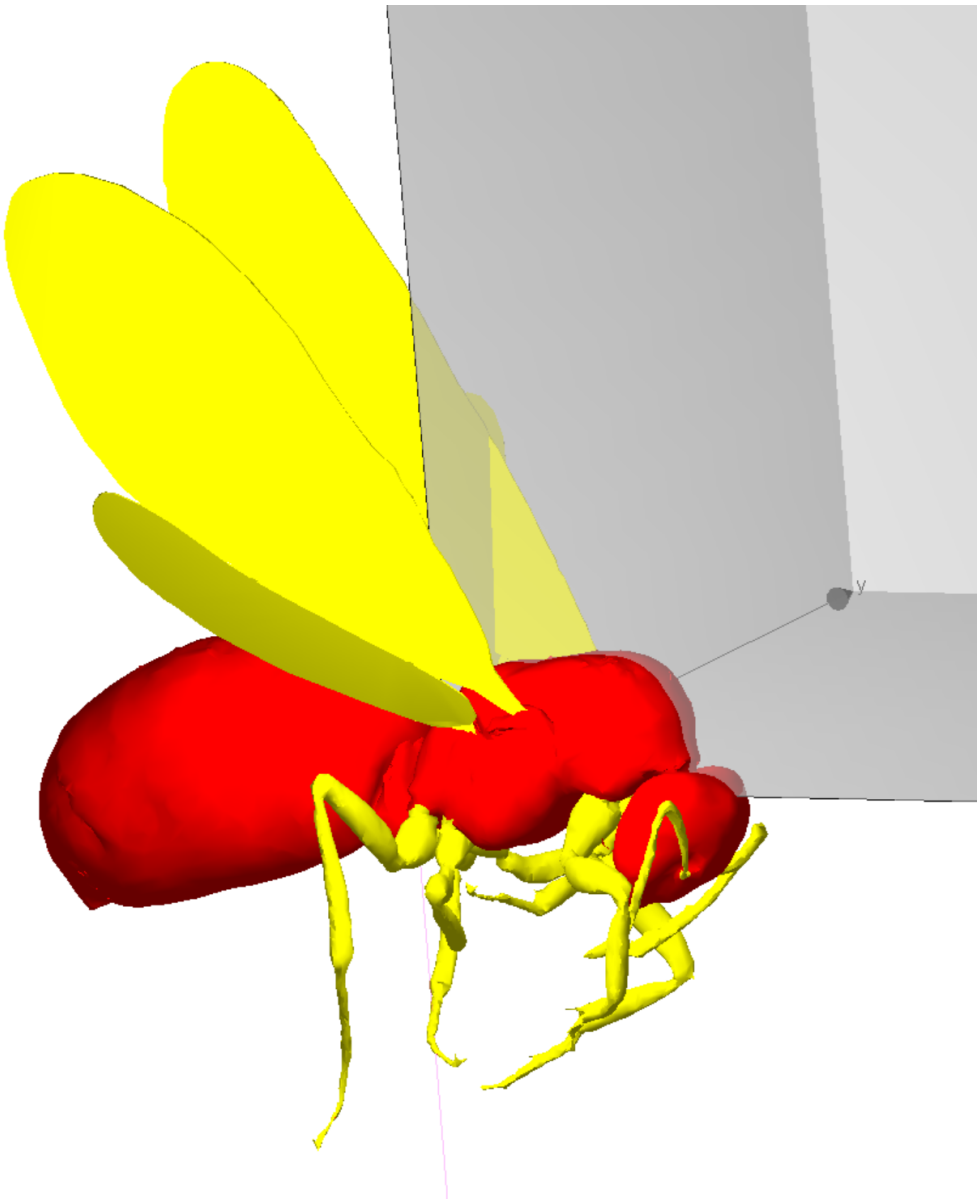

Figure 2.14: WiPL-D Software, of the full Queen ant model. The red section of the body was given the dielectric constant of 34.3, j-18.6 (Stepanian et al., 2018a) and the yellow section, the wings and the limbs the dielectric constant of 4.1, j-0.16 (Chen et al., 2020).

To estimate the average RCS of the insect, two distinct electromagnetic simulations were performed, each designed to account for different possible orientations of the insect relative to the radar beam.

1. 1. **Azimuthal Simulation** ($\alpha - scan$): In this simulation, the incident electromagnetic wave is polarised horizontally, and the RCS is computed over a full 360^o rotation in the azimuthal plane. This configuration effectively simulates the insect rotating about its vertical axis, analogous to a ballerina turning in place on a music box. It captures

variation in RCS as the insect's orientation changes around the horizontal plane.

2. 2. **Elevational Simulation** ($\theta - scan$): In the second simulation, the incident wave is polarised vertically, and the RCS is calculated over 360^o in the elevation plane. This represents the insect performing a forward rotation or a somersault, think woodlouse, simulating changes in RCS as the insect pitches up and down relative to the beam.

These two scanning orientations are designed to approximate the wide range of possible flight directions and body postures insects may adopt in free flight. By combining the results of both simulations, a mean RCS value is derived that represents the insect's average backscatter signature across all possible incident angles.

With an average RCS of the male and female, the ratio of sexes is applied and then this is used to map from the radar variables of our scattered targets to a tangible biological parameter. The assumptions made is the targets are homogenous ant swarm, with the RCS average of ants, the number of ants can then be derived.

Chapter 3

Results: Evaluation of Radar Geodesic Algorithms

The author, Freya I. Addison, designed and wrote a new software package, in python, incorporating the geodesic location module (Geographiclib) (Karney, 2022), specifically to estimate the geodesic location of radar voxels with adaptive refractive corrections, given the position of the radar, elevation, azimuth and direct range. The Geographiclib module (Karney, 2022) requires "s", which is not known directly from radar. The author wrote the Radar Voxel Geodesic Location (Module), to iteratively estimate the geodesic distance (s) across the surface of the Earth between the radar and the radar beam. The Collocation module, also written by the author, enables the radar voxels to be collocated with a secondary source, using either direct distance, the geodesic distance across the Earth (s), or altitude.

The following chapter evaluates the two modules developed. The chapter assesses the performance of both algorithms, the realism of their outputs, the process of validation, and compares results obtained using different Earth models, as outlined in Chapter 1, Section 1.7. Since these algorithms were created from scratch, transforming theoretical ideas into practical applications, validation is the central focus. The context in which these algorithms were designed is also critical. Radar observations are recorded relative to the radar's own position. In research campaigns where multiple instruments aim to observe the same phenomenon, achieving collocation within a universal reference frame is necessary. Furthermore, planning for cross-instrument collocation

ensures better integration. By incorporating geodesy, the standard universal reference frame, into radar positioning and scanning strategies, the likelihood of collocation between instruments is maximized at the start and throughout the campaign. Post-processing verifies collocation, accuracy, and the relative distance between coincident observations.

3.1 Validation

The principle behind verifying the validity of the Radar Voxel Location (Geodesic) code is to corroborate a radar voxel location with a coincident target of a known location. The target needs to be in direct view of the radar, above any ground clutter, and should have a distinctive radar cross section, or be the only object with high reflectivity within the surrounding range gates in order to be identifiable as the known target. This is done by using a highly reflective object, for this case a transmission mast, of known location. A calibrated radar is also necessary, the requirements of which are outlined in Section 2.1. If the peak reflectivity of the mast appears in the same radar voxel that the collocation code selects, then the code is validated, if they do not, then the collocation code does not work.

Validation requires both the direct and indirect methods with the known variables of: ϕ_1, λ_1, ϕ_2, λ_2, α_{12}, r. The Geographiclib module (Karney, 2022) is used with the direct method $(\phi_1, \lambda_1, \phi_2, \lambda_2)$ to deduce the azimuth angle between the radar and the mast, and the geodesic distance, s. By limiting the azimuth, and approximating the range from s, the peak reflectivity of the mast is found within the radar data. The exact azimuth and range of the peak reflectivity are then put into the collocation code to calculate the coordinates of the mast, if they are coincident with the known coordinates of the mast then the Geodesic code is validated.

The UK Met Office (UKMO)'s radars have a wide beamwidth of $\sim 1^o$ (Darlington et al., 2016). Stockland Hill transmission mast is situated (50.807^o, -3.105^o, $466\,m$), standing at 237.4 m tall (Brown, 2014). As the mast has a known location and is within 50 km of the Wardon Hill radar it was selected to be the validation point for the Geodesic code. The Geodesic distance along the surface of the Earth between the Wardon Hill radar and Stockland Hill mast is $s = 38693\,m$; the radar voxel that encompasses this distance according to the Geodesic code is the voxel at ($r = 38700\,m$, $\alpha = 268^o$, $\theta = 0.5^o$). Figure 3.1 shows that there is an extended

peak above 40 dBZ at the predicted 38.7 km (42.5 dBZ) and another at 39.3 km (47.4 dBZ). Figure 3.2 shows a single peak of 33 dBZ at range 38.7 km. This is because the mast's size and metallic composition makes it an object with high scattering properties, so much so that the magnitude of its returned power is "sufficient to saturate the digital filters" (Darlington, 2015). It can be determined that the mast falls within the location of the 38.7 km range gate, (shown in Figure 3.3,) as that is the centre of the peak reflectivity between all three radar voxels displaying peak reflectivity, as illustrated by Figures 3.1 and 3.2, and thus the Geodesic code is valid.

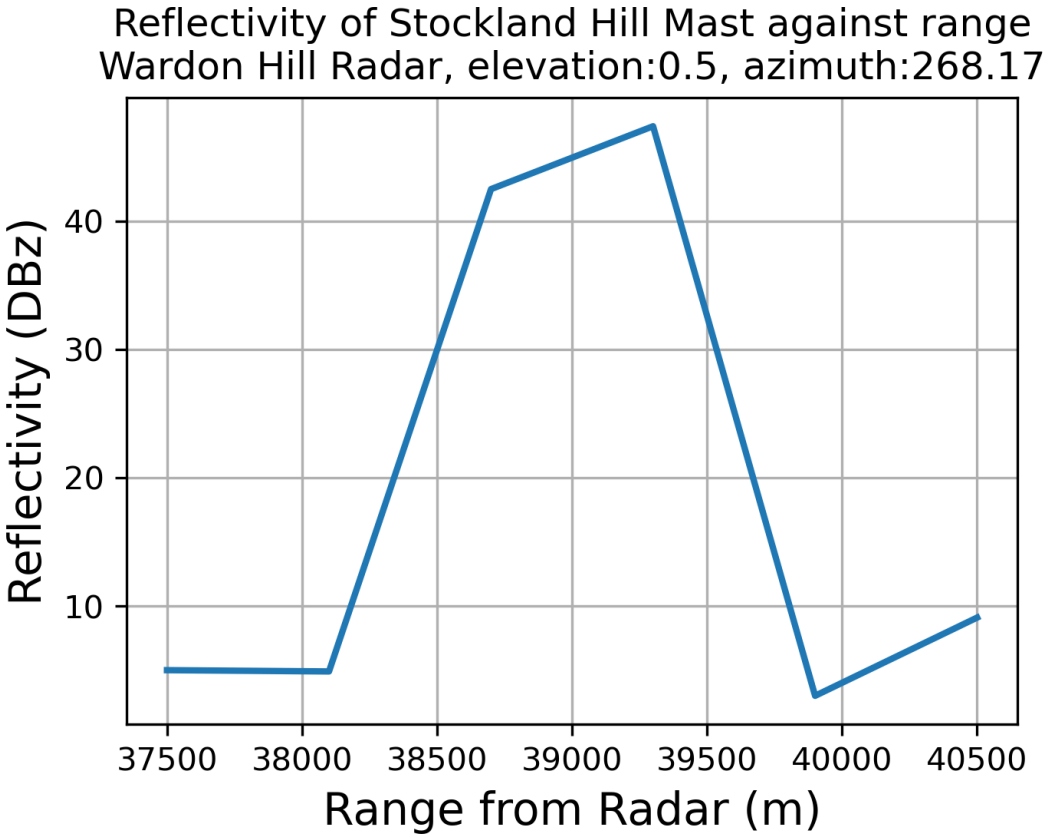

Figure 3.1: Wardon Hill Radar 268 azimuth, 0.5 elevation, reflectivity spike for positional calibration with Stockland Hill Mast.

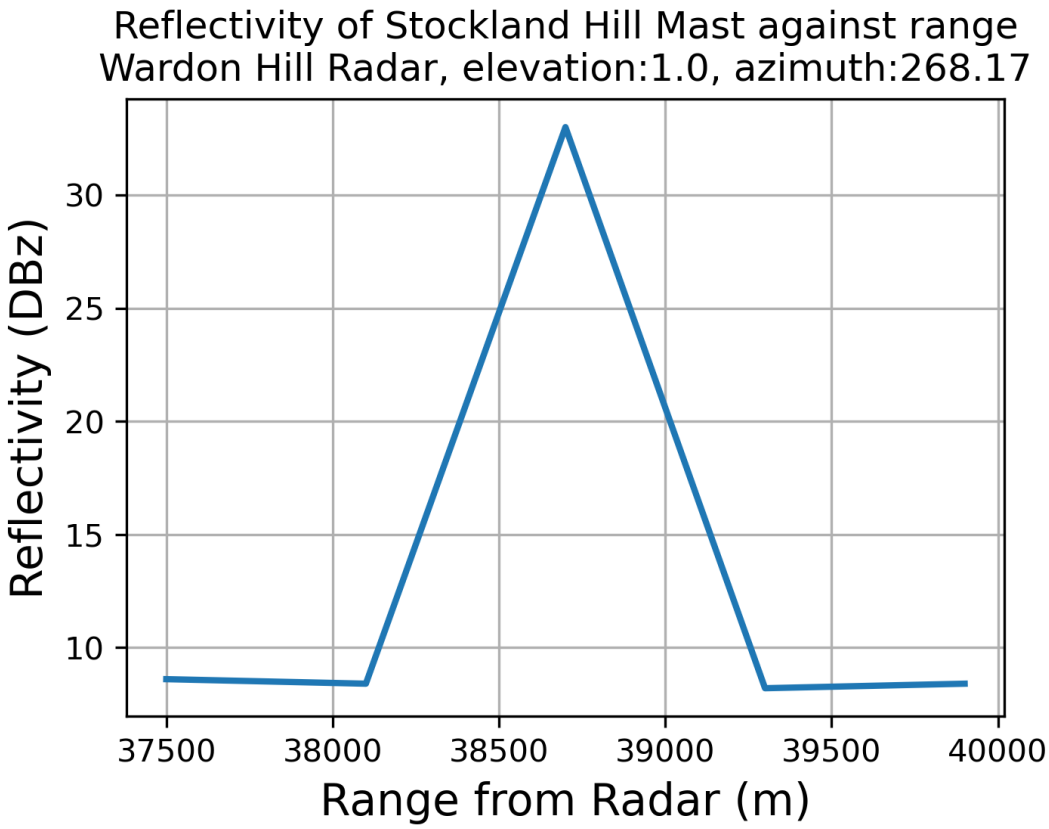

Figure 3.2: Wardon Hill Radar 268 azimuth, 1^o elevation, reflectivity spike for positional calibration with Stockland Hill Mast.

Only one validation is required, because the results are binary, either success or failure. Moreover, finding a similar setup within a 50 km range of a radar is particularly challenging.

Figure 3.3 shows Stockland Mast, the cornered radar voxels, at $\theta = 0.5^o$ ranges $38.7\,km$ and $39.3\,km$ and range $38.7\,km$ at $\theta = 1.0^o$ are displayed in red using the geodetic Earth model, from the UKMO Wardon Hill Radar. These are the boxes which the radar signal is saturated. The upper elevation voxel overlaps with the lower elevation voxels as the radar's beamheight is $\sim 1^o$.

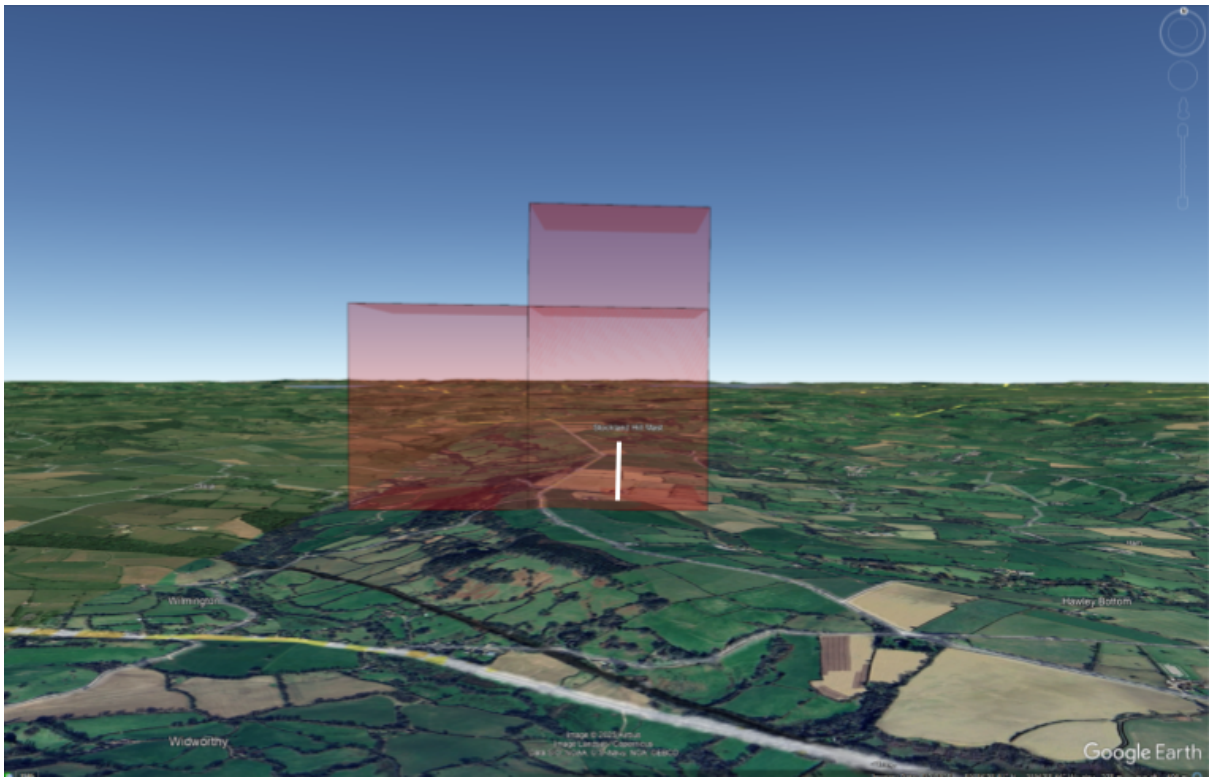

Figure 3.3: Google Earth Image of area covered by peak reflectivity of Stockland Hill Mast using the Geodesic model for the radar voxels (red).

Variable	Mean	Std Dev	Median	Q1 (25%)	Q3 (75%)	Max (abs)
lat_diff_deg	0.0000	0.0013	-0.0000	-0.0001	0.0001	0.0088
lon_diff_deg	-0.0000	0.0022	0.0000	-0.0010	0.0010	0.0097
alt_diff_m	859.6290	1091.5812	294.4029	78.9826	1403.5379	3654.1227
s_diff_m	148.8844	157.3882	94.3501	35.0738	206.6754	980.6085

Table 3.1: Statistical Summary: Geodesic vs UKMO

The methodology was composed with the intent on using with research radars, but ultimately, as the project evolved and calibration requirements became stricter, the UKMO radars were used instead. The reason to stipulate this is because the UKMO now, provide a midpoint location for their radar voxels. The UKMO use a translation from spherical cartesian coordinates to Geodesic using the Proj4 and the azimuthal equidistant projection, this information was sent in an email (Robert Scovell 2023, personal communication, 30th January). Comparing the UKMO and Geodesic locations, the coordinates are fairly on par as shown in Table 3.1, although Figure 3.5 demonstrates how the differences steadily increase with range from the radar and the variability with the interquartile range shaded. The greatest difference in position between models lies within the altitudes, shown in Table 3.1 and Figure 3.4. With a beamheight of

1^o, at $50\,km$ this equates to approximately a voxel height of $0.87\,km$ and the model altitude differences are less than 34% of that voxel height. At $100\,km$, the voxel height is approximately $1.75\,km$ and the altitude difference $\sim$ 43% of that value. At $200\,km$ range this increases to a difference of $\sim$ 68% of altitude difference over voxel height. The variation is increasing as range increases so the averages look different; altitude differences average $87.64\,m$ in the first $50\,km$ in the limited ranges and elevations inputted. The geodesic model used the standard refraction value of $N_s = 313$ compared with the UKMO's constant refraction value. According to UKMO employee Robert Scovell (2023) they use the $\frac{4}{3}R$ model, as discussed in Section 2.3, this does not hold up (Haering and Whitmore, 1995; Doerry, 2013; Bean and Thayer, 1959). The difference in refraction models would explain the discrepancy in altitude. The significance in altitude discrepancy is important as it is reflected in the atmospheric boundary layer, which is the lowest level in the troposphere. This is where terrain and local atmospheric effects have the biggest influence. Given altitude is fundamental for Numerical Weather Prediction Models, local forecasts in particular would be impacted.

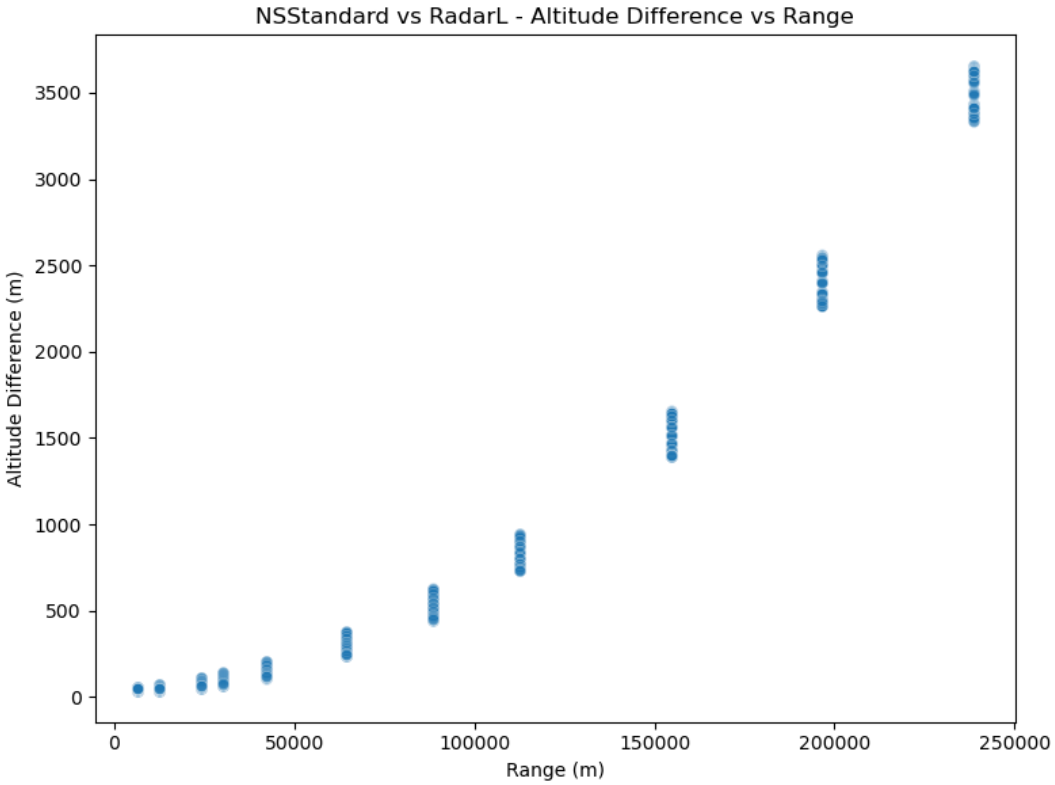

Figure 3.4: Wardon Hill Radar scatter plot showing the spread of altitude differences (see Table 3.1) between the UKMO positional altitude data and the geodesic-calculated values.

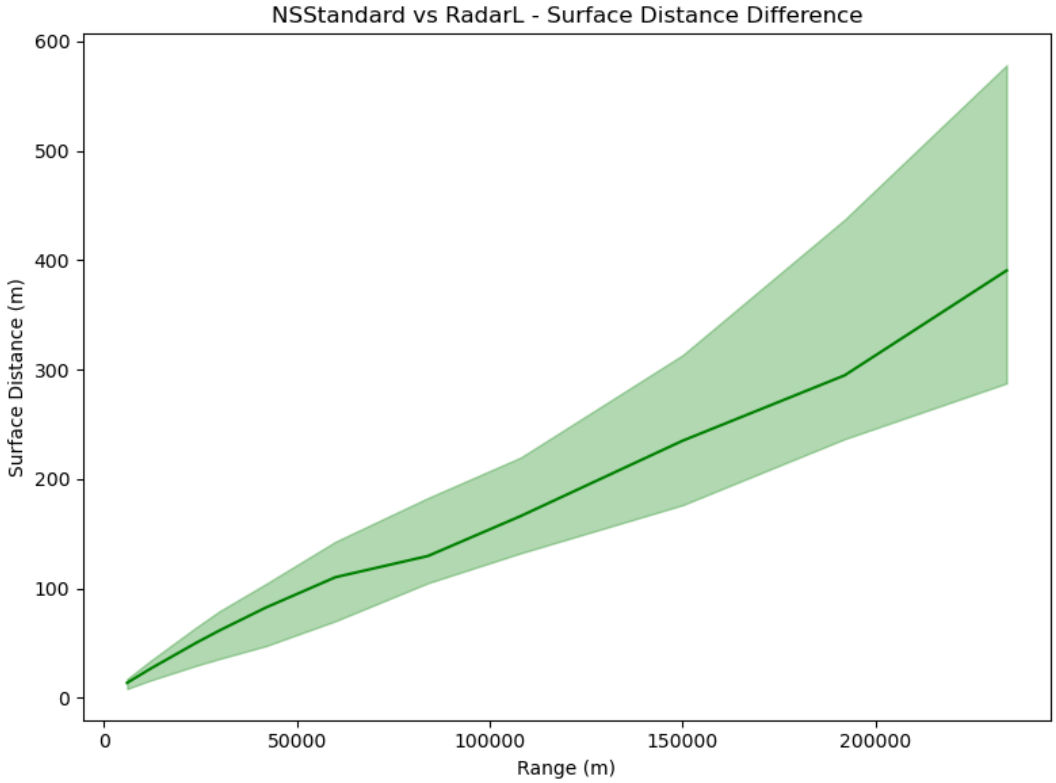

Figure 3.5: Wardon Hill Radar upper and lower quartiles shaded over median surface distance differences (s in meters) between UKMO coordinates and geodesic calculations.

3.2 Comparison Between Flat, Spherical, Elliptical and Geodesic

For the comparison between the models, refraction is not used in order to assess the geometry and projection translations. Three locations were chosen from across the globe to demonstrate the impact that location has when comparing the shape of the Earth models. The locations are Wardon Hill, representing mid-latitude, La Reunion representing the equatorial region, and Troll representing the Poles. The test azimuths, ranges and elevations are listed below in Table 3.2 and the statistical quartiles from python package statistics (The Python Standard Library, n.d.) are listed in Tables 3.3 and 3.4.

s (km)	10, 15, 20, 25, 30, 40, 50, 60, 70, 80, 90, 100, 150, 200
α^o	$\pm$165, $\pm$150, $\pm$135, $\pm$120, $\pm$105, $\pm$90, $\pm$75, $\pm$60, $\pm$45, $\pm$30, $\pm$15, 0, 180
θ^o	0.0, 0.5, 1.0, 2.0, 5.0, 7.0, 10.0, 12.5, 15.0

Table 3.2: Test parameters for s, α, and θ.

$Elevation = 0.5°$				
Radar		**Lower Quartile**	**Median**	**Upper Quartile**
Wardon Hill	$\delta\lambda$	$-1.59 \cdot 10^{-6}$	$1.12 \cdot 10^{-6}$	$4.98 \cdot 10^{-6}$
(50.81833, -2.55472)	$\delta\phi$	$-2.41 \cdot 10^{-6}$	$1.58 \cdot 10^{-6}$	$7.34 \cdot 10^{-6}$
La Reunion	$\delta\lambda$	$-2.83 \cdot 10^{-6}$	$-7.51 \cdot 10^{-7}$	$1.24 \cdot 10^{-6}$
(-21.0803, 55.38930)	$\delta\phi$	$-3.13 \cdot 10^{-6}$	$-7.16 \cdot 10^{-7}$	$1.36 \cdot 10^{-6}$
Troll	$\delta\lambda$	$-2.62 \cdot 10^{-6}$	$-6.27 \cdot 10^{-7}$	$1.40 \cdot 10^{-6}$
(-90.00, 0.00)	$\delta\phi$	$-7.98 \cdot 10^{-6}$	$-1.24 \cdot 10^{-6}$	$4.31 \cdot 10^{-6}$

Table 3.3: The difference in latitude (ϕ) and longitude (λ) between the theoretical midpoint of a radar voxel at elevation 0.5°, located at mid-latitude (Wardon Hill), near the equator (La Reunion), and the poles (Troll), between Geodesic and Flat Earth Model.

$Elevation = 0.5°$				
Radar		**Lower Quartile**	**Median**	**Upper Quartile**
Wardon Hill	$\delta\lambda$	$-4.17 \cdot 10^{-4}$	$-6.02 \cdot 10^{-6}$	$3.65 \cdot 10^{-4}$
(50.81833, -2.55472)	$\delta\phi$	$-5.72 \cdot 10^{-4}$	0.00	$5.78 \cdot 10^{-4}$
La Reunion	$\delta\lambda$	$-3.64 \cdot 10^{-4}$	$1.89 \cdot 10^{-6}$	$3.66 \cdot 10^{-4}$
(-21.0803, 55.38930)	$\delta\phi$	$-3.89 \cdot 10^{-4}$	0.00	$3.89 \cdot 10^{-4}$
Troll	$\delta\lambda$	$-3.56 \cdot 10^{-4}$	$9.08 \cdot 10^{-6}$	$4.61 \cdot 10^{-4}$
(-90.00, 0.00)	$\delta\phi$	$-1.15 \cdot 10^{-3}$	0.00	$1.15 \cdot 10^{-3}$

Table 3.4: The difference in latitude (ϕ) and longitude (λ) between the theoretical Mid Point of a radar voxel, at elevation 15^o, located at mid-latitude (Wardon Hill), near the equator (La Reunion) and the poles (Troll), between Geodesic and Flat Earth Model.

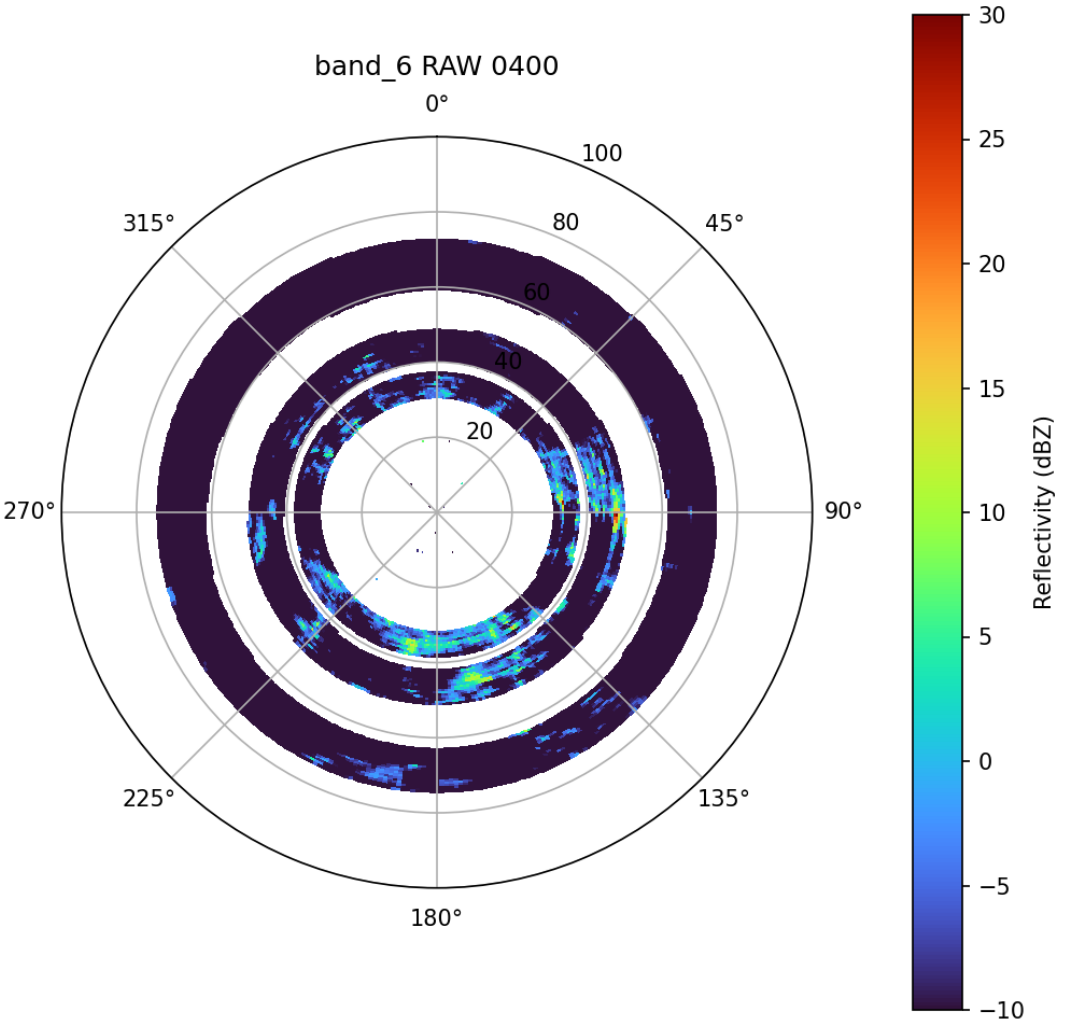

Figure 3.6: Band 4 ($h = 2500 - 3000\,m$), PPI over all elevation at specified altitude, splits into "rings" from Chenies radars at 04:00 on the 9th July 2021.

The elements being compared between the models is the position; latitude, longitude and altitude. For altitude, the averages were taken for each azimuthal ring, for the range, at single elevations (θ). Figure 3.6 pictorially describes an azimuthal ring; at a single elevation there will be just a single ring, but at multiple elevations, there are gaps between the radar cone at different elevations, so when looking at one altitude band there will be gaps where no radar data is present. Altitude was separated by elevation as altitude is dependent on elevation. For the geodesic distance, s the averages were taken for each azimuthal ring, across all elevations for each range; although there will be some impact on s due to altitude and terrain differences, they are insignificant compared to range (r), and for the purpose of comparing models they were not separated any further.

Zooming out to look at the global differences, Figures 3.7 and 3.8 show the difference in coordinates between the Flat Earth (FE) and Geodesic Earth (GE) models. Within Figures 3.7 and 3.8, the first row show the difference in latitude between FE and GE models over a given set of longitudes and the second row show the difference in longitudes between FE and GE models for a given set latitudes at the three test locations, Wardon Hill (mid-latitude), La Reunion (equatorial) and Troll (south-pole). Figure 3.7 is representative of lower elevations, at $\theta = 0.5^o$ and Figure 3.8 is at $\theta = 15^o$ representing higher elevations. The colours, represent every 30^o in azimuth from $0^o <= \alpha <= 330^o$. Figure 3.8 shows the higher elevations ($\theta = 15^o$) and thus higher altitudes, here, there is a fairly even spread in $\delta\lambda$ and $\delta\varphi$ over the 360^o of azimuth. At lower elevations ($\theta = 0.5^o$), although there is some symmetry, the uniformity with range from the radar as shown in Figure 3.8 is not there, and at certain azimuths, i.e $\alpha = 210^o, 240^o$, in Figure 3.7, some of the differences in models are much shorter or longer than at other angles.

Examining the difference in models further at $\theta = 0.5^o$, in Figure 3.7, it shows that Wardon Hill has the smallest spread for the difference in latitude out of all the test locations ranging from $-7.82 \cdot 10^{-5} \leq \delta\lambda \leq 2.55 \cdot 10^{-4}$, positively skewed. Whereas La Reunion and Troll are evenly spread with their min and max difference in latitude. For $90^o \leq \alpha \leq 270^o$, the difference between models appears to have a symmetrical spread in δlatitude and for $-90^o \leq \alpha \leq 90^o$ δlongitude appears to have a symmetrical spread across all locations. The general trend is the greater the distance from the starting location, the greater the difference between Flat Earth and Geodesy. However, the kinks and the varying differences show that terrain has an impact.

Figure 3.8 demonstrates clearly that the further away from the radar the greater the difference in models and thus at higher elevations/altitudes, terrain differences have less of an impact, as shown by the symmetry of the differences. The difference between models at higher elevations ranges from the order of $-1 \cdot 10^{-2} \rightarrow 1 \cdot 10^{-2}$ compared to $\pm 1 \cdot 10^{-4}$ for lower elevations. Longitude varies in a similar way, with coordinates at the Equator showing the smallest differences and the largest at the Poles.

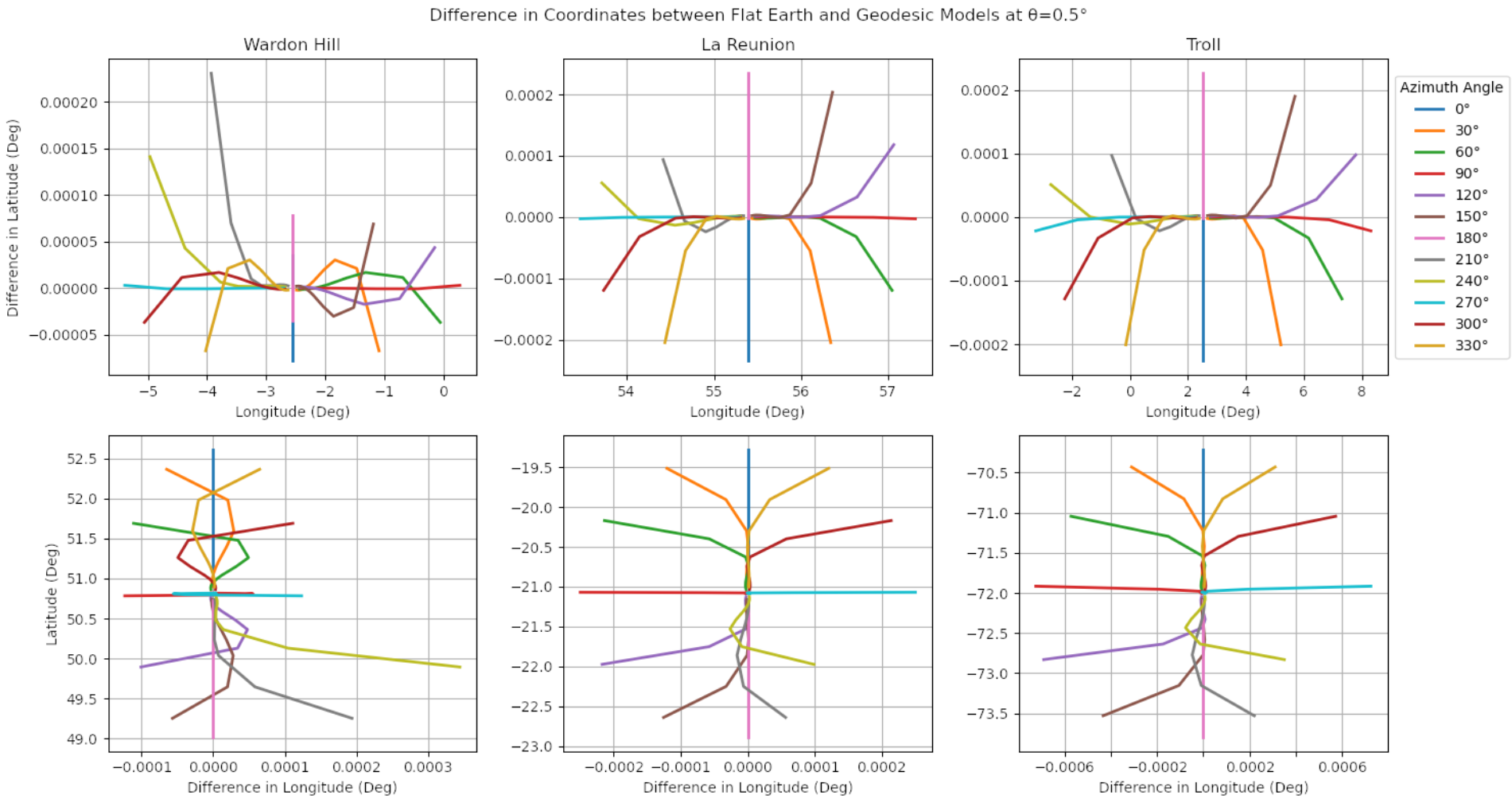

Figure 3.7: Figure of multiplots at *Elevation* $= 0.5^o$ Individual coordinate differences of latitude and longitude between the Flat Earth Model and the Geodesic Model, with refraction excluded. The three graphs represent a mid-latitude position of Wardon Hill, Equatorial with La Reunion and the Poles with Troll.

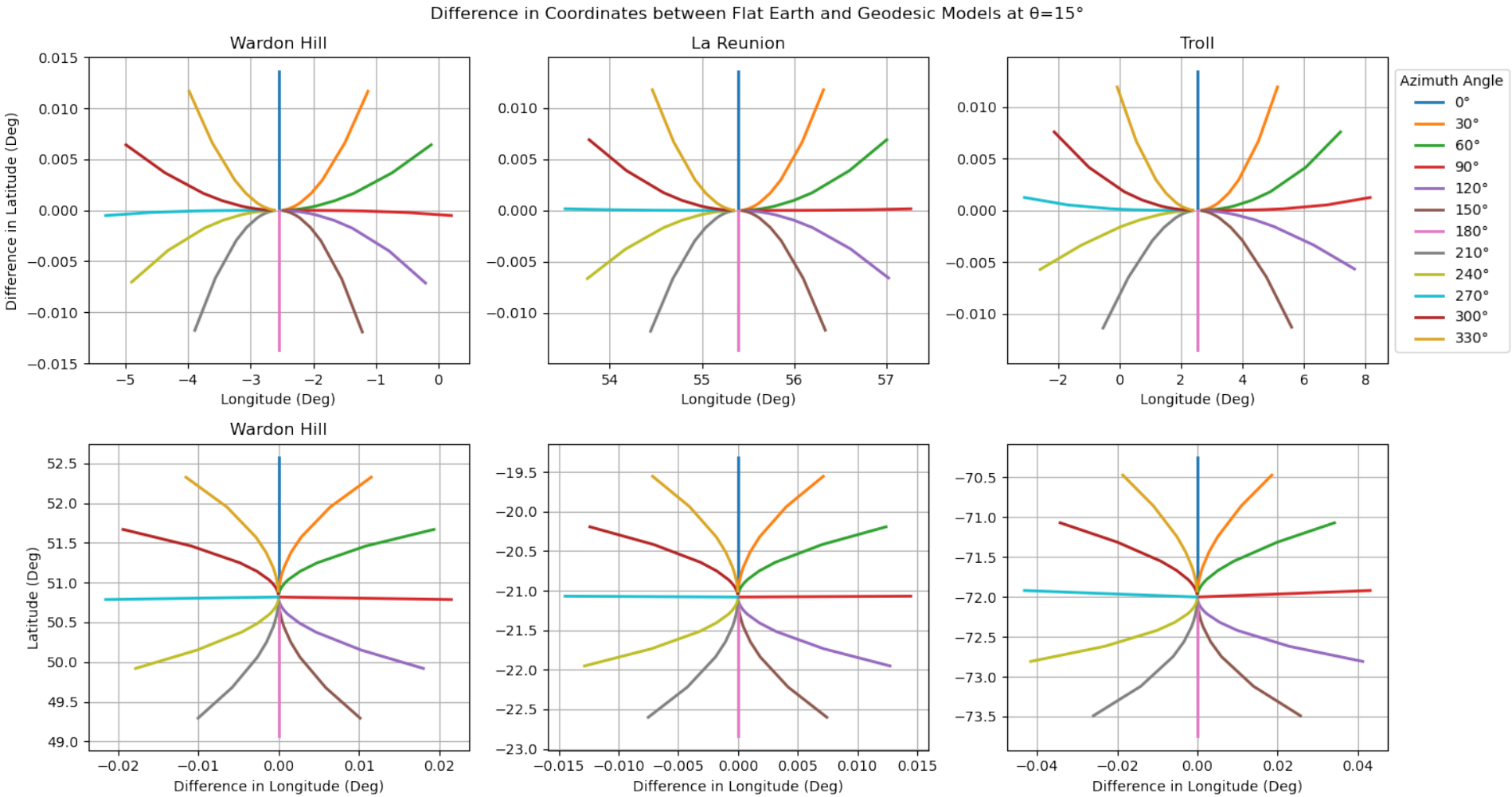

Figure 3.8: Figure of multiplots at *Elevation* = 15^o Individual coordinate differences of latitude and longitude between the Flat Earth Model and the Geodesic Model, with refraction excluded. The three graphs represent a mid-latitude position of Wardon Hill, Equatorial with La Reunion and the Poles with Troll.

At higher elevations, Figure 3.8 show there is a greater difference in the model positions by a factor of ~ 100. This is due to the altitude differences and the impact of the curvature of the Earth which impacts the projection more. Low elevations, for example $\theta = 0.5^o$ are similar to a Flat Earth line at 0^o so the expectation is the coordinates would be correlated, with the differences largely determined by terrain differences. At higher elevations e.g $\theta = 15^o$, the line of sight of the radar has greater deviation from the surface of the Earth and thus, as expected there is a greater difference between the models.

The graphs in Figures 3.9 and 3.10 (Geodesic-Flat), are for location Wardon Hill, show the quartiles from the numpy statistics package (The Python Standard Library, n.d.), these are not error bars but represent the spread of the data with the upper and lower quartiles, and the dot/cross representing the statistical median. The mean of the median altitude difference of Geodesic-Flat over the 200 km distance, is $\sim 37.1\,m$. At close range ($\leq 50\,km$) the difference in s is under $100\,m$ between each model. This is corroborated when comparing the coordinates directly by s with the GeographicLib Direct method. As the range from the radar increases so does the difference between the models, with the average being $500\,m$ and $800\,m$ respectively. As range from the radar increases as does the altitude difference. With spherical versus geodesic there is an exponential increase in difference.

Table 3.5 shows the distribution of altitude differences between Flat Earth Model and the Geodesic Model without Refraction, for s, α and θ from Table 3.2. At the mid-latitudes, the altitude differences are significant, whereas at the equatorial regions and poles the first $30-40\,km$ the difference between models is insignificant. Generally Figure 3.10 and Table 3.5 show that the Flat Earth model overestimates altitude. At $r = 10\,km$, $\theta = 0.5^o$ the beam height is $\sim 175\,m$ so a 21% difference between models is significant. At $r = 50\,km$ the beam height increases and the difference in altitude between models is 4.5% so is less significant. This shows, before accounting for refraction, although closer to the radar altitude has greater similarity between models, it has a bigger impact due to the size of the voxel than that at large ranges $\geq 50\,km$.

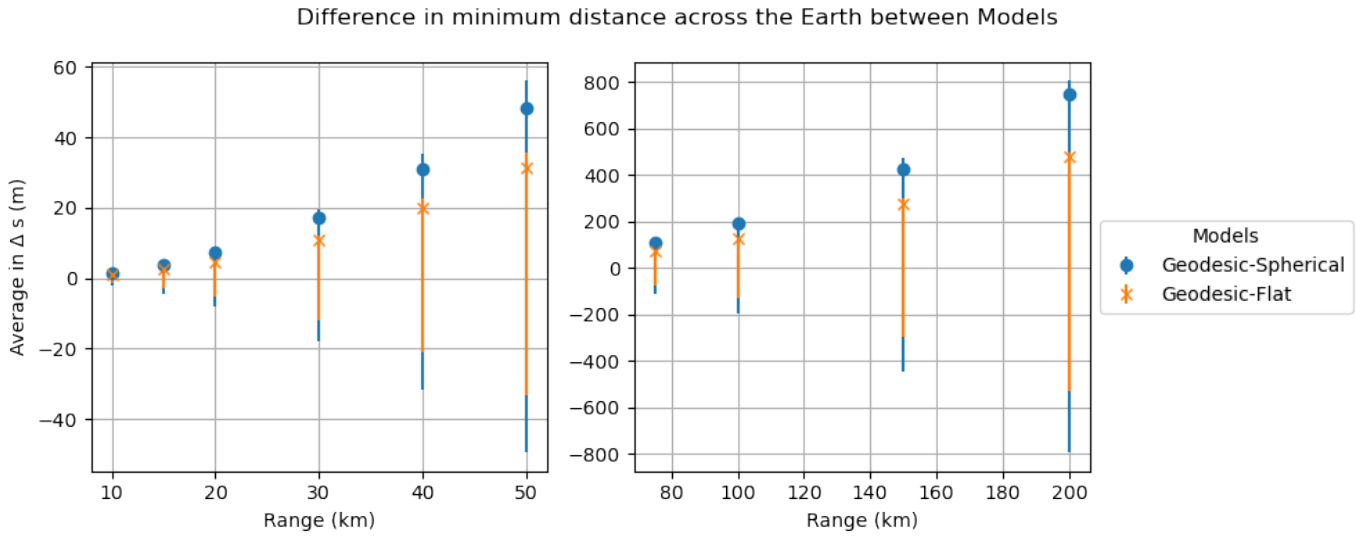

Figure 3.9: Differences in geodesic distance across the surface of the Earth (s), between geometric Earth shape models, using limited elevations.

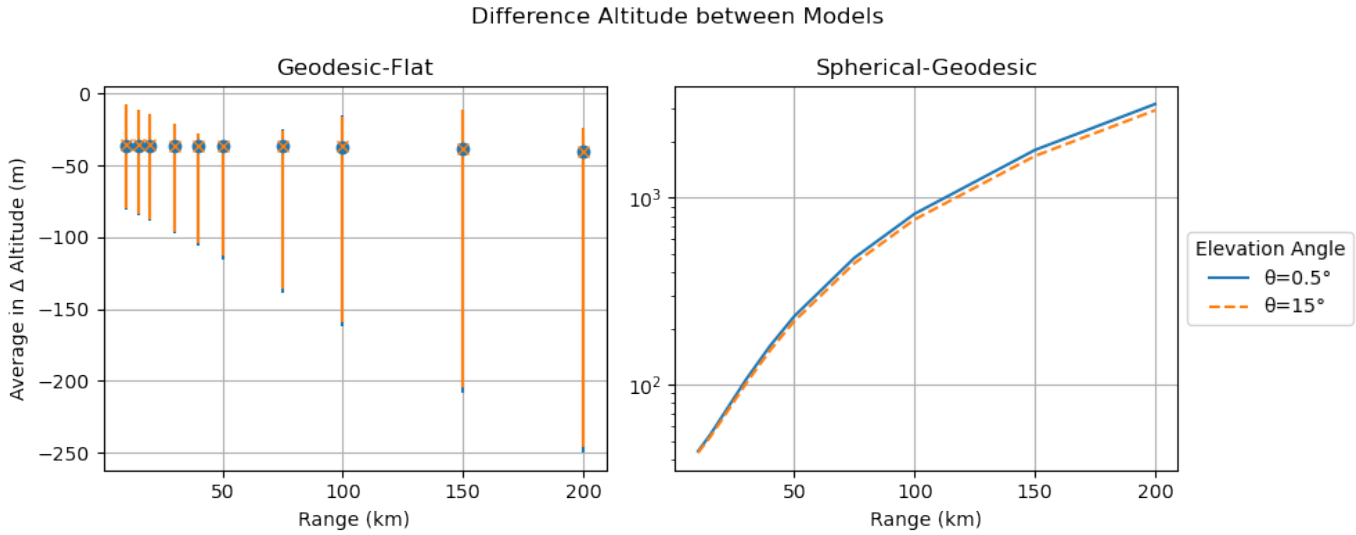

Figure 3.10: Altitude difference between geometric Earth shape models, using limited elevations.

Dataset	Stat	10	15	20	30	40	50	75	100	150	200
Wardon Hill (50.81833, -2.55472)	Min	8.13	10.00	10.35	6.43	1.83	2.49	1.83	30.95	20.06	8.88
	Mean	8.26e6	8.26e6	8.25e6	8.24e6	8.23e6	8.23e6	8.20e6	8.18e6	8.14e6	8.09e6
	Max	9.98e6	9.98e6	9.97e6	9.96e6	9.95e6	9.94e6	9.92e6	9.89e6	9.84e6	9.79e6
La Reunion (-21.0803, 55.38930)	Min	0.11	0.00	0.13	0.08	0.28	0.12	0.14	0.40	0.95	11.88
	Mean	1.34	3.11	5.65	13.01	23.39	36.74	83.02	147.29	328.38	577.26
	Max	3.53	8.23	14.89	34.05	60.97	95.62	215.83	383.56	859.31	1518.25
Troll (-90.00, 0.00)	Min	0.11	0.00	0.14	0.10	0.24	0.07	0.25	0.21	0.40	12.86
	Mean	1.33	3.10	5.64	12.98	23.34	36.66	82.85	146.95	327.61	575.92
	Max	3.52	8.20	14.84	33.94	60.78	95.32	215.15	382.34	856.54	1513.30

Table 3.5: Summary Statistics (Min, Mean, Max) for Wardon Hill, La Reunion, and Troll Across Direct Radar Range (km) between Flat Earth and Geodesic Models without Refraction.

Figures 3.11 and 3.12, using the parameters set out in Table 3.2, show the difference between

the Spherical Earth model with $\frac{4}{3}$R refraction correction and the Geodesic Earth model with N_s refraction. The scale of the differences varies for where one is on Earth; in range and; elevation. Understanding where the radar is situated on the reference frame, and the position of the observations, helps contextualise the observations and where the possible uncertainties lie when choosing a model.

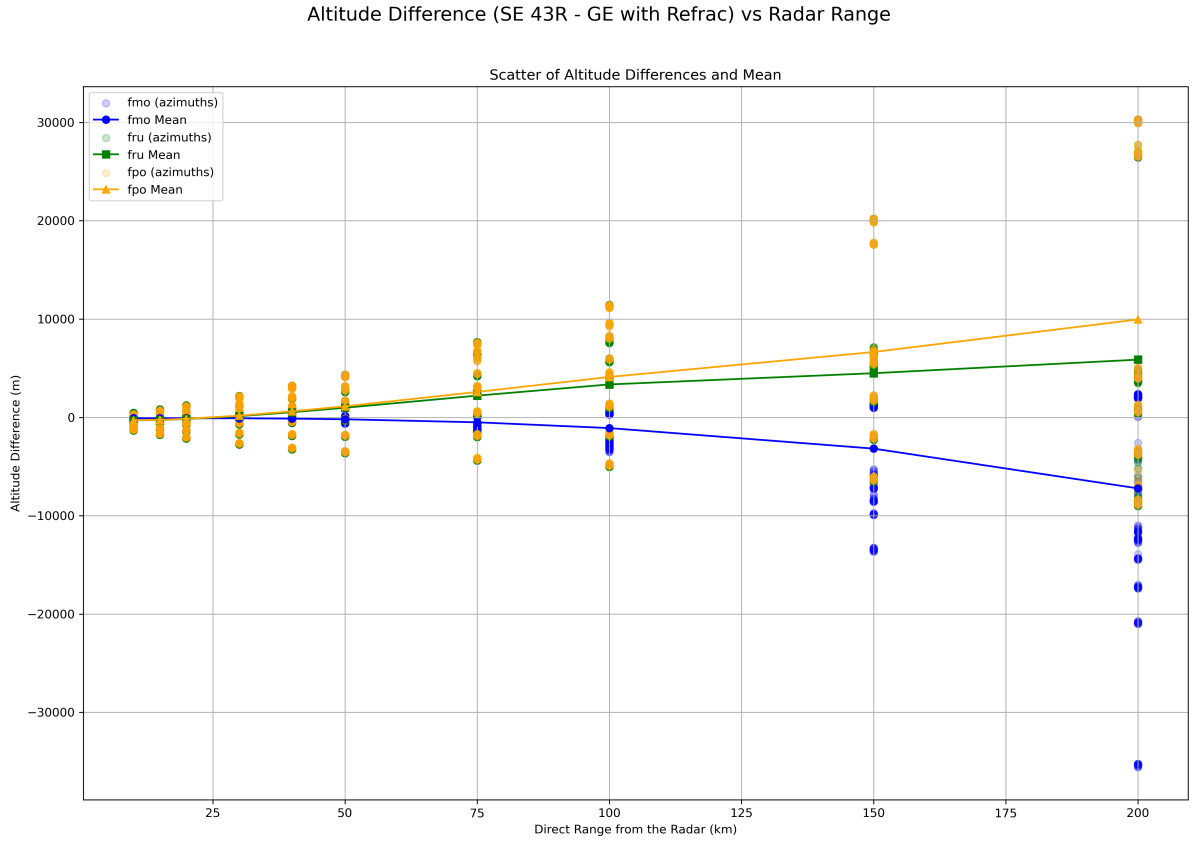

Figure 3.11: FMO: Wardon Hill, FRU: La Reunion, FPO: Troll, the distribution of altitude differences between Spherical Model of the Earth with $\frac{4}{3}$R refraction and Geodesic Model with $N_s = 313$ refraction.

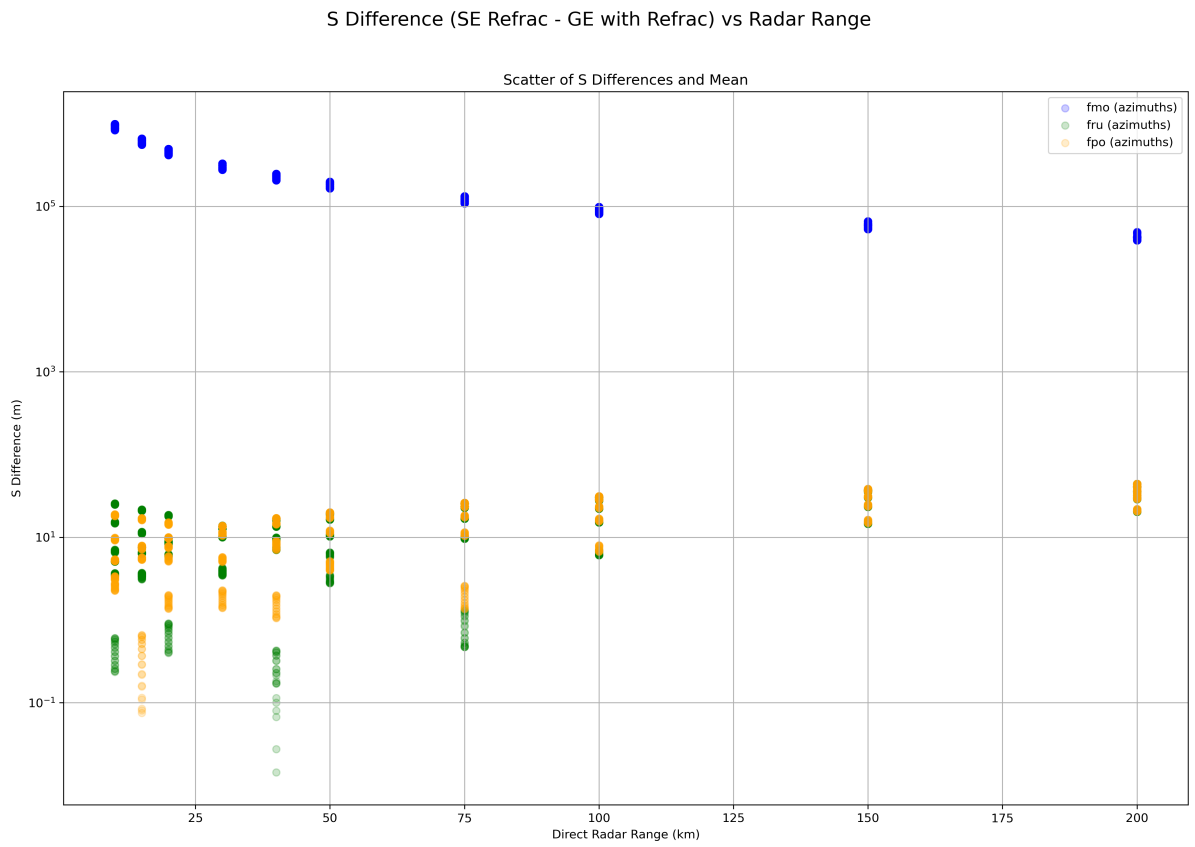

Figure 3.12: FMO: Wardon Hill, FRU: La Reunion, FPO: Troll, the distribution of difference in distance along the surface of the Earth, between Spherical Model of the Earth with $\frac{4}{3}$R refraction and Geodesic Model with $N_s = 313$ refraction.

3.3 Errors

This section describes two sources of error for the Geodesic Toolkit developed. The first lies with the "corner", points of the voxel volume, predominately used for collocation. The second source is from the GeographicLib module itself, quantifying this source of error enhances confidence in the reliability and credibility of the module.

3.3.1 Volume of the Radar

The volume of the radar beam increases with distance from the radar, Equation 3.1 shows how the radar equation is used to measure the volume of the radar $voxel_i$, this is the theoretical volume of the radar voxel. However, the theoretical volume is not used in the geodesic method because of the requirement to bound the radar voxels; defining the edges and vertices of the voxel establishes consistency for the voxel volume and allows bounds to be used. Bounds or qualification limits can then be set for collocation with other observations. One shape that

could be used to represent the voxel volume is a cone, as shown by Equation 3.4. This is the closest approximation to the radar equation however, a cone has a curved surface where vertices would be needed, thus drawing corners is still an issue, and this volume shape does progress the problem any further. A square pyramid, blocks the radar off into neat segments but misses the curvature along the azimuth. The Pi slice can be visualised using Figure 2.2, it improves on the square pyramid by including curvature along beamwidth and height line of sights. For NXPol radar the pi slice has a percentage error of $5-6\%$, decreasing inversely proportional to the range demonstrated in Table 3.6. For the UKMO radar is $5-10\%$. The square pyramid method overestimates the volume for NXPol by around 26% and $19-27\%$ for UKMO.

$$V = \frac{\pi}{4} r_i^2 (r_i - r_{i-1}) \theta_{BW}^2 \tag{3.1}$$

$$V = \frac{1}{3}[(r_i \cos\frac{\theta_{BW}}{2}(2r_i \sin\frac{\theta_{BW}}{2})^2) - (r_{i-1}\cos\frac{\theta_{BW}}{2}(2r_{i-1}\sin\frac{\theta_{BW}}{2})^2)] \tag{3.2}$$

$$V = \frac{\theta_{BW}}{2} r \sin\frac{\theta_{BW}}{2}(r_i - r_{i-1})^2 \tag{3.3}$$

$$V = \frac{\pi}{3}[(r_i \cos\theta_{BW}(2r_i \sin\theta_{BW})^2) - (r_{i-1}\cos\theta_{BW} 2r_{i-1}\sin\theta_{BW})^2)] \tag{3.4}$$

3.3.2 GeographicLib

The assess the error in the GeographicLib module (Karney, 2022), with the three test locations, Wardon Hill, La Reunion and Troll, the Direct and Indirect methods were traversed between to get an a maximum error in the order of 10^{-9} magnitude, showing that the error in this module is insignificant. Table 3.7 show the errors for each location.

Range (km)	10	15	20	25	30	40	50	75	100	150	200
Theoretical	0.00345	0.00775	0.0138	0.0215	0.0310	0.0551	0.0862	0.194	0.345	0.775	1.379
Square	0.00432	0.00977	0.0174	0.0273	0.0393	0.0699	0.109	0.246	0.438	0.986	1.75
Pi Slice	0.00324	0.00733	0.0131	0.0204	0.0293	0.0525	0.0820	0.185	0.329	0.740	1.32
Cone	0.00339	0.00768	0.0137	0.0214	0.0309	0.0549	0.0859	0.193	0.344	0.775	1.38
$\delta TPS\%$	5.93	5.46	5.22	5.08	4.98	4.87	4.79	4.69	4.65	4.60	4.56

Table 3.6: Voxel Volume Changes with Range for $\theta_{BW}, r_i - r_{i-1} = 0.15\,km$.

Location	Variable	Minimum	Maximum	Mean
Warden Hill (50.8183, -2.5547)	α	$-7.29 \cdot 10^{-12}$	$7.29 \cdot 10^{-12}$	$-1.28 \cdot 10^{-15}$
	s	$-2.52 \cdot 10^{-9}$	$1.75 \cdot 10^{-9}$	$-6.13 \cdot 10^{-12}$
La Réunion (-21.0803, 55.3893)	α	$-2.32 \cdot 10^{-12}$	$2.32 \cdot 10^{-12}$	0.00
	s	$-1.99 \cdot 10^{-9}$	$1.87 \cdot 10^{-9}$	$-6.66 \cdot 10^{-11}$
Troll (-90.00, 0.00)	α	$-2.84 \cdot 10^{-14}$	$2.84 \cdot 10^{-14}$	0.00
	s	$-6.98 \cdot 10^{-10}$	$7.06 \cdot 10^{-10}$	$-1.28 \cdot 10^{-10}$

Table 3.7: Inverse/Direct "Error"

3.4 Summary

Regarding the multiplots Figures 3.7 and 3.8, for the elevation angle, $\theta = 15^o$, the difference in latitude between flat earth and geodesic earth models are consistent, as is the difference longitude. For low elevation where $\theta = 0 - 0.5^o$, there is variation. The variation in models is due to localised differences, where the Flat Earth model does not vary but the geoid varies with gravimetric and terrestrial differences, thus when close to ground, at low altitudes these differences are emphasised but at higher altitudes the discrepancies are smoothed over as a position at higher altitude is projected over a larger amount of land.

This chapter evaluates the two algorithms developed: the Radar Voxel Localization Algorithm and the Collocation Method. The Radar Voxel Localization Algorithm estimates the geodesic latitude, longitude, and altitude of each voxel within the radar beam, applying refraction corrections, and referencing them to WGS-84 MSL. The Collocation Method calculates the geodesic distance, altitude difference, and relative position between radar voxels and a secondary data source. The chapter assesses the performance of both algorithms, the realism of their outputs, the process of validation, and compares results obtained using different Earth models, as outlined in Chapter 1.

Since these algorithms were created from scratch, transforming theoretical ideas into practical applications, validation becomes a central focus. The context in which these algorithms were designed is also critical. Radar observations are recorded relative to the radar's own position. In research campaigns where multiple instruments aim to observe the same phenomenon, achieving collocation within a universal reference frame is necessary. Furthermore, planning for cross-instrument collocation ensures better integration. By incorporating geodesy, the chosen universal reference frame, into radar positioning and scanning strategies, the likelihood of collocation between instruments is maximized at the start and throughout the campaign. Post-processing verifies collocation, accuracy, and the relative distance between coincident observations.

To conclude this section, the geodesic coordinates have been verified. The geodesic altitude, with the refraction correction is an improvement upon the UKMO's altitude for radar

voxels. Geodesic location is the most accurate system to use over the entire globe. Coordinates over flat terrain i.e a moor will have greater similarity to a flat Earth projection model, at low elevations, than one which is over undulating surfaces for example rolling hills which would be better represented by a geodesic model. At higher altitudes/elevations, the differences in coordinates become negligible between the different models, thus either could be used, and FE is more efficient, however the reduction in accuracy with altitude still shows the Geodesic model is the superior one to use, regardless.

Chapter 4

Results: Modelled Radar Cross Section of Alate Ants

In this Chapter, the results of simulating a Queen and male alate ants' radar cross section (RCS) are described. The RCS of a target is dependent on the wavelength of the radar, the size, shape and composition (dielectric constant) of the target. The total RCS was calculated for the Met Office, C-band radars only with a 360^o scanning strategy, and thus is not comparable to vertically pointing scanning simulations or other frequency bands of radar.

The RCS of a target can be calculated through; theory, simulations or direct measurements. Determining the RCS of insects, by direct measurements is inherently challenging (Addison et al., 2022) due to the requirement of a known target, which would be difficult to define given the nature of insect size, behaviour, and flight dynamics.

WSR typically operate within three frequency bands: S, C and X-band (World Meteorological Organization, 2023a) with S and C-band making up the majority within the WMO (World Meteorological Organization, 2023a) Each band offers distinct advantages; For example, X-band radars ($2.5 \leq \lambda \leq 4$ cm) have the capability to detect point targets, including biometeors (Torvik et al., 2014; Bauer et al., 2024; Drake et al., 2024). In contrast, C-band ($3.75 \leq \lambda \leq 7.5$ cm) and S-band ($8 \leq \lambda \leq 15$ cm) radars are optimized for capturing backscatter from distributions of targets, which is crucial for large-scale weather observations (World

Meteorological Organization, 2023b). For VLRs insects may appear as a point target (Smith et al., 2000; Drake et al., 2017; Drake et al., 2024), but generally the S and C-band typically observe insects as a collective mass, much like clouds. This makes estimating RCS for a group of insects, such as a swarm of locusts or mayflies, more feasible (Stepanian et al., 2018b; Drake and Reynolds, 2012; Knott et al., 2004; Melnikov et al., 2015), though species diversity can still pose challenges. The RCS can also be used to estimate a biomass, as used through varying methodologies in Kilambi et al. (2018), J. Chapman et al. (2002) and Stepanian et al. (2020). Therefore even knowing a single insect's RCS, has the potential to thread together the information gap between radar observations and a tangible quantitative biomass of an insect swarm.

As the research on RCS simulations of insects is still in its infancy, this chapter will show the results from two branches of models for obtaining the RCS of an alate ant; the anatomical model (Addison et al., 2022), using a detailed render of an alate ant, and the second is prolate ellipsoid model (Mirkovic et al., 2019).

4.1 Biological Description of Alate Ants

Figure 2.11 shows a typical *Lasius niger* ant which, as a Hymenoptera is divided into three segments; the head, the thorax and the abdomen. The six legs of the ant, are jointed and paired from each side of the thorax. The antenna has a distinctive elbow joint, with a longer protruding initial segment, then a near 90^o angle before the usual antenna segmentation. An alate ant, has its wings coming off the mesothorax and metathorax.

Queen ants have a large variation in their mass across their lifetime, therefore the fresh mass measured on or around their nuptial flight is the ideal mass to use. The alate male and female fresh mass range is 3.10 ± 0.23 and 26.035 ± 2.405 mg (Boomsma & Isaaks, 1985) respectively. The males have $\sim 2\%$ smaller variation in their alate biomass than the Queens, with the males at $\sim 7\%$ variation in biomass and the Queens at $\sim 9\%$ variation in biomass. The average length of an alate male is $4.1 \pm 0.6\,mm$ (Nature Spot, n.d.) and a Queen $8.0 \pm 1\,mm$ (Dimensions, n.d.; Ho and Frederickson, 2014).

The muscles grown in order to be capable of flight are very dense, and take up the ma-

jority of the thorax (Matte & Billen, 2021) of an alate ant; once the Queen has mated and landed, she will bite off her wings, and her flight muscles will start to decay, it is posited that these muscles will provide the much-needed nutrients for her first batch of young (Matte and Billen, 2021; Peeters et al., 2020). Regardless, within a few months, the flight muscles of a *L. niger* Queen, will have reduced to insignificance and adipocytes (fat storage cells) grown to occupy the space (Matte & Billen, 2021). The alate males, after their nuptial flight, will die within the next few days. The window of time to measure the fresh mass of an alate ant is narrow, the species, age of the colony, and time of year of flight can also have an impact on mass, (Janet, 1906; Matte and Billen, 2021; Boomsma and Isaaks, 1985; D. Wagner and Gordon, 1999), and the recording of dry versus wet mass will also impact, thus there are many sources of error.

The anatomy of an ant is well known (Peeters et al., 2020; Matte and Billen, 2021; Fedoseeva and Grevtsova, 2020). Every material, at different temperatures and for different frequencies, has its own dielectric constant. The dielectric constant of an ant is not known. The antenna, legs and connection between thorax and abdomen are majority chitin and are categorised as such. Mirkovic et al., 2019 discusses the internal composition for the dielectric constant. The Less Grain Borer Beetle (Nelson et al., 1998) was crushed and the dielectric constant measured to give the approximate value of the body of the beetle, this has been used in multiple studies since to represent insect bodies (Addison et al., 2022), (Mirkovic et al., 2019) and used here. The wings and legs were given the chitin dielectric constant of 4.1-j0.16 extrapolated in Addison et al. (2022) from Chen et al. (2020) and the body was given 34.3-j18.6 (Nelson et al., 1998; Mirkovic et al., 2019). As mentioned previously, the flight muscles are much denser than the typical body material and chitin, in addition, the temperature in-flight will be much greater than anything measured inactively on the ground. Measuring the dielectric constant of an in-flight ant, was beyond the scope of this thesis, and thus using the standard methodologies set out in the existing literature Mirkovic et al. (2019), Addison et al. (2022) and Nelson et al. (1998) was deemed sufficient for comparison.

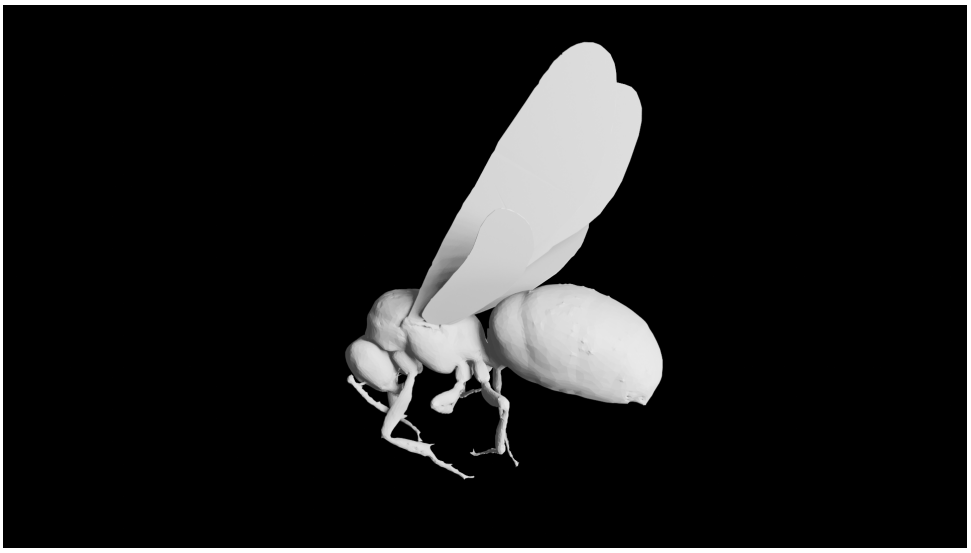

(a) Full Queen Ant

(b) Wingless Queen Ant

(c) Body Only Queen Ant

Figure 4.1: The three body types of the Queen Ant made on Blender. Top to Bottom. a) Full Body, b) Wingless and c) Only Body.

4.2 Data Processing

Previous research (Mirkovic et al., 2019), used ellipsoids to model insects for simulations of insect RCS. (Mirkovic et al., 2019) paper shows the derivation of height to create the ellipsoid models; Equation 4.1. The Biodar group did not record either the fresh or dry mass for the specimens, so the mass was unknown. Hence as an experiment, the height was measured directly in WiPL-D using the measurement tool.

$$h = \frac{6m}{\pi dlw} \tag{4.1}$$

Species	Body Length (mm)	Mass (mg)	RCS (cm^2)	Source
Lasius niger (Q)	8.8	27.8	0.1	Measured, (Dimensions, n.d.), Derived
Xestia xanthographa	17	140	2.7	(Addison et al., 2022)
Spodoptera littoralis	17.5	95	1.0	(Riley, 1985)
Tipula oleracea Linnaeus	17.7	45	0.537	(Hobbs & Aldhous, 2006)
Episyrphus balteatus	11	22.3	0.734	(Wotton et al., 2019)

Table 4.1: Table of insect species where RCS was calculated at S-band, and their associated size information.

The Queen ant was scaled in WiPL-D to fit within the typical size range of a Queen ant, and then measured using WiPL-D's measuring tools, and the measured size is recorded in Table 4.2 along the top row. In Table 4.2, W refers to width; L, length; and H, height, n quarter of the number of plates WiPL-D uses to create the ellipsoid, a is the radius, b, is half the width and c half the height.

The male ant used in this thesis came from a SketchFab 3D Blender Model, created by Sebastian Fiolet and is licensed under Creative Commons Attribution (Fiolet, 2020). The model

Queen Ant								
Measurement	W (mm)	L (mm)	H (mm)	Mass (mg)	n	a	b/a	c/a
WiPL	3.2	8.8	2.7	27.808	16	4.4	0.363636	0.306818
Derived			1.885986					0.214317
Average		8.0 ± 1		26.035 ± 2.405				
Male Ant								
WiPL	0.93	3.4	0.91	2.87	16	1.7	0.273529	0.267647
Derived			1.73349					0.50985
Average		4.1 ± 0.6		3.10 ± 0.23				

Table 4.2: Table of modelled ants, measurements of the features from the Radar Cross Section (RCS) software, WiPL-D.

was then run through WiPL-D CAD to transform it into the WiPL-D model and from there scaled to a size that fell in the typical range of an alate male ant.

Figure 4.1 shows the three Queen Ant models, which were used for the simulations in WIPL-D. Figure 4.1 a) is the Full body Model, which includes all the features including the drawn wings. Figure 4.1 b) is the Wingless model, which has all the features of the ant, directly from the CT scan. Figure 4.1 is the Only Body model, and has the body only, with the legs and antennae removed in Blender and replaced with plates.

4.3 Model Simulation Results and Discussion

The two different derivations of the prolate ellipsoids were simulated, and their RCS comparison is in Figure 4.2. The prolate ellipsoid using an estimated mass to derive the height is closer in estimation to the real, or anatomically correct model of the Queen ant than the measured height and thus is used for all further comparisons.

Two simulations are run, one for the horizontal wave, and one for the vertical. They are run for 360^o around the insect, to get the radar cross section for the different angles the insect could be flying at. This is why, the results form a figure-of-eight, the peaks represent when the insect is flying at 90^o to the radar, the perspective of the full length of the insect, whereas the minimum is when we are seeing the insect front on or from behind. The result is the average RCS for the horizontal and vertical waves at each of the elevation positions for each azimuthal position hence the 2D plots of Figures 4.2, 4.1, 4.4, 4.5 and 4.7 rather than a singular value.

The first simulations that were run were for the different body models of the Queen ant; the aim was to recreate Figure 10 from the (Addison et al., 2022) paper, which is shown in Figure 4.3. Acknowledging the prior research done by (Addison et al., 2022), Figure 10 was recreated for the Queen Ant. Figure 4.3 shows the comparison for Full Body, Wingless and Only Body and the prolate ellipsoid. The Wingless and Full model show very slight differences, emphasized at 90^o and 270^o, however the difference is minor enough to justify not modelling the wings for the alate male ant. This experiment agrees with previous research that membranous wings do not impact the RCS value of a radar and agrees with (Addison et al., 2022) that limbs

and antennae should be modelled.

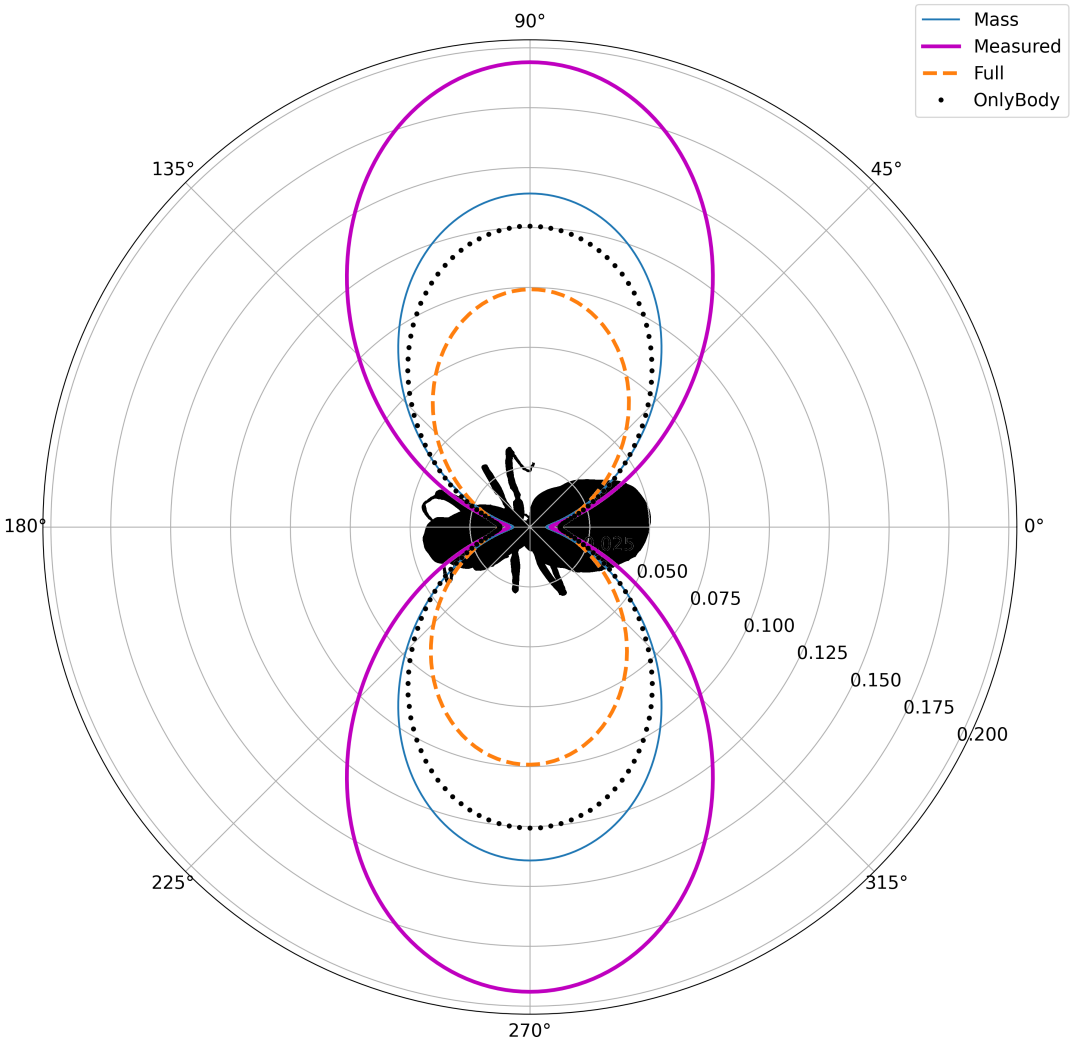

Figure 4.2: Comparison of the modelled polarimetric RCS values (cm^2) for the two types of the derived prolate ellipsoid, measured height and derived height and the Queen Ant Full body model. For a 9.4 GHz radar. Azimuthal Scan (Ballerina).

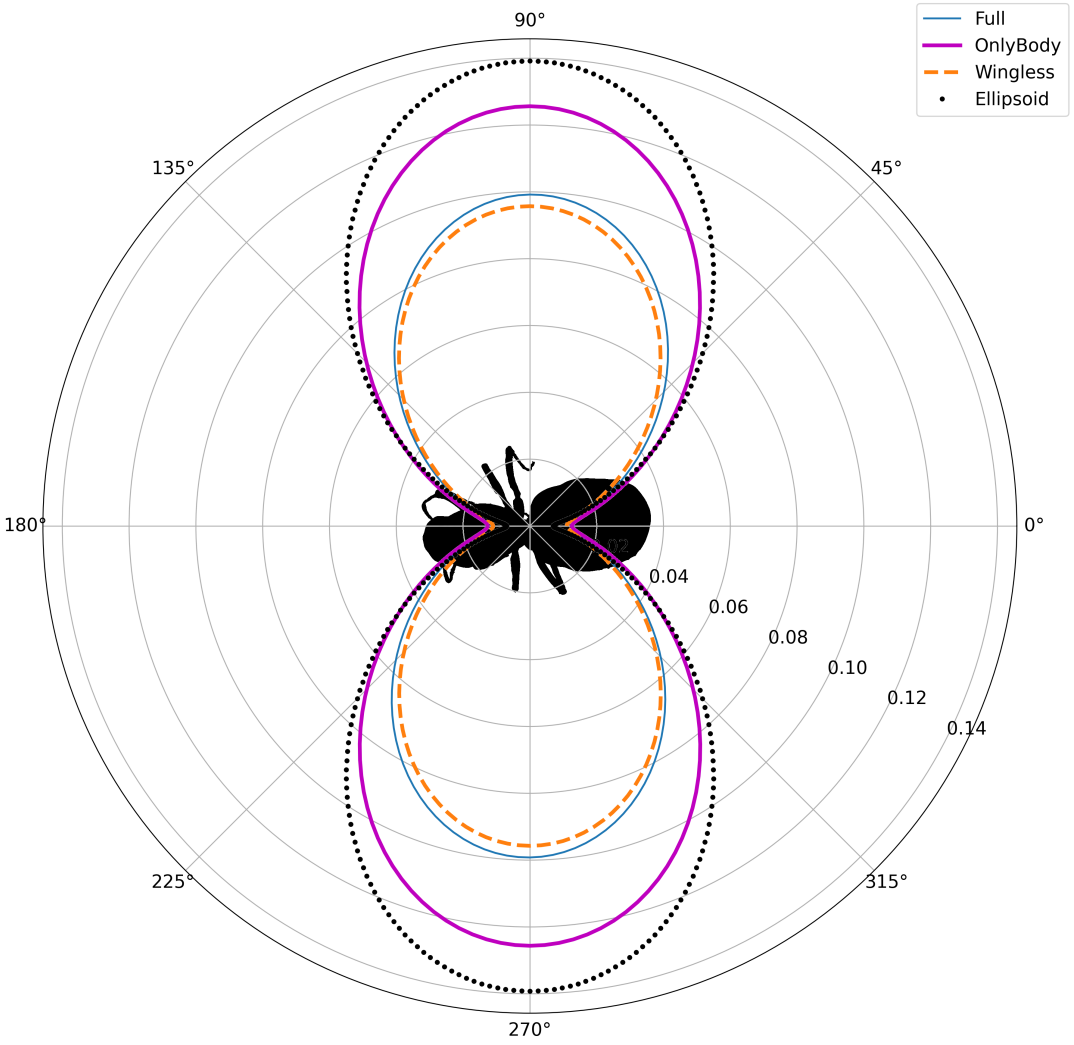

Figure 4.3: Comparison of the modelled polarimetric RCS values (cm^2) for the winged Queen Ant for the Full body model, Wingless model, Only Body model and the derived prolate ellipsoid. The RCS is for a 9.4 GHz radar.

In linear units, Figure 4.4 shows the difference between a Queen and a male ant. The shape difference is similar to that of the ellipsoid comparison in Figure 4.5. Both Figures (4.4 and 4.5) illustrate the significant sex difference in RCS value. The anatomic models' RCS values between

male and female have a greater difference of $\sim 100\,dB$ more than their ellipsoid counterparts. Along the horizontal line $180-0^o$, the ellipsoid models have a greater change in RCS value than the anatomic models. The Queen models look more similar than the males in Figures 4.4 and 4.5, but this is slightly misleading as when comparing the ellipsoid and the anatomic model in Figure 4.3 the differences are visually more clear cut.

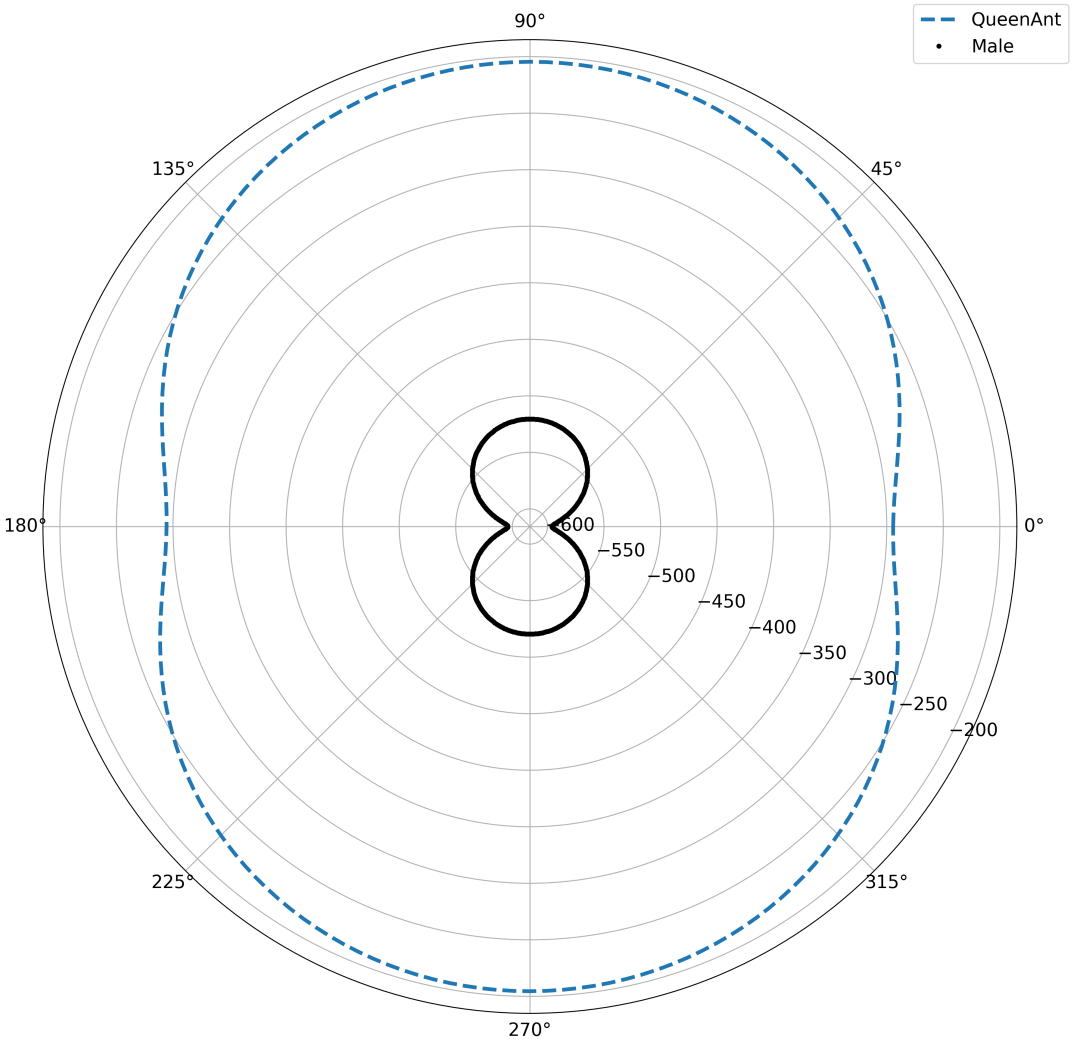

Figure 4.4: Comparison of the modelled polarimetric RCS values (dB) for the winged Queen Ant and the Male Ant. The RCS is for a 9.4 GHz radar.

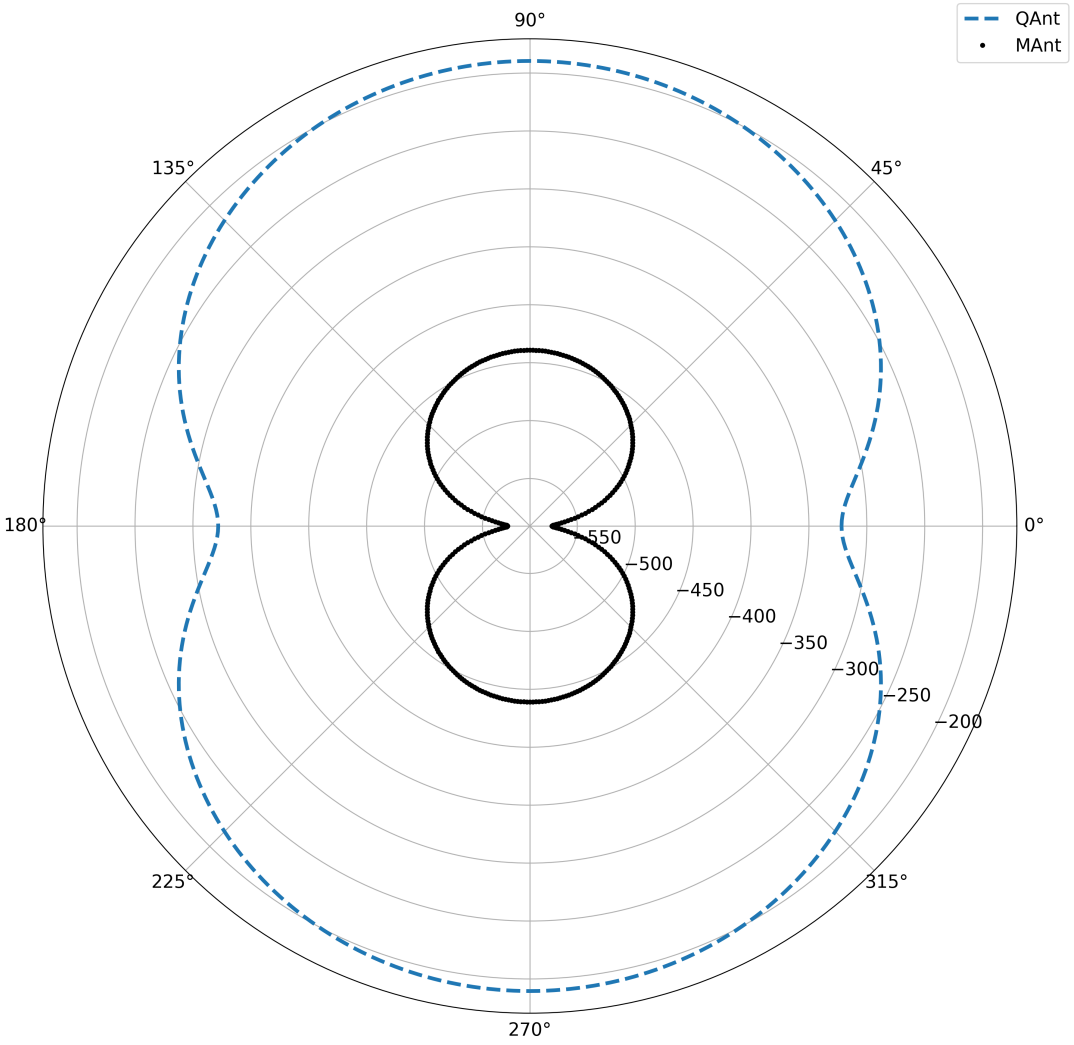

Figure 4.5: Comparison of the modelled polarimetric RCS values (dB) for the Ellipsoid versions of the Queen and the Male Ant, with the height derived using Equation 4.1(Mirkovic et al., 2019) The RCS is for a 9.4 GHz radar.

Figures 4.6 and 4.7 show the RCS value in cm^2 at 5.6 GHz for $\theta = 0^o$. The Queen ant's mean RCS value is $0.1\,cm^2$ for a 9.4 GHz radar and $\sim 0.28\,cm^2$ at C-Band, 5.6 GHz. Table 4.1, is the X-band RCS values for various insects, with the *L. niger* Queen used in this study on the top

row. Although Table 4.1 does not show all the features, the table along with Figure 4 from Riley (1985) shows that this value is in the right order of magnitude, with other research conducted Addison et al. (2022), Hobbs and Aldhous (2006), Wotton et al. (2019) and Riley (1985). Figure 4 from Riley (1985) shows the mass to RCS relationship, and the Queen with a mass in the order of $10^{-2}\,g$ should have a RCS value in the order of $10^{-1}\,cm^2$ which she does; and the male, has a mass in the order of $10^{-3}\,g$ so should have a mass between $10^{-4} - 10^{-5}\,cm^2$ which he does. With the Queen ant having a RCS value of $0.25\,cm^2$ and the male of $1.15 \cdot 10^{-5}\,cm^2$, at 5.6 GHz, this is means the male is approximately 0.004% of the Queen's RCS size.

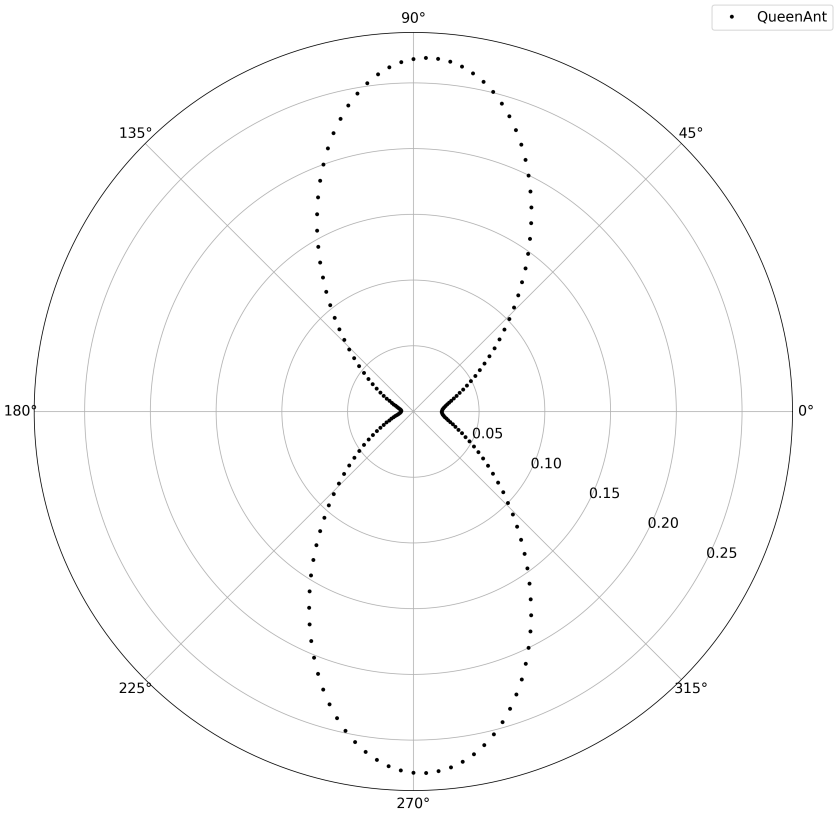

Figure 4.6: Modelled polarimetric RCS values (cm^2) for the winged Queen Ant. For 5.6 GHz radar.

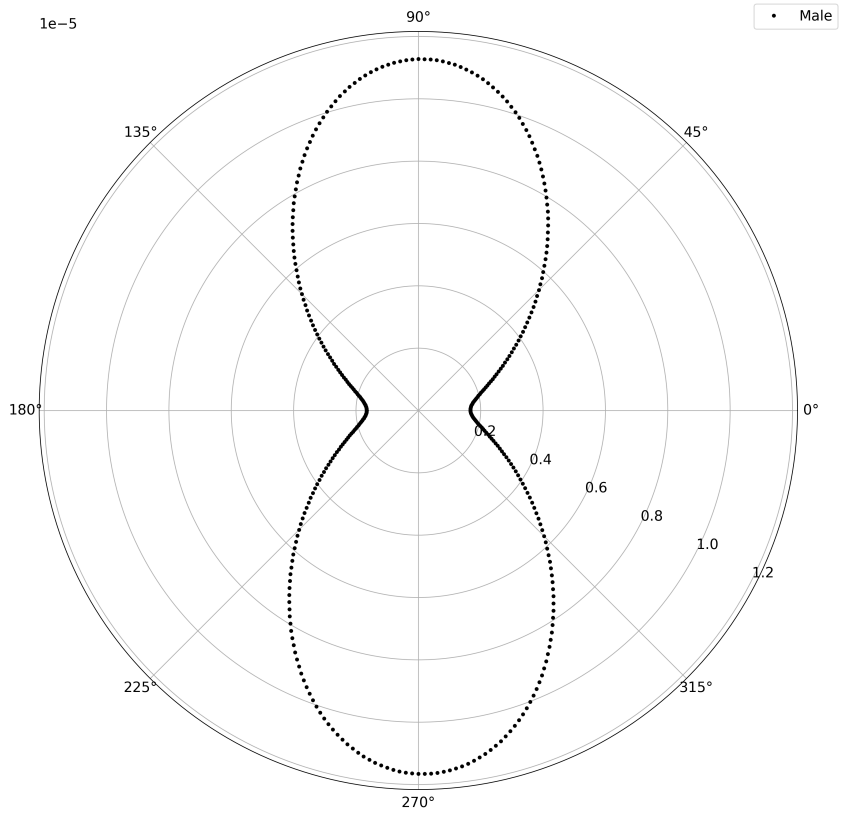

Figure 4.7: Modelled polarimetric RCS values (cm^2) for the Male Ant. For a 5.6 GHz radar.

4.4 Summary

The average RCS of a Queen ant is: $0.11660082599656907\,cm^2$ and the average RCS of a male ant is: $6.00594496564492 \cdot 10^{-6}\,cm^2$ at C-band. The simulations of the ants show a substantial difference in RCS value between an alate male and Queen ant, a factor of $\sim 10^5$. Thus, Queens are likely to be the dominant signal rather than a mix of the sexes. The simulations also show, that the membranous wings of Hymenoptera have an insignificant effect $\sim 0.5\%$ on the RCS of the specimen compared with the scaled wings of a Lepidoptera (Addison et al., 2022). The values of RCS are consistent with studies that measure RCS (Riley, 1985; Hobbs and Aldhous, 2006). The models show improvement and significant difference with the modelling of anatomy

compared with an ellipsoid, as is consistent in Addison et al. (2022)'s study.

Further improvements could lie within the dielectric constant. As every material has a different dielectric constant which changes with temperature and the EM radiation interacting with it. When modelling for a target, there are two components to consider, the dominant material and the most representative. For an aircraft, it does not matter what it is filled with because the external structure is the only aspect which the radar is able to see, although this can be manipulated, for example small RCS values have been manipulated for stealth aircraft (Parker, 2017), but generally external material dominates. With insects, the Addison et al. (2022) paper found that the wings were observed by the radar for the moth and therefore should be modelled. Addison et al. (2022) showed that a different dielectric constant impacted the influence of the limbs on the RCS of the insect thus for ants when in flight mode their thorax is immensely dense with flight muscles and therefore how does that change the RCS of the insect. However through a brief literature search the dielectric constant was within a single order of magnitude (Information Technologies in Society, ITIS Foundation, 2024; Gabriel, 1996), thus was not considered different enough to justify the time spent to split up the thorax on WIPL-D. However, having the known dielectric constant of the ant at the correct temperatures for flight, given the temperatures of water make a difference (Andryieuski et al., 2015), would justify rerunning the models.

What should also be considered is the length of time each of the wing positions are at over the flight, typically longer at a downward position that at top (Sane, 2003). Having this distribution would help with the swarm estimations which is the next step from the individual RCS to the modelled swarms and future biomass distribution comparison.

Chapter 5

Results: Flying Ant Days

This final results chapter presents a practical case study that integrates the geodesic location tool and radar cross-section (RCS) simulations of alate ants, focusing on a relatively homogenous insect population during a temporally constrained biological event: Flying Ant Day (FAD). A confirmed FAD occurrence was identified through a Citizen Science survey, and the resulting observations were collocated with data from the nearest UK Met Office (UKMO) Weather Surveillance Radar (WSR) to demonstrate the ability of the geodesic methods developed in this thesis.

While radar aeroecology has been explored in a range of studies (J. W. Chapman et al., 2011,Stepanian et al., 2020, Vaughn, 1985 ,Martin and Shapiro, 2007, Bauer et al., 2024), including the use of WSR for tracking birds (ENRAM, 2013), RCS simulations for bats (Mirkovic et al., 2016), and Vertical-Looking Radars (VLRs) for insect monitoring (J. Chapman et al., 2002), many limitations persist in both technique and instrumentation (Shamoun-Baranes et al., 2019). WSRs are primarily designed for observing atmospheric microphysical processes such as precipitation and typically operate with radar voxels spanning hundreds of metres to kilometres (Nanding & Rico-Ramirez, 2019). This spatial scale is poorly matched to the centimetre-scale size of insects, making species-level classification infeasible. However, this chapter demonstrates that geodesic referencing can substantially improve the positional accuracy of WSR observations, enabling more precise collocation with other datasets. It further shows how WSRs can be leveraged to monitor large-scale biological phenomena, such as Flying Ant Day (FAD), emphasizing their value for aeroecological research through high temporal resolution and broad

spatial coverage.

As mentioned in Chapter 1, ants are one of the most abundant insects on the planet (Schultheiss et al., 2022). As part of their normal lifecycle Queens and males emerge from their natal nest to mate in the air, once mated, females drop to the ground and attempt to form a new nest. During the copulation, enough sperm is transferred, to last the Queen her entire lifespan (Baer, 2011), up to 26 years in some species (Jemielity et al., 2005).

FAD is a phenomena in the UK which is engrained as a characteristic feature of the summer period by the public; this annual emergence is a natural experiment which has a temporally distinct pattern of activity, detectable by WSRs (PA Media, 2020). Despite numerous studies such as Hart et al. (2018), Van der Have et al. (2011) and Helms (2017), the environmental cues that trigger this emergence are not fully understood. For optimal genetic diversity, many nests need to fly at the same time, and this is not communicated, so the question remains "How do the ants know when to fly?". This chapter details the ant emergences over 2021 and 2022 using WSR observations with the developed geodesic method applied to the analysis to show how this technique may give new insight into the dispersal, quantity and timing of these events; which can pave the way for future ecologists and myrmecologists to explore further the dynamics, conditions and behaviours of these emergences.

5.1 Citizen Science

The Citizen Science (CS) survey was conducted from 2021 to 2023, with a trial in 2020. The two years of focus are 2021 and 2022 as the 2023 season was after the main processing and submission of this thesis. These two years yielded 4806 responses; 2021 had a total of 2721 responses and 2022 totalled to 2085 responses. The population of the UK in 2021 was around 67 million ("Population estimates for the UK, England, Wales, Scotland and Northern Ireland: mid-2021", 2022) thus we must bear in mind comparatively, the survey responses are not statistically representative of the population.

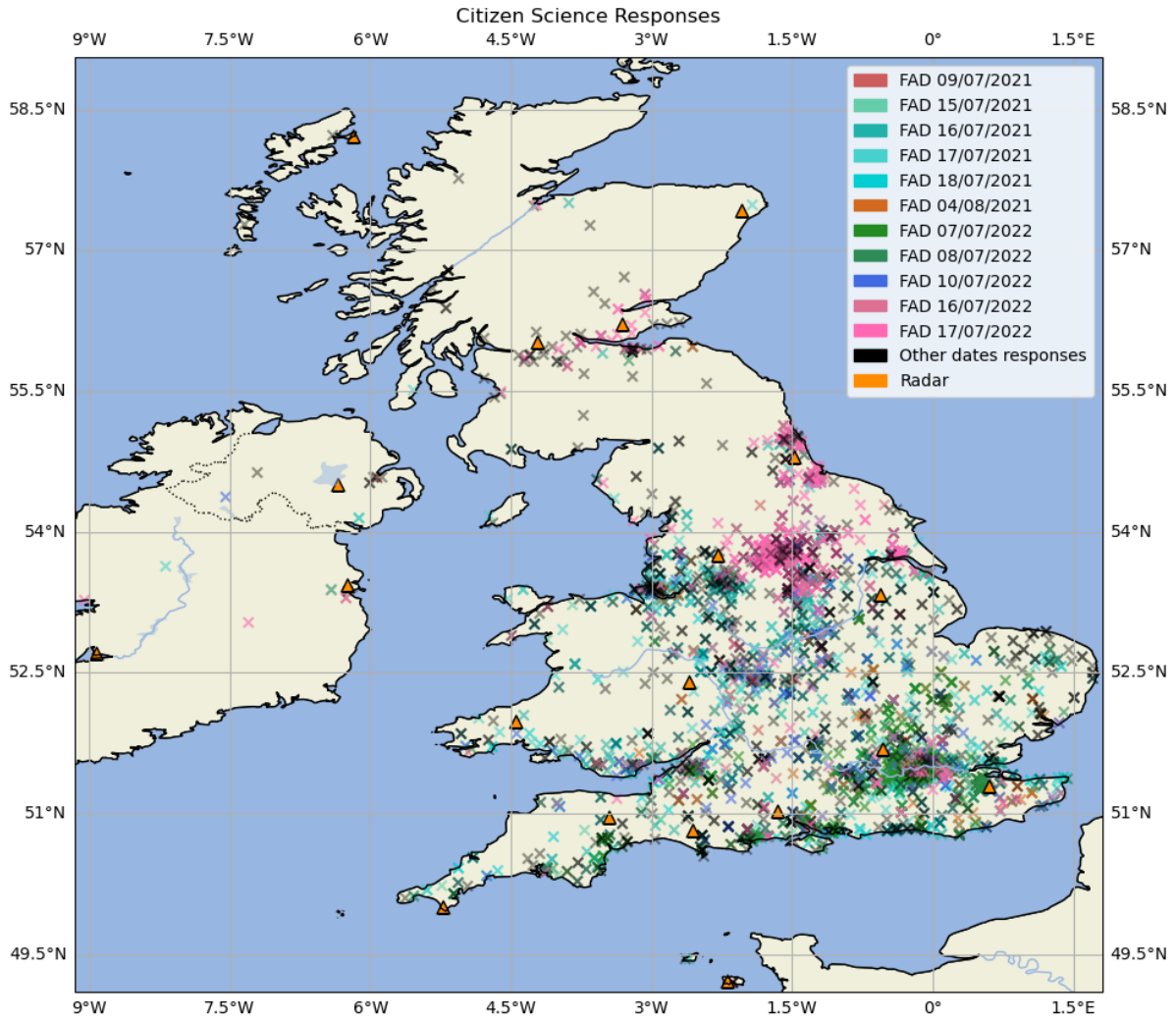

Figure 5.1: Map of all survey responses with valid date and location. Total responses in black, the 11 FAD categorised by colour in the legend.

The classification for a FAD, was defined by the author as a day with ≥ 100 CS responses of sightings. Throughout the season, there will be small flights of ants who opportunistically look to mate, with Hart et al. (2018) reporting at between $65 - 95\%$ of days having flying ant activity between 2012-2014 of their 97-day season. The focus here is on the large emergences which could potentially be picked up by WSR. In 2021, there was a gap between under 60 and above 100 for CS responses; thus, as the first year analysed, 100 was chosen to determine a FAD. In 2022, there were only 2 days, which did not fit this categorisation, of 88 and 84 responses, but they were consecutive to a classified Flying Ant Day.

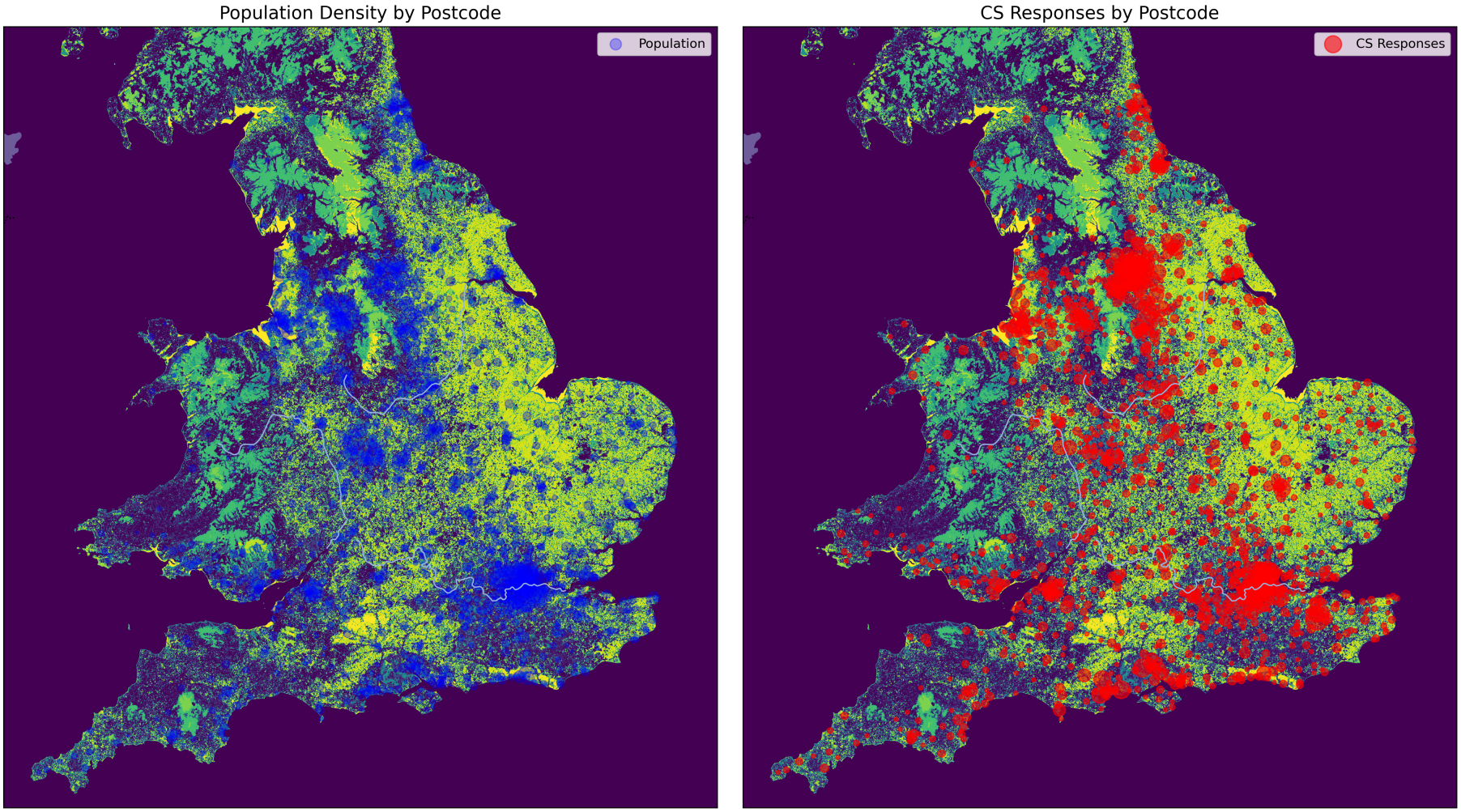

(a) The Population Density from the Office for National Statistics (Liveson, 2017), 2011 census data

(b) Flying Ant Day, Citizen Survey Responses (filtered by valid date and location) from 2021-2022

Figure 5.2: Population vs Citizen Science Survey Responses Density of England and Wales.

The first part of the survey, Question 1, asked respondents to provide the outcode of their postcode (defined in Chapter 1, Section 1.6). Figure 5.2 illustrates the spatial distribution of responses across England and Wales. On the left of Figure 5.2, panel a) shows the population density of the 2011 census in blue (Liveson, 2017), whilst the right-hand panel displays the response density of citizen science (CS) in red. The two distributions are broadly correlated, with notable enhancements in certain areas, such as Leeds, reflecting a bias likely due to the survey's launch location. Encouragingly, every postcode area in England and Wales recorded at least one CS response during the 2021-2022 period.

In contrast, Ireland and Scotland were less well represented, as seen in Figure 5.1. To address this gap, outreach efforts in 2023 included collaboration with the Edinburgh Science Festival to improve representation. The target species, *Lasius niger*, is considered a cosmopolitan species across the UK and Ireland (Atlas, 2025), its relatively uniform distribution in survey responses provides confidence in the spatial representativeness of the dataset.

Figure 5.1 also illustrates the temporal distribution of the reported emergence events, revealing some regional differences. The 9 July 2021 case study was concentrated around the Chenies radar and the North London area, whilst the FAD events 16-17 July 2022 show a broader spatial spread, with notably higher activity in the eastern regions of the UK compared to the west.

Question 2 asked participants to report the date of their ant sighting, enabling the identification of peak periods of ant activity. During July and August, 58% of days in 2021 and 43% in 2022 had a least one CS response. Of these, 11 days were classified as "Flying Ant Days" (FADs), 6 in 2021 and 5 in 2022, as shown in Figure 5.1. These numbers align with Hart et al. (2018)'s study, who identified having at least five FADs per year.

Questions 3 to 5, addressed the timing of sightings, including the time of day, and perceived duration of activity. *L. niger* are known to be active across the 24-hour cycle, but are typically considered nocturnal due to the predominance of their foraging during nighttime. However, CS responses are inherently biased toward daytime activity, particularly in estimating flight duration. Unless respondents deliberately observed the full flight event from emergence to nesting,

Length of Sighting (hrs)	<1	1-2	2-5	>5
Quantifiable (hrs)	1	2	5	8

Table 5.1: Citizen Science Survey, Question 5 Length of Sighting to quantifiable units for processing and data analysis.

estimates of flight length are likely to be unreliable.

To standardise interpretation, responses were grouped using predefined duration categories, as shown in Table 5.1, though this introduces additional subjectivity. A specific issue arose with Question 4, "How long were the ants flying for?", which was amended during the 2021 season to include the clarification "Under an hour if on ground". Even with the correction this resulted in a large bias to "Under an hour". Additionally, responses indicating durations longer than five hours proved difficult to visualise consistently in subsequent analysis. To improve future surveys, this question should follow "Were the ants mostly flying, on the ground, or both?" and be reworded to focus more broadly on "activity duration" rather than flight time alone.

82% of respondents who recorded the time of their observation reported sightings during the afternoon, with only 12% in the morning. This pattern may reflect both the genuine timing of nuptial flight events and observational bias related to human activity patterns.

Figure 5.3 illustrates the timing of initial ant sightings reported by participants, revealing a bimodal pattern with peaks around 11:00 and again in the late afternoon between 16:00 and 17:00. However, the time of initial sighting does not necessarily capture the full duration of winged ant activity. Figure 5.4, which represents the reported periods of ant activity, shows a different pattern, with the first peak occurring around 13:00 and another at 20:00.

To simplify reporting for participants, the citizen science survey asked respondents to indicate the general duration of ant flight using multiple-choice options: $< 1hr, 1-2hrs, 2-5hrs$, and "*all day*", rather than asking for the exact time when activity ceased. This approach minimised participant burden but also introduced some uncertainty, as most respondents were unlikely to observe ants continuously from emergence to nesting. To interpret these responses, Table 5.1 provides the assigned durations for each category.

Comparing the trends, the midday distribution in Figure 5.3 more closely approximates a normal distribution than the corresponding data in Figure 5.4. Notably, there is a difference

of two hours between the first peaks and three hours between the afternoon peaks of the two figures, suggesting that earlier sightings tended to be of shorter duration (1–2 hours), while afternoon activity often persisted longer (1–5 hours).

Further, Figure 5.4 shows that the majority of reports described observations of winged ants both in flight and on the ground. Sightings of ants exclusively on the ground exhibited the least variation in timing, while reports of flying-only ants displayed a more erratic distribution throughout the day. Peak flying activity was observed from 17:00 to 21:00 (sunset), with a smaller midday peak around 13:00 that corresponded with increased ground activity.

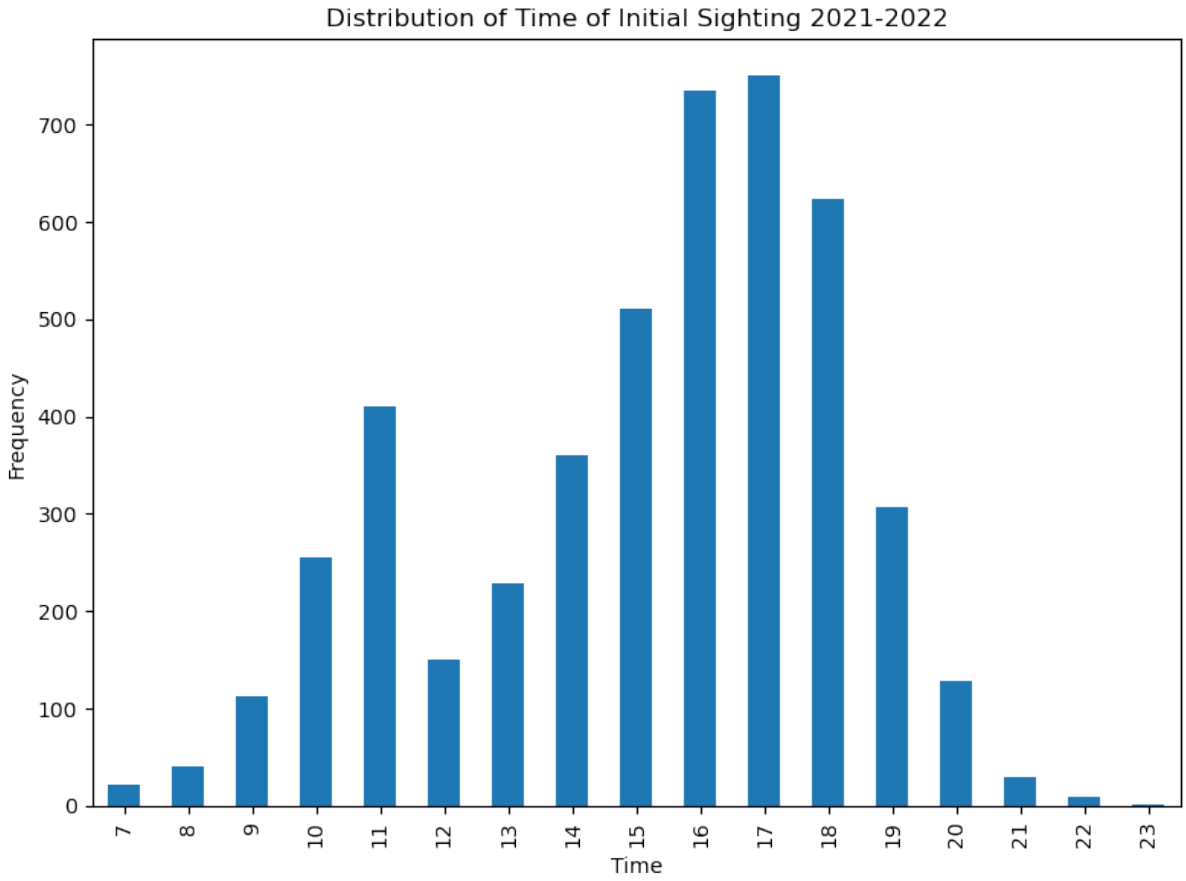

Figure 5.3: Initial time of sighting, grouped by hour from Citizen Science Responses on witnessing alate ants across all dates in 2021-2022.

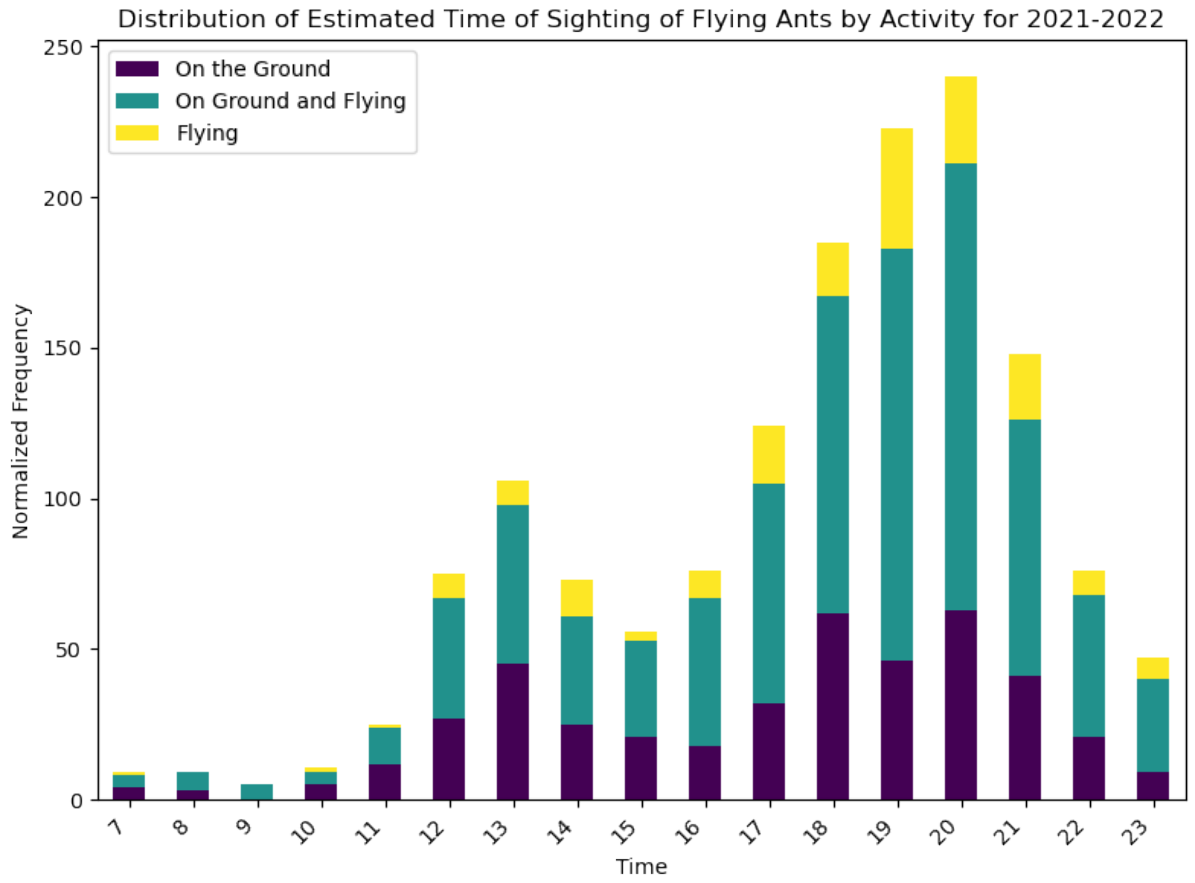

Figure 5.4: Normalized Frequency of activity of alate ants. The time is taken from initial sighting combined by the length of sighting quantified by Table 5.1, with the bottom purple colour representing ants witnessed on the ground only; middle teal ground and flying; and top, yellow flying across all survey responses.

5.2 Radar

The UK Met Office (UKMO) weather surveillance radars (WSRs) were used for the radar analysis for FAD. The primary radar used was Chenies (51.689492^o, -0.5302192^o) which is situated outside the M25, NNW of London. This section details some of the specific insect processing of the radar, maintaining the assumption that the observations do not contain precipitation, and for the FADs the dominant signal will be ants, and thus instead of "insects" or "bioscatterers" ants are used as default. When comparing to non-FAD, the same processing is used as there is no general insect baseline to use as reference.

5.2.1 Filtering

Filtering of the radar data was performed in two stages: first to remove general clutter, and then to isolate insect targets using specific radar variables. To characterize baseline noise, a clear-air reference period was identified on the 11th of July 2021, between 09:00 and 11:30, verified using both archival meteorological records (EUMETSAT & University, n.d.) and the CS survey, which confirmed this was not a Flying Ant Day. During this period, if the Clutter Index, a named variable from the UKMO radar outputs, remained stable relative to its previous value (t–1) across consecutive 10 minute intervals, these values were incorporated into a clutter mask for subsequent filtering.

To identify insects, the methodology was adapted from (Kilambi et al., 2018), who developed equations to distinguish insects from other radar targets. Stepanian et al. (2020) built upon this approach, introducing further criteria such as a 2 km altitude limit; however, in this thesis' analysis, the altitude limitations would be too restrictive when the intention was to to examine the full vertical distribution of ants.

Figure 5.5 illustrates the effect of sequential filtering on radar observations for a representative day. Row 1 displays unfiltered data, highlighting the substantial noise present in raw radar scans. Row 2 applies the initial filtering based on Equations 5.1, removing background clutter but retaining some non-insect echoes. Row 3 employs the more stringent criteria from (Kilambi et al., 2018), supplemented by a cross-correlation ratio (ρ_{HV}) threshold of < 0.4 as per (Lukach et al., 2022), resulting in further refinement and improved specificity for insect targets. Both rows 2 and 3 exclude data identified as clutter during the clear-air reference period.

For this study, prioritizing certainty in insect detection was essential. Therefore, a more conservative filtering approach was adopted, accepting the potential for false negatives to minimize false positives. The Kilambi et al. (2018) methodology proved most suitable for our case, whereas the Stepanian et al. (2020) filters were tailored to mayfly swarms with well-characterized emergence patterns and higher insect biomass. In some later plots, to emphasise the "swarm"-like behaviour a separate refinement of $0.7 <= \rho_{HV} < 0.9$ (Bachmann & Zrnic, 2007), (S.

Gauthreaux & Diehl, 2020).

$$\begin{aligned} -12 < DRlog < 0 \\ Z < 0 \end{aligned} \tag{5.1}$$

$$\begin{aligned} -12.5 < DRlog \\ Z < 45 \\ Z_{DR} < 5 \end{aligned} \tag{5.2}$$

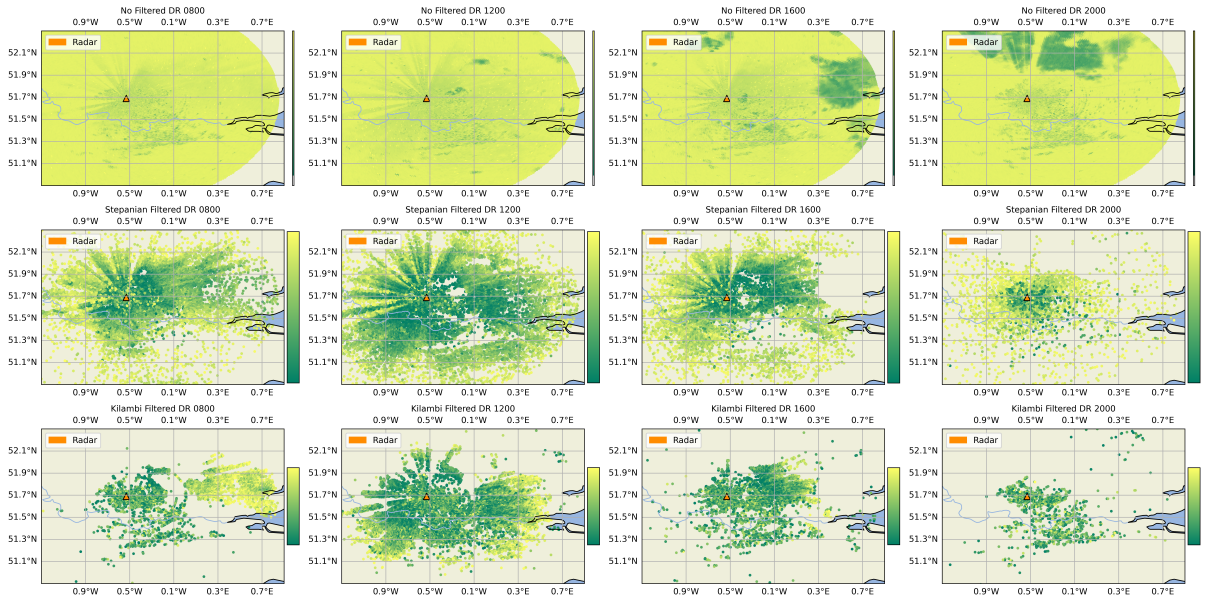

Figure 5.5: Panel to show the effects of different filtering methods, columns are four hourly intervals (08:00, 12:00, 16:00, 20:00), row one is no filter, row two is based from (Stepanian et al., 2020), row three is based on (Kilambi et al., 2018) row two and three both have the clear day filter.

5.2.2 Altitude

As discussed in Chapter 3, the (MO) radar voxel altitude estimates was compared with those derived from geodesic calculations. Figure 5.6 presents a histogram of the differences in voxel altitude for the first 2 km above ground level, using 200 m altitude bands. In this figure, blue bars represent the geodesic altitude estimates (which include estimated atmospheric refraction), while orange bars show the MO altitudes calculated with a $\frac{4}{3}$R spherical Earth radius standard atmosphere refraction (RSE), the "combo" is the overlapping number of coincident altitudes. For an elevation angle of $\theta = 0.5^o$, the MO altitude values range from 155 to 2208 m, while the geodesic altitudes for the same beam and range ($r <= 127.5\,km$) span 185 to 1205 m. Figure

5.7 further illustrates how these altitude estimates affect the interpretation of insect activity. The top row displays the distribution of insect detections for $\theta = 0.5^o$, assuming activity is evenly spread within the radar beam. The subsequent rows break down detections into 200 m altitude bands up to 1 km. Two key observations emerge:

1. **Range effects:** Because each altitude band combines all relevant elevation rays, higher altitude bands correspond to different ranges from the radar. Inner range rings (closer to the radar) represent higher elevation angles, while outer rings correspond to lower elevations.

2. **Spatial isolation of activity:** By splitting detections into altitude bands, distinct clusters become visible. For example Figure 5.7(p) shows a distinct line of activity to the NW of the radar at 20:00 however even in Figure 5.7(d) there is no distinctive feature. At 12:00, Figure 5.7(b) shows there is lots of activity, but only by splitting into altitude bands isolates the columnar activity.

Although these are still broad 200 m bands, isolating regions of interest allows for more detailed analysis of insect distributions within the column. Figure 5.7 demonstrates that altitude assignment has a significant impact on interpreting insect activity, and highlights notable discrepancies between the MO and geodesic altitude estimates for detections meeting the depolarisation ratio (DR) criteria for insects.

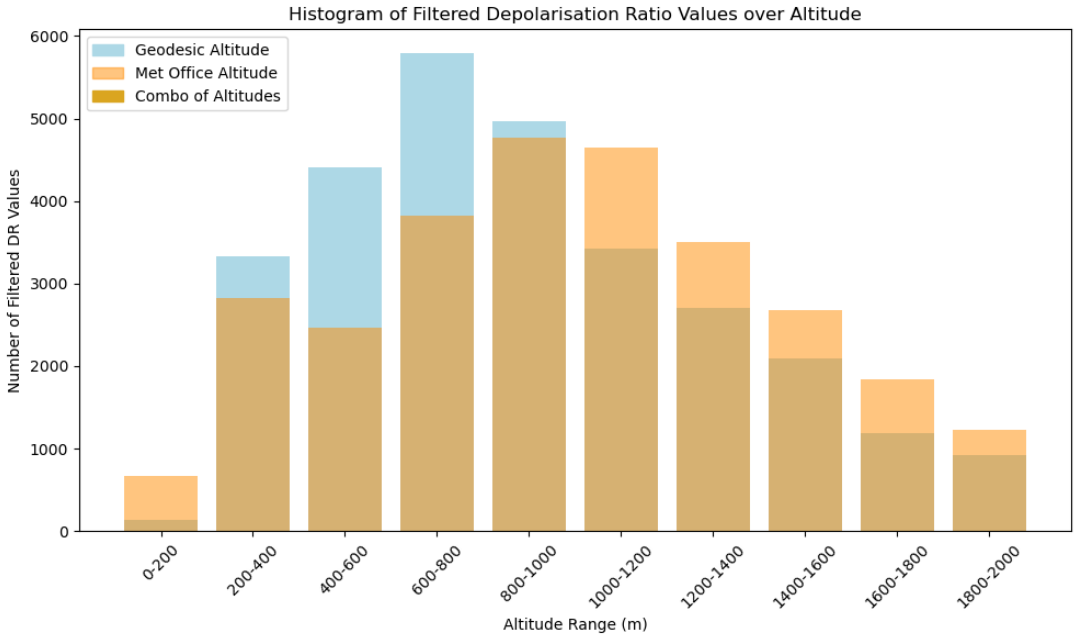

Figure 5.6: Histogram of Difference in Altitude between UK Met Office Position and Geodesic with N_s Refraction Position, of Voxels for Chenies Radar.

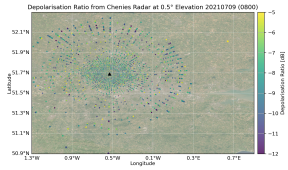

(a) 08:00, $\theta = 0.5^o$

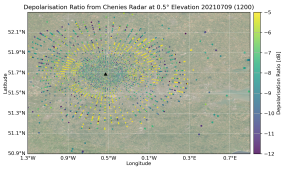

(b) 12:00, $\theta = 0.5^o$

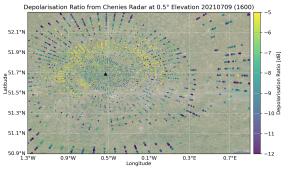

(c) 16:00, $\theta = 0.5^o$

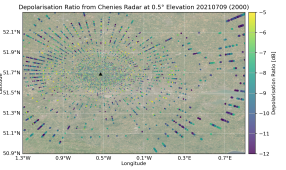

(d) 20:00, $\theta = 0.5^o$

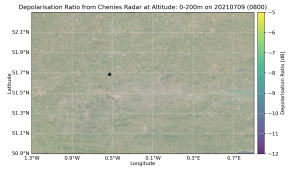

(e) 08:00, $0 \leq h \leq 200\,m$

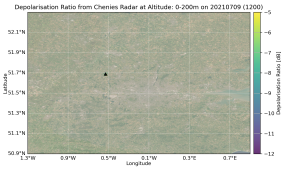

(f) 12:00, $0 \leq h \leq 200\,m$

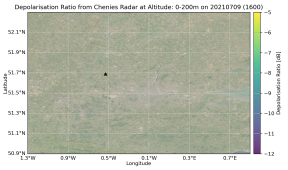

(g) 16:00, $0 \leq h \leq 200\,m$

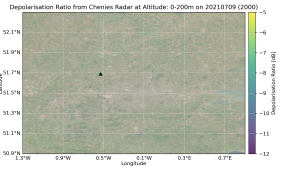

(h) 20:00, $0 \leq h \leq 200\,m$

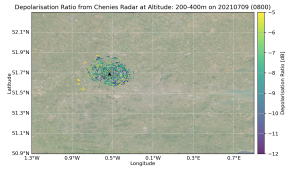

(i) 08:00, $200 \leq h \leq 400\,m$

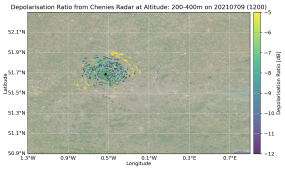

(j) 12:00, $200 \leq h \leq 400\,m$

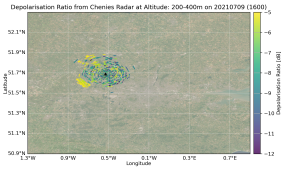

(k) 16:00, $200 \leq h \leq 400\,m$

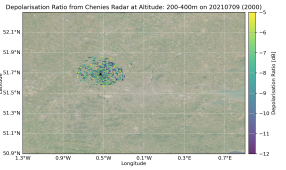

(l) 20:00, $200 \leq h \leq 400\,m$

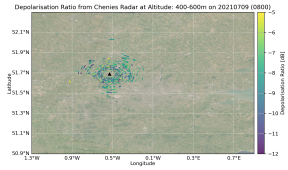

(m) 08:00, $400 \leq h \leq 600\,m$

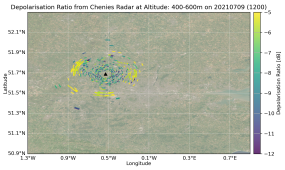

(n) 12:00, $400 \leq h \leq 600\,m$

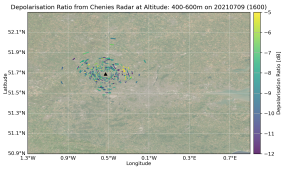

(o) 16:00, $400 \leq h \leq 600\,m$

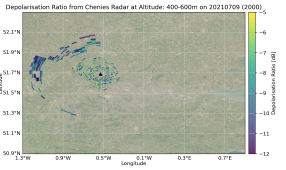

(p) 20:00, $400 \leq h \leq 600\,m$

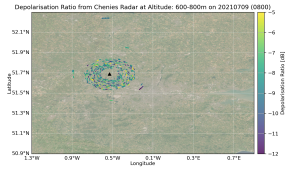

(q) 08:00, $600 \leq h \leq 800\,m$

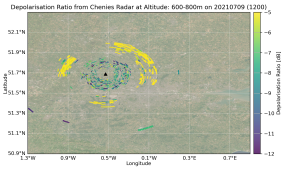

(r) 12:00, $600 \leq h \leq 800\,m$

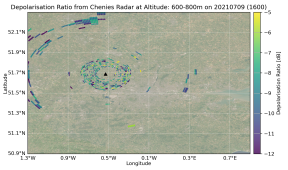

(s) 16:00, $600 \leq h \leq 800\,m$

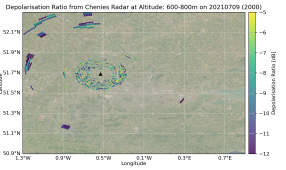

(t) 20:00, $600 \leq h \leq 800\,m$

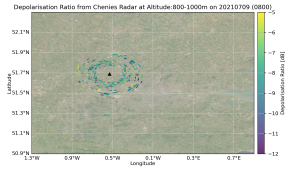

(u) 08:00, $800 \leq h \leq 1000\,m$

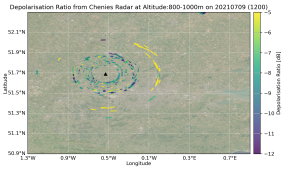

(v) 12:00, $800 \leq h \leq 1000\,m$

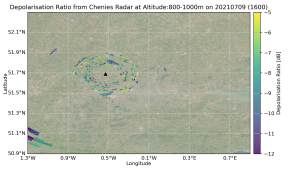

(w) 16:00, $800 \leq h \leq 1000\,m$

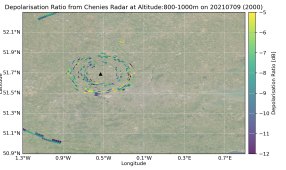

(x) 20:00, $800 \leq h \leq 1000\,m$

Figure 5.7: Panel plot of Filter Depolarisation Ratio, representing insect activity from Chenies Radar over 9th July 2021. Columns are at 4 hourly intervals (08:00, 12:00, 16:00, 20:00), The first row is the lowest elevation at $\theta = 0.5^o$ are altitude bands (200-400 m, 400-600 m, 600-800 m, 800-1000 m).

5.2.3 Biomass

In the context of this thesis, "biomass" refers to the estimated mass of biological material, primarily insects, present in the atmosphere, as detected by radar. For FAD, it is assumed that the dominant radar signal comes from alate ants, so the total measured biomass largely represents the mass of these ants.

The sex ratio of *L. niger* during FAD is not well characterized, but it is generally thought that males are more numerous than Queens. This is because males swarm in large numbers to maximize genetic diversity, while relatively fewer Queens emerge to establish new colonies. Literature estimates the proportion of Queens to males to be around 20% Queens and 80% males, with a possible range from 14% to 30% Queens, based on studies by Boomsma and A. (1990), Fjerdingstad et al. (2002) and Pearson (1987).

Given these ratios, and the radar cross-section (RCS) measurements discussed in Chapter 4, the radar signal is expected to be dominated by Queens, as they are significantly larger than males. Therefore, when converting radar variables into biological parameters, the Queen's RCS, alone, is used as the reference value.

The conversion from WSR measurements to biological estimates involves several steps. Equations 5.3 outline this process. WSR reports the equivalent reflectivity factor Z in decibels (dBZ), while the radar reflectivity η has linear units of cm^2km^{-3}. The conversion includes a factor of 10^3 to match the units, and incorporates radar wavelength λ, as well as the dielectric factor $|K|^2$, which depends on the refractive index and absorption coefficient of the target (see Chapter 2, Section 2.3). WSR uses the precipitation $|K|^2 = 0.93$ (Nanding & Rico-Ramirez, 2019) as default in their Z value, thus this conversion reveals the raw values. Once radar reflectivity η is calculated, it is multiplied by the voxel volume to yield a total cross-sectional area (cm^2). Dividing this by the Queen's RCS provides an estimate of the number of ants detected. Because the radar signal is dominated by Queens, the resulting count is adjusted by the average Queen-to-male ratio (1:4). Finally, to estimate biomass, the number of individuals is multiplied by the average mass of Queens and males according to this ratio.

$$\begin{aligned} \eta &= 10^3 \cdot \frac{\pi^5}{\lambda_4} \cdot Z \cdot |K|^2 \cdot 10^{\frac{dBZ}{10}} \\ IATot &= \eta \cdot V_{voxel} \\ RCS_{Queen} &= 0.11660082599656907 \\ Number_{Ants} &= \frac{IATot}{RCS_{Queen}} \cdot \frac{100}{20} \\ Biomass &= Number_{Ants} \cdot (0.2 \cdot m_{Male} + 0.8 \cdot m_{Queen}) \end{aligned} \tag{5.3}$$

For activity of the radar when taking averages, the average activity is taken for when the conditions are satisfied. For example if only once in a period of four hours a voxel satisfies the biomass conditions as laid out in Equation 5.3, then that is the value used for all the statistics, if it satisfies it 40% of the time then the statistics are carried out for those 40% of times. This is to show the average activity when insect activity is present, rather than looking over the whole domain.

5.3 Trends of FAD

Figure 5.8 is a graph of Chenies radar, with a categorical x-axis, where the dates, are not continuos, showing each of the eleven FADs. The lines are colour coded for the first seven altitude bands up to 4 km and the grey scatter plots the number of CS reports that had Chenies as the closest radar. Each altitude band has its own baseline level activity nominally starting below 10^4, the altitude band 3-4 km is notably higher than the rest of the bands. The altitude bands generally all follow the same trends, just to different degrees on the hourly scale. A FAD appears to average at a peak of around 32,000 ants per cubic kilometre but on the 17-18 July 2021 this is exceeded by a factor of 10. The CS reports are for Chenies radar only, appear a couple of hours later from the start of rise in density in the radar. There is an approximate diurnal cycle shown in both the radar and CS data. The year 2022 FADs appear more evenly distributed in terms of insect activity than 2021 for the Chenies radar.

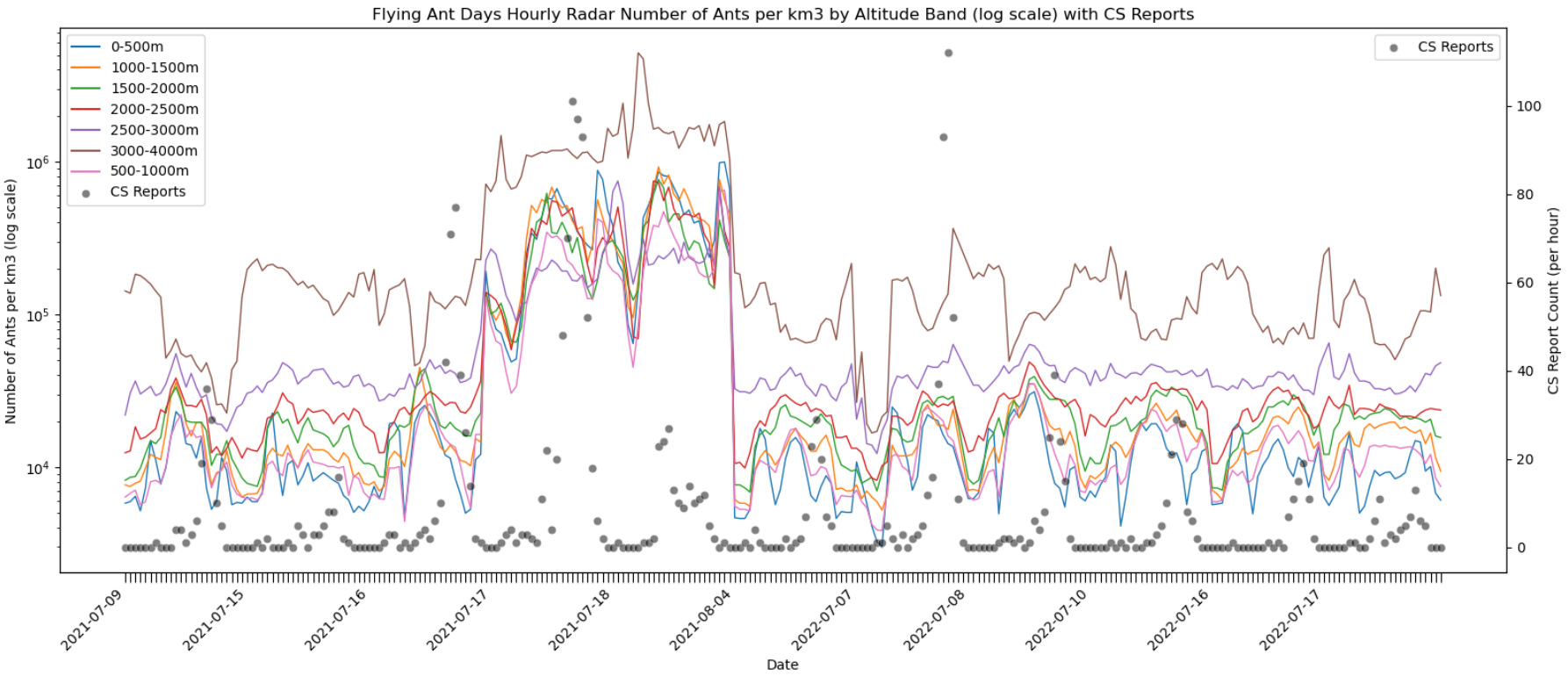

Figure 5.8: Average Number of Ants per km^3 for Chenies Radar, split by altitude bands up to 4 km, for all Flying Ant Days, with the Citizen Science Survey Results on the y2-axis.

Figures 5.9 a), b) and c) are of the exact same measure but each show different amounts. Encouragingly the trends are the same, but dependent on range limits, and altitude, different quantities of biomass are estimated. Why is the median different, well, with increased range there is an increase of voxels and the number of potential voxels with insects increases; additionally there is an increase in volume and also the base-level of activity for the radar to register the signal will be increased. This tells us that whilst Plan Position Indicators (PPIs) can provide general estimates, by using precise geodesic positioning, and isolating hotspots of activity, our biomass estimates will be more representative of the area in question.

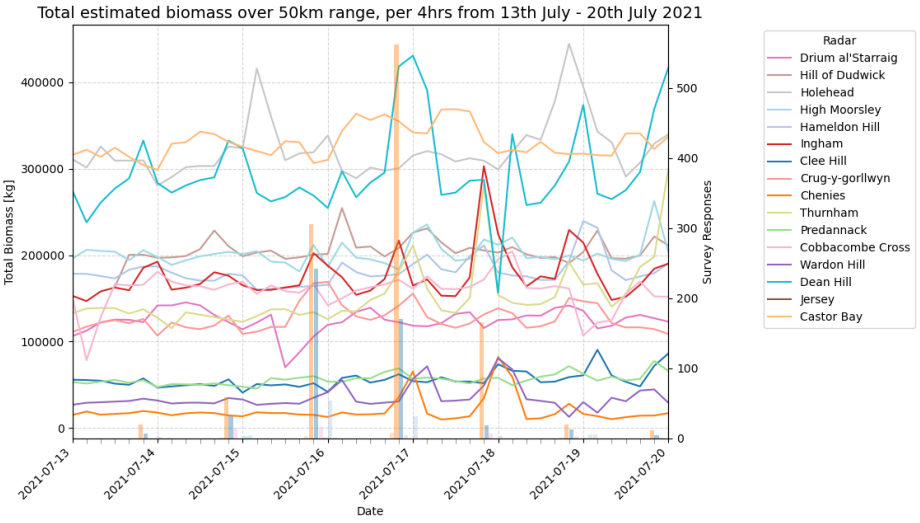

(a) Radar Volume out to 50 km

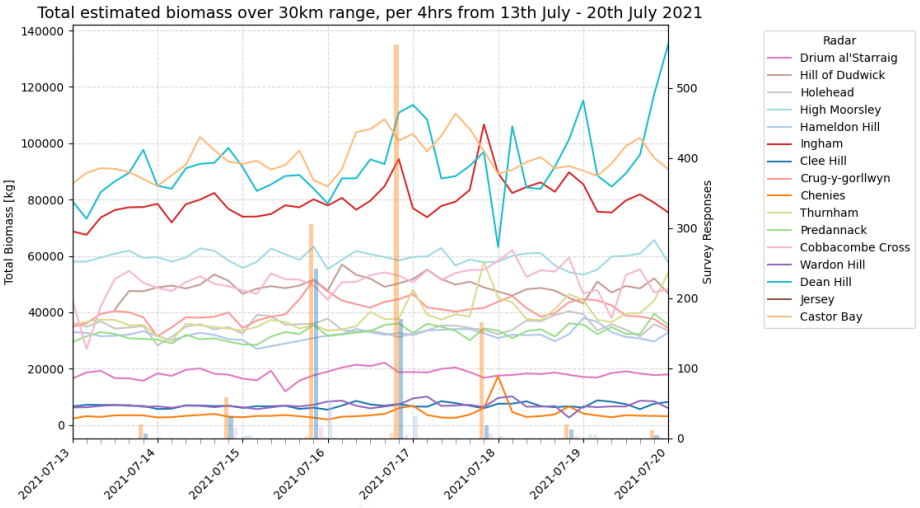

(b) Radar Volume out to 30 km

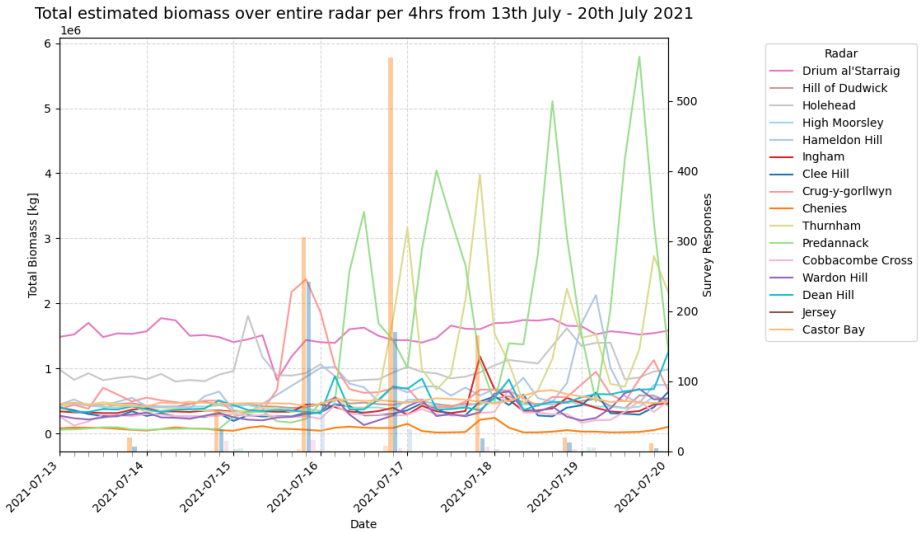

(c) Whole Radar Volume for the 13th to the 20th July 2021

Figure 5.9: Total estimated biomass for radar volume, for the time period 13th to the 20th July 2021, with Flying Ant Days recorded 16th to the 18th July.

5.4 Case Studies

Two case studies are presented in this section, to do an in-depth analysis of the radar data and bring in the CS responses too. The criteria was to be a flying ant day ($\geq$ 100 CS responses), with ± 2 consecutive days to not be a FAD for comparison in general insect activity. The 9th of July 2021 is the first case study, which had 78% responses within 50 km, and 92% within 75 km, the good range (Met Office, 2023), of the 118 responses closest to Chenies radar. A separate analysis was done for all radars for the period 13-20 July, with the FADs 15-18 July 2021. This was to look at more generalised trends and differences, the consecutive days were not completely clear, with precipitation in some areas.

5.4.1 9 July 2021

The 9th of July 2021 was an identifiable "isolated" case with 91% of the 129 survey responses were around a singular radar, Chenies. Figure 5.10 is a series of PPI plots at elevation $\theta = 0.5^o$ and shows the activity, filtered for insects, in DR, for 7, 9, 10 and 11 July, unfortunately Chenies was offline for most of the 8th of July, hence the different time series in Figure 5.10. On 9 July 2021 there is general increase in activity across all four time periods, there are some data points which do not change across the days, which could be eliminated with further filtering or normalisation. On 10 July 2021 at 16:00 there was a rain shower which is seen near the Thames Estuary approximately ($51.3^o < \phi < 51.7^o$) and ($0.2^o < \lambda < 0.5^o$). There was also precipitation present on the 11th of July.

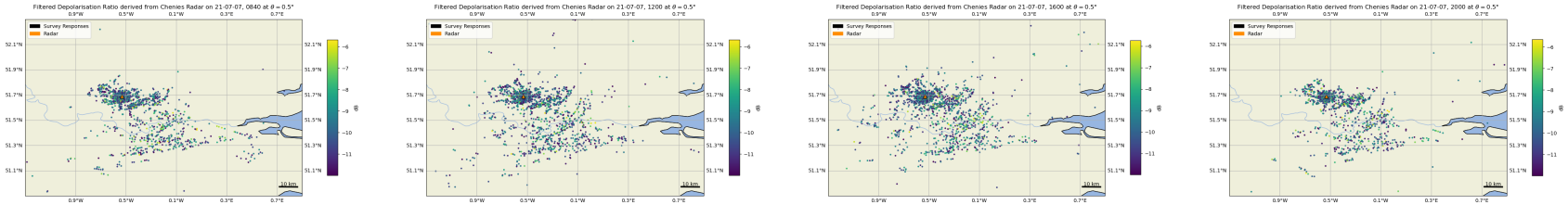

(a) 07/07/2021, 08:40 (b) 07/07/2021, 12:00 (c) 07/07/2021, 16:00 (d) 07/07/2021, 20:00

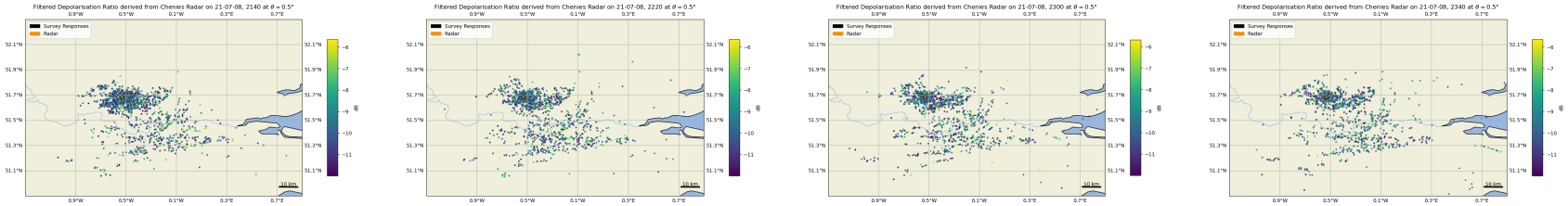

(e) 08/07/2021, 21:40 (f) 08/07/2021, 22:20 (g) 08/07/2021, 23:00 (h) 08/07/2021, 23:40

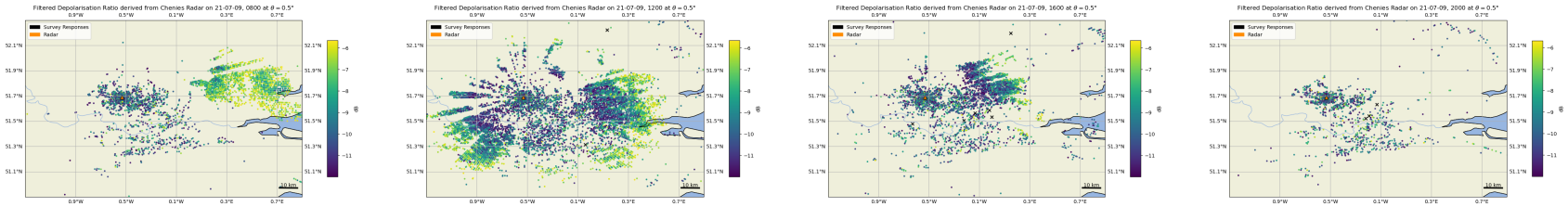

(i) 09/07/2021, 08:40 (j) 09/07/2021, 12:00 (k) 09/07/2021, 16:00 (l) 09/07/2021, 20:00

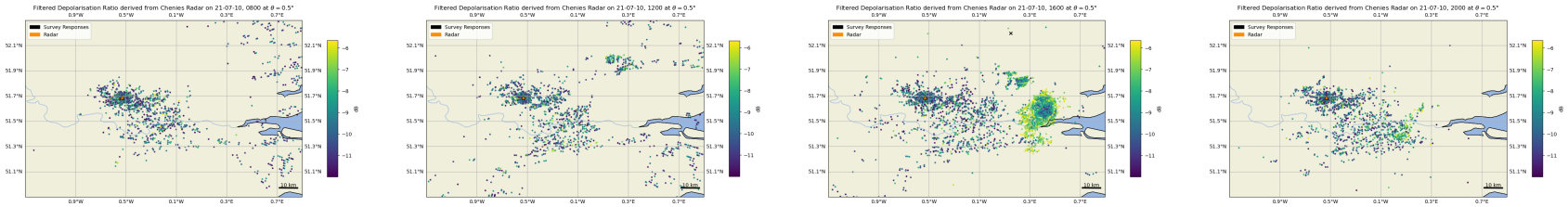

(m) 10/07/2021, 08:40 (n) 10/07/2021, 12:00 (o) 10/07/2021, 16:00 (p) 10/07/2021, 20:00

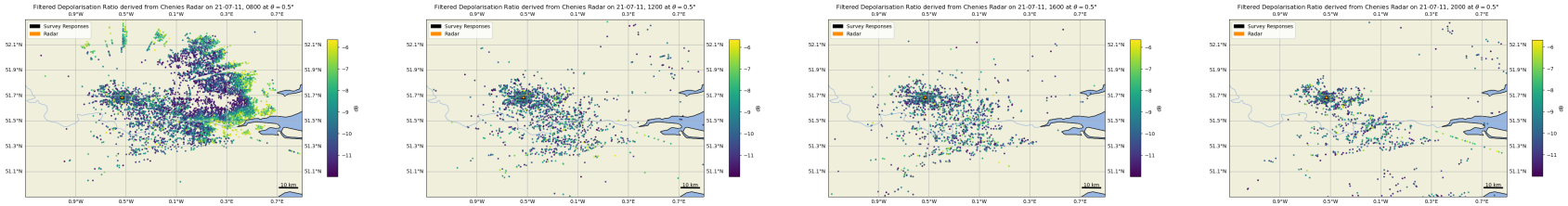

(q) 11/07/2021, 08:40 (r) 11/07/2021, 12:00 (s) 11/07/2021, 16:00 (t) 11/07/2021, 20:00

Figure 5.10: Chenies Radar out to 127.5 km on 9th of July 2021 (Flying Ant Day) with $\pm 2 days$. This is a full Filtered Depolarisation Ratio Map, representing insect activity; with the most amount of activity in yellow and green.

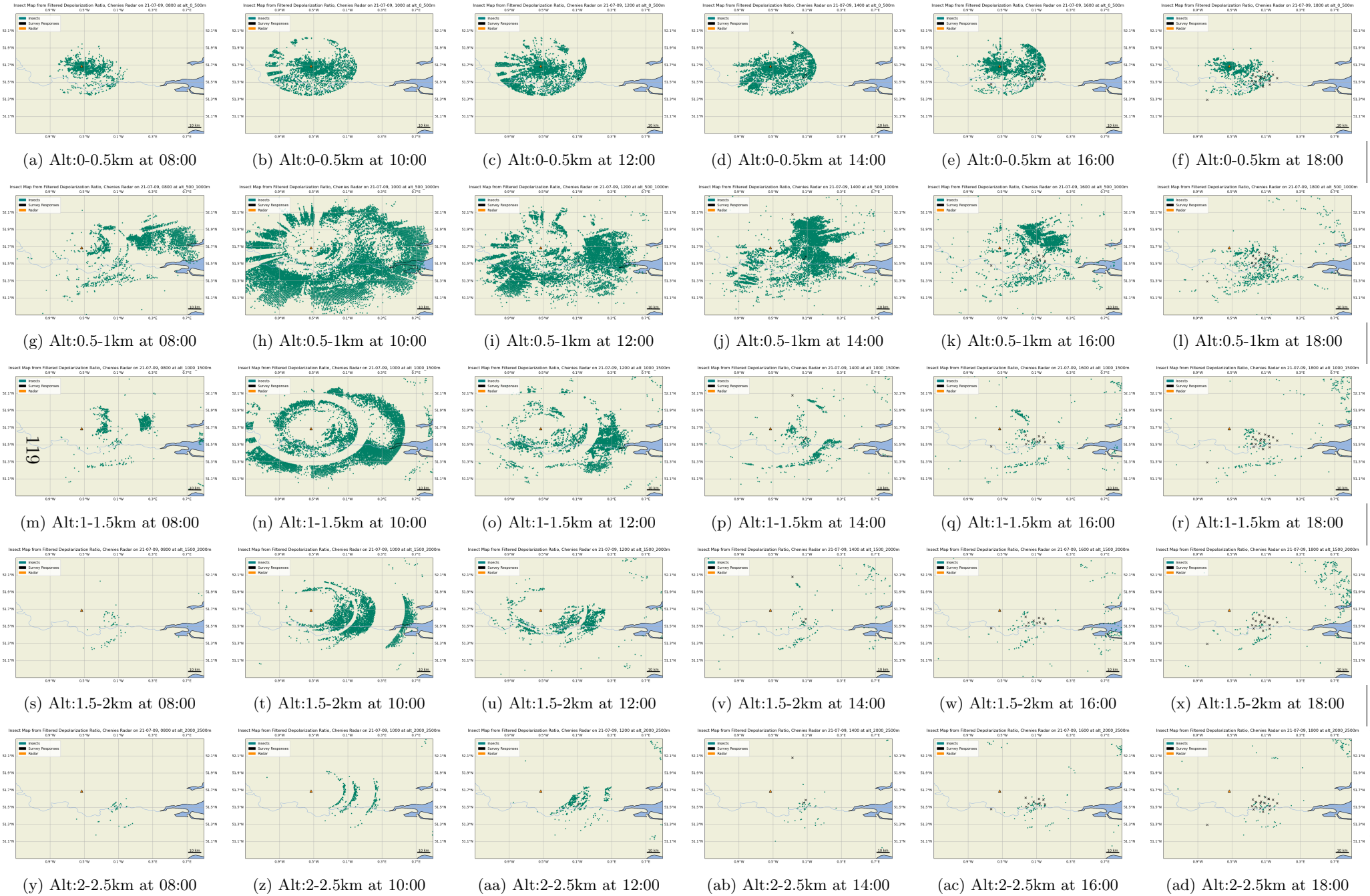

(a) Alt:0-0.5km at 08:00 (b) Alt:0-0.5km at 10:00 (c) Alt:0-0.5km at 12:00 (d) Alt:0-0.5km at 14:00 (e) Alt:0-0.5km at 16:00 (f) Alt:0-0.5km at 18:00

(g) Alt:0.5-1km at 08:00 (h) Alt:0.5-1km at 10:00 (i) Alt:0.5-1km at 12:00 (j) Alt:0.5-1km at 14:00 (k) Alt:0.5-1km at 16:00 (l) Alt:0.5-1km at 18:00

(m) Alt:1-1.5km at 08:00 (n) Alt:1-1.5km at 10:00 (o) Alt:1-1.5km at 12:00 (p) Alt:1-1.5km at 14:00 (q) Alt:1-1.5km at 16:00 (r) Alt:1-1.5km at 18:00

(s) Alt:1.5-2km at 08:00 (t) Alt:1.5-2km at 10:00 (u) Alt:1.5-2km at 12:00 (v) Alt:1.5-2km at 14:00 (w) Alt:1.5-2km at 16:00 (x) Alt:1.5-2km at 18:00

(y) Alt:2-2.5km at 08:00 (z) Alt:2-2.5km at 10:00 (aa) Alt:2-2.5km at 12:00 (ab) Alt:2-2.5km at 14:00 (ac) Alt:2-2.5km at 16:00 (ad) Alt:2-2.5km at 18:00

Figure 5.11: Chenies Radar out to 127.5 km on 09/07/2021. Rows are in 500 m altitude bands, columns are time running from 08:00 to 18:00. Flat Insect Activity from filtered Depolarisation Ratio.

Insect Activity per kilometre cubed Map from Chenies Radar, 09/07/2021

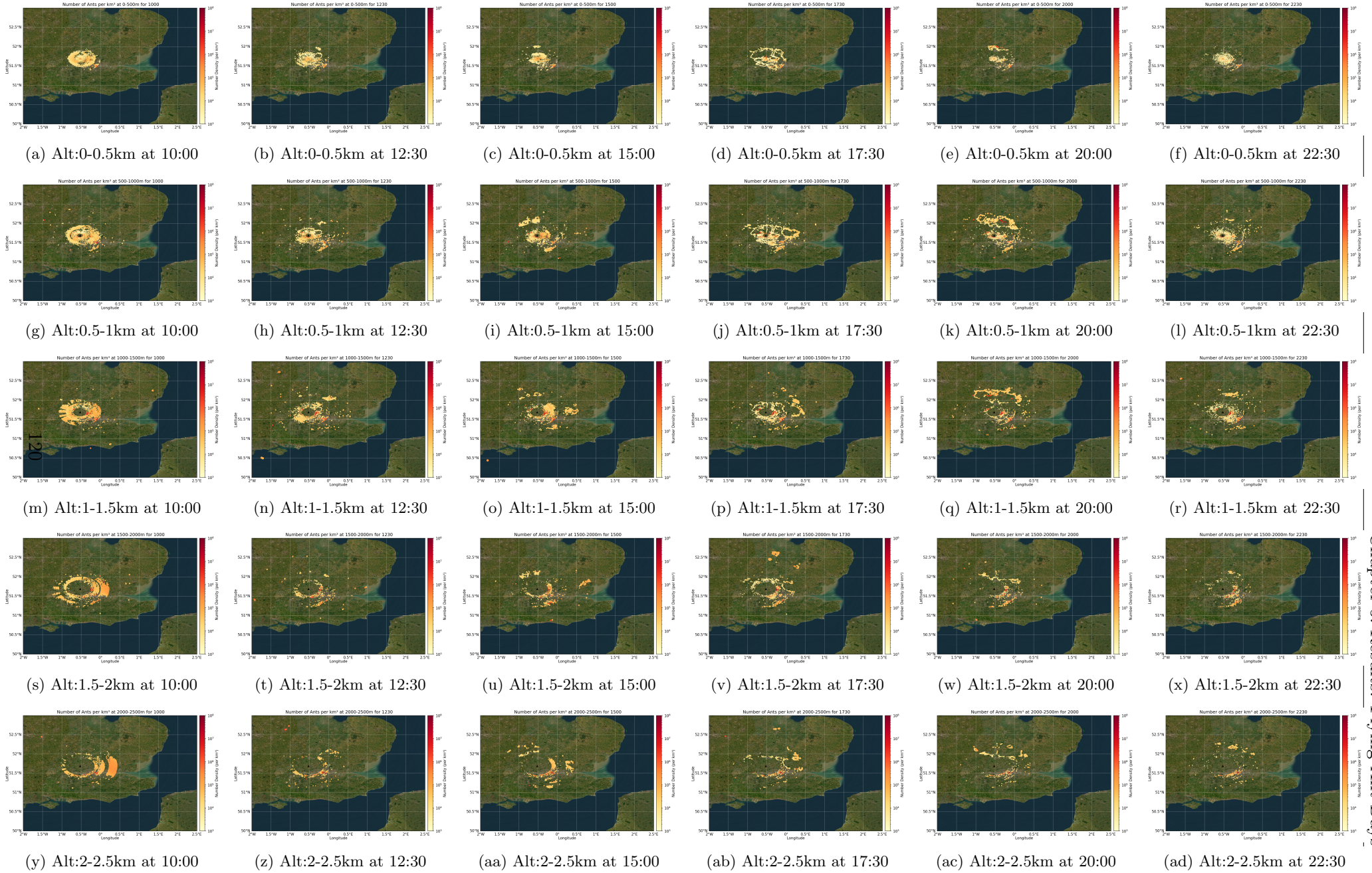

(a) Alt:0-0.5km at 10:00 (b) Alt:0-0.5km at 12:30 (c) Alt:0-0.5km at 15:00 (d) Alt:0-0.5km at 17:30 (e) Alt:0-0.5km at 20:00 (f) Alt:0-0.5km at 22:30

(g) Alt:0.5-1km at 10:00 (h) Alt:0.5-1km at 12:30 (i) Alt:0.5-1km at 15:00 (j) Alt:0.5-1km at 17:30 (k) Alt:0.5-1km at 20:00 (l) Alt:0.5-1km at 22:30

(m) Alt:1-1.5km at 10:00 (n) Alt:1-1.5km at 12:30 (o) Alt:1-1.5km at 15:00 (p) Alt:1-1.5km at 17:30 (q) Alt:1-1.5km at 20:00 (r) Alt:1-1.5km at 22:30

(s) Alt:1.5-2km at 10:00 (t) Alt:1.5-2km at 12:30 (u) Alt:1.5-2km at 15:00 (v) Alt:1.5-2km at 17:30 (w) Alt:1.5-2km at 20:00 (x) Alt:1.5-2km at 22:30

(y) Alt:2-2.5km at 10:00 (z) Alt:2-2.5km at 12:30 (aa) Alt:2-2.5km at 15:00 (ab) Alt:2-2.5km at 17:30 (ac) Alt:2-2.5km at 20:00 (ad) Alt:2-2.5km at 22:30

Figure 5.12: Chenies Radar on 09/07/2021. Rows are in 500 m altitude bands, columns are time running in 2.5 hourly increments from 10:00 to 22:30. Number of Ants per km^3 Insect PPI Map.

Figure 5.11 is another PPI panel plot, using range of Chenies radar out to 127.5 km. The rows in Figure 5.11 are in 500 m altitude bands, and the columns are bihourly times from 08:00 to 18:00. The plots are single colour showing likely presence of insects in teal and the black x's mark the citizen science responses over the same period. Figure 5.11 shows us the difference of insect activity in altitude bands but also the temporal differences with growth until about the middle of the afternoon and then a decrease in activity. The altitude band of up to 500 m, is range limited, due to the angle of the beam. With the cluster of responses at 16:00 and 18:00 there appears to be some level of insect activity above at all altitudes.

Figure 5.12 is using the swarming criteria with $0.7 <= \rho_{HV} < 0.9$ and as seen it shows much greater detail than that of Figure 5.10 and 5.11. The complete time series associated with Figure 5.12 can be viewed at PhdGifs, but the selected timestamps in Figure 5.12 highlight the dynamic, circular patterns (*c*, *j*, *k*, *o* and *q*) and breadth of dispersal observed throughout the day. A persistent background "hum" of activity is apparent near the radar, likely attributable to residual clutter or baseline noise. This artefact could be reduced through improved clutter masking and normalization of baseline activity, further enhancing the accuracy of insect density estimates.

Figure 5.7 i) a PPI at elevation of $\theta = 0.5$ and shows an area of heightened insect activity at $(51.5 < \phi < 52.3, -0.1 < \lambda < 0.8)$. Figure 5.13 illustrates the temporal evolution of an insect activity cluster over this defined region of interest from Figure 5.7 i), from 07:30 to 09:30. At 07:30, elevated activity is observed within the 200–400 m altitude band, predominantly between the coordinates $(52.1^o < \phi < 52.3^o, 0.0^o) < \lambda < 0.6^o$. Over the subsequent two hours, this region of activity expands spatially, indicating the growth and dispersal of the cluster.

From Figure 5.13 i), the same area of activity initially presents as a single, coherent cluster under the elevation conditions of $\theta = 0.5^o$. However, analysis across multiple altitude bands and time intervals reveals additional complexity. By 07:40, the first emergence of activity above 600 m is detected, although this signal remains confined to a narrow horizontal range ($0.0 < h < 0.2$ km. By 08:10, the vertical distribution of intensity changes, with a pronounced peak forming between 200 and 400 m. As time progresses, both the intensity and spatial extent of the cluster

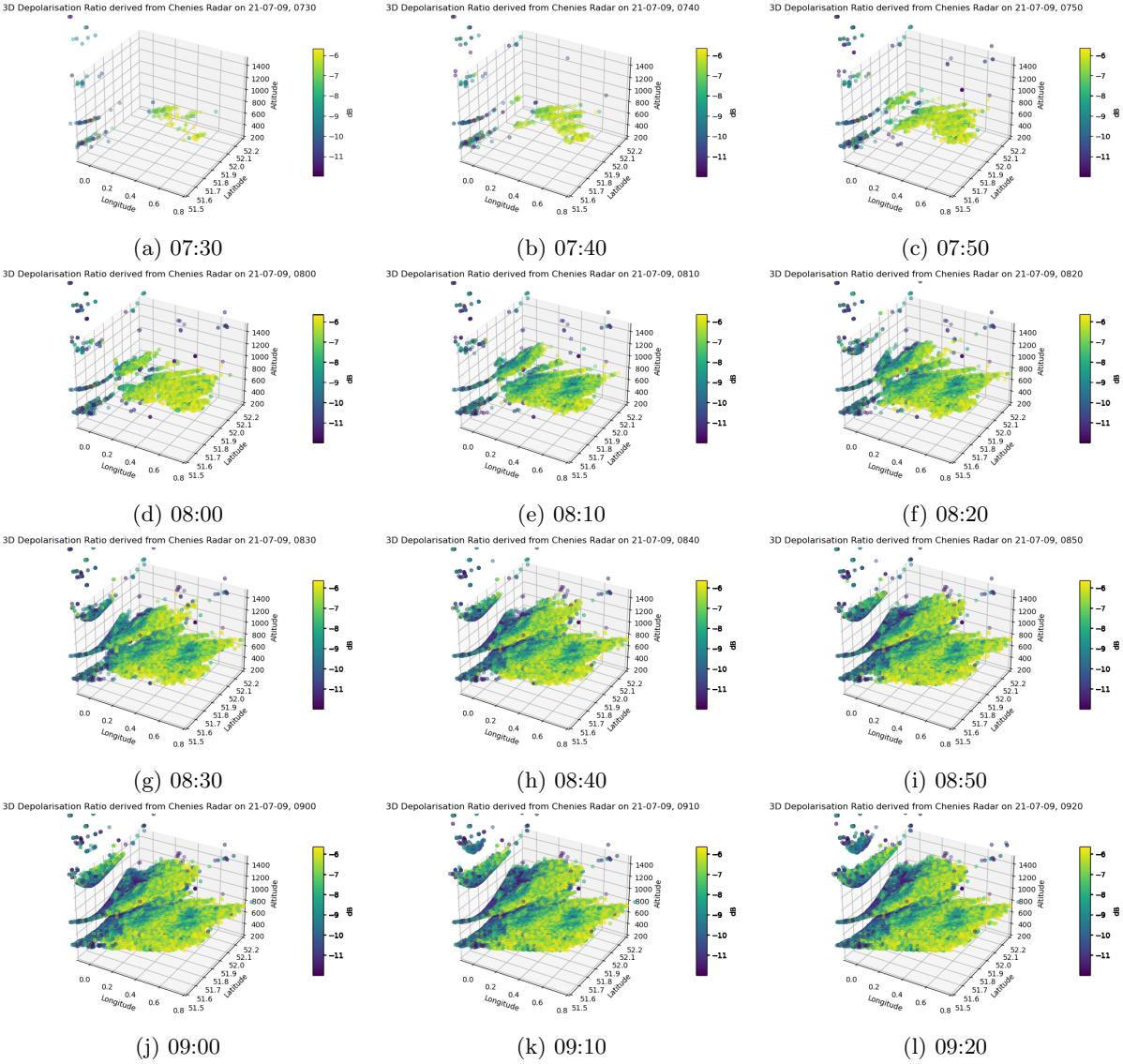

(a) 07:30 (b) 07:40 (c) 07:50

(d) 08:00 (e) 08:10 (f) 08:20

(g) 08:30 (h) 08:40 (i) 08:50

(j) 09:00 (k) 09:10 (l) 09:20

Figure 5.13: Cluster 1 from Chenies Radar on 9th July 2021, Filtered Depolarization Ratio representing Insect Activity.

increase, demonstrating continuous growth and vertical development throughout the observed period.

These observations highlight the dynamic nature of insect clusters, with both spatial and vertical expansion occurring over relatively short timescales.

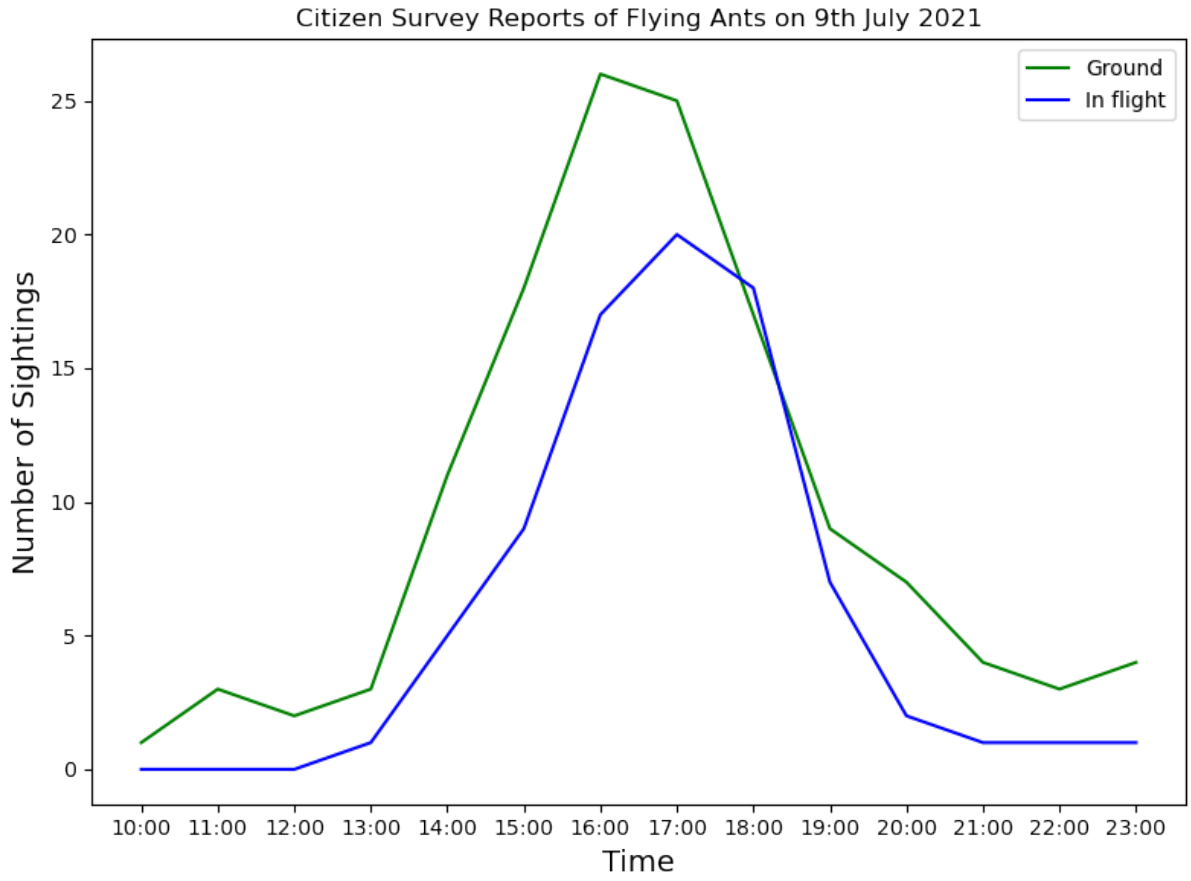

Figure 5.14: Citizen Science Survey Winged Ants Sightings 9th July 2021

Analysis of the CS survey responses for this day reveals a pronounced peak in ant sightings between 16:00 and 18:00 shown in Figure 5.14. By visually inspecting Figure 5.11 and and employing collocation tools, the cluster of relevant survey responses can be geographically isolated within the region defined by $-0.3 \leq \lambda \leq 0.1^o$ longitude and $51.4 \leq \phi \leq 51.7^o$ latitude. Figure 5.15 focuses on the period from 15:00 to 19:20, spanning approximately hour on either side of the primary CS sighting peak. In all plots there is higher values of biomass, $10^4 - 10^5$ around the kilometre mark and longitude -0.3^o to -0.25^o approximately which appears in every plot, this is an artefact of the radar data, which should be ignored. Going through each time step at Figure 5.15 a) 1500, the biomass is approximately 10^3 at 1-1.25 km. At 15:30, b) most of

the altitude band 1.5-1.75 km has a base level of about 10 g or less of biomass. At 16:00 the higher altitudes are quite scattered with a low biomass, but at 16:30 whilst the Figure 5.15 d) still looks scattered, the volume is filling in at higher altitudes and subsequently and increase of biomass. At 17:00 the increase in biomass is shown at lower altitudes under 250 m and at 17:30 there is wide dispersal but more defined altitude gaps are appearing. The higher biomass values are at latitudes north of 51.70 and largely in the first 500 m of altitude. 18:00 is similar to 17:30 and there is further emphasis on the altitude, and slightly less volume covered. 18:30 there is a significant change, with good ground coverage of biomass below 250 m, there is a large altitude gap spanning around 0.25-1/1.25 km.The ground cover continues to increase until peaking at 18:45 (not shown) and by 18:50 it starts to decrease so at 19:00, Figure 5.15 i), the ground coverage is restricted to $-0.15 \leq \lambda \leq -0.05^{o}$, towards the corner of the graph there is still activity scattered over the altitudes, but by 19:20 the ground coverage has pretty much gone, there is less activity in the corner, but a consistent more defined band of around $10\,gkm^{-3}$ at approximately 1.75 km. These temporal changes are clearly captured in Figure 5.15, illustrating the dynamic patterns of flying ant activity throughout the afternoon.

Figure 5.16 presents a three-dimensional plot depicting the number of ants per cubic kilometre within the restricted region defined by $52.0 <= \phi <= 52.6$, $-1 <= \lambda <= -0.5$ a subsection from Figure 5.12. This time series illustrates the diurnal variation in ant number density, with values rising and falling from the early morning through the late afternoon of the 9th of July 2021. Figure 5.16 is a focused subset of the broader PPI plot shown in Figure 5.12, which captures the overall spatial distribution of insects on Flying Ant Day.

With the CS data, radar columns can be isolated over these regions to look at the dynamics of activity. Figure 5.18 displays the time series of insect activity within a 5 km column centered on the postcode (NW7) of a CS survey respondent. The centroid of the postcode, which covers an area of $12.3\,km^2$, was used as the reference location for analysis. According to the radar data, peak activity in this column occurred at 10:00. However, the CS respondent first observed ants, both on the ground and in flight, at 15:45, with activity lasting approximately 2–5 hours.

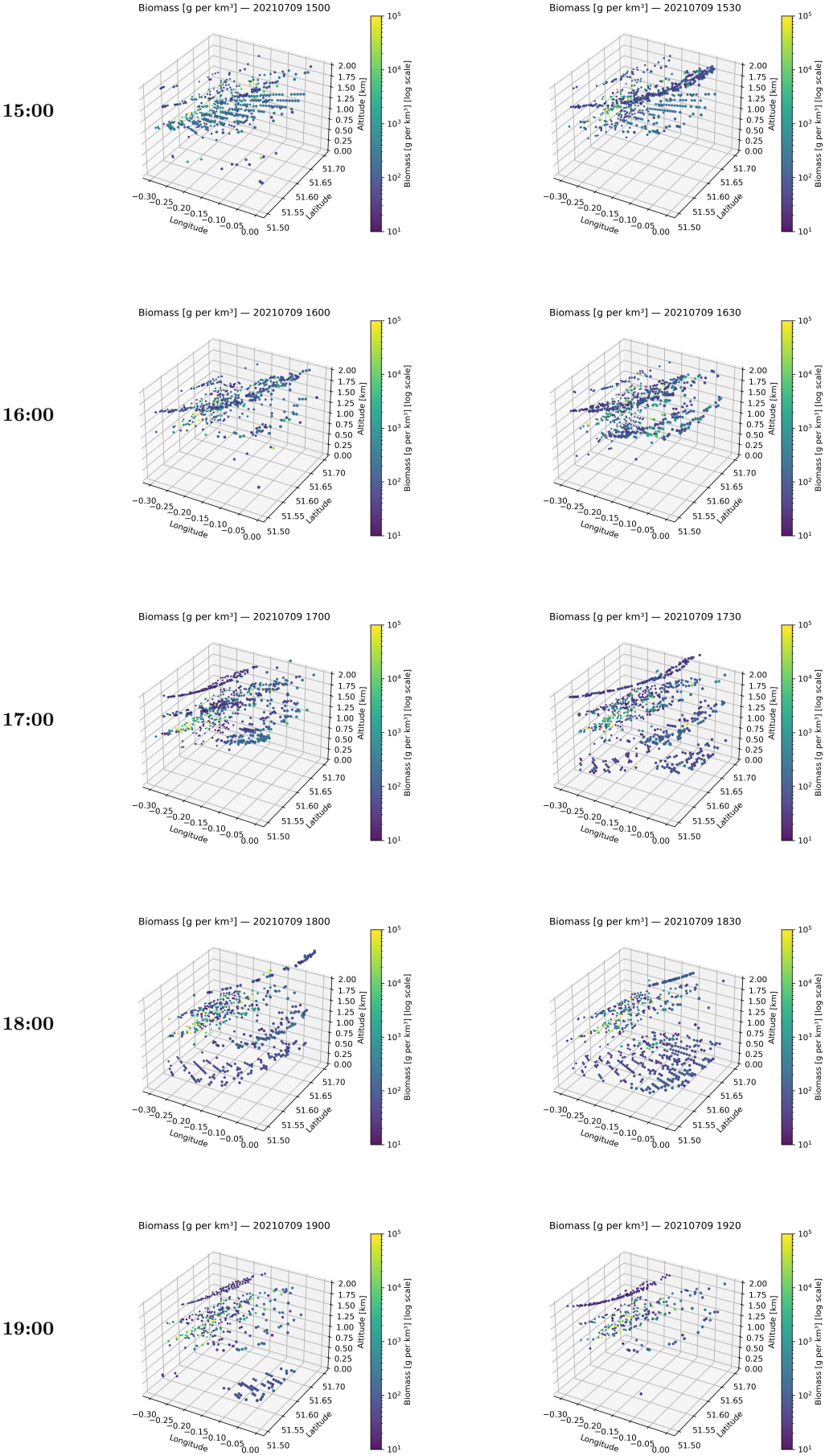

Figure 5.15: Cluster 3 from Chenies Radar on 9th July 2021, Biomass

Source	Mean	Median	LQ	UQ	Min	Max	Voxel Count
Chenies - Overall	1973	80	37	214	3	522175	39759
Chenies - Day (0500–2100)	1512	83	40	200	3	395788	32288
Chenies - Night	3963	64	27	439	3	522175	7471
Thurnham - Overall	8681	94	36	490	2	979150	65122
Thurnham - Day (0500–2100)	8105	92	37	410	2	979150	46944
Thurnham - Night	10168	99	34	712	3	836124	18178
Combined Overall	6722	93	38	588	-	-	101903
Combine Day (0500–2100)	6012	91	40	530	-	-	76631
Combined Night	8165	97	33	706	-	-	25272

Table 5.2: Biomass (grams) distribution between radars and combination for area Latitude Limits (51.5^o, 51.7^o), Longitude Limits (0^o, 0.25^o) for 9th of July 2021.

The radar data indicates that the highest density of insect activity was observed at the 1 km altitude band, with lower densities detected closer to the surface. Notably, despite the postcode centroid being only 22 km from the radar, a clear discrepancy exists between the timing and nature of radar-detected and ground-based observations.

The column of 5 km, is much larger than the W9 postcode area of $1.9\,km^2$. Figure 5.19 shows the activity does not exceed 2 km over the whole day. There is an increase in ground activity at 10:00 which spreads out and increases in intensity by 12:00, but by 14:00, majority is further aloft and overall there is less volume with activity, there is a spatial increase and intensity increase at 16:00 very little changes at 18:00 at 20:00 the space between active voxels increases and at 22:00 the dispersal is increased and the volume covered is less.

For the postcode SE15, the area is $5.9\,km^2$ which is similar to the column, however the activity is largely isolate to North of 51.48^o and West of -0.04^o. The two notable exceptions are at 12:00 and 16:00 where there is low density, but increased volume of ants spatially. The CS report, noted only a few ants “Between 10 and 30”, both on the ground and in-flight from 15:30 for 1-2 hours, which although could correspond with the radar data, it is not conclusive. There is a column of radar activity up to 2.5 km throughout the the time period largely at the corner of the plot in Figure 5.20.

These column plots highlight how each method captures different aspects of ant emergence and dispersal, underscoring the value of integrating both remote sensing and citizen science data to fully characterize these events.

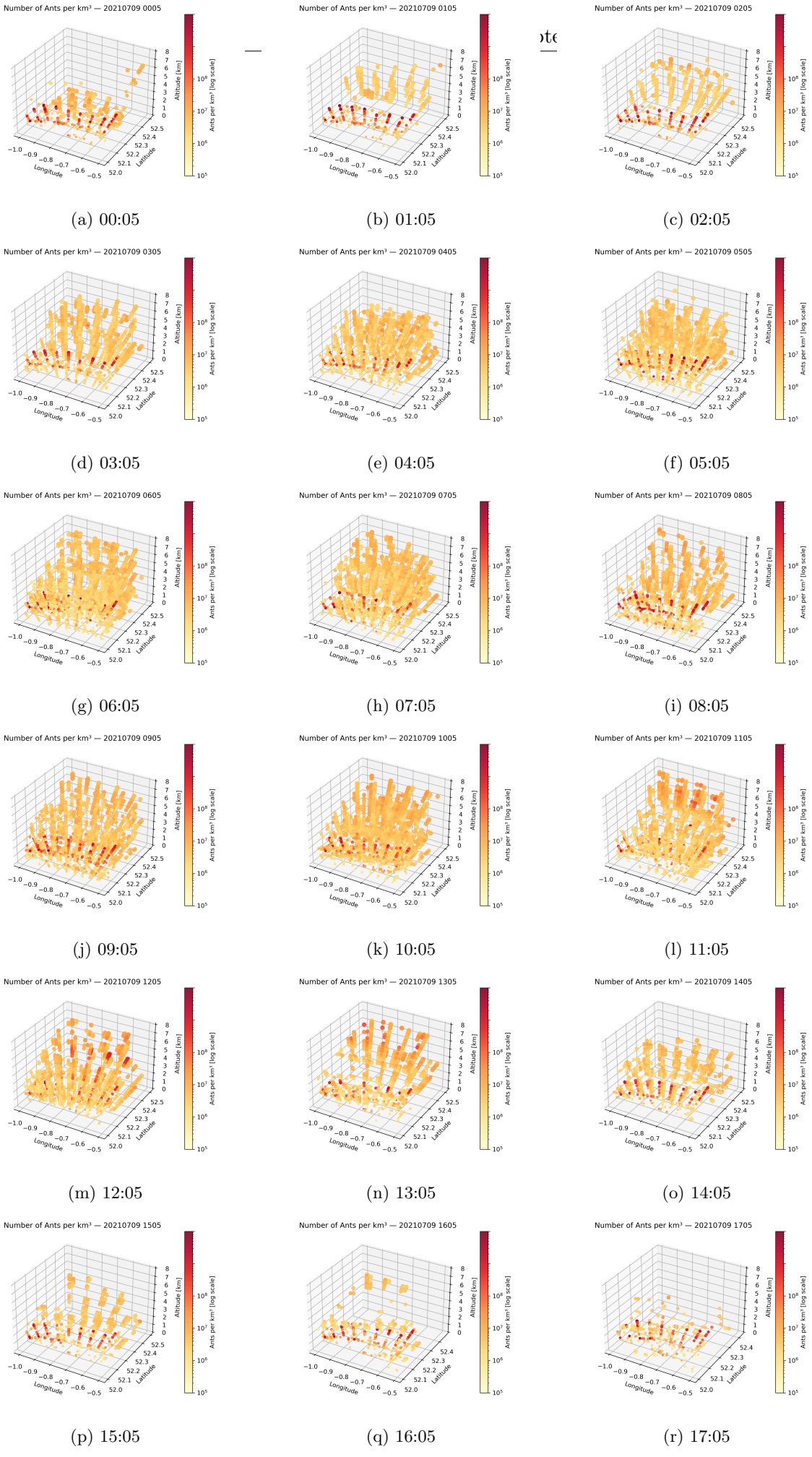

(a) 00:05 (b) 01:05 (c) 02:05

(d) 03:05 (e) 04:05 (f) 05:05

(g) 06:05 (h) 07:05 (i) 08:05

(j) 09:05 (k) 10:05 (l) 11:05

(m) 12:05 (n) 13:05 (o) 14:05

(p) 15:05 (q) 16:05 (r) 17:05

Figure 5.16: Cluster 6 from Chenies Radar on 9th July 2021, Number of Ants per km^3.

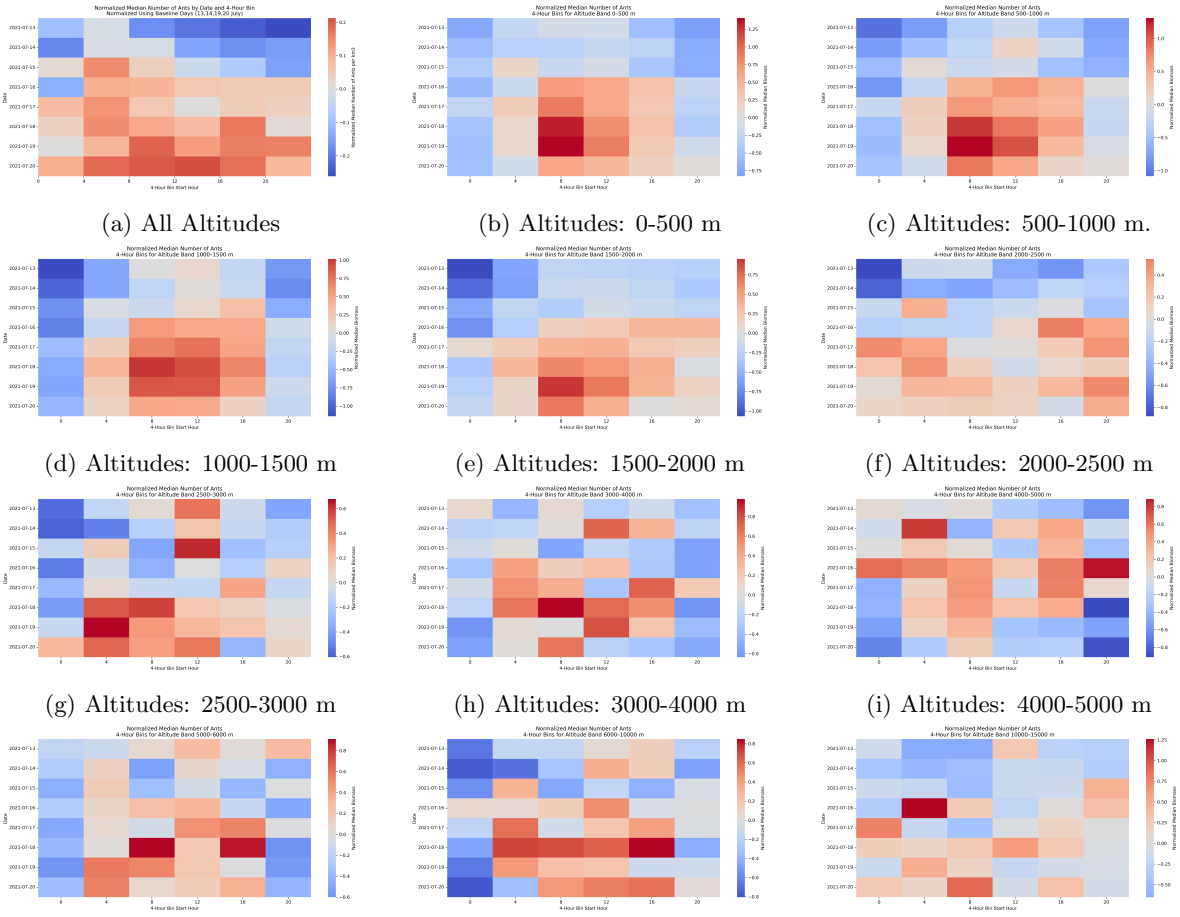

(a) All Altitudes

(b) Altitudes: 0-500 m

(c) Altitudes: 500-1000 m.

(d) Altitudes: 1000-1500 m

(e) Altitudes: 1500-2000 m

(f) Altitudes: 2000-2500 m

(g) Altitudes: 2500-3000 m

(h) Altitudes: 3000-4000 m

(i) Altitudes: 4000-5000 m

(j) Altitudes: 5000-6000 m

(k) Altitudes: 6000-10000 m

(l) Altitudes: 10000-15000 m

Figure 5.17: Heatmap across all radars at different altitude bands for the period of 13-20 July 2021, to identify anomalies of activity over the 4 hourly time periods.

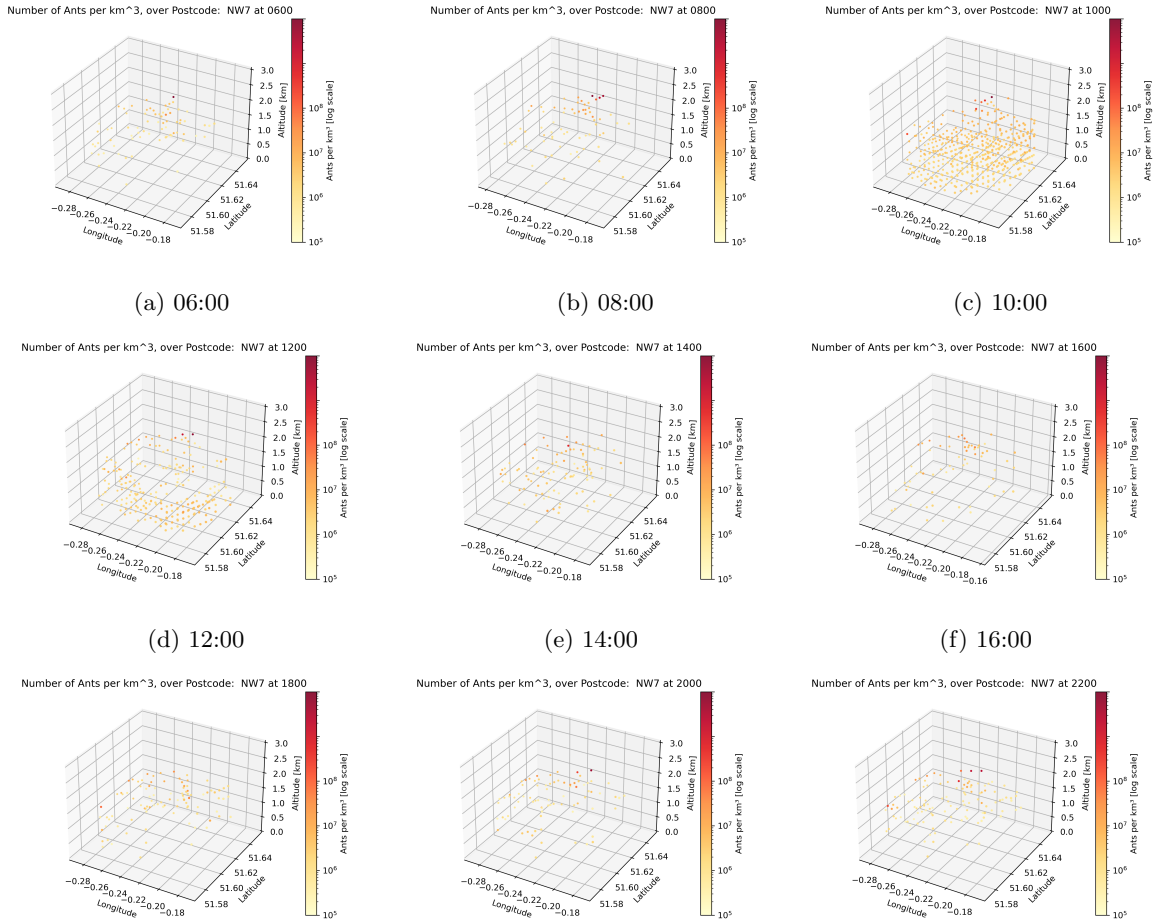

(a) 06:00 (b) 08:00 (c) 10:00

(d) 12:00 (e) 14:00 (f) 16:00

(g) 18:00 (h) 20:00 (i) 22:00

Figure 5.18: Column of 5 km centered around NW7 postcode from CS Data centroid with Number Density of Ants from Radar: Chenies on 9th July 2021.

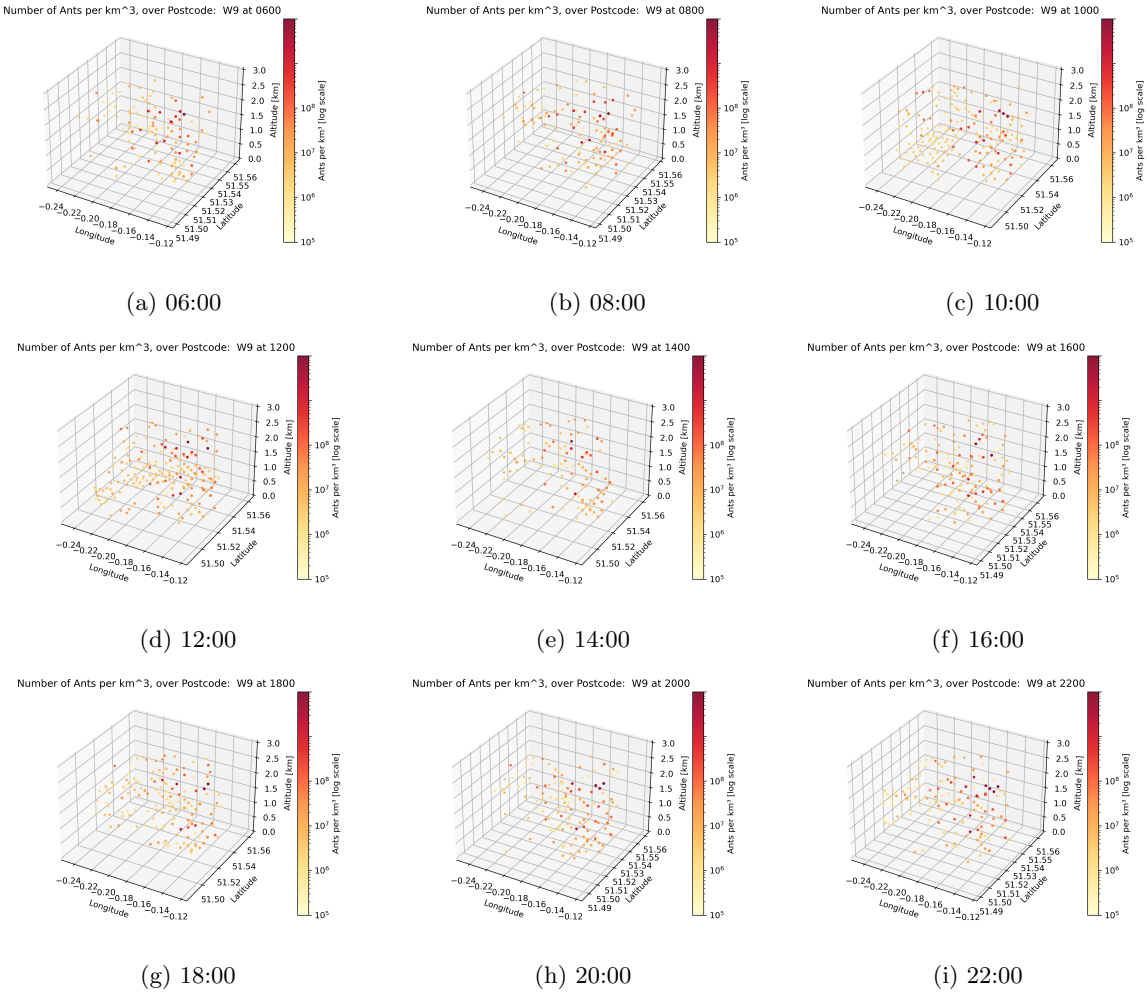

(a) 06:00 (b) 08:00 (c) 10:00

(d) 12:00 (e) 14:00 (f) 16:00

(g) 18:00 (h) 20:00 (i) 22:00

Figure 5.19: Column of 5 km centered around W9 postcode from CS Data centroid with Number Density of Ants from Radar: Chenies on 9th July 2021.

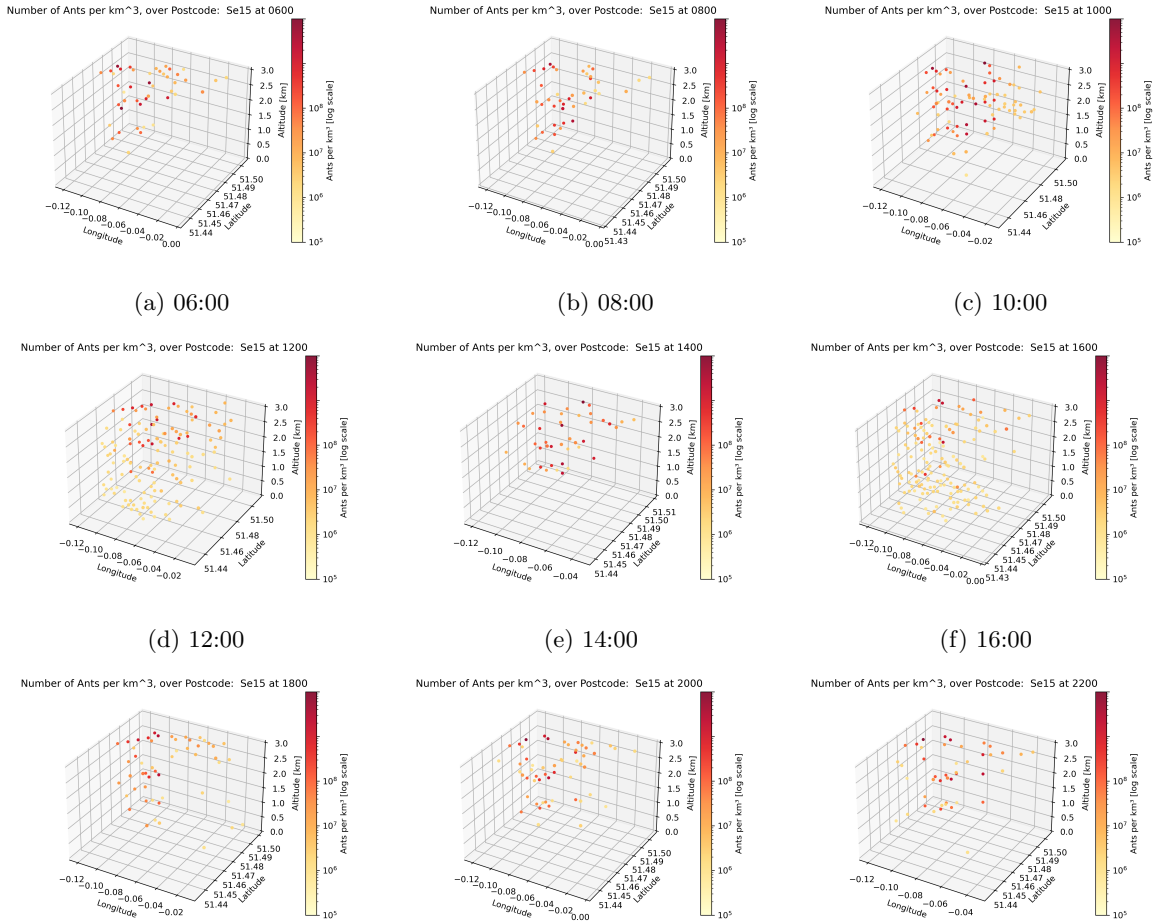

(a) 06:00 (b) 08:00 (c) 10:00

(d) 12:00 (e) 14:00 (f) 16:00

(g) 18:00 (h) 20:00 (i) 22:00

Figure 5.20: Column of 5 km centered around SE15 postcode from CS Data centroid with Number Density of Ants from Radar: Chenies on 9th July 2021.

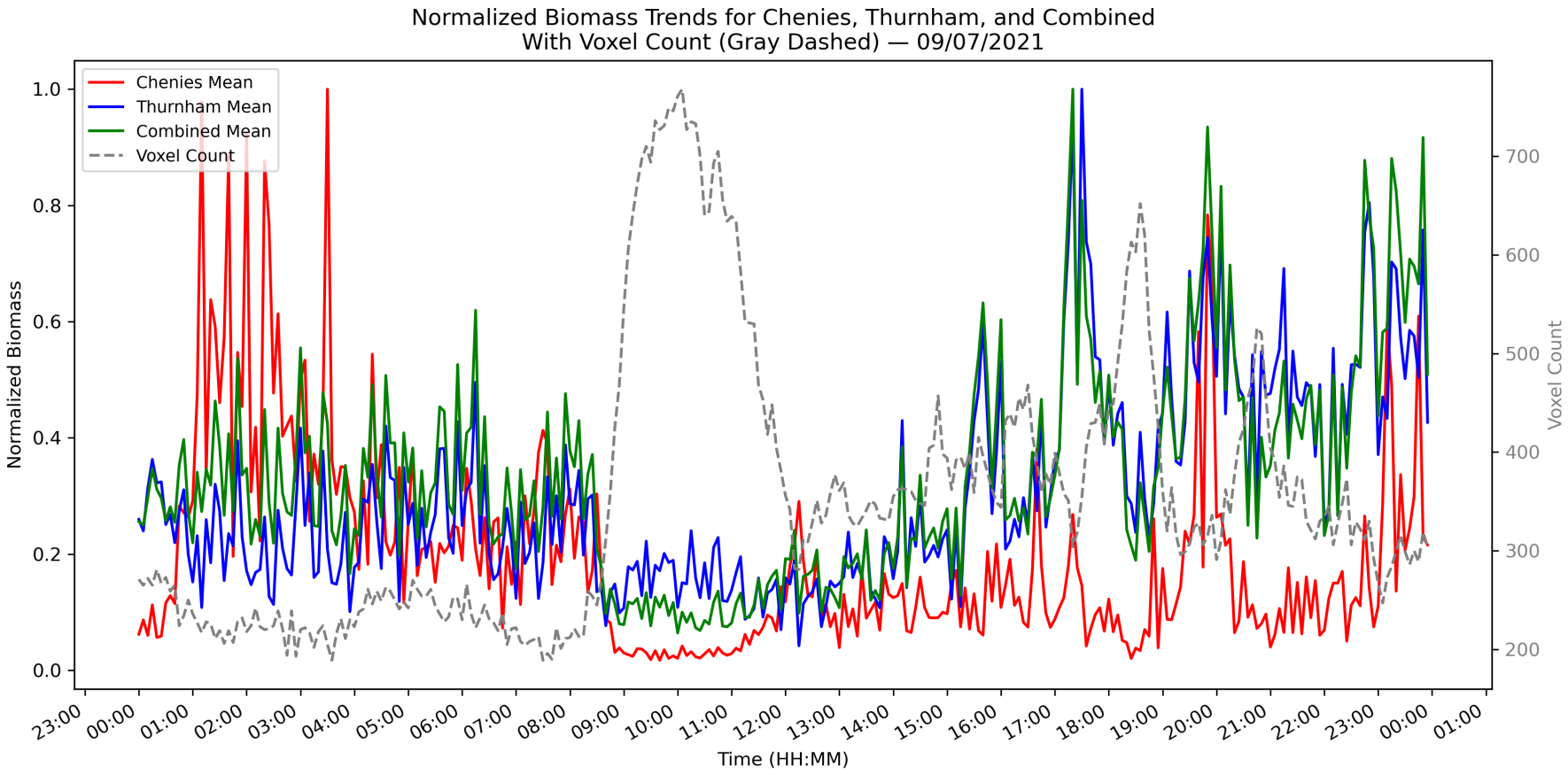

Figure 5.21: Normalised Biomass for Chenies and Thurnham, with number of voxels of activity for 9th July 2021.

Figure 5.21 shows the normalized biomass for each radar and the combination; The y2 axis shows the number of voxels within the defined area of Figure 5.22, that have insect activity. In Figure 5.21, the normalized mean biomass is depicted for Chenies in red, Thurnham in blue and the weighted (by volume) collocated voxels in green. Generally the two radars show the same trends with a few notable exceptions. The first few hours Chenies has greater biomass; 04:00-08:00 the two radars are consistent in quantity and trends. The period from 09:00-11:00 shows a high number of voxels with activity but overall very low biomass and using Figure 5.22(e) and 5.22(f) this is demonstrated with greater clarity. For most of the day Thurnham shows greater biomass than Chenies. Thurnham shows biomass peaks at approximately 15:00 and 17:30, this latter peak shows a marked difference from Chenies, these features can be examined more closely in Figure 5.22.

Figure 5.22 displays radar voxels from the Chenies and Thurnham UKMO WSRs, where there is collocation, a weighted (by volume) average is used, in this Figure the average is the median. The volume is also used to scale the voxels, most of the voxels are similar in size as this area is fairly equidistant from each of the two WSRs, however Chenies is marginally closer than Thurnham and thus has fractionally smaller voxels.

Table 5.2 summarises the daily biomass (g) for the area defined in Figure 5.22, with latitude limits (51.5^o, 51.7^o) and longitude limits (0^o, 0.25^o). Table 5.2 distinctly shows there is greater biomass at night than during the day, but greater dispersal during the day signified by the increase in voxel count. The majority of the voxels between radars are similar between location and times demonstrated by the consistency of minimum, maximum, medians and interquartile range. General behaviour can be captured by the median, but the mean has greater sensitivity to intense events.

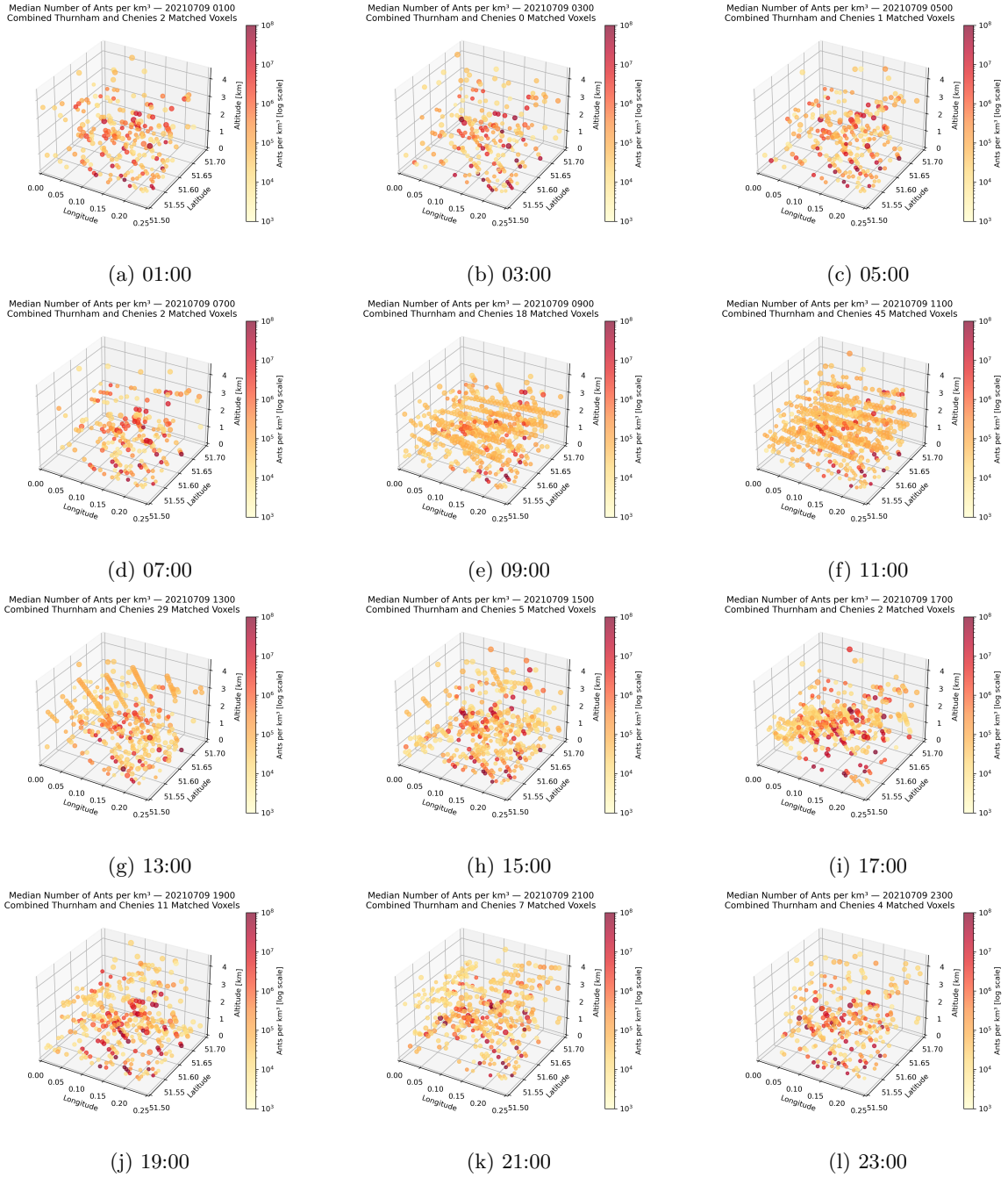

(a) 01:00 (b) 03:00 (c) 05:00

(d) 07:00 (e) 09:00 (f) 11:00

(g) 13:00 (h) 15:00 (i) 17:00

(j) 19:00 (k) 21:00 (l) 23:00

Figure 5.22: Median Number of Ants per cubic kilometre combined Chenies and Thurnham matching voxels for the 9th of July 2021.

5.4.2 13-20 July 2021

The next case study was for the time period 13th-20th July 2021, which contained FADs 15-18th July. Instead of focussing on a single radar, all the WSRs with data present are used for analysis.

Figure 5.23(a) shows that there is an increase across the board in activity from mid 16th July, and 00:00 to 08:00 on the 15th of July. Figure 5.17 shows a panel plot of heat maps, these are to highlight "anomalies". Figure 5.17 a) is of all the radars, and the whole radar volume, and it looks quite different from the other plots. It shows there was an increase in activity largely across all time bands predominantly on the 20th of July. On the 13th of July the last four hour block of the day from 20:00 to 00:00 there is significantly less activity. The 15th-18th of July are the FADs which is probably the expected increase, and whilst it shows some, its not as significant as 08:00-16:00 on the 20th of July. However, that is not the full picture, we could do this for each radar, but another way of looking it is through the altitude bands, which is shown in the rest of the Figure 5.17. For 0-500 m, we see see no significant differences from 20:00-04:00 but from 16th onwards there is an increase in activity most significant on the 18th and 19th of July, between 08:00 and 16:00. 2000-2500 m there is less significance but an increase is seen more between the 17th to the 19th of July. The highest band, is more randomly distributed. 6-10 km biggest difference is on the 18th of July 04:00-20:00 encompassing the entire daylight hours, but shows a strange decrease across most days between 00:00-04:00. 1000-1500 m altitude band shows a more expected pattern with increases on the 16th-19th of July between 08:00 and 20:00 with the largest middle of the day on the 18th of July and the 19th of July. When looking at individual radars, there were less areas of significance and more isolated to a specific time period. On the 20th of July there was rain over large parts of the UK, which was not filtered out.

Figure 5.23(b) presents the general diurnal cycle of aerial activity during the study period. A broad increase in activity is observed beginning on 17 July, peaking before a gradual decline starting mid-day on 19 July. However, beyond this overall trend, the data reveal more nuanced dynamics. Notably, each altitude band appears to maintain a distinct baseline level of activity, an observation consistent across all radars, as shown in Figure 5.9. The background purple shading in Figure 5.23(b) indicates nighttime periods, defined here as approximately 21:00 to 05:00. The diurnal cycles vary by altitude: activity in the 0–2.5 km and 2.5–3 km bands tends

to be more synchronized, whereas higher altitudes, particularly the 4–5 km and 5–6 km bands, exhibit markedly different temporal patterns.

The normalized total estimated biomass over the entire WSR volume shows most WSRs having similar levels or correlated peaks with each other, Drium al'Starraig was greatly outside of the normalised range with a dip three times as large on the 15th July, thus excluded from Figure 5.23(c). Figure 5.24 and 5.23(c) shows most WSRs have peaks on the 16th, the 17th or the 18th of July; The 19th of July sees elevation during the night and then dips back to 0 during the day and High Moorsley leading the way with another peak. Holehead, has a peak on 15th starting before sunrise, High Moorsley also has a peak overnight of the 16th to 17th of July. Drium al'Starraig has a wide peak of increased activity right the way through 17th to 19th of July. Castor bay increases slightly daytime on the 16th and 17th of July and then big rise on 18th of July which gradually drops in time, but steeply in biomass through the night into the 19th of July.

Figure 5.23(c) shows most of the radars with Drium al'Starraig excluded, the normalisation here was done for the 2 days before and after the FAD, the dotted lines represent the upper and lower limits for estimated biomass sex ratios. The trend is clearer in this graph with fewer extremes, with most WSRs having an increase on the 17th through to 18th of July which drops on the 19th of July. Some radars have a peak on the 15th of July 2021.

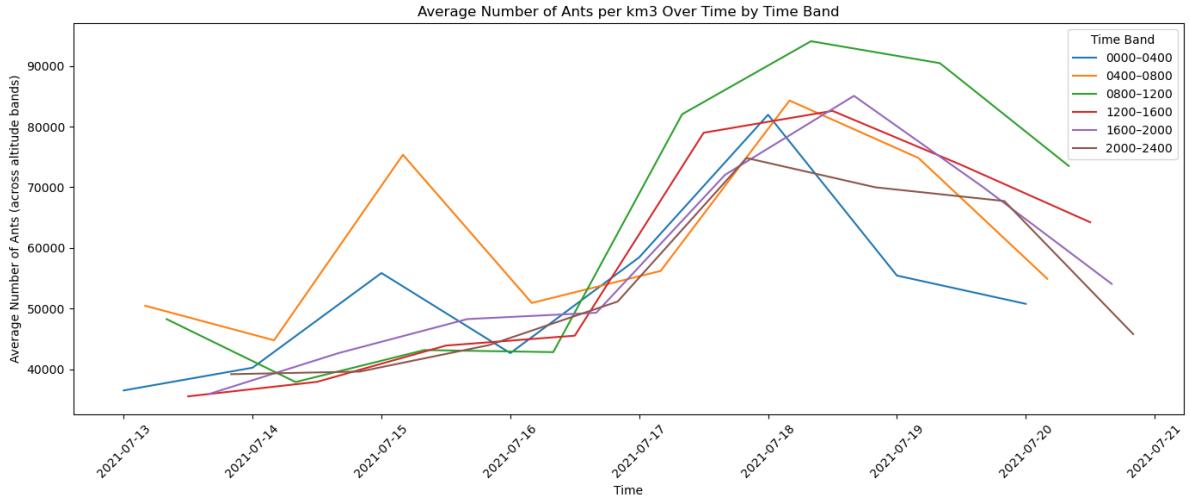

(a) Average Number of Ants per cubic metre over all radars for 4 hourly time bands for period 13th to the 20th of July 2021, FAD 15th to the 18th of July.

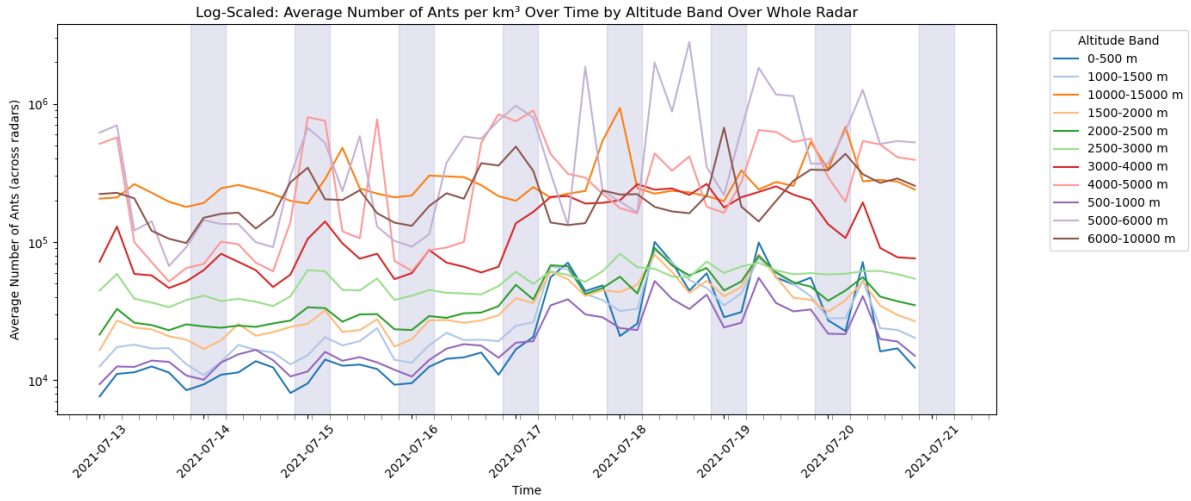

(b) Average Number of Ants per km^3 over all radars split per altitude band for period 13-20th July 2021, FAD 15-18th.

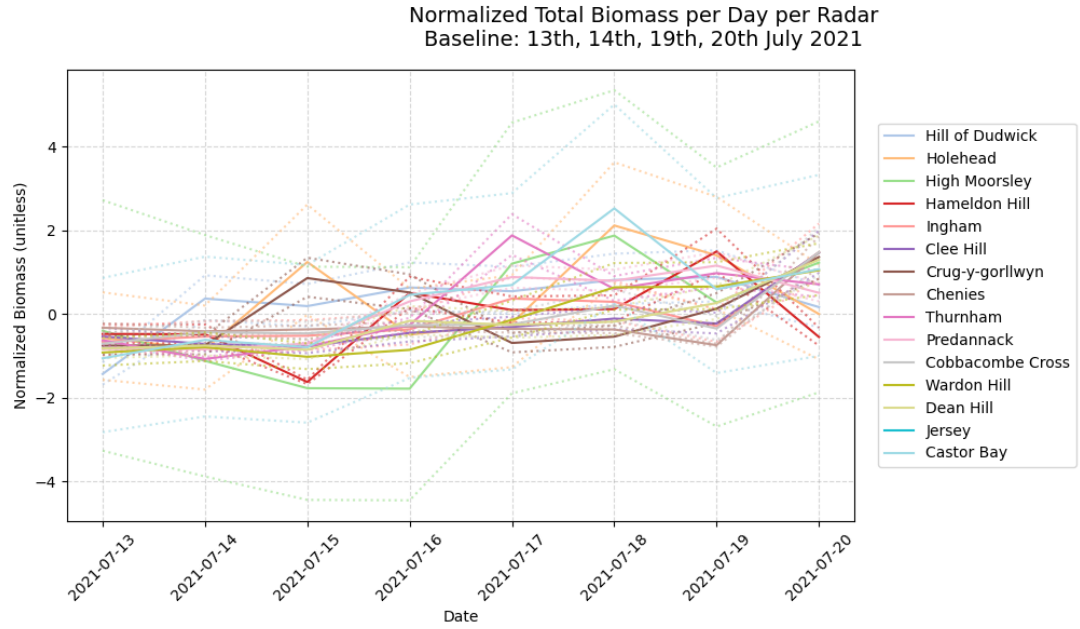

(c) Upper and lower limits are dashed lines, normalized biomass for period 13–20th July 2021, FAD 15–18th.

Figure 5.23: Summary plots of radar-derived ant activity and biomass across radars for 13–20th July 2021.

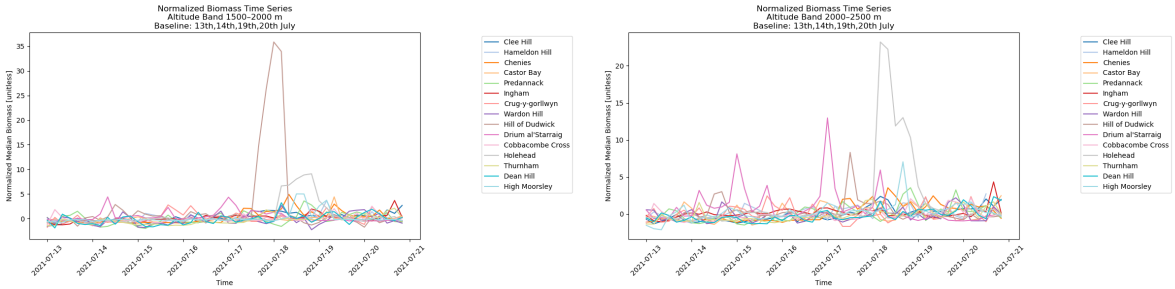

(a) Altitude: 1500-2000 m

(b) Altitude: 2000-2500 m

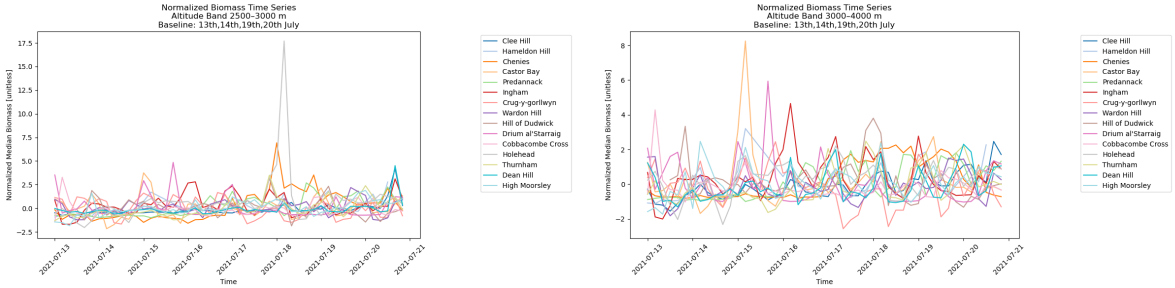

(c) Altitude: 2500-3000 m

(d) Altitude: 3000-4000 m

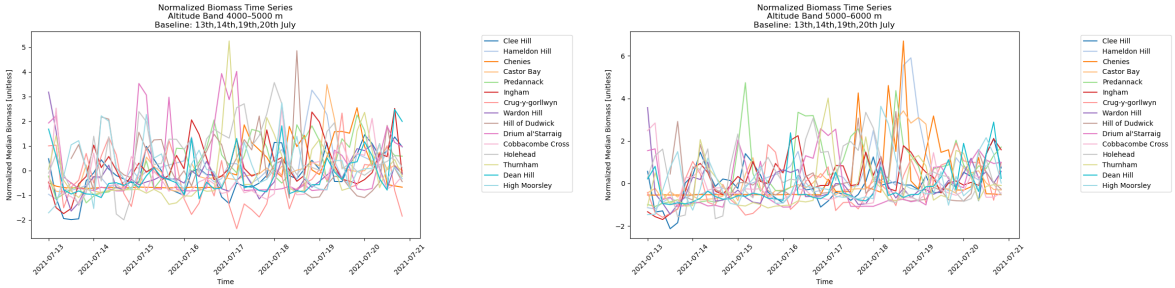

(e) Altitude: 4000-5000 m

(f) Altitude: 5000-6000 m

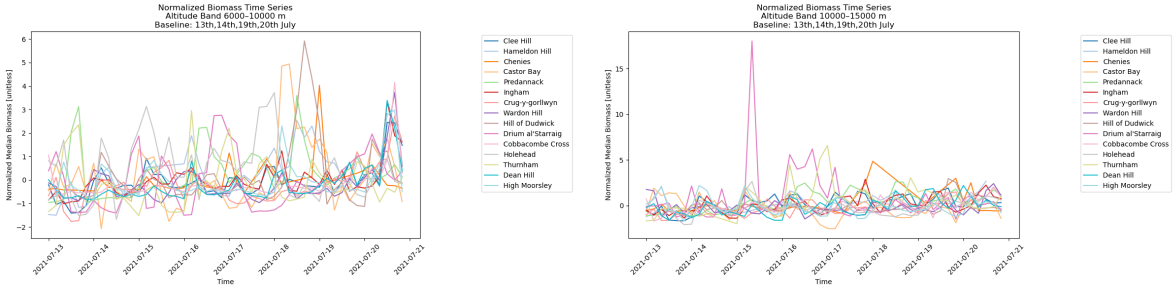

(g) Altitude: 6000-10000 m

(h) Altitude: 10000-15000 m

Figure 5.24: Timeseries Normalised Biomass 13-20th of July.

5.5 Conditions

This thesis is about testing the geodesic methods and precision and not about making informed analysis relating to environmental conditions and aeroecological behaviours, the following section is a very brief to show the potential of what incorporating these different disciplines could do. To investigate the environmental factors influencing Flying Ant Day events, 1 km HadUK-Grid data for minimum and maximum daily temperatures were extracted for each postcode corresponding to a CS Survey response. Data processing was restricted to days with recorded sightings of winged ants; days without observations were excluded. This approach was necessary due to the vast spatial coverage of the UK (over $240,000\,km^2$) and the temporal extent of the flying ant season (approximately four months), which would otherwise result in an unmanageable data volume with limited interpretative value for non-event days.

For days with positive CS reports, the minimum and maximum temperatures associated with each postcode (outcode) area were analysed. Winged ants were observed in areas with minimum temperatures as low as -1^oC and maximum temperatures up to 40^oC. Specifically for flying (alate) ants, their presence was recorded in outcode areas where minimum temperatures were above 3^oC.

Additional meteorological context was provided using the Met Office Daily Weather Reports (Met Office National Meteorological Library and Archive, 2021). Analysis of the synoptic conditions revealed that the persistence of high-pressure systems over the UK is strongly associated with multi-day Flying Ant Day events. However, high pressure was not a necessary or sufficient condition for single-day events, as such a relationship was not observed. With sustained high-pressure systems, the emergence of flying ants was guaranteed if the minimum number (5) of FADs (Hart et al., 2018) had already occurred, which suggests a quantitative limit of ants for each season.

A focused case study of the period 14–19th of July 2021, characterised by a sustained high-pressure system moving from the southwest, revealed a clear spatial and temporal progression of flying ant sightings. CS responses initially appeared in western regions and along a north-south axis, before spreading to cover much of the UK and eventually concentrating along the southern

and southeastern coastlines. During this period, daily minimum temperatures were generally above 10^{o}C, and maxima exceeded 20^{o}C. Wind gusts remained below 20 knots, and mean wind speeds were typically under 10 knots. Minimum grass temperatures below 7–8^{o}C appeared to be loosely associated with increased insect activity, as did total daily sunshine hours above 10. However, these relationships were positive but weak and not sufficient to predict emergence reliably.

The observed dispersal patterns, emergences occurring as broad spatial clusters, suggest that combining these observations with modelled or interpolated wind fields could yield further insights into the spread and movement of flying ant swarms. At this stage the only conclusions that can be drawn, is that there is no single environmental factor that can determine or predict the a Flying Ant Day emergence; but with experts and proper modelling this is an area of future work.

5.6 Summary

This chapter demonstrates the successful integration and application of the novel geodesic methodology and the simulation of the RCS of ants applicable for WSR observations to investigate a specific aeroecological phenomenon: the annual nuptial flights of ants in the UK. The primary goal was to illustrate the effectiveness and utility of the geodesic techniques rather than to draw definitive ecological conclusions. This is also the first time WSR have been used to systematically study FADs.

Analysis revealed that ant emergences occurred on at least five distinct days across July and August per year for all years study conducted. Using enhanced geodesic precision and data collocation from multiple WSRs, the following key insights into FADs were obtained:

- Quantified the biomass of ant emergences during FAD
- Determined aerial densities during FADs
- Identified the altitudinal ranges of ant emergences
- Improved temporal resolution of FAD activity patterns

CS observations provided complementary ground-based data but were subject to human observational biases and were spatially limited to ground level. In contrast, WSR provided observations beginning at approximately $100\,m$ altitude and extending upward, with volumes ranging from hundreds of cubic meters near the radar to cubic kilometers at greater ranges, at a temporal resolution of every 5 minutes. Significantly, WSR data indicated insect activity extending frequently up to between 4 and 5 km.

Comparison of traditional UKMO spherical refraction models with the novel geodesic method showed substantial altitude discrepancies. The geodesic approach provided more consistent altitude-density distributions, highlighting peak insect densities in the 3–4 km altitude band, whereas the UKMO model reported most densities inaccurately below $500\,m$. WSR observations also identified two daily peaks in ant activity, with significant variation at local scales, reflecting complex dynamics not captured by broader spatial analyses alone.

Detailed analyses at a high temporal resolution (every 5 minutes) highlighted insect densities between $10^3 - 10^8$ per cubic kilometre during intense emergences. Typical background densities ranged between $10^4 - 10^5$ of ants per cubic kilometre, with longerperiods of increased activity averaging hourly densities from $10^3 - 10^6$.

Biomass retrievals revealed considerable variability, with recorded biomass ranging dramatically across radar volumes, from as low as 50 kg to upwards of 500,000 kg, suggesting intrinsic geographical, systematic, or methodological biases. Within targeted smaller volumes $51.50^o \leq \phi \leq 51.7^o$, $0.00^o \leq \lambda \leq 0.25^o$, a $\sim 56\,km^2$, baseline biomass typically ranged around 5 kg, spiking to around 20 kg during significant emergences.

Collocating two WSR voxels and combining the data is a fairly novel concept, the code presented in Chapter 2, helps standardise this for potential a integration tool in the WSR community.

These results showcase how the improvement in geodesic precision significantly enhances the interpretive power of WSR data, particularly regarding the vertical distribution of FADs. The collocation methodology further enabled precise identification and analysis of specific emergence

events, providing a powerful framework for future explorations of insect behaviour dynamics linked to environmental conditions.

Chapter 6

Discussion and Conclusions

This thesis has woven together strands of several different disciplines, incorporating various techniques to produce a novel contribution to the field. Although the final weave is incomplete, as is typical in any body of scientific research, this chapter reflects on the journey undertaken, summarises the detailed insights gained, and identifies areas that remain open for further exploration.

6.1 Motivation

The primary motivation for this thesis arises from a fundamental limitation in how Weather Surveillance Radar (WSR) data are traditionally handled: observations are typically referenced relative to the radar location, rather than their true positions within the surveyed atmosphere. This issue is compounded by the fact that quantitative assessments of positional accuracy and associated uncertainties are generally absent in standard processing routines, especially when transforming radar data into various gridded coordinate systems. Given that WSR observations span large spatial scales, from tens of cubic metres up to kilometres, enhancing positional precision and rigorously quantifying uncertainty would significantly broaden the applicability of these observations. By designing and implementing a code toolkit intended for adoption by the broader radar community, this thesis not only addresses these gaps within the aeroecological research but also aims to influence standard processing practices, or at a minimum, prompt a re-examination of current approaches to locational positioning and accuracy.

This thesis does not attempt to comprehensively analyses or model all variables influencing radar observations or ant emergences. The literature review and preliminary exploration of refraction provided insights into the complexity of this topic, clearing indicating that a complete analysis would require an entire thesis in itself. Nevertheless, as demonstrated in Results Chapter 3, even modest refinements can significantly improve upon the flawed methodologies currently prevalent in standard WSR processing environments. A thorough modelling of environmental and conditions was beyond the scope of this work, although it could have provided deeper contextual detail for understanding the FAD conditions. Additionally, the constraints arising from limitations in the Citizen Science Survey and a scarcity of ground-based observations, meant that the ecosystem feedback mechanisms and the behavioural aspects of flying ants could not be extensively explored in this research, nor was it the primary focus.

6.2 Key Contributions

The research presented in this thesis significantly advances the positional accuracy of radar observations by integrating principles of geodesy and refining methods for addressing atmospheric refraction. Specifically, it demonstrates that the widely use $\frac{4}{3}R$ standard method employed in WSR systems, including by the UK Met Office (UKMO), is inadequate, and illustrates how even modest improvements, such as applying a standardised refractive index (N value), can yield meaningful enhancements. Discussions are already underway with the UKMO to implement this refined algorithm into operational use. Furthermore, the developed Coding Toolkit is a substantial contribution, providing geodesic coordinates for radar voxel boundaries and offering flexible matching criteria, including direct distance and altitude comparisons, the toolkit facilitates more accurate and versatile integration of radar data, beneficial across various scientific applications. The details of these contributions are outlined below.

6.2.1 Location of Radar Voxels

Accurate geodesic positioning (ϕ, λ, h) of radar voxels provides precise location data aligned with a global reference frame. The UKMO currently includes geodesic coordinates (latitude, ϕ and longitude, λ) within radar outputs, closely matching (within 0.01^o) those computed in Chapter 3. This consistency reinforces the validity of the methodology developed here and demonstrates its potential utility for radar systems that do not routinely provide geodesic co-

ordinates.

The methodology outlined in this thesis calculates voxel altitudes using fundamental geometric principles based on an ellipsoidal Earth model and aligns them with a universal reference frame. Crucially, it integrates a flexible template to account for atmospheric refraction, accommodating approximate, modelled, or observed refractive index values. By contrast, the UKMO standard practice of applying the refraction model assumes a simplified uniform spherical geometry over an ellipsoid, resulting in significant altitude overestimations.

Accurate altitude determination is critical for correctly collocating radar observations with biological phenomena. For instance, Figure 5.23(b), highlights how insect activity layers vary distinctly with altitude, underscoring the need for precision. Inaccuracies in altitude measurement can significantly impact the analysis and interpretation of insect clustering and their relationships to specific atmospheric and environmental conditions. For example, using the UKMO standard method at a range of $127\,km$ and an elevation angle of $\theta = 0.5^o$, altitudes span from 155 m to an unrealistic 6190 m, whereas geodesically calculated altitudes range accurately between 185 m and 2360 m.

Figure 5.6 further illustrates how different range rings at distinct altitude bands become meaningful only through accurate geodesic computation across multiple elevations. Elevation-based PPI plots can identify the spatial spread of insect activity, but applying precise altitude constraints significantly enhances the clarity of localised events. Since insect flight dynamics vary greatly, some insects are altitude-limited, while others rely on thermal uplifts for high ascension, clear altitude delineation allows aeroecologists not only to gain deeper insights into atmospheric biomass distribution but also refine insect identification based on radar-derived variables. Additionally, it supports more accurate exploration of relationships between insect behaviours and altitude, which vary according to atmospheric and environmental contexts.

6.2.2 Radar Cross Section (RCS) of an Ant

This is the first work to report the RCS of male and female ants. The striking difference between the RCS reported in Chapter 4 between Queen and males ants is analogous to comparing an emperor penguin to an ant. Given the typical nuptial flight sex ratio, approximately

20 Queens for every 80 males, this substantial disparity mean Queen ants overwhelmingly dominate the radar signal, while males become effectively undetectable. During nuptial flights, the Queen's abdomen reaches its maximum size, typically more than twice the size of the male's abdomen (Keller & Passera, 1990). The wings of alate ants were simulated to not hold a significant difference on the RCS but the limbs did. Additionally, the thorax of alate ants is notably dense (Matte & Billen, 2021). Future research might explore varying the dielectric properties and temperature of thoracic material, potentially yielding different RCS outcomes and refining the detection methodology.

6.2.3 Ant Species

Two notable temporal discrepancies were observed in the case studies presented in this thesis. Firstly, there was a mismatch between the timing of citizen science observations and radar detections, potentially resulting from altitude differences between ground-level observations and radar sampling. Secondly, emergence events frequently occurred as two distinct peaks: an initial smaller emergence followed later by a larger one. This may be attributed to species-specific differences in emergence timing, as different ant species typically initiate their nuptial flights at varying times (Talbot, 1945), with *Lasius niger* typically outnumbering *Lasius flavus* (Boomsma & Leusink, 1981). Additionally, environmental factors, particularly weather, can delay or interrupt emergences, causing variability in flight timing, sometimes by several hours or even a day. For example significant ant activity on the morning of the 17th July 2022 contradicted typical timing patterns documented in previous research. These observations underline the need for further detailed analysis and multidisciplinary collaboration, particularly involving ecologists, to refine interpretations and deepen the understanding of ant emergence dynamics.

6.3 Future Work

This thesis has revealed important new insights into the aerial behaviours of ants, particularly relating to the phenomenon known as Flying Ant Day (FAD). Nevertheless, fundamental questions remain unanswered, echoing uncertainties highlighted in earlier work by (Hart et al., 2018) and others: "Why do ants fly precisely when they do?" Addressing this core question will require a sustained and multidisciplinary research approach, leveraging the potential for the detailed tracking demonstrated in this thesis.

A logical next step is the establishment of comprehensive, long-term monitoring programs, extending and enhancing the methodologies pioneered by Hart's citizen science approach by (Hart et al., 2018). Such studies would ideally involve continous observations at multiple ant nest locations spanning diverse environmental conditions and habitats, repeated consistently over several consecutive years. Each observational site should be equipped with detailed local instrumentation, including weather stations for atmospheric conditions, and additional sensors for soil moisture, soil temperature, and radiation levels. High-resolution video monitoring at these nests would enable researchers to systematically document key behavioural milestones, such as the timing of hibernation initiation, emergence from hibernation, first appearance of wings on alates, and the precise timing and duration of nuptial flights.

Detailed records from these observational studies could facilitate the development of predictive criteria such as accumulated "degree days", which might refine our ability to forecast nuptial flight events based on localised environmental triggers. Alternatively, these data might reinforce existing hypotheses that emergence is governed by complex interactions among multiple environmental variables, rather than singular deterministic factors.

In Feitosa et al. (2016)'s study of neotropical ants in the Atlantic Forest, the malaise trap captures were generally limited to hourly counts between 07:00 and 18:00, Formicinae had a shorter periodicity than the CS reports saw in our study illustrated in Figure 5.4, with the Formicinae captured 12:00 and 18:00 peaking in mid-afternoon. Thus adding Malaise traps next to nest sites to be counted hourly within a time frame representative of the activity from the WSR and CS responses would be a complementary dataset to add in future studies.

Furthermore, advances in radar technology could considerably enhance our ability to track and interpret swarm behaviour. Specifically, deploying vertically-looking radars near ant nests may enable improved detection of initial emergence formation and ground-based dispersion patterns. Using a Range Height Indicator (RHI) scanning pattern would enable greater detail in the vertical resolution of the observations. Integrating ground-level observations with additional radar scanning strategies will significantly enhance our understanding of the temporal and spatial dynamics of emergent behaviour, allowing for more accurate interpretations of radar-derived

biomass estimates.

Additionally, moving beyond the single-insect RCS simulations employed in this thesis towards sophisticated, whole-swarm modelling represents another promising avenue. Detailed dielectric constant measurements under realistic flight temperature and radiation conditions, representative of actual WSR operating environments, would enhance the accuracy of radar observations of insect swarms. Conducting formal, controlled, laboratory experiments to accurately determine the dielectric properties of various insect species at relevant atmospheric temperatures and radiation frequencies could significantly improve radar-based insect monitoring techniques.

Finally, robust interdisciplinary collaboration should be pursued to integrate advanced atmospheric modelling, including wind profiles, atmospheric pressure variations, temperature gradients, humidity, and soil conditions, with biological data. Such integrated analyses could offer valuable insights into the specific environmental cues driving the emergence and flight behaviours of ants, ultimately refining our understanding of aeroecological processes and informing broader ecological studies.

6.4 Reflections on Interdisciplinarity

Typically, a PhD involves becoming an expert within a narrowly defined niche, requiring a clear element of novelty in the research. In contrast, the original saying "a jack of all trades" once served as a compliment, highlighting someone's ability to demonstrate proficiency across multiple disciplines. These two perspectives, narrow specialisation versus broad interdisciplinary knowledge, rarely intersect. However, this thesis explicitly argues for such an intersection, bring together insights and methodologies from Geodesy, Weather Surveillance Radar, Software Engineering, Radar Aeroecology, Citizen Science and studies of Flying Ant Day (FAD).

The author's primary expertise developed through this PhD lies in geodesy, with the coding toolkit at the heart of the thesis deeply grounded in geodetic mathematics. Software engineering provided the necessary framework to integrate and operationalise this toolkit, while atmospheric science enabled its practical application within radar and aeroecological contexts.

Consequently, radar aeroecology emerged as the overarching field that integrates these diverse elements.

Despite the broad interdisciplinary nature of this research, there are inherent limtations to a single researcher's knowledge. In this thesis, such limitations particularly arose in two areas: the behavioural ecology of ants, and detailed atmospheric/environmental processes. These specific knowledge gaps are addressed in recommendations for future research.

Additionally, interdisciplinary work creates inherent tensions and complexities when translating concepts and validating methods across disciplinary boundaries. For example, a planned results chapter on collocating radar and aircraft data was ultimately omitted due to challenges including the absence of radar calibration and difficulties clearly relating aircraft-radar collocation outcomes to the aeroecological narratives, that finally brought the PhD together.

Furthermore, validation approaches varied significantly across the interdisciplinary spectrum, encompassing technical, empirical and participatory methods. The citizen science dataset exemplifies these complexities: although it provided valuable insights and high participant engagement, the data quantity and spatial resolution, limited by postcode outcodes, constrained meaningful volumetric comparisons and detailed population assessments. This reflects broader methodological challenges inherent in comparing insect densities to radar beam volumes.

Finally, resource limitations and methodological complexities inevitably constrained the scope of crossing multiple disciplinary boundaries. Recognising and addressing these limitations provides a clear direction for refining future interdisciplinary research efforts.

6.5 Conclusions

This thesis demonstrates that incorporating geodesic positioning into radar data processing significantly enhances the spatial accuracy of radar voxels and their collocation with other instruments or datasets. When atmospheric refraction is also accounted for, particularly in altitude calculations, the resulting improvements enable high-fidelity analyses of the vertical airspace, an essential advancement for aeroecological applications.

WSR offers exceptional temporal and spatial coverage that far exceeds what is achievable using traditional field-based or manual observational methods. It allows for continuous monitoring over large areas and can capture dynamic atmospheric and biological processes with high frequency. However, radar systems are not without limitations. Chief among these constraints is taxonomic resolution, radar can detect the presence of biological targets but cannot easily differentiate species, and reduced sensitivity in the lowest atmospheric layers, particularly within the first few hundred meters above the ground, where many insect behaviours of ecological importance occur.

The refined geodesic precision significantly enhances the interpretive power WSR data for aeroecology, particularly regarding the vertical distribution of insect emergences. Accurate geolocation of radar volumes allows for finer vertical stratification of insect activity, revealing subtle yet ecologically significant differences in altitude-specific emergence behaviours (G. Hu et al., 2016; Chilson et al., 2012). For example, precise altitude measurements will enable researchers to distinguish distinct layers of insect activity related to meteorological phenomena, such as boundary layer dynamics and temperature inversions, which are critical determinants of insect dispersal and migration patterns (Drake and Reynolds, 2012; Bauer et al., 2017).

The implementation of the collocation methodology further enhances this analytical capability by aligning WSR observations with complementary environmental datasets, such as weather station data, satellite imagery, and citizen science reports. This spatial and temporal alignment permits robust identification and analysis of specific emergence events, creating opportunities to explore how environmental conditions like temperature gradients, humidity fluctuations, and wind patterns influence insect emergence dynamics (Stepanian et al., 2018b; Shamoun-Baranes et al., 2019). The combined precision and collocation methods thus provide a powerful framework for future explorations into insect behaviour, ecology, and their interactions with changing climate and environmental conditions (Nieminen et al., 2000; Westbrook and Eyster, 2017).

The citizen science (CS) dataset collected as part of this research, while subject to spatial and sampling biases, nonetheless provides valuable insight into the timing and distribution of Flying Ant Days (FAD). These datasets help identify regions of frequent emergence and fa-

cilitate focussed analysis around key radar sites. Despite inherent variability in public-sourced data, the consistency of responses across multiple events supports the utility of citizen science for guiding radar-based aeroecological studies.

A key contribution of this thesis is the quantification of RCS for both Queen and male ants, revealing a striking disparity in detectability, with Queens dominating the radar signal. Importantly, the study also demonstrates that the presences of wings in alate Hymenoptera does not significantly affect their RCS, contrary to some assumptions. This has meaningful implications for interpreting radar data and distinguishing between flying insect groups. Future work exploring the dielectric properties of other common insect taxa in the UK, such as aphids, will further support species differentiation and ecological inference from radar returns.

Moreover, the potential of Range Height Indicator (RHI) scans on FADs remains underexplored. These vertical profiles could reveal more nuanced radar signatures associated with ant swarms and help refine out understanding of their vertical distribution and movement patterns.

Taken together, this research establishes that radar, when paired with precise geospatial positioning and refined physical characterisation of insect targets, is a powerful tool for aeroecology. It not only enhances our ability to track and understand insect emergent behaviours such as FAD but also lays the groundwork for a broader integration of atmospheric radar in ecological and entomological studies.

Bibliography

Addison, F. I., Dally, T., Duncan, E. J., Rouse, J., Evans, W. L., Hassall, C., & Neely, R. R. (2022). Simulation of the Radar Cross Section of a Noctuid Moth. *Remote Sensing*, *14*(6), 1494. https://doi.org/10.3390/rs14061494

Addison, F. I. (2025, June). *Radarvoxelgeolocation* (Version v0.0.1). Zenodo. https://doi.org/10.5281/zenodo.15747473

AghaKouchak, A., Chiang, F., Huning, L. S., Love, C. A., Mallakpour, I., Mazdiyasni, O., Moftakhari, H., Papalexiou, S. M., Ragno, E., & Sadegh, M. (2020). Climate extremes and compound hazards in a warming world. *Annual Review of Earth and Planetary Sciences*, *48*(Volume 48, 2020), 519–548. https://doi.org/https://doi.org/10.1146/annurev-earth-071719-055228

American Meteorological Society. (n.d.). Effective Earth Radius.

American Meteorological Society. (2024a). Radar resolution. Retrieved June 25, 2025, from https://glossary.ametsoc.org/wiki/Radar_resolution

American Meteorological Society. (2024b, March). Radar Reflectivity [Glossary entry].

Andryieuski, A., Kuznetsova, S. M., Zhukovsky, S. V., Kivshar, Y. S., & Lavrinenko, A. V. (2015). Water: Promising opportunities for tunable all-dielectric electromagnetic metamaterials. *Scientific Reports*, *5*(1), 13535. https://doi.org/10.1038/srep13535

Anjita, N., & J, I. (2023). Leveraging weather radars for desert locust monitoring. *Remote Sensing Applications: Society and Environment*, *31*, 100983. https://doi.org/10.1016/j.rsase.2023.100983

Atlas, N. B. N. T. (2025). *Lasius niger (linnaeus, 1758)*. National Biodiversity Network Trust Atlas. Retrieved May 14, 2025, from https://species.nbnatlas.org/species/NHMSYS0000873237

Bachmann, S., & Zrnic, D. (2007). Spectral Density of Polarimetric Variables Separating Biological Scatterers in the VAD Display. *Journal of Atmospheric and Oceanic Technology*, *24*(7), 1186–1198. https://doi.org/10.1175/JTECH2043.1

Baer, B. (2011). The copulation biology of ants (hymenoptera: Formicidae). *Myrmecological News*, *14*, 55–68. https://doi.org/10.25849/myrmecol.news_014:055

Bar-On, Y. M., Phillips, R., & Milo, R. (2018). The biomass distribution on Earth. *Proceedings of the National Academy of Sciences*, *115*(25), 6506–6511. https://doi.org/10.1073/pnas.1711842115

Bartomeus, I., Potts, S., Steffan-Dewenter, I., Vaissiere, B., Woyciechowski, M., Krewenka, K., Tscheulin, T., Roberts, S., Szentgyörgyi, H., Westphal, C., & Bommarco, R. (2014). Contribution of insect pollinators to crop yield and quality varies with agricultural intensification. *PeerJ*. https://doi.org/10.7717/peerj.328

Bauer, S., Chapman, J. W., Reynolds, D. R., Alves, J. A., Dokter, A. M., Menz, M. M. H., Sapir, N., Ciach, M., Pettersson, L. B., Kelly, J. F., Leijnse, H., & Shamoun-Baranes, J. (2017). From agricultural benefits to aviation safety: Realizing the potential of continent-wide radar networks. *BioScience*, *67*(10), 912–918. https://doi.org/10.1093/biosci/bix074

Bauer, S., Shamoun-Baranes, J., Nilsson, C., Farnsworth, A., Kelly, J. F., Reynolds, D. R., Dokter, A. M., Krauel, J. F., Petterson, L. B., Horton, K. G., & Chapman S Bauer, J. W. (2019). Ecography 861 The grand challenges of migration ecology that radar aeroecology can help answer. *Natural Resources Inst., Univ. of Greenwich*. https://doi.org/10.1111/ecog.04083

Bauer, S., Tielens, E. K., & Haest, B. (2024). Monitoring aerial insect biodiversity: A radar perspective. *Philosophical Transactions of the Royal Society B, Biological Sciences*. https://doi.org/https://doi.org/10.1098/rstb.2023.0113

Bean, B. R., & Thayer, G. D. (1959). Models of the Atmospheric Radio Refractive Index. *Proceedings of the IRE*, *47*(5), 740–755. https://doi.org/10.1109/JRPROC.1959.287242

Bell, J. R., Aralimarad, P., Lim, K. S., & Chapman, J. W. (2013). Predicting Insect Migration Density and Speed in the Daytime Convective Boundary Layer. *PLoS ONE*, *8*(1), 54202. https://doi.org/10.1371/journal.pone.0054202

Bell, J. R., Blumgart, D., & Shortall, C. R. (2020). Are insects declining and at what rate? an analysis of standardised, systematic catches of aphid and moth abundances across

great britain. *Insect Conservation and Diversity*, *13*(2), 115–126. https://doi.org/https://doi.org/10.1111/icad.12412

Bent, A. E. (1943). *Radar echoes from atmospheric phenomena* (tech. rep.). Massachusetts Institute of Technology. Radiation Laboratory.

Bessel, F. W. (1825). The calculation of longitude and latitude from geodesic measurements. *Astronomische Nachrichten*. https://doi.org/10.1002/asna.18260041601

Biological Records Centre. (2024). Asian Hornet Watch. Retrieved November 17, 2024, from https://www.brc.ac.uk/app/asian-hornet-watch

Blender Online Community. (n.d.). Blender - a 3D modelling and rendering package. Retrieved June 25, 2025, from http://www.blender.org

Boomsma, J. J., & A., G. (1990). Intraspecific variation in ant sex ratios and the trivers-hare hypothesis. *Evolution*, *44*(4), 1026–1034. https://doi.org/https://doi.org/10.2307/2409564

Boomsma, J. J., & Isaaks, J. A. (1985). Energy investment and respiration in queens and males of Lasius niger (Hymenoptera: Formicidae). *Behavioral Ecology and Sociobiology*, *18*(1), 19–27. https://doi.org/10.1007/BF00299234

Boomsma, J. J., & Leusink, A. (1981). Weather conditions during nuptial flights of four European ant species. *Oecologia*, *50*(2), 236–241. https://doi.org/10.1007/BF00348045

Brown, M. (2014). The Transmission Gallery: Stockland Hill.

Burkholder, E. F. (2008). *The 3-D Global Spatial Data Model: Foundation of the Spatial Data Infrastructure*. CRC Press, Taylor; Francis Group.

Campbell, J. W., & Hanula, J. L. (2007). Efficiency of malaise traps and colored pan traps for collecting flower visiting insects from three forested ecosystems. *Journal of Insect Conservation*, *11*. https://doi.org/10.1007/s10841-006-9055-4

Chapman, J. W., Drake, V. A., & Reynolds, D. R. (2011). Recent Insights from Radar Studies of Insect Flight. *Annual Review of Entomology*, *56*(1), 337–356. https://doi.org/10.1146/annurev-ento-120709-144820

Chapman, J. W., Reynolds, D. R., & Wilson, K. (2015). Long-range seasonal migration in insects: Mechanisms, evolutionary drivers and ecological consequences. *Ecology Letters*, *18*(3), 287–302. https://doi.org/https://doi.org/10.1111/ele.12407

Chapman, J., Smith, A., Woiwod, I., Reynolds, D., & Riley, J. (2002). Development of vertical-looking radar technology for monitoring insect migration. *Computers and Electronics*

in Agriculture, *35*(2), 95–110. https://doi.org/https://doi.org/10.1016/S0168-1699(02)00013-3

Chen, H., Li, X., Yu, W., Wang, J., Shi, Z., Xiong, C., & Yang, Q. (2020). Chitin/MoS2Nanosheet Dielectric Composite Films with Significantly Enhanced Discharge Energy Density and Efficiency. *Biomacromolecules*, *21*(7), 2929–2937. https://doi.org/10.1021/acs.biomac.0c00732

Chilson, P. B., Frick, W. F., Stepanian, P. M., Shipley, J. R., Kunz, T. H., & Kelly, J. F. (2012). Estimating animal densities in the aerosphere using weather radar: To z or not to z? *Ecosphere*, *3*(8), art72. https://doi.org/https://doi.org/10.1890/ES12-00027.1

Chilson, P. B., Stepanian, P. M., & Kelly, J. F. (2017). Radar Aeroecology. In P. B. Chilson, W. F. Frick, J. F. Kelly, & F. Liechti (Eds.), *Aeroecology* (pp. 277–309). Springer International Publishing. https://doi.org/10.1007/978-3-319-68576-2_12

Chowdhury, S., Dubey, V. K., Choudhury, S., Das, A., Jeengar, D., Sujatha, B., Kumar, A., Kumar, N., Semwal, A., & Kumar, V. (2023). Insects as bioindicator: A hidden gem for environmental monitoring. *Frontiers in Environmental Science*, *11*. https://doi.org/10.3389/fenvs.2023.1146052

Cui, K., Hu, C., Wang, R., Li, S., Wu, D., & Ma, S. (2019). Quantifying insect migration across Bohai strait using weather radar. *The Journal of Engineering*, *2019*(19), 6095–6098. https://doi.org/10.1049/joe.2019.0197

Cunningham-Eurich, I., Kontou, D., Yordanova, M., Maeda-Obregon, A., Favreau, E., Wang, J., Hart, A. G., & Sumner, S. (2023). Using citizen science data to assess the population genetic structure of the common yellowjacket wasp, vespula vulgaris. *Insect Molecular Biology*, *32*(6), 634–647. https://doi.org/https://doi.org/10.1111/imb.12862

Dalton, D., Berger, V., Kirchmeir, H., Adams, V., Botha, J., Halloy, S., Hart, R., Svara, V., Torres Ribeiro, K., Chaudhary, S., & Jungmeier, M. (2024). A framework for monitoring biodiversity in protected areas and other effective area-based conservation measures : Concepts, methods and technologies. *Protected Area Technical Report Series*. https://doi.org/https://doi.org/10.2305/HRAP7908

Dalton, R. M., Underwood, N. C., Inouye, D. W., Soulé, M. E., & Inouye, B. D. (2023). Long-term declines in insect abundance and biomass in a subalpine habitat. *Ecosphere*, *14*(8), e4620. https://doi.org/https://doi.org/10.1002/ecs2.4620

Darlington, T., Edwards, R. A., Lissaman, V. A., Riley, R., & Sugier, J. (2016). *Designing an operational C-band radar to realise the benefits of dual-polarization* (tech. rep.). Met Office. https://www.metoffice.gov.uk/binaries/content/assets/mohippo/pdf/library/mo-technical-documents/designing_c_band_radar_2016.pdf

Darlington, T. (2015, March). *Development, evaluation and applications of the Cyclops-DP Weather Radar Processing system* [Doctoral dissertation, University of Bath]. moz-extension://fb1c357f-e9c5-462c-afab-1f3c899b7fc8/enhanced-reader.html?openApp&pdf=https%3A%2F%2Fpurehost.bath.ac.uk%2Fws%2Fportalfiles%2Fportal%2F187945432%2FThesisFinalForPrint.pdf

Deakin, R. E. (2009). THE NORMAL SECTION CURVE ON AN ELLIPSOID. http://www.mygeodesy.id.au/documents/Normal%20Section.pdf

Deakin, R. E. (2010). THE LOXODROME ON AN ELLIPSOID. http://www.mygeodesy.id.au/documents/Loxodrome%20on%20Ellipsoid.pdf

Didham, R. K., Basset, Y., Collins, C. M., Leather, S. R., Littlewood, N. A., Menz, M. H. M., Müller, J., Packer, L., Saunders, M. E., Schönrogge, K., Stewart, A. J. A., Yanoviak, S. P., & Hassall, C. (2020). Interpreting insect declines: Seven challenges and a way forward. *Insect Conservation and Diversity*, *13*(2), 103–114. https://doi.org/https://doi.org/10.1111/icad.12408

Dimensions. (n.d.). Black Garden Ant (Lasius Niger). Retrieved June 25, 2025, from https://www.dimensions.com/element/black-garden-ant-lasius-niger

Doerry, A. W. (2013). *Earth Curvature and Atmospheric Refraction Effects on Radar Signal Propagation* (tech. rep. No. January). Sandia National Laboratories. Albuquerque, New Mexico. http://prod.sandia.gov/techlib/access-control.cgi/2012/1210690.pdf

Dokter, A. M., Desmet, P., Spaaks, J. H., van Hoey, S., Veen, L., Verlinden, L., Nilsson, C., Haase, G., Leijnse, H., Farnsworth, A., Bouten, W., & Shamoun-Baranes, J. (2019). Biorad: Biological analysis and visualization of weather radar data. *Ecography*, *42*(5), 852–860. https://doi.org/https://doi.org/10.1111/ecog.04028

Doviak, R. J., & Zrnic, D. S. (1993). *Doppler Radar and Weather Observations* (Second). Elsevier. https://doi.org/10.1016/C2009-0-22358-0

Drake, V. A., Chapman, J. W., Lim, K. S., Reynolds, D. R., Riley, J. R., & Smith, A. D. (2017). Ventral-aspect radar cross sections and polarization patterns of insects at x band and

their relation to size and form. *International Journal of Remote Sensing*, *38*(18), 5022–5044. https://doi.org/10.1080/01431161.2017.1320453

Drake, V. A., & Reynolds, D. R. (2012). *Radar entomology: Observing insect flight and migration*. CABI. https://www.cabi.org/bookshop/book/9781845935566

Drake, V. A., Hao, Z., & Wang, H. (2024). Monitoring insect numbers and biodiversity with a vertical-beam entomological radar. *Philosophical Transactions of the Royal Society B, Biological Sciences*. https://doi.org/10.1098/rstb.2023.0117

English, S. (2019, August). Why we need to protect weather prediction from radio frequency interference. https://www.ecmwf.int/en/about/media-centre/science-blog/2019/why-we-need-protect-weather-prediction-radio-frequency

ENRAM. (2013). Home. Retrieved October 2, 2024, from https://www.enram.eu

Eschliman, C., & Horton, K. (2023, March). *A primer for using weather surveillance radar to study bird migration*. birdcast.info. Retrieved November 3, 2024, from https://birdcast.info/news/a-primer-for-using-weather-surveillance-radar-to-study-bird-migration/

EUMETSAT & University, H. (n.d.). Satellite Visible Archive. Retrieved June 25, 2025, from satellite/satellite-visible-archive.html

Fabry, F. (2015). *Radar Meteorology: Principles and Practice*. Cambridge University Press.

Fairman, J., Schultz, D., Kirshbaum, D., Gray, S., & Barrett, A. (2017). Climatology of size, shape, and intensity of precipitation features over great britain and ireland. *Journal of Hydrometeorology*, *18*. https://doi.org/10.1175/JHM-D-16-0222.1

Fedorov, A., Beichel, R., Kalpathy-Cramer, J., Finet, J., Fillion-Robin, J.-C., Pujol, S., Bauer, C., Jennings, D., Fennessy, F. M., Sonka, M., Buatti, J., Aylward, S. R., Miller, J. V., Pieper, S., & Kikinis, R. (2012). 3d slicer as an image computing platform for the quantitative imaging network. *Magnetic Resonance Imaging*, *30*(9), 1323–1341. https://doi.org/10.1016/j.mri.2012.05.001

Fedoseeva, E. B., & Grevtsova, N. A. (2020). Flight muscles degeneration, oogenesis and fat body in lasius niger and formica rufa queens (Hymenoptera: Formicidae). *Russian Entomological Journal*, *29*(4), 410–420. https://doi.org/10.15298/RUSENTJ.29.4.08

Feitosa, R. M., da Silva, R. R., & Aguiar, A. P. (2016). Diurnal flight periodicity of a neotropical ant assemblage (hymenoptera, formicidae) in the atlantic forest. *Revista Brasileira de Entomologia*, *60*(3), 241–247. https://doi.org/https://doi.org/10.1016/j.rbe.2016.05.006

Fiolet, S. (2020). Black Ant Model. Retrieved June 25, 2025, from https://sketchfab.com/3d-models/black-ant-model-54db3a0ee3c947168c7f3755ca684217#download

Fischer, E. M., Sippel, S., & Knutti, R. (2021). Increasing probability of record-shattering climate extremes. *Nature Climate Change*, *11*, 689–695. https://doi.org/10.1038/s41558-021-01092-9

Fjerdingstad, E. J., Gertsch, P. J., & Keller, L. (2002). WHY DO SOME SOCIAL INSECT QUEENS MATE WITH SEVERAL MALES? TESTING THE SEX-RATIO MANIPULATION HYPOTHESIS IN LASIUS NIGER. *Evolution*, *56*(3), 553–562. https://doi.org/10.1554/0014-3820(2002)056[0553:WDSSIQ]2.0.CO;2

Fortson, L., Masters, K., Nichol, R., Borne, K., Edmondson, E., Lintott, C., Raddick, J., Schawinski, K., & Wallin, J. (2011). Galaxy zoo: Morphological classification and citizen science. *Advances in Machine Learning and Data Mining for Astronomy*. https://arxiv.org/abs/1104.5513

Fukushima, T. (2011). Precise and fast computation of a general incomplete elliptic integral of second kind by half and double argument transformations. *Journal of Computational and Applied Mathematics*, *235*(14), 4140–4148. https://doi.org/10.1016/j.cam.2011.03.004

Gabriel, C. (1996). *Compilation of the dielectric properties of body tissues at rf and microwave frequencies* (Technical Report No. AL/OE-TR-1996-0037). Occupational and Environmental Health Directorate, Radiofrequency Radiation Division, Brooks Air Force Base. Texas, USA.

Gamble, Gavin. (2020). Ant recording and identification. https://www.naturespot.org.uk/ant_recording_ID

Garratt, M., Breeze, T., Jenner, N., Polce, C., Biesmeijer, J., & Potts, S. (2014). Avoiding a bad apple: Insect pollination enhances fruit quality and economic value. *Agriculture, Ecosystems and Environment*, *184*, 34–40. https://doi.org/https://doi.org/10.1016/j.agee.2013.10.032

Garratt, M., Potts, S., Banks, G., Hawes, C., Breeze, T., O'Connor, R., & Carvell, C. (2019). Capacity and willingness of farmers and citizen scientists to monitor crop pollinators and pollination services. *Global Ecology and Conservation*, *20*, e00781. https://doi.org/https://doi.org/10.1016/j.gecco.2019.e00781

Gauthreaux, J., Sidney A. (1970). Weather Radar Quantification of Bird Migration. *BioScience*, *20*(1), 17–19. https://doi.org/10.2307/1294752

Gauthreaux, S., & Diehl, R. (2020). Discrimination of Biological Scatterers in Polarimetric Weather Radar Data: Opportunities and Challenges. *Remote Sensing*, *12*(3), 545. https://doi.org/10.3390/rs12030545

Goulson, D. (2019). *Insect declines and why they matter* (tech. rep.). The Wildlife Trusts. Suffolk Wildlife Trust. https://www.suffolkwildlifetrust.org/sites/default/files/2019-11/Insect%20declines_embargoed_version_PRINT%205.pdf

Grimaldi, D., & Engel, M. S. (2005). *Evolution of the insects*. Cambridge University Press.

Haering, E. A., & Whitmore, S. A. (1995). *FORTRAN program for analyzing ground-based radar data: Usage and derivations, version 6.2* (tech. rep.). NASA. https://www.researchgate.net/publication/24301905_FORTRAN_program_for_analyzing_ground-based_radar_data_Usage_and_derivations_version_62

Hallmann, C. A., Sorg, M., Jongejans, E., Siepel, H., Hofland, N., Schwan, H., Stenmans, W., Müller, A., Sumser, H., Horren, T., Goulson, D., & de Kroon, H. (2017). More than 75 percent decline over 27 years in total flying insect biomass in protected areas. *PLOS ONE*. https://doi.org/https://doi.org/10.1371/journal.pone.0185809

Hart, A. G., Hesselberg, T., Nesbit, R., & Goodenough, A. E. (2018). The spatial distribution and environmental triggers of ant mating flights: using citizen-science data to reveal national patterns. *Ecography*, *41*(6), 877–888. https://doi.org/10.1111/ecog.03140

Helms, J. (2017). The flight ecology of ants (hymenoptera: Formicidae). *Myrmecological News*, *26*.

Helms IV, J. (2018). The flight ecology of ants (hymenoptera: Formicidae). *Myrmecological News*, *26*, 19–30. https://doi.org/10.25849/myrmecol.news_026:019

Hill, A. P., Prince, P., Piña Covarrubias, E., Doncaster, C. P., Snaddon, J. L., & Rogers, A. (2018). Audiomoth: Evaluation of a smart open acoustic device for monitoring biodiversity and the environment. *Methods in Ecology and Evolution*, *9*(5), 1199–1211. https://doi.org/https://doi.org/10.1111/2041-210X.12955

Ho, E. K. H., & Frederickson, M. E. (2014). Alate susceptibility in ants. *Ecology and Evolution*, *4*(22), 4209–4219. https://doi.org/10.1002/ece3.1291

Hobbs, S., & Aldhous, A. (2006). Insect ventral radar cross-section polarisation dependence measurements for radar entomology. *IEE Proceedings - Radar, Sonar and Navigation*, *153*(6), 502. https://doi.org/10.1049/ip-rsn:20060019

Hu, G., Lim, K. S., Horvitz, N., Clark, S. J., Reynolds, D. R., Sapir, N., & Chapman, J. W. (2016). Mass seasonal bioflows of high-flying insect migrants. *Science*, *354*(6319), 1584–1587. https://doi.org/10.1126/science.aah4379

Hu, Y., Limaye, A., & Lu, J. (2020). A spark of 3d revisualization: New method for re-exploring segmented data. *bioRxiv*. https://doi.org/10.1101/2020.08.01.222869

Information Technologies in Society, ITIS Foundation. (2024, June). Tissue Properties Database, Version 4.2: Dielectric Properties. https://doi.org/10.13099/VIP21000-04-2

International Association of Oil and Gas Producers. (2023). Wgs 84 – epsg:4326 [EPSG Geodetic Parameter Dataset, Version 10.086]. *EPSG Registry*.

IUCN. (2022). The IUCN Red List of Threatened Species. Retrieved June 25, 2025, from https://www.iucnredlist.org

Jallad, M., Mintchev, N., Pietrostefani, E., Daher, M., & Moore, H. L. (2022). Citizen social science and pathways to prosperity: Co-designing research and impact in beirut, lebanon. *International Journal of Social Research Methodology*, *25*(6), 769–782. https://doi.org/10.1080/13645579.2021.1942664

Janet, C. (1906). *Remplacement des muscles vibrateurs du vol par des colonnes d'adipocytes, chez les fourmis, apres le vol nuptial*. Ducourtieux. https://books.google.co.uk/books?id=-I0Z0AEACAAJ

Jemielity, S., Chapuisat, M., Parker, J. D., & Keller, L. (2005). Long live the queen: Studying aging in social insects [Epub 2005 Dec 31]. *Age (Dordrecht, Netherlands)*, *27*(3), 241–248. https://doi.org/10.1007/s11357-005-2916-z

Karney, C. F. F. (2022). GeographicLib 2.0. Retrieved June 25, 2025, from https://geographiclib.sourceforge.io/C++/2.3

Karney, C. F. F. (2011). *Geodesics on an ellipsoid of revolution* (tech. rep.). MIT. http://geographiclib.sourceforge.net/geod.html

Karney, C. F. F. (2013). Algorithms for geodesics. *Journal of Geodesy*, *87*(1), 43–55. http://geographiclib.sourceforge.net/geod.html

Keller, L., & Passera, L. (1990). Fecundity of Ant Queens in Relation to their Age and the Mode of Colony Founding. *Insectes Sociaux*, *37*(2), 116–130. https://doi.org/10.1136/bjo.35.5.315

Kilambi, A., Fabry, F., & Meunier, V. (2018). A Simple and Effective Method for Separating Meteorological from Nonmeteorological Targets Using Dual-Polarization Data. *Journal*

of Atmospheric and Oceanic Technology, *35*(7), 1415–1424. https://doi.org/10.1175/JTECH-D-17-0175.1

Knott, E. F., Schaeffer, J. F., & Tulley, M. T. (2004). *Radar cross section*. SciTech Publishing.

Kolundzija, B. M. (1999). Electromagnetic modeling of composite metallic and dielectric structures. *IEEE Transactions on Microwave Theory and Techniques*, *47*(7), 1021–1032. https://doi.org/10.1109/22.775434

Kolundzija, B., Ognjanovic, J., Sarkar, T., & Harrington, R. (1996). Wipl: A program for electromagnetic modeling of composite-wire and plate structures. *IEEE Antennas and Propagation Magazine*, *38*(1), 75–79.

Kolundzija, B. M., & Djordjevic, A. R. (2002). *Electromagnetic Modeling of Composite Metallic and Dielectric Structures*. Artech House.

Krakiwsky, E. J., & Thomson, D. B. (1974). *GEODETIC POSITION COMPUTATIONS* (tech. rep.). University of New Brunswick. http://www2.unb.ca/gge/Pubs/LN39.pdf

Kramer, B. H., Schaible, R., & Scheuerlein, A. (2016). Worker lifespan is an adaptive trait during colony establishment in the long-lived ant Lasius niger. *Experimental Gerontology*, *85*. https://doi.org/10.1016/j.exger.2016.09.008

Kumar, S. (2014). Study on history fitness and life cycle of drosophila (drosophila melanogaster). *Journal of Entomology and Zoology Studies*. https://www.entomoljournal.com/archives/2014/vol2issue1/PartB/8-6-28-155.pdf

Kunz, T. H., Gauthreaux, S. A., Hristov, N. I., Horn, J. W., Jones, G., Kalko, E. K. V., Larkin, R. P., McCracken, G. F., Swartz, S. M., Srygley, R. B., Dudley, R., Westbrook, J. K., & Wikelski, M. (2008). Aeroecology: Probing and modeling the aerosphere. *Integrative and Comparative Biology*, *48*, 1–11. https://doi.org/https://doi.org/10.1093/icb/icn037

Lack, D. (1959). Migration across the sea. *Ibis*, *101*(3-4), 374–399. https://doi.org/https://doi.org/10.1111/j.1474-919X.1959.tb02395.x

Lack, D., & Varley, G. (1945). Detection of birds by radar. *Nature*, *156*, 446. https://doi.org/https://doi.org/10.1038/156446a0

Lee, H., Romero, J., & Team, C. W. (2023). Climate change 2023: Synthesis report. contribution of working groups i, ii and iii to the sixth assessment report of the intergovernmental panel on climate change. *IPCC*, *6*, 184. https://doi.org/10.59327/IPCC/AR6-9789291691647

Lee, S.-J., & Yun, H.-S. (2025). Nationwide adjustment of unified geodetic control points for the modernization of south korea's spatial reference frame. *Applied Sciences*, *15*(10). https://doi.org/10.3390/app15105500

Li, H.-J., & Kiang, Y.-W. (2005). Radar and Inverse Scattering. In *The electrical engineering handbook* (pp. 671–690). Elsevier. https://doi.org/10.1016/B978-012170960-0/50047-5

Li Vigni, I., & Melati, M. R. (1999). Examples of seed dispersal by entomochory. *Acta Botanica Gallica*, *146*(2), 145–156. https://doi.org/10.1080/12538078.1999.10515813

Lin, L., Chen, X., Hu, R., & Zhao, Z. (2020). The Refraction Correction of Elevation Angle for the Mean Annual Global Reference Atmosphere. *International Journal of Antennas and Propagation*, *2020*, 1–7. https://doi.org/10.1155/2020/2438515

Lister, B. C., & Garcia, A. (2018). Climate-driven declines in arthropod abundance restructure a rainforest food web. *Proceedings of the National Academy of Sciences*, *115*(44), E10397–E10406. https://doi.org/10.1073/pnas.1722477115

Liveson, B. R. (2017). Population density of the United Kingdom. Retrieved June 25, 2025, from https://mapsontheweb.zoom-maps.com/post/167230291380/population-density-of-the-united-kingdom

Lukach, M., Dally, T., Evans, W., Hassall, C., Duncan, E. J., Bennett, L., Addison, F. I., Kunin, W. E., Chapman, J. W., & Neely, R. R. (2022). The development of an unsupervised hierarchical clustering analysis of dual-polarization weather surveillance radar observations to assess nocturnal insect abundance and diversity. *Remote Sensing in Ecology and Conservation*, *8*(5), 698–716. https://doi.org/10.1002/rse2.270

Martin, W. J., & Shapiro, A. (2007). Discrimination of bird and insect radar echoes in clear air using high-resolution radars. *Journal of Atmospheric and Oceanic Technology*, *24*(7), 1215–1230. https://doi.org/10.1175/JTECH2038.1

Matte, A., & Billen, J. (2021). Flight muscle histolysis in Lasius niger queens. *ASIAN MYRMECOLOGY*, *13*, 2021. https://doi.org/10.20362/am.013003

Melnikov, V. M., Istok, M. J., & Westbrook, J. K. (2015). Asymmetric radar echo patterns from insects. *Journal of Atmospheric and Oceanic Technology*, *32*(4), 659–674.

Merry, C. L., & Vanicek, P. (1974). *A METHOD FOR ASTRO-GRAVIMETRIC GEOID DETERMINATION* (tech. rep.). University of New Brunswick.

Met Eireann. (2023). Met Eireann is replacing the weather radar at Shannon Airport. Retrieved June 25, 2025, from https://www.met.ie/met-eireann-is-replacing-the-weather-radar-at-shannon-airport

Met Office. (n.d.). Rainfall Radar. Retrieved June 25, 2025, from https://www.metoffice.gov.uk/weather/learn-about/how-forecasts-are-made/observations/rainfall-radar#:~:text=Each%20radar%20provides%20data%20out,the%20British%20Isles%20is%20produced.

Met Office. (2023). *National meteorological library and archive factsheet 15 — weather radar*. Met Office. Retrieved June 2, 2024, from https://www.metoffice.gov.uk/binaries/content/assets/metofficegovuk/pdf/research/library-and-archive/library/publications/factsheets/factsheet_15-weather-radar-2020_2023.pdf

Met Office National Meteorological Library and Archive. (2021). Daily Weather Summary: July 2021.

Meteoworld. (2015, March). Meteorological Radar at the World Radiocommunication Conference. Retrieved June 25, 2025, from https://public.wmo.int/en/resources/meteoworld/meteorological-radar-world-radiocommunication-conference

Min, C., Chen, S., Gourley, J. J., Chen, H., Zhang, A., Huang, Y., & Huang, C. (2019). Coverage of China New Generation Weather Radar Network. *Advances in Meteorology*. https://doi.org/10.1155/2019/5789358

Mirkovic, D., Stepanian, P. M., Kelly, J. F., & Chilson, P. B. (2016). Electromagnetic model reliably predicts radar scattering characteristics of airborne organisms. *Scientific Reports*, *6*, 35637. https://doi.org/10.1038/srep35637

Mirkovic, D., Stepanian, P. M., Wainwright, C. E., Reynolds, D. R., & Menz, M. H. M. (2019). Characterizing animal anatomy and internal composition for electromagnetic modelling in radar entomology. *Remote Sensing in Ecology and Conservation*, *5*(2), 169–179. https://doi.org/10.1002/rse2.94

Montgomery, G. A., Belitz, M. W., Guralnick, R. P., & Tingley, M. W. (2021). Standards and best practices for monitoring and benchmarking insects. *Frontiers in Ecology and Evolution*, *8*. https://doi.org/10.3389/fevo.2020.579193

Morris, David. (2021, March). Hovering ship optical-illusion photograph [Courtesy of David Morris / APEX; featured in PEOPLE, Mar 5 2021]. Retrieved June 25, 2025, from https://www.bbc.co.uk/news/uk-england-cornwall-56286719

Murphy, A. M., Ryzhkov, A., & Zhang, P. (2020). Columnar Vertical Profile (CVP) Methodology for Validating Polarimetric Radar Retrievals in Ice Using In Situ Aircraft Measurements. *Journal of Atmospheric and Oceanic Technology*, *37*(9), 1623–1642. https://doi.org/10.1175/JTECH-D-20-0011.1

Mwansat, G., Turshak, L., & Okolie, M. (2015). Insects as important delicacy for birds: Expanding our knowledge of insect food ecology of birds in the tropics. *Journal of International Scientific Publications: Ecology and Safety*, *9*, 434–441. https://doi.org/10.:--

Nanding, N., & Rico-Ramirez, M. (2019, November). *Ict for smart water systems: Measurements and data science - precipitation measurement with weather radars*. Springer Nature. https://doi.org/10.1007/698_2019_404

Nature Spot. (n.d.). Small Black Ant - Lasius niger. Retrieved June 25, 2025, from https://www.naturespot.org.uk/species/small-black-ant

Neely III, R. R., Bennett, L., Blyth, A., Collier, C., Dufton, D., Groves, J., Walker, D., Walden, C., Bradford, J., Brooks, B., Addison, F. I., Nicol, J., & Pickering, B. (2018). The NCAS mobile dual-polarisation Doppler X-band weather radar (NXPol). *Atmospheric Measurement Techniques*, *11*(12), 6481–6494. https://doi.org/10.5194/amt-11-6481-2018

Nelson, S. G., Hartley, P. G., & Lawrence, K. C. (1998). RF and microwave dielectric properties of stored-grain insects and their implications for potential insect control. *Transactions of the American Society of Agricultural Engineers*, *41*(3), 685–692. https://doi.org/10.13031/2013.17194

Newtspeare, W. (2011). The earth's equatorial bulge. Retrieved June 25, 2025, from https://squishtheory.wordpress.com/the-earths-equatorial-bulge/

Nieminen, M., Leskinen, M., & Helenius, J. (2000). Doppler radar detection of exceptional mass-migration of aphids into finland. *International Journal of Biometeorology*, *44*(4), 172–181. https://doi.org/10.1007/s004840000064

Nilsson, C., Dokter, A. M., Verlinden, L., Shamoun-Baranes, J., Schmid, B., Desmet, P., Bauer, S., Chapman, J., Alves, J. A., Stepanian, P. M., Sapir, N., Wainwright, C., Boos, M., Gorska, A., Menz, M. H. M., Rodrigues, P., Leijnse, H., Zehtindjiev, P., Brabant, R., ... Liechti, F. (2019). Revealing patterns of nocturnal migration using the European weather radar network. *Ecography*, *42*(5), 876–886. https://doi.org/10.1111/ecog.04003

Noordijk, J., Morssinkhof, R., Boer, P., Schaffers, A. P., Heijerman, T., & Sykora, K. V. (2008). How ants find each other; temporal and spatial patterns in nuptial flights. *Insectes Sociaux*, *55*, 266–273. https://doi.org/https://doi.org/10.1007/s00040-008-1002-9

Norberg, U. M. (1986). Evolutionary convergence in foraging niche and flight morphology in insectivorous aerial-hawking birds and bats. *Ornis Scandinavica (Scandinavian Journal of Ornithology)*, *17*(3), 253–260. Retrieved October 2, 2024, from http://www.jstor.org/stable/3676835

Numpy. (n.d.). ArgPartition. Retrieved June 25, 2025, from https://numpy.org/doc/stable/reference/generated/numpy.argpartition.html%20https://github.com/numpy/numpy/blob/v1.25.0/numpy/core/fromnumeric.py#L779-L858

O'Connor, R. S., Kunin, W. E., Garratt, M. P. D., Potts, S. G., Roy, H. E., Andrews, C., Jones, C. M., Peyton, J. M., Savage, J., Harvey, M. C., Morris, R. K. A., Roberts, S. P. M., Wright, I., Vanbergen, A. J., & Carvell, C. (2019). Monitoring insect pollinators and flower visitation: The effectiveness and feasibility of different survey methods. *Methods in Ecology and Evolution*, *10*(12), 2129–2140. https://doi.org/https://doi.org/10.1111/2041-210X.13292

Ordnance Survey. (2020). *A Guide to Coordinate Systems in Great Britain*. www.os.uk

Ordnance Survey. (2022, May). *Code-point – overview* (Version 3.0) [Introduction of GeoPackage format; split from original User Guide and Technical Specification]. Ordnance Survey Ltd. Retrieved June 25, 2025, from https://www.ordnancesurvey.co.uk/documents/product-support/user-guide/code-point-overview-v3.0.pdf

PA Media. (2020, July 18). *It's not raining-just a 50-mile wide cloud of flying ants*. Retrieved June 25, 2025, from https://www.theguardian.com/uk-news/2020/jul/18/its-not-raining-just-a-50-mile-wide-cloud-of-flying-ants

Parker, M. (2017). Chapter 18 - radar basics. In M. Parker (Ed.), *Digital signal processing 101 (second edition)* (Second Edition, pp. 231–240). Newnes. https://doi.org/https://doi.org/10.1016/B978-0-12-811453-7.00018-4

Pearson, B. (1987). The sex ratio of heathland populations of the ants lasius alienus, lasius niger and their hybrids. *Insectes Sociaux*, *34*(3), 194–203. https://doi.org/10.1007/BF02224084

Peeters, C., Keller, R. A., Khalife, A., Fischer, G., Katzke, J., Blanke, A., & Economo, E. P. (2020). The loss of flight in ant workers enabled an evolutionary redesign of the thorax

for ground labour. *Frontiers in Zoology*, *17*(1), 33. https://doi.org/10.1186/s12983-020-00375-9

Petsopoulos, D., Lunt, D. H., Bell, J. R., Kitson, J. J. N., Collins, L., Boonham, N., Morales-Hojas, R., & Evans, D. M. (2021). Using network ecology to understand and mitigate long-term insect declines. *Ecological Entomology*, *46*(4), 693–698. https://doi.org/https://doi.org/10.1111/een.13035

Pfeiffer. (2017). Lasius niger queen dorsal. Retrieved June 25, 2025, from http://www.antbase.net/new-species/august-2017/lasius-niger-queen-dorsal-big.html

Population estimates for the uk, england, wales, scotland and northern ireland: Mid-2021. (2022). Office for National Statistics. Retrieved May 14, 2025, from https://www.ons.gov.uk/peoplepopulationandcommunity/populationandmigration/populationestimates/bulletins/annualmidyearpopulationestimates/mid2021

Powney, G. D., Carvell, C., Edwards, M., Morris, R. K. A., Roy, H. E., Woodcock, B. A., & Isaac, N. J. B. (2019). Widespread losses of pollinating insects in britain. *Nature Communications*, *10*. https://doi.org/10.1038/s41467-019-08974-9

Prather, M. J., & Hsua, J. C. (2019). A round Earth for climate models. *Proceedings of the National Academy of Sciences of the United States of America*, *116*(39), 19330–19335. https://doi.org/10.1073/pnas.1908198116

Probert-Jones, R. (2014). The History of the First Twenty-Five Years of Radar Meteorology in the United Kingdom. *Occasional Papers on Meteorological History*, *14*, 1–44. https://www.rmets.org/sites/default/files/hist14.pdf

Reddit. (2017). Is this a lasius niger queen? Retrieved July 3, 2025, from https://www.reddit.com/r/ants/comments/6ig40w/is_this_a_lasius_niger_queen/

Rennie, S. J. (2012, November). *Doppler weather radar in Australia* (tech. rep.). The Centre for Australian Weather and Climate Research. Melbourne.

Reppert, S. M., & de Roode, J. C. (2018). Demystifying monarch butterfly migration. *Current Biology*, *28*(17), R1009–R1022. https://doi.org/https://doi.org/10.1016/j.cub.2018.02.067

Riley, J. (1985). Radar cross section of insects. *Proceedings of the IEEE*, *73*(2), 228–232. https://doi.org/10.1109/PROC.1985.13135

Rosch, N. (2011). The derivation of algorithms to compute elliptic integrals of the first and second kind by Landen-transformation. *Boletim de Ciencias Geodesicas*, *17*(1), 03–22. https://doi.org/10.1590/s1982-21702011000100001

Roy, H. E., Martinou, A. F., Pocock, M. J., Werenkraut, V., & Roy, D. B. (2024). The global reach of citizen science for monitoring insects. *One Earth*, *7*, 552–557. https://doi.org/doi:10.1016/j.oneear.2024.03.009

Saltikoff, E., Friedrich, K., Soderholm, J., Lengfeld, K., Nelson, B., Becker, A., Hollmann, R., Urban, B., Heistermann, M., & Tassone, C. (2019). An overview of using weather radar for climatological studies: Successes, challenges, and potential. *Bulletin of the American Meteorological Society*, *100*(9), 1739–1752. https://doi.org/10.1175/BAMS-D-18-0166.1

Sanchez-Bayo, F., & Wyckhuys, K. A. (2019). Worldwide decline of the entomofauna: A review of its drivers. *Biological Conservation*, *232*, 8–27. https://doi.org/https://doi.org/10.1016/j.biocon.2019.01.020

Sane, S. P. (2003). The aerodynamics of insect flight. *Journal of Experimental Biology*, *206*(23), 4191–4208. https://doi.org/10.1242/jeb.00663

Schultheiss, P., Nooten, S. S., Wang, R., Wong, M. K. L., Brassard, F., & Guenard, B. (2022). The abundance, biomass, and distribution of ants on earth. *Proceedings of the National Academy of Sciences*, *119*(40), e2201550119. https://doi.org/10.1073/pnas.2201550119

Shamoun-Baranes, J., Nilsson, C., Bauer, S., & Chapman, J. (2019). Taking radar aeroecology into the 21st century. *Ecography*, *42*(5), 847–851. https://doi.org/https://doi.org/10.1111/ecog.04582

Sjoberg, L. E., & Shirazian, M. (2012). Solving the Direct and Inverse Geodetic Problems on the Ellipsoid by Numerical Integration. *Journal of Surveying Engineering*, *138*(1), 9–16. https://doi.org/10.1061/(ASCE)SU.1943-5428.0000061

Smith, A., Reynolds, D., & Riley, J. (2000). The use of vertical-looking radar to continuously monitor the insect fauna flying at altitude over southern england. *Bulletin of entomological research*, *90*, 265–77. https://doi.org/10.1017/S0007485300000389

Spartan Colloege of Aeronautics and Technology. (2021, November). The History of Radar. Retrieved June 25, 2025, from https://www.spartan.edu/news/the-history-of-radar/

Starrlight, A., Konstadia, L., & Sebastiaan, A. K. (2019). Altricial-precocial spectra in animal kingdom [Ecosystem based management and the biosphere: a new phase in DEB re-

search]. *Journal of Sea Research*, *143*, 27–34. https://doi.org/https://doi.org/10.1016/j.seares.2018.03.006

Stepanian, P. M., Entrekin, S. A., Wainwright, C. E., Mirkovic, D., Tank, J. L., & Kelly, J. F. (2020). Declines in an abundant aquatic insect, the burrowing mayfly, across major North American waterways. *Proceedings of the National Academy of Sciences*, *117*(6), 2987–2992. https://doi.org/10.1073/pnas.1913598117

Stepanian, P. M., Mirkovic, D., & Chilson, P. B. (2018a). A polarimetric Doppler radar time-series simulator for biological applications (N. Horning & C. Duncan, Eds.). *Remote Sensing in Ecology and Conservation*, *4*(4), 285–302. https://doi.org/10.1002/rse2.80

Stepanian, P. M., Mirkovic, D., & Chilson, P. B. (2018b). A polarimetric Doppler radar time-series simulator for biological applications (N. Horning & C. Duncan, Eds.). *Remote Sensing in Ecology and Conservation*, *4*(4), 285–302. https://doi.org/10.1002/rse2.80

Stepanian, P. M., & Wainwright, C. E. (2018). Ongoing changes in migration phenology and winter residency at bracken bat cave. *Global Change Biology*, *24*(7), 3266–3275. https://doi.org/https://doi.org/10.1111/gcb.14051

Sumner, S., Bevan, P., Hart, A. G., & Isaac, N. J. (2019). Mapping species distributions in 2 weeks using citizen science. *Insect Conservation and Diversity*, *12*(5), 382–388. https://doi.org/https://doi.org/10.1111/icad.12345

Talbot, M. (1945). A Comparison of Flights of Four Species of Ants. *The American Midland Naturalist*, *34*(2), 504–510.

The Python Standard Library. (n.d.). statistics - Mathematical statistics functions. Retrieved June 25, 2025, from https://docs.python.org/3/library/statistics.html%20https://github.com/python/cpython/blob/3.11/Lib/statistics.py

Thompson, J. N. (1998). Rapid evolution as an ecological process. *Trends in Ecology and Evolution*, *13*, 329–332. https://doi.org/doi:10.1016/s0169-5347(98)01378-0

Tong, Z.-Y., Wu, L.-Y., Feng, H.-H., Zhang, M., Armbruster, W. S., Renner, S. S., & Huang, S.-Q. (2023). New calculations indicate that 90percent of flowering plant species are animal-pollinated. *National Science Review*, *10*(10), nwad219. https://doi.org/10.1093/nsr/nwad219

Torvik, B., Olsen, K. E., & Griffiths, H. D. (2014). X-band measurements of radar signatures of large sea birds. *2014 International Radar Conference*, 1–6. https://doi.org/10.1109/RADAR.2014.7060266

Uhler, J., Haase, P., Hoffmann, L., Hothorn, T., Schmidl, J., Stoll, S., Welti, E. A. R., Buse, J., & Müller, J. (2022). A comparison of different malaise trap types. *Insect Conservation and Diversity*, *15*(6), 666–672. https://doi.org/https://doi.org/10.1111/icad.12604

UK Butterfly Monitoring Scheme. (2024). Welcome to the UKBMS. Retrieved November 17, 2024, from https://ukbms.org

UK Governement. (2021). Office for National Statistics.

UK Pollinator Monitoring Scheme. (2024). FIT Counts: help us monitor pollinators. Retrieved November 17, 2024, from https://ukpoms.org.uk/fit-counts

Van der Have, T., Pedersen, J., & Boomsma, J. (2011). Mating, hybridisation and introgression in Lasius ants (Hymenoptera: Formicidae). *Myrmecological News*, *15*, 109–115.

van Gasteren, H., Krijgsveld, K. L., Klauke, N., Leshem, Y., Metz, I. C., Skakuj, M., Sorbi, S., Schekler, I., & Shamoun-Baranes, J. (2019). Aeroecology meets aviation safety: Early warning systems in europe and the middle east prevent collisions between birds and aircraft. *Ecography*, *42*(5), 899–911. https://doi.org/https://doi.org/10.1111/ecog.04125

Vanicek, P., & Krakiwsky, E. (1982). *Geodesy: The Concepts*. North-Holland Publishing Company.

Vaughn, C. (1985). Birds and insects as radar targets: A review. *Proceedings of the IEEE*, *73*(2), 205–227. https://doi.org/10.1109/PROC.1985.13134

Vincenty, T. (1975). Direct and Inverse solutions of geodesics on the ellipsoid with application of nested equations. *Survey Review*, *22*(176), 88–93. https://www.ngs.noaa.gov/PUBS_LIB/inverse.pdf

Wagner, D. L., Grames, E. M., Forister, M. L., Berenbaum, M. R., & Stopak, D. (2021). Insect decline in the anthropocene: Death by a thousand cuts. *Proceedings of the National Academy of Sciences*, *118*(2), e2023989118. https://doi.org/10.1073/pnas.2023989118

Wagner, D., & Gordon, D. M. (1999). Colony age, neighborhood density and reproductive potential in harvester ants. *Oecologia*, *119*(2), 175–182. Retrieved January 15, 2025, from http://www.jstor.org/stable/4222293

Walker, D. W., Smigaj, M., & Tani, M. (2021). The benefits and negative impacts of citizen science applications to water as experienced by participants and communities. *WIREs Water*, *8*(1), e1488. https://doi.org/https://doi.org/10.1002/wat2.1488

Wang, R., Kou, X., Cui, K., Mao, H., Wang, S., Sun, Z., Li, W., Li, Y., & Hu, C. (2022). Insect-equivalent radar cross-section model based on field experimental results of body length and orientation extraction. *Remote Sensing*, *14*(3). https://doi.org/10.3390/rs14030508

Weisstein, E. W. (n.d.). Elementary Function. Retrieved June 25, 2025, from https://mathworld.wolfram.com/ElementaryFunction.html

Westbrook, J., & Eyster, R. (2017). Doppler weather radar detects emigratory flights of noctuids during a major pest outbreak. *Remote Sensing Applications: Society and Environment*, *8*, 64–70. https://doi.org/https://doi.org/10.1016/j.rsase.2017.07.009

Wilcove, D. S., & Wikelski, M. (2008). Going, going, gone: Is animal migration disappearing. *PLOS Biology*. https://doi.org/https://doi.org/10.1371/journal.pbio.0060188

Wilson, E. O. (1969). Mechanisms of insect dispersal: Migration and dispersal of insects by flight. *Science*, *166*(3905), 592–592. https://doi.org/10.1126/science.166.3905.592.a

Wolff, C. (n.d.). Sidelobe Suppression. Retrieved June 25, 2025, from https://www.radartutorial.eu/06.antennas/an70.en.html

World Meteorological Organization, W. (2023a). *Guide to operational weather radar best practices volume i: Weather radar network programme design* (tech. rep. No. WMO-No. 1257). Technical Commissions (former) ¿ Commission for Instruments and Methods of Observation (CIMO). https://library.wmo.int/idurl/4/68826

World Meteorological Organization, W. (2023b). *Guide to operational weather radar best practices volume ii: Weather radar technology* (tech. rep. No. WMO-No. 1257). Technical Commissions (former) ¿ Commission for Instruments and Methods of Observation (CIMO). https://library.wmo.int/idurl/4/68827

Wotton, K. R., Gao, B., Menz, M. H., Morris, R. K., Ball, S. G., Lim, K. S., Reynolds, D. R., Hu, G., & Chapman, J. W. (2019). Mass Seasonal Migrations of Hoverflies Provide Extensive Pollination and Crop Protection Services. *Current Biology*, *29*(13), 2167–2173. https://doi.org/10.1016/j.cub.2019.05.036

Yi, Y. (2007). *On improving the accuracy and reliability of gps/ins-based direct sensor georeferencing* [Doctoral dissertation, The Ohio State University]. https://kb.osu.edu/bitstreams/b37b2478-7041-523e-ad80-545af01636e0/download

Zeng, Y., Blahak, U., Neuper, M., & Jerger, D. (2014). Radar beam tracing methods based on atmospheric refractive index. *Journal of Atmospheric and Oceanic Technology*, *31*(12), 2650–2670. https://doi.org/10.1175/JTECH-D-13-00152.1

Zhang, L. (2005). Implications of geodesy, spatial reference systems, and map projections in processing, conversion, integration, and management of gis data. *Proceedings of the 1st Saudi GIS Symposium*. http://www.saudigis.org/FCKFiles/File/SaudiGISArchive/1stGIS/Papers/10.pdf

Zooniverse. (2024). About the Zooniverse. Retrieved November 17, 2024, from https://www.zooniverse.org/about#highlights